Faculty of Engineering and Physical Sciences

Materials Engineering Department

Achieving ultra-high strength of Al-Cu-Li and Al-Zn-Mg-Cu alloys by the combination of High Pressure Torsion and age hardening

By

Jiahui Dong

Thesis for the degree of Doctor of Philosophy

July 2021

UNIVERSITY OF SOUTHAMPTON

FACULTY OF ENGINEERING AND PHYSICAL SCIENCES

SCHOOL OF MATERIALS ENGINEERING

Doctor of Philosophy

ACHIEVING ULTRA-HIGH STRENGTH OF Al-Cu-Li AND Al-Zn-Mg-Cu ALLOYS BY THE COMBINATION OF HIGH PRESSURE TORSION AND AGE HARDENING

By Jiahui Dong

Abstract

This report presents an experimental study on two types of heat treatable aluminium alloys to determine the best process for achieving ultra-high-strength materials by means of severe plastic deformation (SPD) and heat treatment. It is well-known that age hardening and grain refinement are two mechanisms that contribute to strengthening. Accordingly, high pressure torsion (HPT), which induces an ultra-fine grain (UFG) structure, combined with artificial ageing were performed on an Al-Cu-Li and an Al-Zn-Mg-Cu alloy.

A series of hardness measurements against various ageing times and temperatures were investigated to provide an insight into strengthening. A strong increase in hardness of Al-Cu-Li alloys was achieved through the combination of age hardening and HPT. Specifically, following solution treatment, materials were processed through five turns of HPT at room temperature (RT), followed by low temperature ageing (i.e. T4-HPT-AA). For the Al-Cu-Li alloy, a micro-hardness up to ∼240 Hv for ageing 110 ^{o}C/60h with the maximum percentage increase of 8.5% after as-HPT condition was achieved. However, the low temperature ageing after HPT does not improve the hardness of Al-Zn-Mg-Cu alloy. Besides, a further improvement in the hardness to ∼260 Hv for Al-Cu-Li was accomplished by a pre-ageing 110 ^{o}C/24h before HPT in combination with a post-HPT ageing process at 110 ^{o}C for approximately 180h (i.e. T6-HPT-AA). These novel multi-stage processes give rise to an increase in hardness by a factor of 2 as

compared to the T4 condition (~120 Hv). Under the same process sequence using similar ageing temperatures, the Al-Zn-Mg-Cu alloy shows post-HPT age-softening. However, a reduced age-softening rate was obtained compared with the sample that had undergone solution treatment followed by HPT and ageing process, which connotes the stability of the material increased due to pre-HPT ageing.

As both T4-HPT-AA and T6-HPT-AA processes do not enhance the hardness of the Al-Zn-Mg-Cu alloy, further investigations in microstructural analysis were performed only on Al-Cu-Li alloy. Accordingly, X-ray diffraction (XRD), Transmission electron microscopy (TEM), Differential scanning calorimetry (DSC) and Atom probe tomography (APT) characterisation techniques were conducted on the optimum condition processed Al-Cu-Li alloy in all stages of two processing procedures (T4-HPT-AA and T6-HPT-AA) from solution treatment to final ageing hardening. Aimed at improving the understanding of the combined strengthening effects of HPT and age hardening on the strength of the 3rd generation Al-Cu-Li alloy.

Grain size of T4 and T6-processed samples was dramatically refined during HPT from microscale level ~3 μm down to ~ 90 nm and ~ 115 nm, respectively. Such small grain size (UFG structure) was retained after subsequent peak ageing 110 ^{o}C /60h in T4-HPT-AA and 110 ^{o}C /180h in T6-HPT-AA conditions. In addition, HPT introduces large amount of dislocations with the highest dislocation density of 3.50×10^{14} m^{-2} in T4-HPT condition. No long-range ordered precipitates were observed by both XRD and TEM techniques after HPT and subsequent ageing treatments. Instead, atom probe tomography (APT) provided clear evidence that Cu-Mg co-clusters are homogeneously distributed in the matrix of T4 and T6 processed samples, and they segregate strongly to the grain boundaries (GBs) during HPT. Further ageing treatment after HPT leads to the segregation of clusters at the dislocations.

Finally, a strengthening model that incorporates dislocation hardening, grain boundary hardening, solid solution strengthening and a new short-range order cluster strengthening mechanisms was used to predict the yield strength of the Al-Cu-Li alloy. In this work, for the first time, a new cluster strengthening model is addressed to provide detailed explanations for each individual type of cluster strengthening mechanism, i.e. clusters in matrix, at grain boundaries and dislocations. The predicted strength from the model demonstrates that the combined effect of all three types of Cu-Mg clusters is the dominant mechanism for the high strength of the Al-Cu-Li alloy.

Research Thesis: Declaration of Authorship

I, Jiahui Dong, declare that the thesis entitled

Achieving ultra-high strength of Al-Cu-Li and Al-Zn-Mg-Cu alloys by the combination of High Pressure Torsion and age hardening

and the work presented in the thesis are both my own, and have been generated by me as a result of my own original research.

I confirm that

- This work was done wholly or mainly while in candidature for a research degree at this University;
- Where any part of this thesis has previously been submitted for a degree or any other qualification at this University or any other institution, this has been clearly stated;
- Where I have consulted the published work of others, this is always clearly attributed;
- Where I have quoted from the work of others, the source is always given. With the exception of such quotations, this thesis is my own work with the help of my supervisors on writing and proofreading;
- I have acknowledged all main sources of help;
- Where the thesis is based on work done by myself jointly with others, I have made clear exactly what was done by others and what I have contributed myself;
- Part of this work has been submitted as:

1. **Jiahui Dong**, Nong Gao, Ying Chen, Lingfei Cao, Hui Song, Hannes Fröck, Benjamin Milkereit, Marco J Starink, *Achieving ultra-high strength of Al-Cu-Li alloys by the combination of High Pressure Torsion and age-hardening,* submitted to Material Science Engineering: A.

2. **Jiahui Dong**, Nong Gao, Ying Chen, Marco J Starink, *A strengthening model due to defect-cluster interactions for an Al-Cu-Li alloy processed by the combination of High Pressure Torsion and age-hardening,* submitted to Material Science Engineering: A.

Signature:…………………

Date: 19/08/2021

Acknowledgements

I would like to express my sincere appreciation to the following people who provided strong supports to me, and this thesis would not be possible without their supports.

First and foremost, a huge thanks to my supervisors Professor Marco J Starink and Dr Nong Gao, for their invaluable advice, continuous support, and patience throughout the whole course of my PhD research. Their immense knowledge and plentiful experience have encouraged me all the time during my PhD study.

I would like to thank the Faculty of Engineering and the Environment at the University of Southampton for their financial support throughout my study.

Additionally, I gratefully acknowledge Dr Ying Chen, Xiamen University of Technology, China, Prof Lingfei Cao, Electron Microscopy Centre of Chongqing University, China, and Prof Benjamin Milkereit, University of Rostock, Germany, for their invaluable help in the TEM, APT and DSC experiments.

I would also like to thank all the staff and students in the Material Engineering Group at the University of Southampton for their insightful comments and suggestions.

Finally, I would like to express gratitude to my Mom and Dad for their unwavering support and belief in me. Without their love and financial support for all these years, I would have never achieved this.

CONTENTS

Abbreviations

AA	Artificial ageing
APB	Anti-phase boundary
APT	Atom probe tomography
ARB	Accumulative roll-bonding
ASR	Asymmetric rolling
BCC	Body-centered cubic
BF	Bright field
BSE	Back-scattered electrons
CEC	Cyclic extrusion compression
CP	Commercial purity
CRSS	Critical resolved shear stress
DC	Direct current
DF	Dark field
DSC	Differential scanning calorimetry
EBSD	Electron back scatter diffraction
ECAP	Equal channel angular pressing
EDS	Energy dispersive spectroscopy
FCC	Face-centered cubic
FIB	Focused ion beam
FWHM	Full width at half the maximum
GBs	Grain boundaries
GNDs	Geometrically necessary dislocations
GP zone	Guinier-Preston zone
HAADF	High angle angular dark field
HAGBs	High angle misorientation grain boundaries
HPT	High pressure torsion
HREM	High-resolution electron microscopy
HRTEM	High-resolution transmission electron microscopy
IB	Integral breath
IVAS	Imago Visualization and Analysis Software

LAGBs	Low angle misorientation grain boundaries
MAUD	Materials Analysis using Diffraction
OIM	Orientation imaging microscopy
OM	Optical microscopy
PAS	Positron annihilation spectroscopy
PFZs	Precipitation-free zone
PV	Pseudo-Voigt
RCS	Repetitive corrugation straightening
RT	Room temperature
SAED	Selected area electron diffraction
SCC	Stress corrosion cracking
SEM	Scanning electron microscopy
SFs	Stacking faults
SPD	Severe plastic deformation
SSDs	Statistically stored dislocation
SSSS	Super saturated solid solution
STD	Standard deviation
STEM	Scanning transmission electron microscopy
TEM	Transmission electron microscopy
UFG	Ultra-fine grain
VRC	Vacancy-rich cluster
XRD	X-ray diffraction

Nomenclature

b	Burgers vector
c_j	Concentrations of alloying elements in solid solution
C_p	the heat capacity
D_c	the crystallite size
d	the grain diameter
$\mathrm{d}_{\mathrm{max}}$	the characteristic distance
dl	the change of arc displacement
$d\gamma$	the incremental shear strain
f_1	the fraction of A-B cluster
f_2	the fraction of A segregated to dislocations
f_3	the fraction of B segregated to dislocations
f_4	the fraction of A-B co-clusters segregated to dislocations
P	total number of intersections
P_k	the preferred orientation function
f^{cl}	the volume fraction of the clusters
G	shear modulus
h	the disk thickness
Hv_0	the intrinsic hardness
Hv	the Vickers hardness
I_i^{calc}	the structure factor of the cells
k_{HP}	Hall-Petch constant
k_j	the strengthening factor for individual elements
$\bar{L}$	Mean intercept length
L_k	Lorentz-Polarization factor
L_{total}	Total length of lines
M	Taylor factor
N	the number of revolutions
N_{HV}	the number of indentations
R	the radial distance from disk centre

r	the radius of the cylinder
T	Temperature
T_g	Glass transition temperature
U_{el}	the elastic energy associated with a dislocation
$\bar{x}$	the average value of indentations
x_i^{HV}	the value of individual indentation
x_{Cu}	the concentrations of Cu atoms in Al matrix
x_{Mg}	the concentrations of Mg atoms in Al matrix
$y_{\mathrm{A},1}$	the number of A atoms in clusters-matrix
$y_{\mathrm{B},1}$	the number of B atoms in clusters-matrix
$y_{\mathrm{A},2}$	the number of A atoms in clusters-GBs
$y_{\mathrm{B},2}$	the number of B atoms in clusters-GBs
$y_{\mathrm{A},3}$	the number of A atoms in clusters-dislocations
$y_{\mathrm{B},3}$	the number of B atoms in clusters-dislocations
α_1	an empirical constant ranging from 0.2-0.5, taken 0.3 in Al alloys
α_2	a constant to evaluate yield strength increment due to grain boundary
γ_{SRO}	the change in energy per unit area on slip plans
$< \varepsilon^2 >^{1/2}$	the internal lattice microstrain
k_{HP}	Hall-Petch constant
$\Delta H_{\mathrm{A-B}}$	the enthalpy of A-B clusters in the matrix
$\Delta H_{\mathrm{A-B-gb}}$	enthalpy of A-B clusters at the GBs
$\Delta\sigma_{gb}$	grain boundary strengthening
$\Delta\tau_0$	the intrinsic critical resolved shear stress of the grains
$\Delta\tau_{cl}$	the contribution due to co-clusters
$\Delta\tau_d$	the contribution due to dislocation
$\Delta\tau_m$	the modulus strengthening component
$\Delta\tau_{SRO}$	the short range order strengthening component
$\Delta\tau_{ss}$	the contribution due to solid solution strengthening
$\Delta\tau_{tot}$	the total critical resolved shear stress of the grains
ε_{eq}	the equivalent strain

ε_{true}	the true strain
θ	the glancing angle of diffraction, the Bragg angle
μ_{cl}	the average cluster ($M_mA_aB_b$) modulus
γ	the plastic shear strain
γ_{SRO}	the change in energy per unit area on slip plans
v	the Poisson’s ratio
π	the universal constant in the Debye-Scherrer formula
ρ_{dis}	Dislocation density
ρ_{gb}	Grain boundary density
ρ_{GND}	dislocation density of geometrically necessary dislocations
ρ_{SSD}	dislocation density of statistically stored dislocations
σ	the tensile flow stress
σ_o	the instrinic yield strength
σ_y	the yield strength
τ	the shear flow stress
φ	the rotation angle
χ^2	the residual function

List of Figures

List of Tables

Chapter 1 Introduction

1.1 Background and motivation

The third generation of Al-Li alloys has been developed since the last decade. In recent years, under the increasing demand for fuel efficiency and cost efficiency, Al-Cu-Li alloys have gained great attention for their uses in the aircraft industry and aerospace programmes owing to their lightweight combined with a balance of damage tolerance and good formability [1–3]. In particular, they have recently been employed in many advanced aerospace applications such as Boeing 777, Airbus 380, NASA space shuttle in view of their low density, high specific strength and stiffness combined with a balance of fracture toughness and fatigue cracking growth resistance [4,5]. An experimental Al-2.88Cu-1.34Li-1.03Mg-0.09Zr (wt. %) alloy with a composition similar to the 3rd generation of Al-Li alloys was designed based on retaining or optimising the critical properties of the 2024-T351 alloy. This alloy possesses a yield strength of ~325-350 MPa, good age formability, fatigue crack growth resistance and toughness [6].

7xxx (Al-Zn-Mg-Cu) series aluminium alloys have been extensively used in modern airframe manufacture due to their numerous benefits, including high specific strength, good strength (approximately $>$ 600 MPa), weight saving, good toughness and generally enhanced performance. Among these alloys, 7449 (Al-8.1Zn-2.25Mg-1.75Cu) was designed to replace 7150 alloys, particularly for applying the upper wing skin of aircraft [7].

Both Al-Zn-Mg-Cu and Al-Cu-Li are heat treatable Al alloys. The strengthening mechanisms mainly rely on age hardening, which consists of solution treatment, quench, and ageing. This treatment causes the formation of small uniformly dispersed particles of second phase, termed ‘precipitates’, that inhibit the dislocation motion, thus increasing the strength [8,9].

Besides, grain refinement can also lead to a significant increase in the strength of metallic materials. In principle, grain boundaries act as obstacles to dislocation, and materials resist deformation by dislocation pile-up at grain boundaries. The pile-up of dislocations creates a driving force, which pushes these dislocations to adjacent grains. The reduction in grain size results in fewer dislocations pile-up at GBs, requiring considerable stress to move dislocations to the next grains, increasing the strength of materials [10]. Given this, the fabrication of ultra-fine grain (UFG) structure through severe plastic deformation (SPD) is an effective method. UFG materials contain almost entirely homogeneous and equiaxed microstructures with an average grain size less than 1 μm (100-1000 nm) and with high angle grain boundaries (misorientation angle greater than 15^o) [11]. As one of the most popular severe plastic deformation (SPD) techniques, high pressure torsion (HPT) involves processing through a combination of compressive force and torsional straining. HPT-processed materials possess a high density of dislocations and, in many cases, achieve exceptional levels of grain refinement to UFG microstructure [12].

In addition, the formation of clusters and co-clusters were observed in many Al-based metallic alloys during solution treatment or low temperature ageing in the past three decades [13–16]. These clusters have been accepted to be the dominant strengthening factor due to a short-range order strengthening mechanism. More recently, the UFG Al-Cu-Mg (AA2024) [17] and Mg-Gd-Y-Zn alloys [18] processed by HPT showed the segregation and clustering of solutes at GBs. Such clusters serve as obstacles to grain growth and stabilise the nanosized grains via pinning the grain boundaries, providing an extra strengthening effect in UFG alloys.

To exploit the strengthening mechanisms that contribute to the high strength of metallic alloys, several detailed models which incorporate the grain refinement and dislocation strengthening contributions were proposed [19–22]. In subsequent works, the solute atoms were also considered as part of strengthening effects, and segregation of solute atoms at grain boundaries was detected in the 7075 and 7136 Al alloys after SPD processing [23–25]. On this basis, a physically-based model incorporating solute clusters and segregation cluster-defect complexes strengthening was then established by Chen et al. [26], which successfully predicted the strength of the UFG Al-Cu-Mg alloy. However, this model does not provide detailed explanations for each individual type of cluster strengthening mechanism, i.e. clusters in matrix, clustering at GBs and dislocations. In addition, although there are some works on the dislocation-solute interaction [16], very little is known about the enthalpy change of clustering at dislocations and amount of strengthening provided by these dislocation-solute complex structures. Hence, the understanding of the strengthening due to clusters on defects is discussed, and enthalpy values of different types of clusters are estimated in this work.

Several existing studies show that the hardness and strength of materials can be substantially improved by HPT processing [27–30]. However, the combinational strengthening effects of HPT and age hardening are difficult to achieve because it is still a challenge to generate fine precipitates within ultra-fine grains through subsequent ageing while retaining the small grain size and high dislocation density [31]. To date, many combinations of ECAP and ageing have been successfully used to enhance the strength of Al alloys, especially pre-ECAP solution treatment combined with post-ECAP low temperature ageing [32–36]. In contrast, only a few works have been published regarding the strengthening effects provided by the combination of HPT and age hardening [31,37,38]. Among them, only one publication is on the Al-Cu-Li alloy [31]. So far, no study has been conducted on the combined effects of HPT and age hardening on the strength of the Al-Zn-Mg-Cu alloy.

1.2 Aims and objectives

This research aims to obtain ultra-high strength via the combined effects of HPT and artificial ageing (AA) in age-hardenable alloys. The work focuses on Al-Cu-Li and Al-Zn-Mg-Cu alloys as they are age hardenable alloys with two or more alloying elements involved in hardening. According to an empirical relationship between yield strength and hardness $\sigma_y \approx 3HV$, micro-hardness measurements can provide an indication of the yield strength. Accordingly, two different processing conditions were performed on two types of Al alloys. (1) Solution treatment + HPT + artificial ageing (i.e. T4-HPT-AA). (2) Solution treatment + artificial ageing + HPT + artificial ageing (i.e. T6-HPT-AA).

In this work, a series of micro-hardness tests as a function of the ageing time at various temperatures was measured for both alloys prepared in two processing conditions. The processing temperature and ageing time used to obtain the highest strength of materials were selected as the optimum processing condition. The combination of HPT and age hardening, which usually enhance the strength of the metals and alloys, has been found to be ineffective in improving the strength of 7449 Al alloys. Therefore, only Al-Cu-Li alloys processed by the optimum condition were investigated for further microstructural analysis.

Several techniques, including X-ray diffraction (XRD) and transmission electron microscopy (TEM) were conducted to assess the grain features, microstructural characteristics of Al-Cu-Li alloy in each stage of processing condition. Dislocation densities were evaluated by analysing XRD line broadening profiles based on the Rietveld method. Atom probe tomography (APT) was used to examine the behaviour of solute clusters, and differential scanning calorimetry (DSC) was employed to explore the thermal effects that occur in different processing conditions. Finally, a strengthening model that includes grain boundary hardening, dislocation strengthening, solid solution strengthening and a new short-range order strengthening mechanisms is applied to evaluate the contributions of strengthening mechanisms and predict the yield strength of Al-Cu-Li alloy.

1.3 Thesis structure

The PhD thesis is structured as follows: Chapter 1 presents the background, motivation, aims and objective of the current research. A comprehensive literature review is given in Chapter 2, containing fundamental knowledge regarding the studied materials (Al-Cu-Li and Al-7449), the introduction of strengthening mechanisms, HPT technique, characterization techniques, as well as strength models. Chapter 3 describes the detailed experimental processing procedures used in this research. Also, it explains the rationale for the chosen experimental methods.

Chapter 4 investigates the optimum processing conditions for obtaining the highest hardness of materials by performing a series of micro-hardness tests on the materials. In addition, a discussion on the micro-hardness of materials subjected to the combined effects of HPT and age hardening is presented in this chapter. In chapter 5, the microstructural evolution of Al-Cu-Li alloy is investigated by XRD and TEM, and a discussion on the microstructure is given. Segregation of solute elements and clustering at GBs and dislocations in an ultrafine-grained Al-Cu-Li alloy are studied by APT and DSC in Chapter 6. In Chapter 7, the strength of Al-Cu-Li is predicted by existing models, and a new modified cluster strengthening model is established. This chapter also analyses and estimates the amount of solute atoms clustered at the defects and the enthalpy value involved in the modified cluster strengthening model. Finally, Chapter 8 summarises the main conclusions from the current research and suggestions for future works.

Chapter 2 Literature review

2.1 Introduction of aluminium

2.1.1 History of aluminium and its production

Aluminium is the third most abundant metallic element in the earth's crust, and its alloys are the second most widely used alloy system today [39]. In 1808, Al was first identified as a chemical element by Sir Humphry Davy, and then Danish chemist Hans Christian Orsted in 1825 claimed to have isolated Al, but it was controversial. Two years later, Friedrich Wohler modified Orsted's experiment to produce Al, and he is generally credited as the first person to have done so. In 1886 Hall and Heroult independently invented a process for the electrolytic reduction of pure metallic aluminium [39]. This invention enabled large-scale production of Al as a commercially viable undertaking.

Raw aluminium exists in all types of clay. Bauxite containing 25% aluminium oxide was chosen to produce aluminium oxide (alumina) by digestion with a sodium hydroxide solution under pressure, known as the Bayer process. Therefore, the modern manufacture of aluminium is achieved by two processes: the Bayer process and the Hall-Heroult process. The Bayer process refers to refining aluminium ore to obtain alumina, and Hall-Heroult process is developed to smelt the aluminium oxide to form pure aluminium [39].

Pure or near pure metallic aluminium has numerous valuable properties such as low density, low melting point, great corrosion resistance, good workability, good thermal and electrical conductivity. These properties allow it useful in an extensive range of applications. In addition, high strength Al or further valuable features can be accomplished by adding suitable alloying elements and heat treatments. For this reason, aluminium alloys can be categorised into different groups based on the main alloying element added and mechanical or thermal treatment [40].

2.1.2 Aluminium alloy categories

Generally, aluminium alloys fall into two main categories, cast and wrought, and each of these two categories has its own system of identification. The wrought system has a 4-digit system, and the cast system has a 3-digit and 1-decimal place system. Each category can be subdivided into heat treatable and non-heat treatable alloys [41,42].

The wrought alloy nomenclature system is listed in Table 2-1 below [41]. The first digit represents the alloy group in terms of the major alloying elements. The second digit defines alloy modification, and the last two digits identify alloys or other aluminium purities. The cast alloys nomenclature is also given in Table 2-1 [41]; the first digit represents major alloying addition, the following two digits show individual alloys in the group. Finally, the last digit serves the product form: casting is 0, and ingot is 1 [40].

The 1xxx, 3xxx, and 5xxx series in wrought aluminium alloys are defined as non-heat treatable group. These alloys do not respond to strengthening via heat treatment, and they acquire strengthening by work hardening or strain hardening. The heat treatable aluminium alloys include 2xxx, 6xxx, and 7xxx series. Their optimum mechanical properties can be achieved through heat treatment process. 4xxx series contains both heat treatable and non-heat treatable materials. Moreover, cast alloys 2xx.x, 3xx.x, 4xx.x and 7xx.x groups are heat treatable. Alloy indications often contain basic temper designation, shown in Table 2-2 [43]. Where, **H** - Strain hardened, **T** - Thermally treated. **O** - Annealed, **F** - As-fabricated and **W** – Solution treated [40,43].

Table 2- 1. The wrought Al alloys designation system [41].

4-digit designation	**Major alloying elements**
1xxx	99.00% Al minimum
2xxx	Cu
3xxx	Mn
4xxx	Si
5xxx	Mg
6xxx	Mg, Si
7xxx	Zn
8xxx	Others

3-digit designation	**Major alloying elements**
1xx.x	>99.00% Al
2xx.x	Cu
3xx.x	Si plus Cu or Mg
4xx.x	Si
5xx.x	Mg
7xx.x	Zn
8xx.x	Sn
9xx.x	other

Table 2- 2. The Cast Al alloys designation system [42].

Suffix letter	
F	As-fabricated
O	Annealed wrought products
H **Cold worked (strain hardened)**	1− Cold worked only 2− Cold work& partially annealed 3− Cold worked& stabilised
W	Solution treated
T **Heat treatment**	1− Partial solution + natural ageing 2− Annealed cast only 3− Solution + cold work 4− Solution + natural ageing 5− Artificial ageing only 6− Solution + artificial ageing 7− Solution + stabilising 8− Solution + cold work + artificial ageing 9− Solution + artificial ageing + cold work

2.1.3 Strengthening mechanism of Al alloys

Most heat treatable Al alloys are strengthened by precipitation hardening, also termed as age hardening. The process consists of three steps: (1) Solution treatment: the alloy is heated above solvus temperature in single phase region to allow solute atoms to be dissolved and a homogenous solid solution is attained; (2) Quenching: Rapid quenching (cooling) to obtain a non-equilibrium supersaturated solid solution (SSSS); (3) Artificial ageing: Controlled heating of the supersaturated solid solution at intermediate temperature (above room temperature but well below the solvus temperature) in multi-phase region to form finely dispersed precipitates within the grains [8]. These precipitates act as obstacles to impede dislocation motion, leading to larger forces for dislocation to pass the precipitates. Consequently, the strength and hardness of materials can be enhanced.

Non-heat treatable Al alloys may respond to hardening by solid solution, often coupled with work hardening [44]. The strength of these alloys is improved by alloying aluminium with additional elements in solid solution, and these alloys include Al-Mn, Al-Si and Al-Mg. The strain field introduced by these solute atoms interacts with the strain fields of dislocations, leading to an enhancement in the strength of alloy [45]. In addition, the strength can be further increased through strain hardening or work hardening, which is accomplished via processes such as cold rolling, stretching, drawing through dies, or HPT and ECAP processing.

Here in the present report, two heat-treatable Al-Cu-Li and Al-Zn-Mg-Cu alloys were studied. For that reason, attention is paid mainly to the precipitation hardening mechanism.

2.2 Al-Cu-Li and its strengthening mechanism

2.2.1 Al-Cu-Li

Due to the high demand for high specific strength materials in space programmes and the aircraft industry for fuel efficiency and better performance, many aluminium alloys with different contents of Li and Cu have been developed over the last four decades. It has been reported that adding 1% of lithium to aluminium will lead to a reduction of density up to ~3% and an improvement in Young's elastic modulus by ~6% [46]. Moreover, the strength of Al-Li alloys strongly depends on the content of Li. Hagiwara et al. [47] reported that the addition of Li to AA2219 alloy introduced a continual increase in strength, with the content of Li increasing up to 1.25%. Moreover, Kumar and Heubaum [48,49] found that the desirable combination of strength and toughness for Al-Li alloy was achieved when alloy containing ~1.3% lithium, beyond this level results in a significant decrease in strength.

The 1st generation Al-Li alloy Al-4.45Cu-1.21Li-0.51Mn (AA2020) was reported in the late 1950s for the wing component in aircraft application [50]. It lasted for more than 20 years without fracture or corrosion issues until the 1960s. It was withdrawn from commercial application due to poor ductility and high brittleness [1]. After that, the 2nd generation Al-Li materials contained over 2 wt. % of Li content was developed. Although weight reduction was attractive, these 2nd Al-Li alloys exhibited a significant in-plane and through-thickness anisotropy in their tensile properties. Additionally, they performed low short-transverse fracture toughness, poor thermal stability and corrosion resistance. For that reason, the 3rd generation Al-Li alloys such as 2094, 2095, 2096, 2097, etc. were developed with reduced Li concentration, which gives desirable combinations of properties for a variety of commercial uses [1].

The alloy studied in this report is Al-Cu-Li (Al–2.88Cu–1.34Li–1.03Mg) alloy, whose composition is similar to the 3rd generation Al-Li alloys.

2.2.2 Age hardening

The desirable mechanical properties of 3rd generation Al-Li alloys are attributed mainly to age hardening. The ternary Al-Cu-Li alloys have a complex precipitation sequence, revealing aspects of both Al-Cu and Al-Li binary systems. The Al-Cu sequence gives GPI, GPII (θ'') and $\theta'(Al_2Cu)$ precipitates [51]. The Al-Li sequence can generate δ' (Al_3Li) phase, and the formation of this strongly depends on the content of Li [52]. Furthermore, the addition of other minor alloy elements, such as Mg, Zr and Ag, will significantly alter their phase equilibria and make the precipitation sequence even more diverse. Adding Mg to Al-Cu-Li alloys may result in the formation of Cu-Mg co-cluster (GPB zones) or $S/S'(Al_2CuMg)$ phases. The presence of S' phase was found near the grain boundaries, which will generate a precipitation-free zone (PFZs) [53,54]. Furthermore, a small amount of Zr will cause the formation of β' (Al_3Zr) phase. Omega (Ω) precipitates will be formed when adding Ag and Mg in Al-Cu-Li alloys [55]. Although the formation of several co-precipitation metastable phases is involved in strengthening of Al-Cu-Li alloys, produced T_1 (Al_2CuLi) phase was reported to be the primary precipitates attributed to the strengthening by Gayle et al. [56].

Additionally, according to the processing condition and composition of the alloy, other minor phases such as T_2 (Al_6CuLi_3) and T_B may also be formed, especially at grain boundaries [57]. Each of these precipitates is in competition for Cu or Li solute and nucleation sites, and the size and distribution of them are controlled by heat treatment processes [58]. Most Al alloys decompose via complex decomposition paths involving the formation of metastable phases/precipitates. Understanding the decomposition paths is essential for designing novel materials. Hence, the various possible precipitates including δ' phase, θ' phase, T_1 phase, S' and S phases, β' phase, Ω phase and clusters are discussed in detail respectively in the following section.

δ′ phase

The precipitation sequence of the binary Al-Li system was first discovered by Silcock et al. [59] as:

$$\text{SSSS} \rightarrow \delta' \, (Al_3Li) \rightarrow \delta \, (AlLi)$$

SSSS stands for supersaturated solid solution that is derived from quenching after solution treatment of alloy. The metastable δ′ phase (Al_3Li) has a $L1_2$ face-centered cubic (FCC) structure and a similar lattice constant with the Al matrix; this gives δ′ phase a coherent precipitate [56]. Two morphological types of δ′ phase have been observed; it takes a dot-shaped when it precipitates homogeneously throughout the matrix and exhibits lenticular shape when it is flanking GPI zones or around θ′ phase, as shown in Fig. 2-1 [56,60]. It has been observed that δ′ particles can be cut by dislocations in under-aged materials and bypassed in over-aged materials upon deformation [60]. Four possible strengthening mechanisms provided by δ′ phase in Al-Li system has been summarised by Noble et al. [61–63]: (1). Anti-phase boundary (APB) formed by dislocation pairs; (2). Misfit strain between Al matrix and precipitates; (3). Precipitates shearing by moving dislocation; (4). Different shear modules between precipitates and matrix. In fact, the degree of strengthening contributed by δ′ depends on the volume fraction and the size distribution of particles. For those alloys that contain a relatively low content of Li (e.g., 2xxx alloys), the volume fraction of δ′ will be lower than alloys (e.g., 809x), which results in the strengthening contribution from δ′ becomes much less than other precipitates in those alloys [64]. It is noticeable that even if δ′ contributes hardening in Al-Li-X alloys, the δ′ near the grain boundaries will reduce the ductility and toughness owing to the highly shearable behaviour of δ′ particles. This induces planar slip and causes high stress concentration at grain boundaries [61].

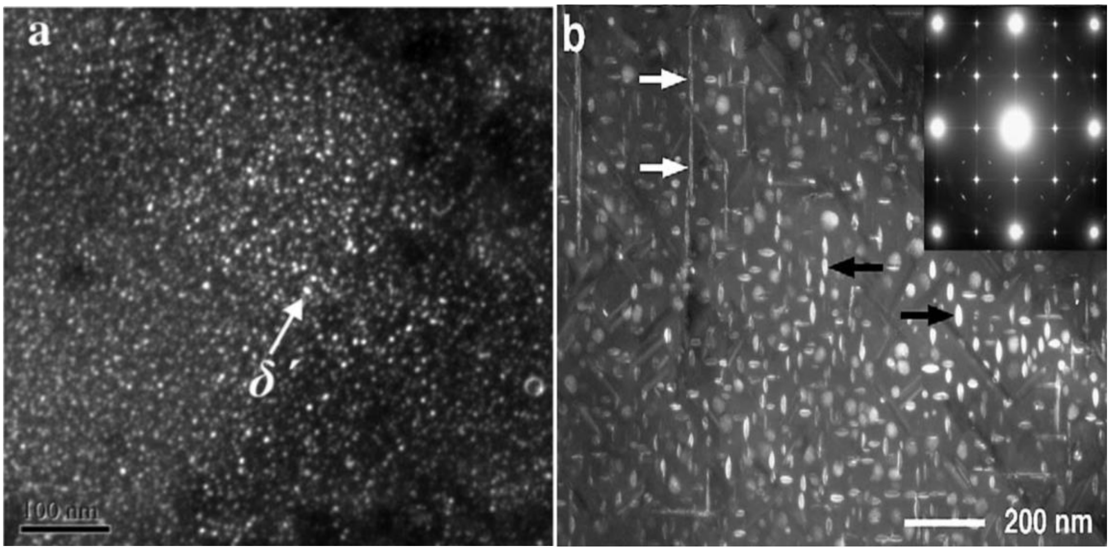

Figure 2- 1. Dark-field TEM images of (a) dot-shaped δ′ phase homogeneously throughout the matrix [63], and (b) lenticular shaped δ′ phase precipitated around θ' phase indicated by white arrows. And smaller lenticular δ′ phase flanking the GP zones indicated by black arrows [56].

<u>θ′ phase</u>

θ′ phase is a semi-coherent metastable phase, precipitates with a body-centred tetragonal structure. It appears as thin platelets or disks morphology lying on $\{0\ 0\ 2\}_{Al}$ plane, shown as Fig. 2-2. The precipitation sequence is given by:

$$\text{SSSS} \rightarrow \text{GPI zones} \rightarrow \text{GPII } (\theta'') \rightarrow \theta' \rightarrow \theta\ (Al_2Cu)$$

The addition of Cu in the Al-Li system does not affect the basic character of the δ′ precipitation reaction, but it does initiate additional precipitation reactions that benefit for strengthening in Al-Li alloys, such as precipitation reaction of θ′ phase (Al_2Cu) [65,66]. It has been shown that the nature of metastable and equilibrium phases that precipitates in the alloy is dependent on the ratio of Cu: Li and temperature of ageing [67]. For instance, Al-Li alloys contain higher Li content (>2 wt. %) and lower Cu content (<2 wt.%), the strengthening precipitate θ′ will be suppressed, and T_1 phase will form [68]. Besides, the θ′ phase has not been formed when the Cu: Li ratio <1: 3 [66]. Moreover, θ′ is treated as the dominant addition giving rise to the peak strengthening effect in Al-Cu alloys with or without Li [59].

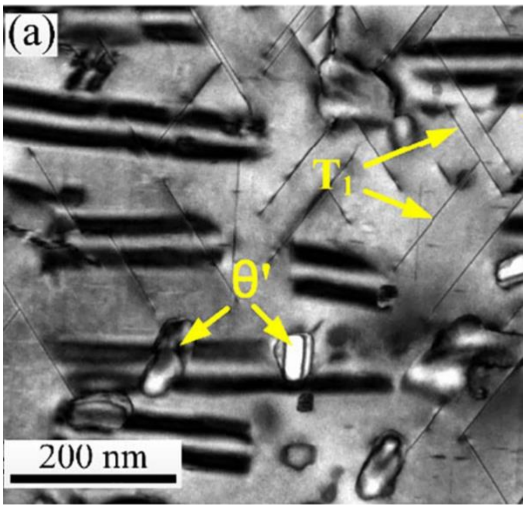

Figure 2- 2. Bright-field TEM image of 2196 Al-Li alloy under over-aged (170 °C/72 h), θ′ and T_1 precipitates are indicated by yellow arrows [69].

T_1 phase

Apart from the metastable θ′ phase, the addition of Cu also introduce a hexagonal structure T_1 (Al_2CuLi) equilibrium phase that forms as thin platelets on {1 1 1} matrix planes, as shown in Fig. 2-2 and Fig. 2-3 [69,70]. Among the S′, θ′, and δ′ phase, T_1 precipitates are generally considered to be the dominant hardening phase in the aged Al-Cu-Li alloys such as 2090 and 2195 alloys, since it behaves as a non-shearable barrier that impedes the dislocation motions [56,67,71]. The formation of T_1 follows the sequence of

$$\text{SSSS} \rightarrow \delta' + T_1 \rightarrow T_1$$

It has been found that it preferentially nucleates heterogeneously at dislocations in Al-Li-Cu alloys due to diffusional transformation. Consequently, applying plastic deformation before artificial ageing significantly influences their precipitation kinetics and the size of T_1 precipitates. The plastic deformation prior to ageing can increase the number of heterogeneous nucleation sites, resulting in a uniform distribution of heterogeneously T_1 precipitates [72–74]. Moreover, it was reported that the nucleation of T_1 phase could be strongly promoted through the addition of a minor amount (<1 wt. %) of Mg and Ag. The combined addition of Mg and Ag results in the uniform formation of T_1 particles with finer grain size, hence enhancing the strength of Al-Li alloys [75]. Nevertheless, adding a single element of Ag only makes a minor contribution to their precipitation [75].

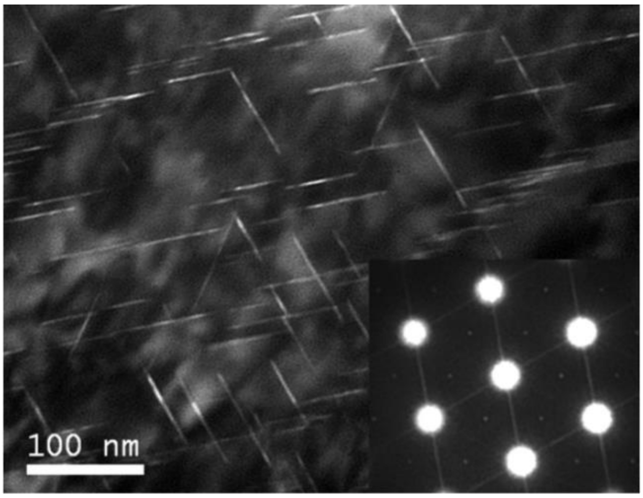

Figure 2- 3. Dark field TEM image showing the distribution of the T1 precipitates in the Al-Li-Cu alloy in T8 treatment [70].

S′ and S phases

With the addition of Mg to higher-Cu containing Al-Cu-Li alloy such as AA2090, the formation of θ′ is suppressed and instead of the S′ phase precipitates [66]. For the alloys that contain higher Li and lower Cu, i.e. 8090, S′ phase acts as the predominant Cu-bearing phase [2]. Whereas, as the ratio of Cu: Mg gradually decreases, the formation of T_1 is totally suppressed, and the Cu-bearing phase is now instead of by S′ phase, as in the case of alloy AA2091 (Al-2Li-2.2Cu-1.5Mg-0.08Zr) [66]. The precipitation sequence was suggested by Wang and Starink [76], given as:

$$\text{SSSS} \rightarrow \text{GPB zone (Cu-Mg co-cluster + GP zones)} \rightarrow S''/\ \text{GPB2} \rightarrow S' \rightarrow S$$

Where GPB (Guinier-Preston-Bagaryatsky) are ordered Cu-and Mg-rich zones in the form of thin rods along $<100>_\alpha$ directions. GPB2/S″ was thought to be fully coherent with the Al-rich phase. The lath-shaped semi-coherent S′ phase has an orthorhombic structure. It lies on $\{2\ 1\ 0\}$ matrix plane along $< 100 >$ directions. S phase has a similar structure and orientation as S′ phase except for a marginal difference in lattice parameters. Both S′ and S phases have the composition of Al_2CuMg. Moreover, two distinct S phases with different lattice parameters were identified in Al-2.5Cu-1.5Mg alloy [77]. The two different morphologies of S phase, i.e. lath-shaped and rod-shaped are shown in Fig. 2-4.

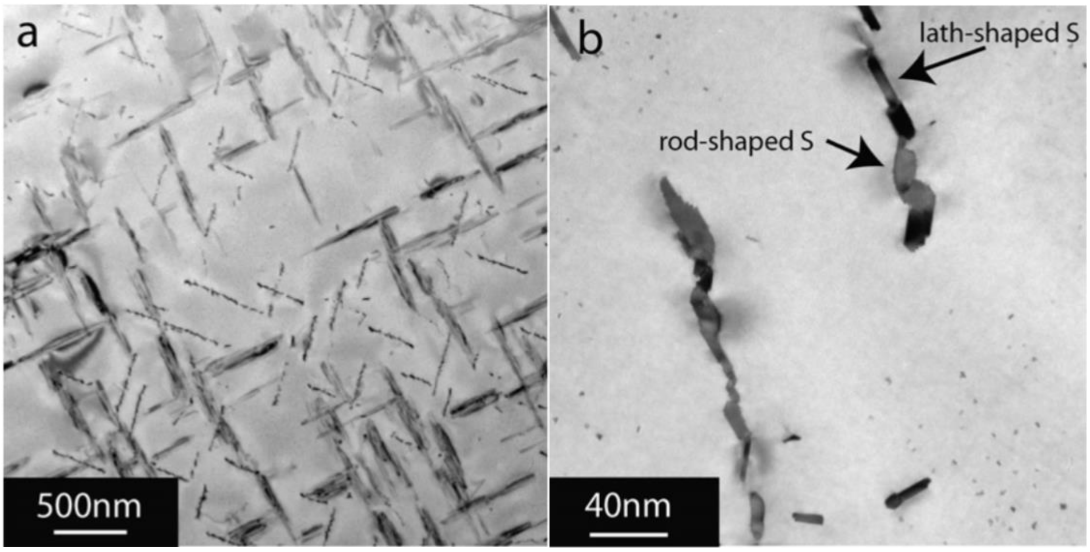

Figure 2- 4. Bright-field TEM image of S phase precipitates after ageing for (a) low-magnification and (b) high-magnification at 200 °C/9 h [77].

β′ phase

The addition of Zr in Al is associated with the formation of β′ (Al_3Zr) phase, which can effectively inhibit recrystallisation. The spherical and coherent β′ precipitates have the $L1_2$ structure shown in Fig. 2-5 [78]. Moreover, they are so stable that they can pin the grain and sub-grain boundaries in the thermomechanical processing of commercial Al alloys because of low solid solubility and sluggish diffusion of Zr in Al, and the small misfit between β′ and matrix reduces coarsening [79]. On the one hand, the effectiveness of inhibiting recrystallisation and the β′precipitation behaviour will not be affected with the addition of Li alloying elements. On the other hand, β′ phase serves as preferential heterogeneous nucleation sites for strengthening precipitates δ′ [80,81]. Later on, β′ phase was also found as preferential nucleation sites for θ′ and T_1 phases to a lesser extent [82], leading to an apparent acceleration during ageing process.

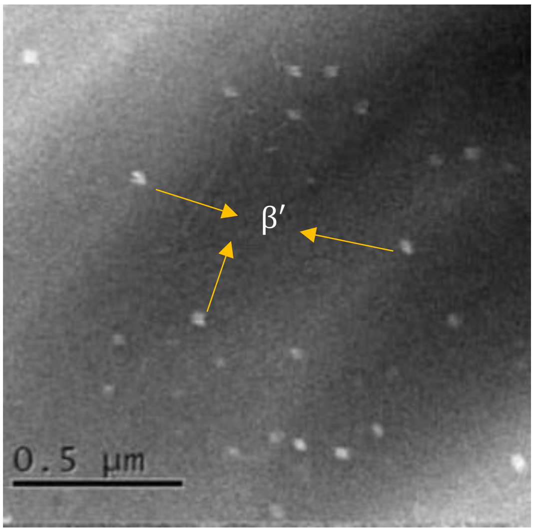

Figure 2- 5. STEM microstructures of spherical β′precipitates (indicated by yellow arrows) formed in 2198 Al-Li alloy aged after 2.5 h [78].

Ω phase

For the formation of omega Ω (Al_2Cu) phase on $\{1\ 1\ 1\}_\alpha$ matrix, many explorations related to its structure was developed. Observed crystal structures containing tetragonal, monoclinic, hexagonal and orthorhombic until Starink and Wang reviewed that the Ω phase was likely to be orthorhombic [83–86]. It has been shown that the nucleation of Ω phase can be promoted by adding a small amount of silver to Al-Li-Cu-Mg alloys. Mg plays an essential role in Ω phase, while Ag is merely acting as a catalyst for Ω phase formation [55]. The precipitation of Ω phase is shown in Fig. 2-6 [84].

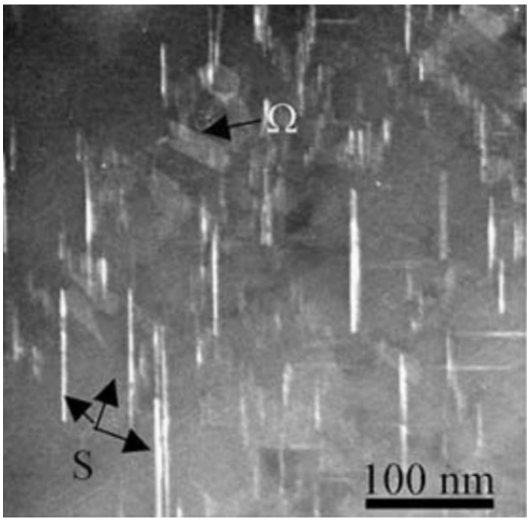

Figure 2- 6. TEM dark field image of quenched and stretched (T351) Al-2.81Cu-1.05Mg-0.41Mn (wt. %) alloy after ageing at 150°C/48h, Ω and S phases are indicated by arrows [84].

Cluster and co-clusters

Co-clusters are metastable structures including two or more different alloying atoms that retain the host lattice structure. In the early stages of decomposition of solution treated alloys, clusters are generated in the form of small precipitates (as small as 10 atoms) from a metastable solution through a solute clustering process [13]. Such solute clusters are believed to form through rapid solute diffusion mediated by vacancies inherited from quenching from solution heat treatment. The simplest co-cluster is a dimer (shown in Fig. 2-7).

Unfortunately, most microstructural analysing techniques, e.g. TEM and High-resolution electron microscopy (HREM) cannot resolve such small size clusters, while Atom probe (APT) do allow the detection of analysing these clusters. These clusters and co-clusters have been detected in many Al-based metallic alloys such as Al–Zn–Mg–Cu [15,87], Al-Mg-Ag [88], Al-Cu-Mg [13,16,89] and Al-Mg-Si [14,90] alloys, with a size as small as ~0.3 nm. As the cluster and co-clusters are shearable, the Orowan strengthening mechanism will not be applicable. Therefore, many strengthening mechanisms (i.e. short-range order strengthening, modulus hardening and chemical hardening) related to obstacle shearing are used to explain the strengthening effects [13].

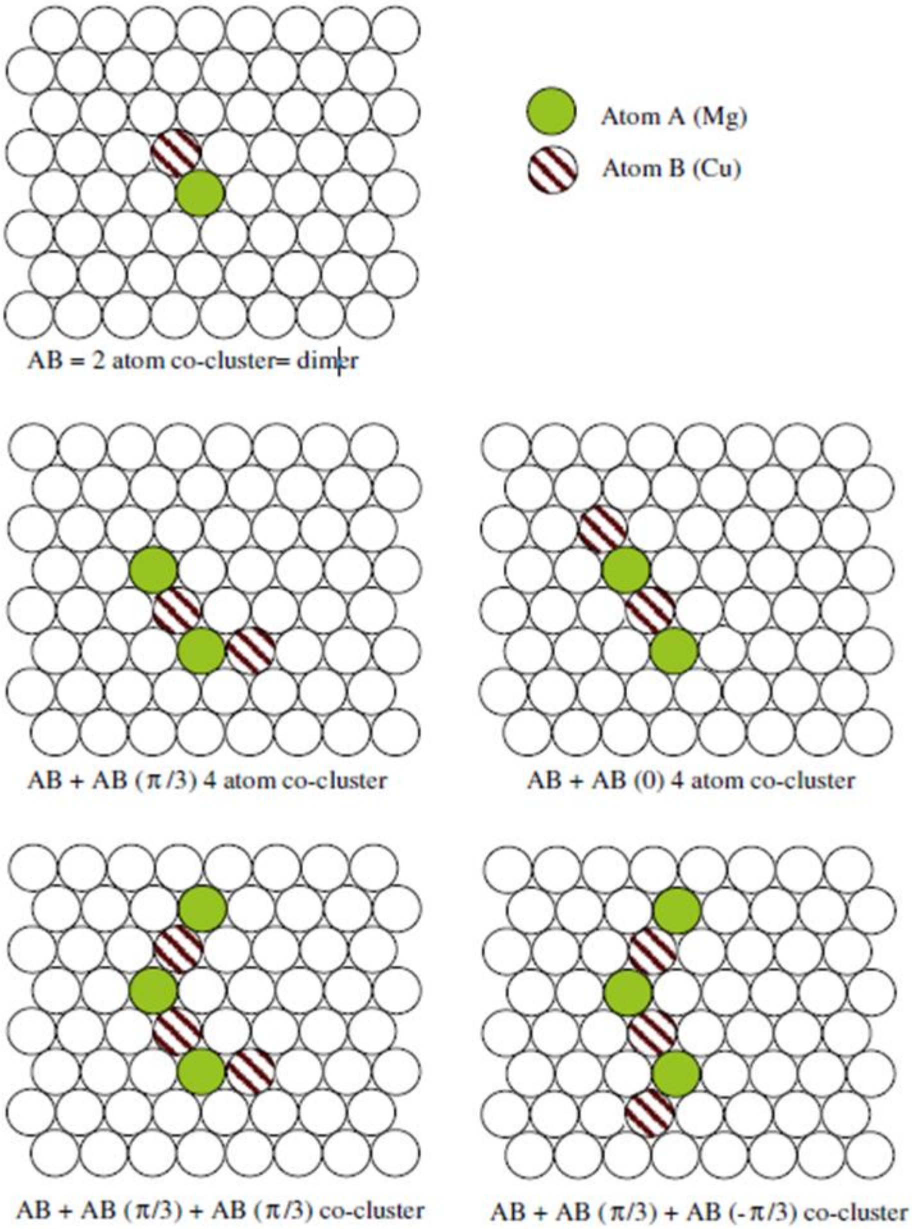

AB = 2 atom co-cluster= dimer

AB + AB (π/3) 4 atom co-cluster

AB + AB (0) 4 atom co-cluster

AB + AB (π/3) + AB (π/3) co-cluster

AB + AB (π/3) + AB (- π/3) co-cluster

Figure 2- 7. The schematic diagram of co-cluster [13].

2.3 Al-Zn-Mg-Cu and its strengthening mechanism

2.3.1 Al-Zn-Mg-Cu

The 7xxx series precipitation hardening Al alloys are based on either the ternary Al-Zn-Mg or the quaternary Al-Zn-Mg-Cu system, which are utilised widely in the aerospace industry due to their high specific strength, high ductility and excellent stress corrosion cracking (SCC) resistance [91,92]. This type of alloy contains Zn, Mg and Cu as the main alloy elements and some other minor amount of additives such as Zr, Mn, Fe, Si, etc.

2.3.2 Age hardening

These main mechanical properties of 7xxx series alloys strongly rely on the main precipitates formed during heat treatment and the heat treatment routes, and the precipitation greatly depends on the alloy composition. Accordingly, many alloys have been developed with increasing solute content and varying the ratio between three main alloying additions to obtain high strength [3]. The addition of these elements produces a classical accepted precipitation sequence through the age hardening process, which is given by [93]:

$$\text{SSSS} \rightarrow \text{GP zones (GPZs)} \rightarrow \text{Metastable } \eta' \rightarrow \text{Stable } \eta$$

GPs are Guinier-Preston zones; it was confirmed that two distinct GP zones in tertiary Al alloys: GPI and GPII exist within artificially aged 7xxx Al alloys [91,94]. Furthermore, η' ($MgZn_2$) and η ($MgZn_2$) are intermediate and equilibrium phase, respectively. Therefore, both GP zones and metastable η' are either indirectly or directly contributing to the peak hardening effect.

GPs Zones

Under an early stage of precipitation, GP zones are formed since the energy of nucleation barrier for direct formation of stable precipitation is high. These fine-scale zones are solute-enriched regions, which obstructs dislocation motions thus contributes to strengthening. With the aid of high-resolution transmission electron microscopy (HRTEM) and selected area electron diffraction (SAED), two types of GP zones with different structures were observed in Al-Zn-Mg alloy [94]. These observations were proposed in detail by L. K. Berg [94]. GPI zones are spherical Mg-rich clusters, and the structure of GPI zones was suggested to be coherent with Al matrix, located on $\{0\ 0\ 1\}_{Al}$ plan with the internal ordering of Zn and Al/Mg on the matrix lattice [95]. They are formed when quenched Al-Zn-Mg alloy undergoes RT ageing and later found to generate over a wide ageing temperature range up to ~150 ^{o}C [96]. However, GPII zones are thin plates vacancy-rich clusters, created at a high ageing temperature after quenching from temperature above 450 ^{o}C and followed by ageing temperature above 70^{o}C [96,97]. According to diffraction evidence, the GPII zones are also coherent with the Al matrix and were found as a zinc-rich layer situated on $\{1\ 1\ 1\}$ plan with the internal ordering of elongated $\langle 1\ 1\ 0\rangle$ domains. TEM images of GPI and GPII zones are shown in Figs. 2-8 (a) and (d) [97].

The TEM images of GPs zones distributions were reported in many research [98,99]. Generally, either GPI or GPII can serve as precursors to η' phase. In practice, the role of GP zones on the precipitation of η' and the strength of Al-Zn-Mg alloys is disputable. The precise precipitation sequence still remains to be investigated. For example, Gang and Cerezo [93] and Chen et al. [100] proposed that only GPI zones and η' phase are formed during ageing process, and GPI zones act as the precursor to η' phase. Nevertheless, Berg et al. [94] and Fan et al. [101] observed that both GPI and GPII zones were formed in the alloy after ageing process.

With Cu present, the precipitation sequence of Al-Zn-Mg-Cu becomes more complicated. It is known that Cu plays a significant role in the decomposition of supersaturated solid solution [102]. It is also suggested that the addition of Cu can alter the morphology of GPs zones and increase the GPs zones solvus temperature [103,104]. For instance, GP zones in Al-Zn-Mg alloys shown a spherical shape. Nevertheless, Al-Zn-Mg-Cu alloy GPI was observed to be spherical and GPII to be ellipsoidal [104]. It has also been found that the ageing kinetics and quench sensitivity of Al-Zn-Mg alloys are raised with the adding of Cu [103,105].

η′and η phases

The η′ phase has been considered as predominantly hardening phase in Al-Zn-Mg alloys as the maximum strength are typically associated with the dispersion of fine η′ particles. The formation of η′ phase occurs and coexists with GP zones when the Al-Zn-Mg-Cu alloy is aged at temperature in a range of ∼60−180 ^{o}C [96]. Moreover, it nucleates preferentially at the four types of nucleation sites: (1). GP zones of overcritical size; (2). Quenched-in clusters-rich vacancies; (3). Concentration fluctuation left behind by dissolving GP zones in low concentration alloys ($C_{Zn} \leqslant$ 2.5%); (4). Impurity atoms [96]. Based on many crystal structure models either from X-ray diffraction or HRTEM analysis, η′ has been commonly recognised as a hexagonal cell structure with a=0.496 nm and c=1.402 nm, and it is semi-coherent with Al matrix. Furthermore, it has plate-shaped with a thickness of ∼3 nm and a diameter of 5 nm [106]. Moreover, η phase is transformed from its precursor η′ phase, and this equilibrium $MgZn_2$ phase is incoherent with Al matrix. The structure of equilibrium phase η has a hexagonal lattice (a = 0.521 nm, c = 0.860 nm) with a stoichiometric composition of $MgZn_2$ [94]. TEM images of η and η′ phases are shown in Figs. 2-8 (b-c) [97].

Other precipitates may be formed depending on the ageing temperature and the composition of those minor additive elements such as S (Al_2CuMg) and T ($Mg_3Zn_3Al_2$), but they are thought not to contribute to the hardening of Al-Zn-Mg-Cu alloy [107].

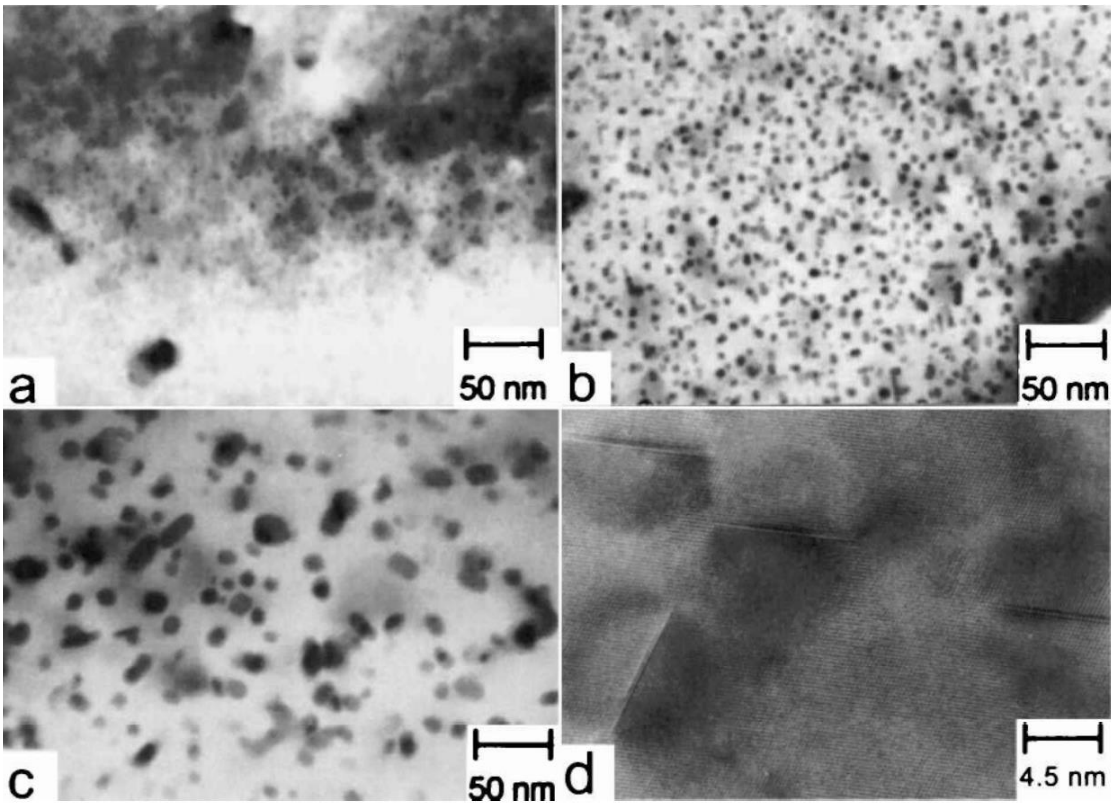

Figure 2- 8. TEM images of (a). GP(I) zones; (b). η′ precipitates (100 h, 115°C, solution temperature 550°C); (c) η and η′ particles (100 h, 145°C, solution temperature 450°C); (d) high-resolution image of GP(II) [97].

There are some factors that affect precipitation sequences. As reported, depending on ageing temperature and alloy composition, η′ phase can be nucleated through GP zones or can nucleate on the agglomerates of alloying atoms and vacancies, which is regarded as vacancy-rich cluster (VRC) [96,106]. As remarked by Dupasquier et al. [108], two families of VRC are generated during or immediately after quenching. They are differed by the content of Zn and thermal stability, the more stable giving the richest in Zn content [108]. The VRCs form during or after immediate quenching, and they disappear from alloys simultaneously with the formation of GP zones, hence may having a significant effect on the precipitation process and GPs zone formation. Chinh et al. [104] suggested that the formation regimes of GPZs and η′ are different in Al-Zn-Mg alloys, but they are strongly overlapping in Al-Zn-Mg-Cu alloys. They found that in Al-Zn-Mg alloys precipitation of η′ phase occurs on ageing at 130 ^{o}C, but GP zones cannot form. However, in Al-Zn-Mg-Cu alloys, the formations of VRCs and GP zones are from quenching and ageing, respectively. Both VRCs and GPZs assist the nucleation of η' phase. Therefore the precipitation sequence after quenching and ageing at 130 ^{o}C is given as [104]:

$$\text{In Al-Zn-Mg:} \quad \text{SSSS} \rightarrow \text{VRCs} \rightarrow \eta' \rightarrow \eta$$

$$\text{In Al-Zn-Mg-Cu:} \quad \text{SSSS} \rightarrow \text{VRCs} + \text{GP zones (formed at } 130^{o}\text{C)} \rightarrow \eta' \rightarrow \eta$$

In addition, in industrial praxis hardening of Al-Zn-Mg alloy, plastic deformation will be applied after quenching to release the residual stress and quench distortion (strain less than 5%). The plastic deformation induces large dislocation density, which can alter the precipitation sequence. In principle, precipitates are more likely to nucleate on dislocations as lower free energy change required for nucleation [109,110]. In addition, dislocation causes short-circuit diffusion path for solutes, leading to faster growth and coarsening of precipitates on dislocation than in bulk [111,112]. Moreover, the presence of precipitation on the dislocations naturally stimulates the stable phases η rather than metastable phases η'. Additionally, Deschamps et al. [110] pointed out the influences of pre-straining or pre-deformation and ageing process parameters on precipitating sequence. The pre-deformation increases kinetics of ageing process and directly forms equilibrium η on dislocations without precipitating intermediate η' phase.

2.4 Severe plastic deformation

Forging, rolling, compression and extrusion are conventional metal processing methods of achieving smaller grain size materials. In such methods, materials undergo multi-pass plastic strain processing with von Mises strain less than 2.0 in each pass. The increase in strain accompanied by the subsequent passes results in a significant reduction of the thickness and diameter of materials. Whereas for structural use, bulky dimension is required. Therefore, it is crucial to have a process that imposes a large strain on the bulk material with nearly unchanged dimensions, in which case the materials can be used as structural parts [113,114].

Severe plastic deformation is a grain refinement method that imposes a massive plastic strain over 4.0 on materials without significant overall shape-changing. Prior to the SPD process, grain refinement has been accomplished mainly by above conventional processing methods and subsequent annealing. The minimum grain size obtained through these workings has been approximately 10 µm. While processing by SPD is able to convert the coarse grain materials into UFG materials whose mean grain size is less than 1 µm [113]. In addition, the dimensions during SPD process has remained via geometries of special tools, which avoids the free flow of material and leads to hydrostatic pressure. Hydrostatic pressure gives high strain and induces high dislocation density in the process, thereby improving the strength of materials [115].

Various SPD techniques have already been established, such as high pressure torsion (HPT), equal channel angular pressing (ECAP) [115], accumulative roll-bonding (ARB) [116], repetitive corrugation, cyclic extrusion compression (CEC) [117] and repetitive corrugation straightening (RCS) [118]. Among them, the most popular processes are HPT and ECAP techniques which have been well-proposed to fabricate UFG materials. In this review, attention is paid to HPT processing, although it has limitations for structural applications because only small samples are workable.

2.4.1 The principle of high pressure torsion

High pressure torsion is a technique in which the sample, generally in the form of small disk, is torsionally deformed under hydrostatic pressure; the principle of HPT is depicted schematically in Fig. 2-9 [30]. The device consists of an upper and a lower anvil, the disk sample is located in a spherical depression which is in between the inner surfaces of two anvils. When starting to operate, the sample is subjected to a large pressure, typically 2 to 6 GPa, and simultaneously a rotational strain is provided through surface friction force between sample and anvils.

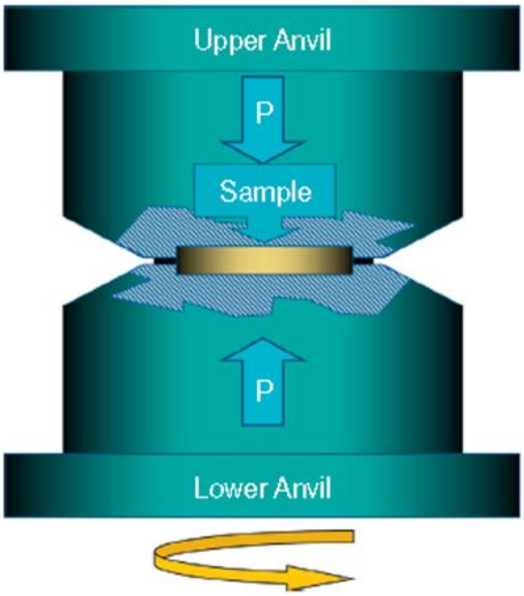

Figure 2- 9. Schematic principle of quasi-constrained HPT device [30].

HPT devices are mainly divided into two different types according to their geometry of anvils and the extent of outward flow of materials. One is non-outward flow during the processing, also called constrained HPT (see Fig. 2-10 (a) [12]); the disk sample suffers a lateral restriction. In this design of the device, the sample is placed within a cavity in the lower anvil, and the high compressive pressure is applied when a plunger from the upper anvil moves into the cavity. In this case, the thickness of disk remains unchanged, and the shear strain is given by [115]:

$$\gamma = \frac{r}{h}\varphi \tag{2- 1}$$

Where r is the radial distance from disk centre, h is the thickness of the disk, and φ is the rotation angle in radians. Another type is referred to as Quasi-constrained HPT, which is commonly used today and is shown in Fig. 2-10 (b). The combined depths of two depressions of two anvils are designed to be slightly less than the thickness of the sample so that some limited outward flow occurs during operating. Consequently, there is a reduction in the thickness of the material, h. In order to estimate strain applied in HPT, the incremental shear strain $d\gamma$ is given by [119]:

$$d\gamma = \frac{dl}{h} \tag{2- 2}$$

Where, dl is the change of arc displacement and $dl = r\varphi$, shown in Fig. 2-11, the incremental shear strain $d\gamma$ is now given by:

$$d\gamma = \frac{dl}{h} = \frac{r\varphi}{h} \tag{2- 3}$$

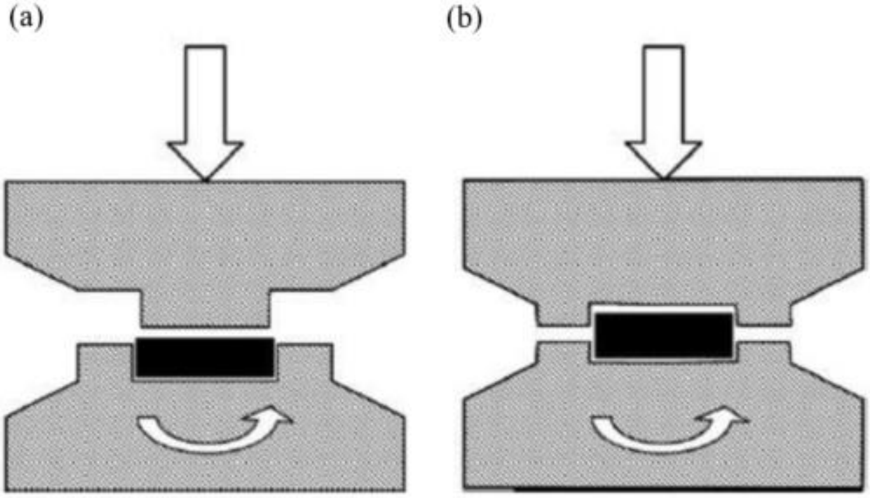

Figure 2- 10. Schematic illustration for constrained HPT (a) and Quasi-constrained HPT [12].

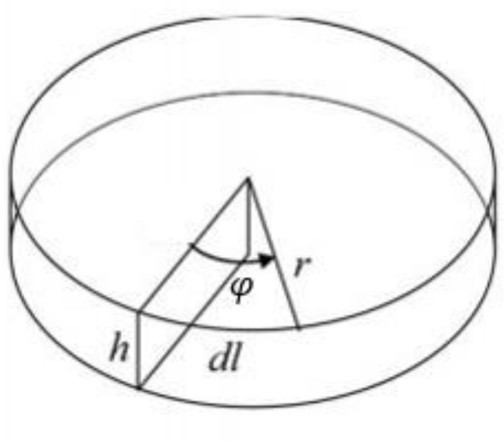

Figure 2- 11. Schematic of estimating true strain of disk samples [119].

Since $\varphi = 2\pi N$, where N signifies the number of revolutions, if thickness, h, is assumed to be independent of rotation angle, φ, it follows from formal integration that the shear strain is given by [119]:

$$\gamma = \frac{2\pi N r}{h} \tag{2- 4}$$

The equivalent strain has been calculated in many publications through von Mises criterion relationship, given as:

$$\varepsilon_{eq} = \frac{\gamma}{\sqrt{3}} \tag{2- 5}$$

In some papers, this is also termed as effective strain and defined as:

$$\varepsilon_{ef} = \frac{2\pi N r}{\sqrt{3} h} \tag{2- 6}$$

The use of Eq. 2-4 and 2-5 are obeyed only for a small imposed shear strain, when large shear strain $\gamma \geq 0.8$, the equivalent strain now becomes [27]:

$$\varepsilon_{eq} = \frac{2}{\sqrt{3}} \, ln\left[(1+\frac{\gamma^2}{4})^{\frac{1}{2}}+\frac{\gamma}{2}\right] \tag{2- 7}$$

Another relationship was developed to incorporate the reduction of thickness as a consequence of the applied pressure, P. The true strain is now given by [27]:

$$\varepsilon_{true} = ln\left[1+(\frac{r\varphi}{h})^2\right]^{\frac{1}{2}} + ln\frac{h_0}{h} \tag{2- 8}$$

Where h_0 represents initial thickness, and h signifies final thickness. Since $\frac{r\varphi}{h} \gg 1$, the Eq. 2-8 is then simplified to:

$$\varepsilon_{true} = ln(\frac{r\varphi}{h}) + \ln(\frac{h_0}{h}) = \ln\frac{r\varphi h_0}{h^3}) = \ln(\frac{2\pi rNh_0}{h^3}) \tag{2- 9}$$

Also, the true logarithmic strain can be expressed as:

$$\varepsilon_{true} = ln(1+\varepsilon_{eq}) = ln\,(1+\frac{r\varphi}{\sqrt{3}h}) = ln\,(1+\frac{2\mathrm{r}\pi\mathrm{N}}{\sqrt{3}\mathrm{h}}) \tag{2- 10}$$

This latter equation is usually simplified to:

$$\varepsilon_{true} = ln\,(\frac{2r\pi N}{\sqrt{3}h}) \tag{2- 11}$$

Therefore, Eq. 2-4 to 2-11 provide the relationships that can estimate the total strains on the disks subjected to HPT. Additionally, based on Eq. 2-11, it is obvious that the amount of true strain changes depending on the radial position measured from the centre. The maximum strain is found along the periphery, the minimum value of zero strain at the centre when r = 0. Hence, a conclusion is drawn that the strain varies across the whole disk, leading to a significant inhomogeneity in the microstructure. Nevertheless, a reasonable homogeneous microstructure was observed in many HPT-processed materials when the processing is continued through a sufficient number of torsional revolutions [120], and the details will be discussed in the next Section 2.4.2.

2.4.2 Variation of inhomogeneity caused by HPT

In principle, the imposed strain changes across the diameter of the disk sample with a minimum strain (= 0) at the central region, which can result in an inhomogeneous microstructure. However, many experimental results suggested that there is a potential to accomplish a homogeneous microstructure through gradual revolution. To investigate the homogeneity of microstructure after HPT, the correlation of local micro-hardness measured by Vickers micro-hardness with the microstructural images taken by TEM is the most convenient method. Consequently, materials including high-purity Ni [28], austenitic steel [29], commercial purity (CP) Al [27], Al-Mg-Sc alloy [121] and Cu [122] were shown to have lower hardness in the central region at the beginning of deformation. In contrast, materials such as high purity Al was reported to have a higher hardness in the centre and lower value in the peripheral at the early stage [123]. However, the microstructures of both types of materials become reasonable homogeneous across the surface of the disk as the torsional and compression strain reach sufficiently high values.

Al-3Mg-0.2Sc (wt. %) as a representative of inhomogeneity microstructures by processing through HPT deformation, i.e. highest Hv in the edge, lowest Hv in the centre. The variations of hardness across the horizontal mid-section of the samples under a pressure of 1 GPa at a rotation speed of 1 revolution per minute (rpm) were recorded in Fig. 2-12 [121]. The results have shown a non-uniform distribution of Hv across the disk diameter with a significant lower Hv in the centre under a low pressure of 1 GPa for 1 turn. These results showed that the hardness reaches a maximum of approximately ∼140-150 Hv at both outer edges but reduces to ∼95 Hv at the centre of the disk.

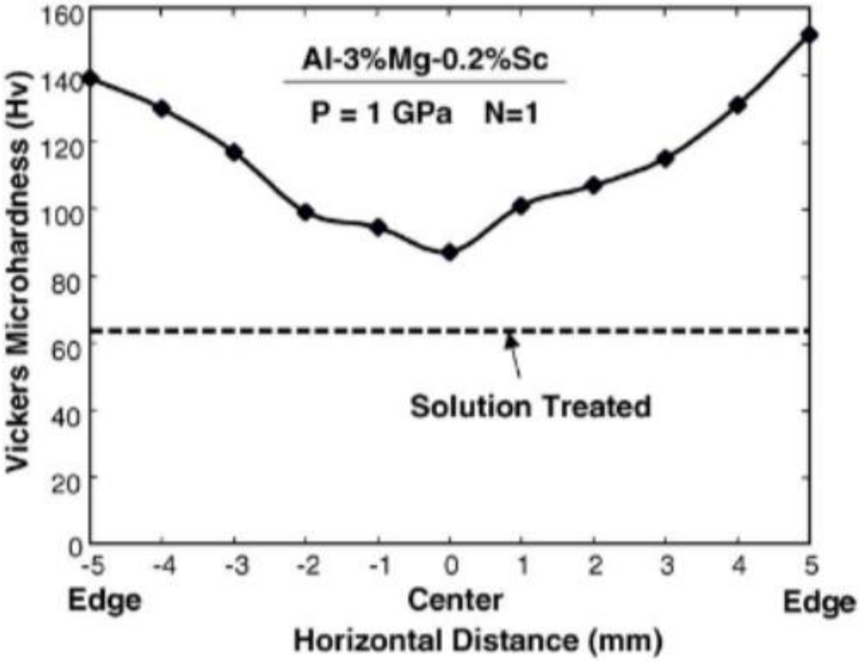

Figure 2- 12. Variation of Hv micro-hardness along the diameter of the Al-Mg-Sc disk deformed by 1 GPa of HPT [121].

By contrast, high purity aluminium was observed to have an inverse result from previous observations in that the peripheral regions of disk have a lower hardness value, see Fig. 2-13 (a). It is well known that pure Al has high stacking fault energy as well as recovery rate [123]. As strain in the central region is lower than that of the edge, the microstructure evolution occurs much quicker in the edge. In pure Al, this results in a fast recovery rate in the periphery and a delayed recovery rate in the centre. As a result, the hardness in the centre is initially higher than the edge. In addition, Fig. 2-13 (b) illustrates that the inhomogeneity at the centre region reduces as the rotation number increases. When the number of turns exceeds five, hardness distribution becomes more homogeneous (see Fig. 2-13(c)), and this is because the microstructure of the periphery reaches an equilibrium condition with continuously increasing strain [123]. It is noted that hardening due to HPT is relatively limited in pure Al. Nevertheless, with low stacking fault energy or low recovery process materials like commercial Al [27], the microstructural evolution is slow. The hardness will reach the highest in the periphery initially, and large imposed strains are needed to achieve a homogenous microstructure.

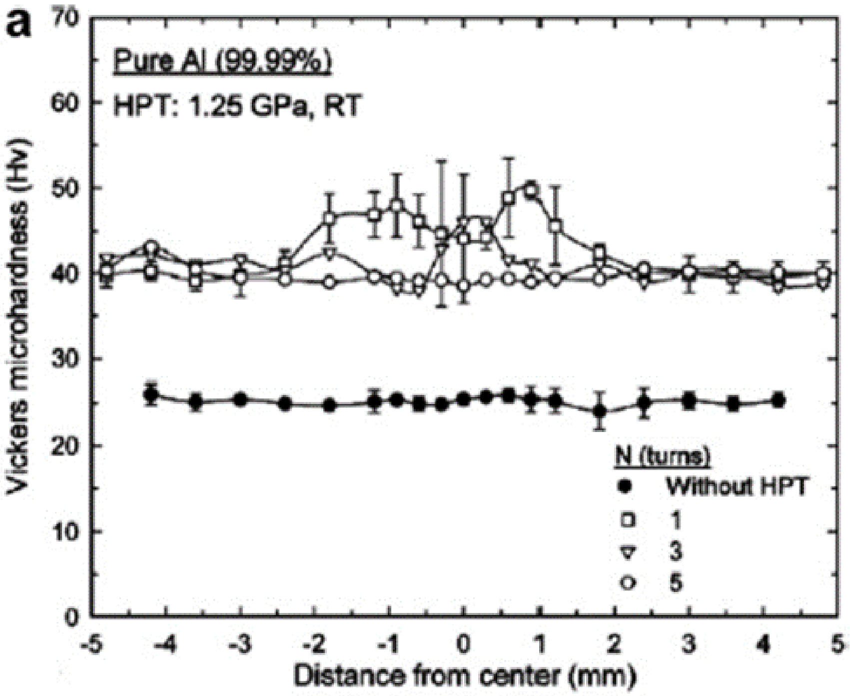
a
Pure Al (99.99%)
HPT: 1.25 GPa, RT
Vickers microhardness (Hv)
Distance from center (mm)
N (turns)
● Without HPT
□ 1
▽ 3
○ 5
0
10
20
30
40
50
60
70
-5
-4
-3
-2
-1
0
1
2
3
4
5

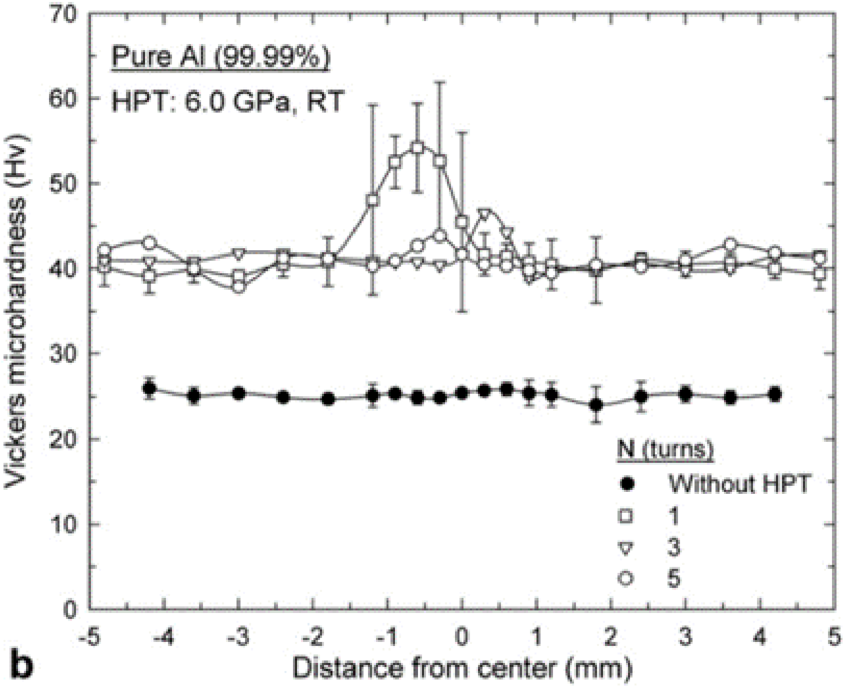
b
Pure Al (99.99%)
HPT: 6.0 GPa, RT
Vickers microhardness (Hv)
Distance from center (mm)
N (turns)
● Without HPT
□ 1
▽ 3
○ 5
0
10
20
30
40
50
60
70
-5
-4
-3
-2
-1
0
1
2
3
4
5

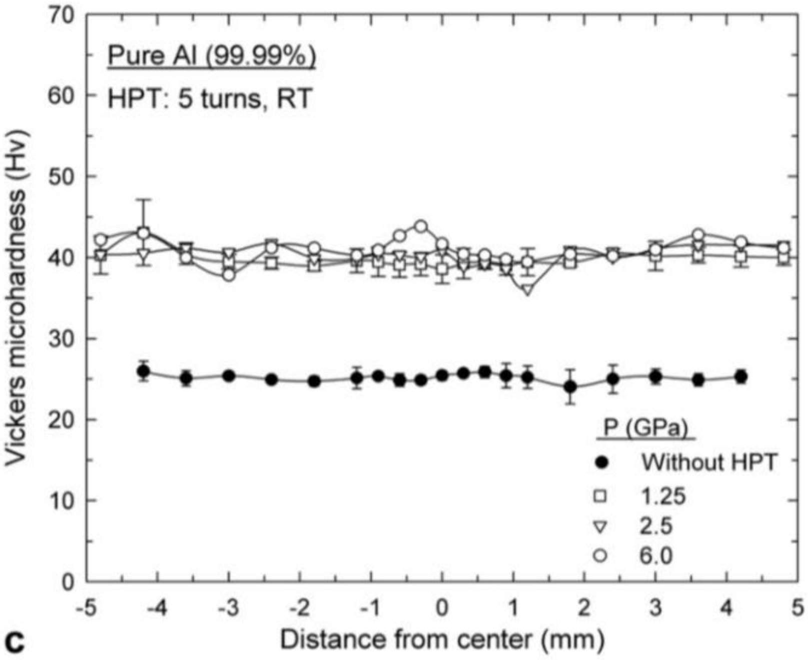

Figure 2- 13. The average hardness versus distance from the centre of high purity al disk after processed by HPT under different number of turns with (a) 1.25 GPa; (b) 6.0 GPa; (c) under 5 turns [123].

Besides, two factors influence the development of homogeneity: imposed pressure and rotation number [124]. A high purity Ni was processed by HPT under different applied pressure 1 GPa and 9 GPa. The variations of hardness across two samples showed an inhomogeneity microstructure, i.e. lowest Hv at the centre and highest Hv at the edge of the sample. The results showed that the uniformity in hardness improves with increasing applied pressure. Moreover, a relationship between the number of rotational turns (N) and hardness (Hv) was observed, indicating that higher rotational revolutions are capable of achieving a reasonably homogenous UFG microstructure [124].

In addition**,** an examination was reported to determine the influences of sample dimension on the hardness and homogeneity. The observations showed that the disks with different dimensions approach saturated hardness level at almost the same geometrical position, which indicates the homogeneity is independent of the sample dimension. Also, a conclusion was drawn that the extent of strain hardening depends on the region on the disk; this observation was determined by investigating the distribution of dislocation density [28]. Dislocation density was measured to have the lowest value in the centre and the highest value in the edge of the disk, which has the same tendency as micro-hardness. Therefore, it can be concluded that more pronounced strain hardening happened in the outer region of the disk [28].

2.4.3 Limitation of HPT

The HPT process has three major drawbacks: a). The sample size is so small that the applicability is rather limited to a laboratory scale. b). The sample shape is in the form of the disk that is not suitable for many industrial applications compared to wire or sheet forms; c). As the strain is generated in proportion to the distance from the disk centre, an inhomogeneous microstructure distribution is developed across the diameter. The mechanical properties and microstructure should be homogeneous throughout the whole sample for practical application [125].

In order to overcome these drawbacks, the HPT using a ring-shaped sample instead of a disk. Harai et al. [126,127] demonstrated that the ring sample facility is a simple modification of the anvils used for disk samples in the conventional HPT machine, as illustrated in Fig. 2-14. Using a ring-shaped HPT sample not only eliminate a less-strained centre part but also scale up the sample. For traditional HPT sample size is limited to disks with dimensions around 10 mm in diameter. However, the applications using ring samples are made of 20 mm in outer diameter, with the ring width of 3 mm for pure Al. The outer diameter is extended to 30 mm for pure Cu [128,129], 40 mm for Al-3Mg-0.2Sc alloy [130], and even diameter of 100 mm for pure Al was achieved [126]. A disk sample used in traditional HPT application compared with the ring sample as shown in Fig. 2-15 [126].

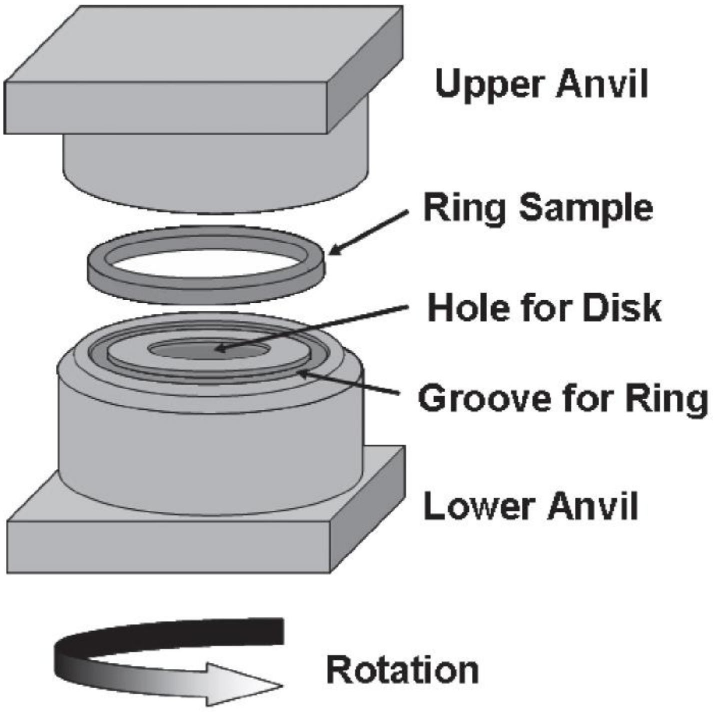

Figure 2- 14. Schematic illustration of HPT for ring and disk samples [126].

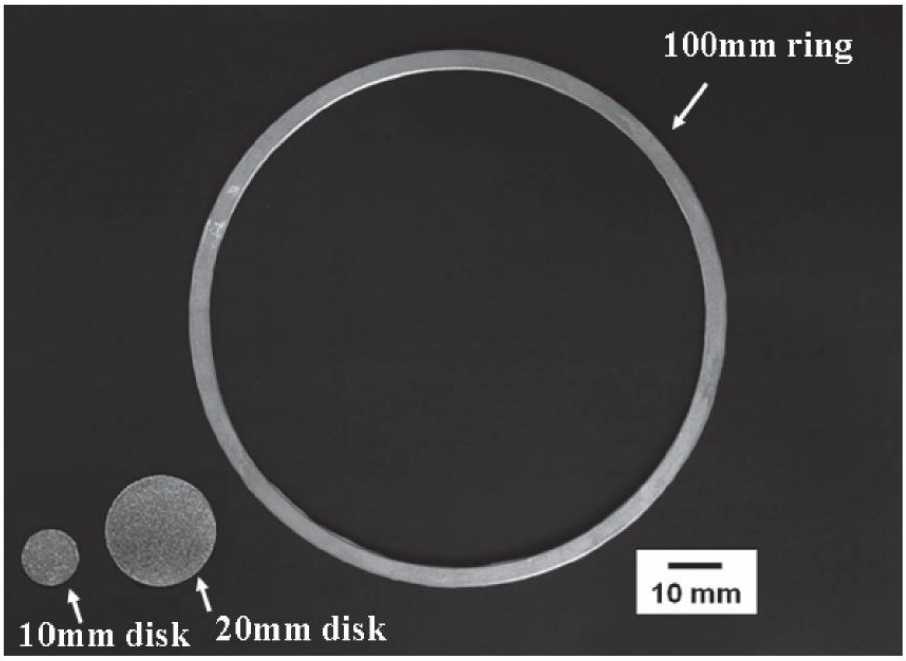

Figure 2- 15 Appearance of 10 mm and 20 mm disk samples compared with a 100 mm ring sample [126].

2.4.4 Strengthening of UFG materials processed by HPT

As described earlier, the high strain generated by HPT process produces a high density of dislocations in microstructure, resulting in effective grain refinement. Many physical properties of materials with such small grain size are far better than those with coarse grains. Both yield strength and hardness increase with decreasing grain size, in agreement with conventional grain refinement and follow the Hall-Petch relationship.

$$\sigma_y = \sigma_0 + Kd^{-1/2} \qquad (2\text{- }12)$$

An empirical equation has been used in many works. The relationship between yield strength and hardness is given as $\sigma_y \approx 3\mathrm{HV}$ [131], and therefore, the Hall-Petch equation is equivalent to:

$$Hv = Hv_0 + Kd^{-1/2} \qquad (2\text{- }13)$$

Where σ_0 is lattice friction stress, Hv_0 is constant hardness for the particular material, and K is a constant representing grain boundary resistance to deformation; d is the grain diameter. In principle, smaller grain size resists dislocation pile-up at grain boundary leading to large stress needed for the material to deform, thus increasing strength. However, reverse HP slope is observed when grain size below ~ 20 nm, i.e. with continued reduction in grain size, the hardness begins to decrease [132]. Some explanations for reverse HP relationship given so far are the effect of triple junction, coble creep, transition from cutting to bypassing of dislocation and nanocrystals as a 2-phase composite.

Besides the grain refinement, solid solution hardening is also one of the major mechanisms for improving the strength of Al alloy as the alloy comprises a variety of elements. Such alloying elements differ from the matrix atoms in size and shear modulus, resulting in variation and distortion of strain field. The strain field interacts with the strain field of dislocations causes impediment in dislocation motion and thus enhance the strength of materials [133]. Additionally, solute atoms were proposed can also provide an extra improvement in strength through the formation of precipitates [36,134,135]. It was pointed out later on that the precipitates were nucleated heterogeneously on the grain boundaries and dislocations, which only play a small contribution to hardening during ageing. It has been reported that the contribution of solid-solution hardening to the hardness becomes more significant as the concentration of solute atoms increases [136]. Nevertheless, it has been shown that solid solution has only $<$15% contribution for total hardening effects. However, the solute atoms can promote extra grain refinement through solute-matrix mismatch [136], as well as improve the thermal stability of UFG materials [137].

SPD techniques have been reported to either influence the distribution of solute atoms in precipitation hardening alloys via precipitation decomposition or by segregating solute atoms to dislocations and GBs. The modification of microstructure caused by SPD can be ascribed to four mechanisms: (1). High strain induced by SPD produces fragmentation of pre-existing precipitates [138,139]; (2). The dissolution of precipitates during SPD at ambient temperature [140]; (3). Acceleration of precipitation observed in Al alloy at high temperature ($>$100 ^{o}C) [141–144]; (4) The orientation change and isotopically growth of precipitates to spherical shape owing to loss of the low interfacial energy between precipitates and Al matrix [144].

Due to the unique solute nanostructure formed through the decomposition of supersaturated solid solution (SSSS) and solute segregation at grain boundaries (GBs), SPD-induced grain refinement achieves optimisation by dynamic balance between grain refinement and grain growth processes [145]. The equilibrium GB segregation on nano-sized grain materials shows that the solute segregation reduces the GB energy and stabilises crystalline defects [146,147]. Furthermore, it has been found that solute segregation level varies from one grain boundary to another, and it is highly dependent on processing temperature and nature of individual grain boundary. Moreover, increasing the rotational number and processing time of HPT results in a strong development of solute segregation at GBs [145]. Therefore, the existence of solute atoms segregation at grain boundaries hinder grain growth and pin the migration of GBs, which explains that the higher solute segregation at GBs results in a stronger grain refinement effect.

2.4.5 Al-Zn-Mg-Cu alloys processed by HPT

The evolution of homogeneity of age hardenable Al-7136 alloys was evaluated after undergone the HPT processing by 1/8, ¼, 1, 2, 3 and 4 turns. The micro-hardness measurements were carried out along the diameter of the samples, with colour-coded contour maps displayed the hardness distribution, and corresponding positional microstructure was observed by TEM [148]. First, all the hardness distribution of the samples under different rotational numbers (N) shows the minimum Hv in the centre of disks (Fig. 2-16), which is similar to earlier results of Ni, Cu, commercial Al-based alloys. From the microstructure observation, equiaxed grains exist in both centre and edge regions of the disk after 1 turn, but smaller grain size was measured in the edge, resulting in higher hardness values.

Additionally, the presence of arrays of aligned η phase precipitate in the edge region is also evidence of a higher hardness value due to the fragmentation of larger particles during HPT. Second, the hardness was found to increase significantly after 1/8 turn and continues to grow up to maximum Hv values (~280) at 1 turn with the average grain size of ~200 nm at centre, and ~120 nm and precipitates ~10-20 nm at periphery. After this, there is a decrease in hardness between 1 turn and 2 turns. After 2 turns, even though the grain size reduced in both centre and periphery, the size of precipitates increased (~25-30 nm) and predominantly formed at grain boundaries. These increased sizes of precipitates imply that the number of obstacles used to impede dislocation motions is reduced, thereby decreasing hardness from N=1 to N=2. Thereafter, a gradual continuation in the reduction of hardness with increasing straining was noticed at 3 turns and 4 turns, suggesting a result of recovery or recrystallisation during higher strains HPT process. In addition, higher hardness with an average grain size less than 100 nm was obtained when samples subjected to ECAP prior to HPT because of the initial existence of a supersaturated condition [148].

Annealed-condition of Al-7075 was also processed by HPT under the different number of revolutions. Annealed Al-7075 contains a highly elongated grains, which is responsible for the lower hardness. After samples were processed by 5 turns of HPT at

RT, high hardness in the edge with the grain size of ∼250 nm was obtained, and equiaxed microstructure was characterised by Orientation imaging microscopy (OIM) images. However, it is unusual that a reasonable hardness homogeneity is not fully attained after 5 turns of HPT process, and twice of differences were measured between grain size in centre and edge (∼500 nm in the centre).

Besides, a measurable increase Hv was noticed between 5 and 10 turns (Fig. 2-17), implying a further increase of strain is required to fully establish the saturation structural condition and homogenous structure. To explore this observation, mechanical tests were carried out after HPT process, showing a decrease in the flow stress. Besides, significantly high elongation to failure up to 700% at a strain rate of $10^{-4}s^{-1}$ (Fig. 2-18) after undergone 5 or 10 revolutions at 623K, resulting in improvement of ductile and superplasticity behaviour. Moreover, like most alloys, the increase in hardness was higher in the edge and lower in the centre of the disks at the beginning (N=1 or 2) [149]. The same observation was found as Al-7136 that the hardness increases dramatically around the periphery after 1/8 turns [148].

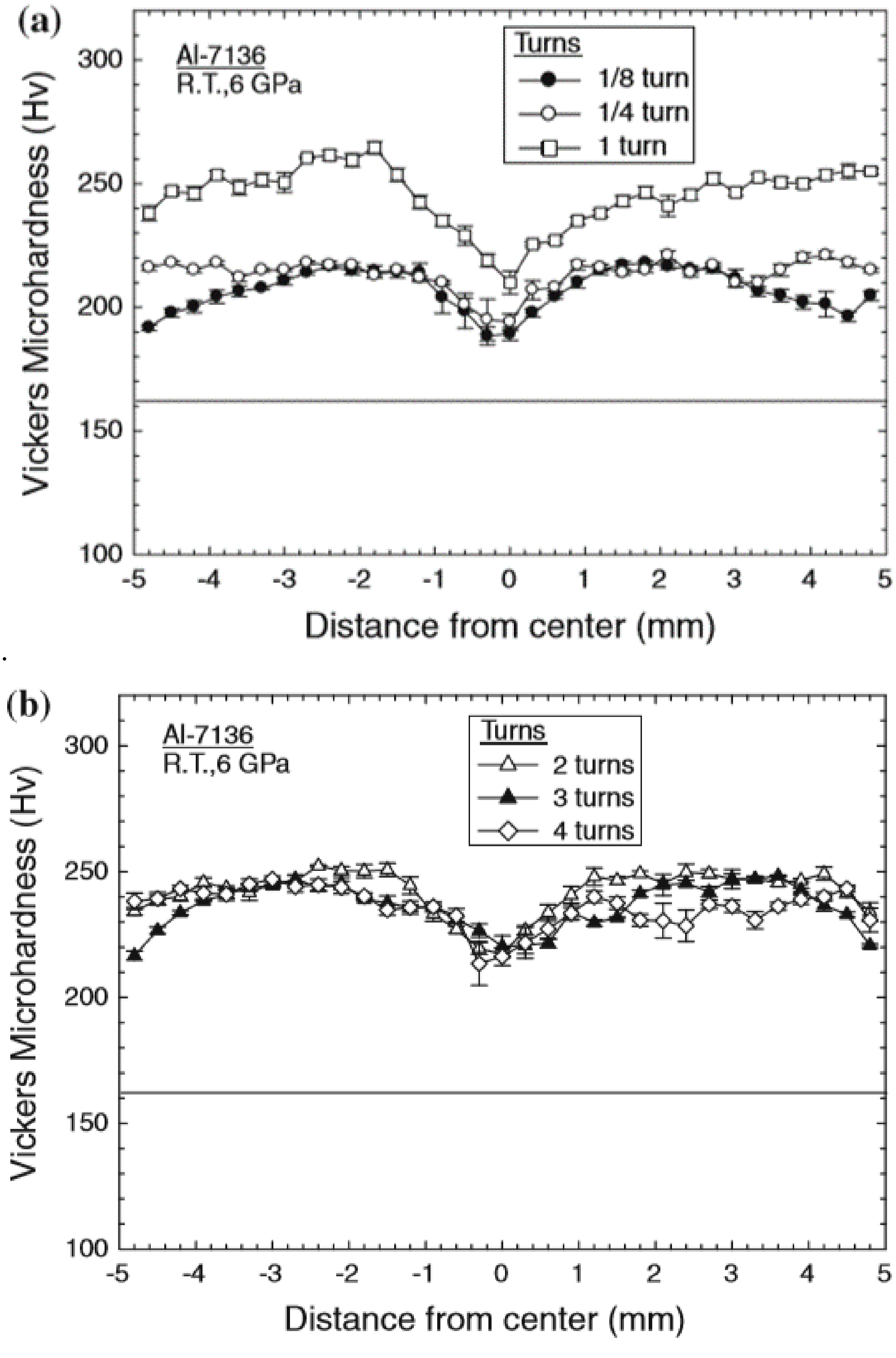

Figure 2- 16. Micro-hardness measured when Al-7136 alloys processed by HPT by (a) 1/8, 1/4, 1 turn and (b) 2, 3 and 4 turns [148].

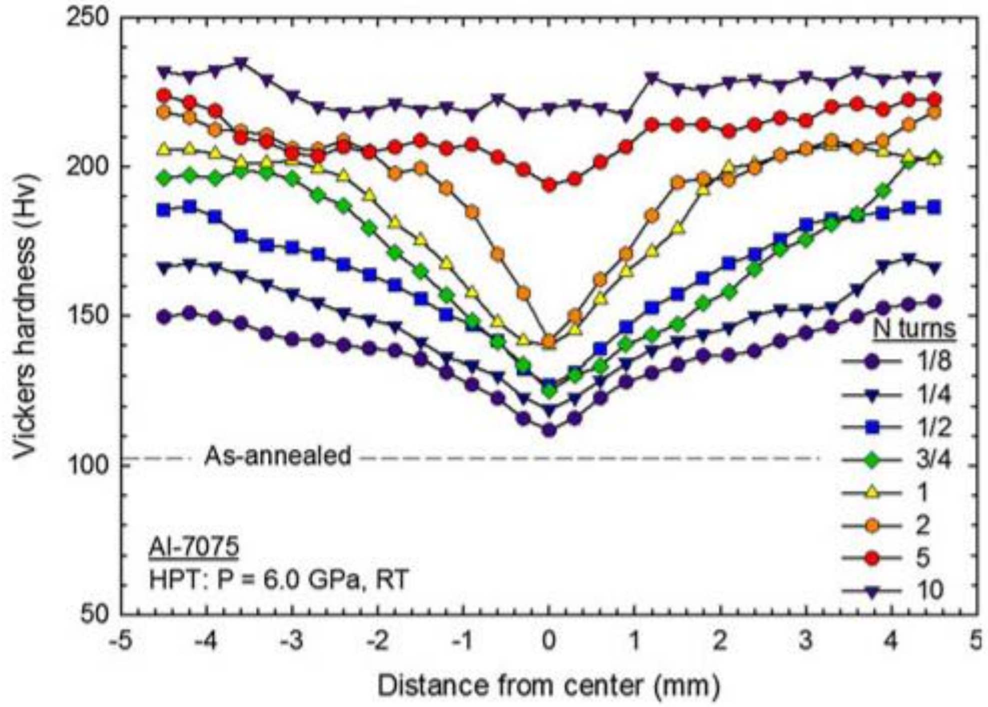

Figure 2- 17 Hardness against the distance from the centre of disks under the different number of HPT revolutions from1/8 to 10 turns for AA7075 [149].

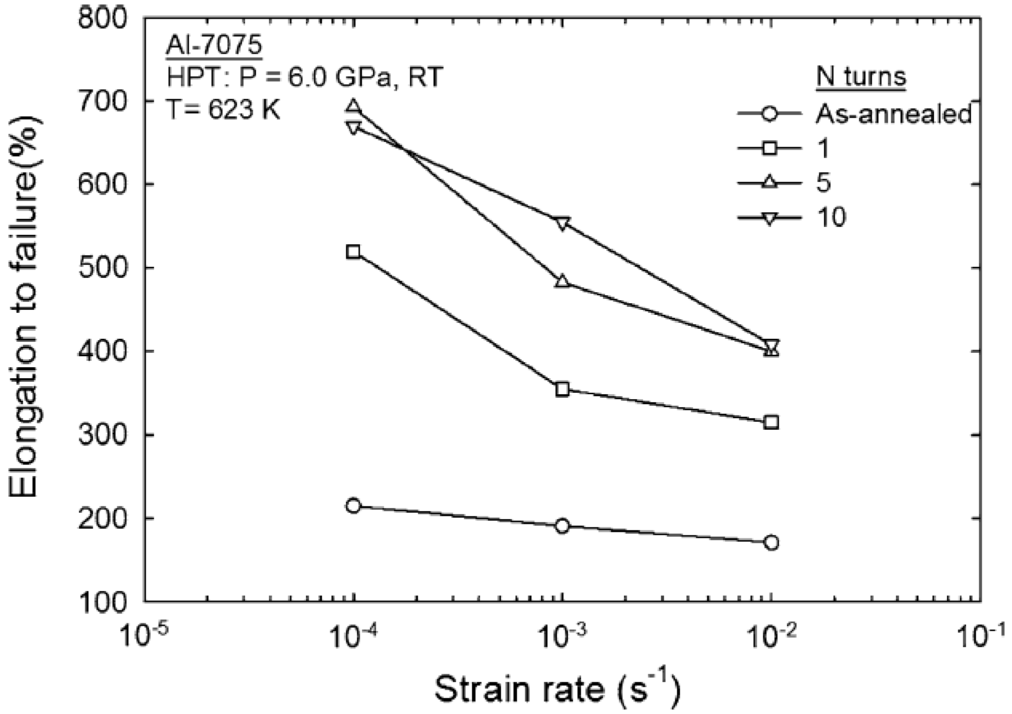

Figure 2- 18. Elongation to failure curve for HTP-processed Al-7050 under different number of revolutions versus the strain rate [149].

2.4.6 Al-Cu-Li alloys processed by SPD

In a cold rolled Al-Li 2198-T8 alloy (i.e. solution treatment + quenching + pre-deformation under tension + peak ageing at 175^{o}C) was subjected to HPT under a pressure of 3 GPa for 2 revolutions with the rotation speed of 0.5 rpm. Optical microscopy (OM) and TEM were used to characterise the microstructural feathers of HPT processed Al-Li 2198-T8 material [150]. From the optical microscopy image shown in Fig. 2-19, no grain boundaries can be seen after etching the material, and this connotes that the grain size has been reduced down to sub-micron level during HPT. Furthermore, the fine grains with high misorientation angles can be detected from the SAED pattern, and a high dislocation density was observed from TEM images (Fig. 2-20). In addition, micro-hardness was measured around 250 Hv. Such a high hardness is typically ascribed to the formation of high dislocation density and grain refinement. During HPT, high pressure and strain induce dynamic recrystallization that causes the formation of an equiaxed microstructure with strongly distorted grains. Hansen [151] and Miyajima [152] suggested that dislocations generally start to form during starting stage of plastic deformation and followed by low angle misorientation grain boundaries (LAGBs) (i.e. dislocation cells). As the amount of plastic deformation increases, more dislocations occur, finally producing the structure with high angle misorientation grain boundaries (HAGBs). It is well established that LAGBs structure is more likely to allow slip transferring and provide a relatively weak barrier to dislocation motions compared with HAGBs [153]. Hence, HAGBs usually are contributing to the strengthening of materials even though only minor contributions. Thus, HPT induced HAGBs is beneficial for the strength of Al 2198-T8 alloy.

Additionally, the Al-Cu-Li 2099 alloy with a composition Al-2.8Cu-1.6Li (wt. %) was deformed through ECAP under various processing conditions followed by annealing treatment [154]. The microstructure was examined by TEM, EBSD, and Scanning electron microscopy (SEM) Back-scattered electrons (BSE) mode. In that work, the experimental results have shown ECAP processing provides a successful strength improvement for Al-Cu-Li 2099 alloy while maintaining ductility. This is achieved by forming fine and homogenous precipitation of T_1 phase during annealing, which enhances the elongation to failure.

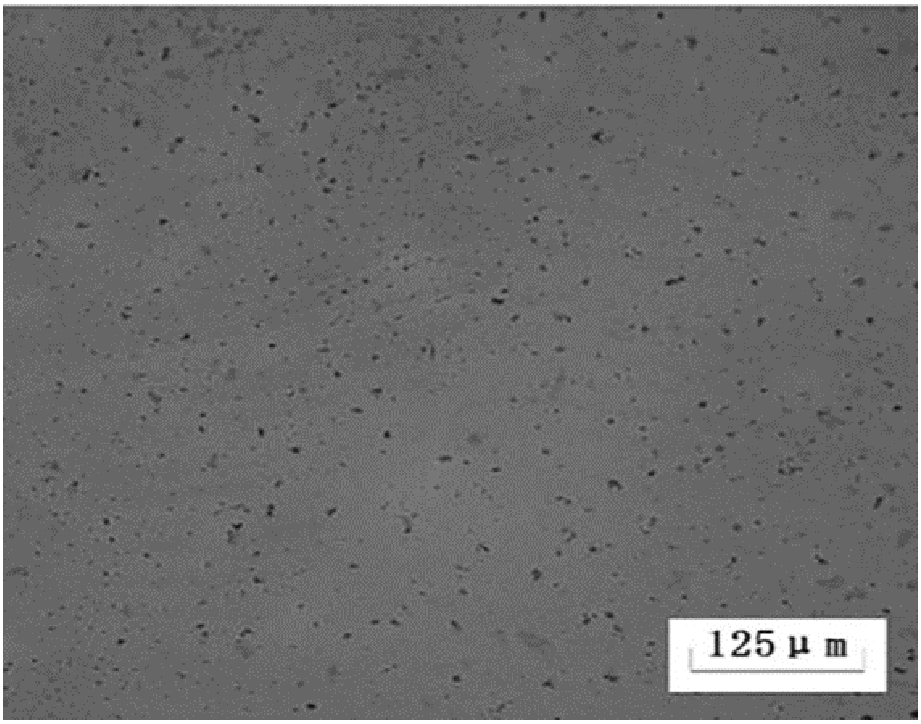

Figure 2- 19. Microstructure of HPT 2198-T8 disk observed by high magnification optical microscopy [150].

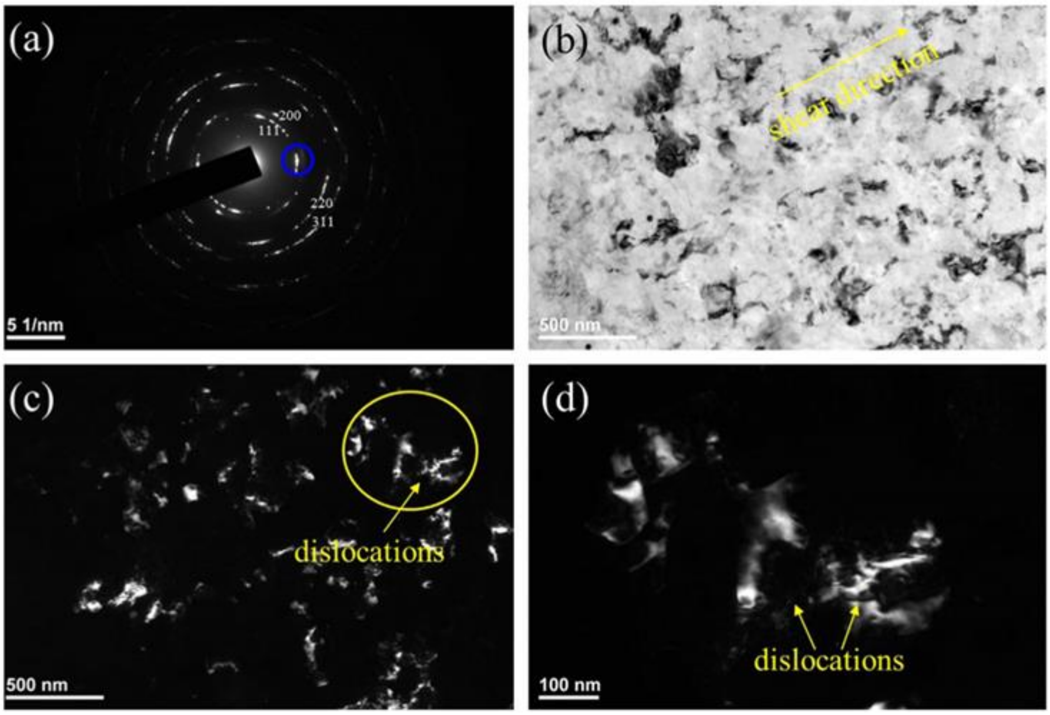

Figure 2- 20. TEM images of HPT 2198-T8 (a) SAED pattern; (b) bright field; (c) dark field; (d).dislocation in a single grain [150].

2.4.7 Effect of ageing on microstructure of HPT processed materials

For most aluminium based alloys that consist of substantial amounts of alloying elements, ageing treatment accompanied by pre-solution treatment is an effective process to strengthen the alloys, this process is termed as age hardening. Besides, due to the formation of UFG structure by HPT, this processing can create a large amount of grain boundaries (GBs) that act as preferential nucleation sites to promote heterogeneous precipitation [155]. This large amount of GBs generated by HPT will provide different ageing behaviours for those UFG aluminium alloys. In addition, many research publications have reported that the HPT-processed and then ageing treated alloys can improve the strength of materials [31,32,34,35,38,156].

In point of fact, the ageing effects of the HPT deformed UFG materials is significantly different from that of coarse-grained materials. The precipitation sequence during ageing may be affected because of the presence of UFG structure. An absence of metastable precursor phase was found in Al-1.7Cu (at%) alloy that is aged at 100 ^{o}C/24h after ECAP processing [138]. In the research, the stable θ phase was formed at grain boundaries without the formation of precursor metastable phase θ' and θ''. Besides, Al-1Mg-4Cu (wt. %) alloy was subjected to HPT and followed by ageing at 150 ^{o}C for 48 hours. The TEM images showed an absence of the formation of semi-coherent S and S’ phases, and instead, the formation of Cu-Mg clusters was detected which is responsible for the strengthening effect [157]. As mentioned in Section 2.2.2, solute clustering is typically formed by rapid solute diffusion mediated by vacancies. At room temperature, HPT introduces not only dislocations but also a significant fraction of vacancies. A large concentration of deformation-induced vacancies disappears by diffusion to sinks at grain boundaries and the remaining vacancies agglomerate into vacancy clusters. The mean clusters size differs in various materials and is influenced by the activation energy for migration of vacancies in the given material [158].

Moreover, a recently published report has stated that HPT-processed Mg-Re alloy aged at 120 ^{o}C and 200 ^{o}C result in a changed precipitation sequence [18]. The formation of metastable β′ and β′′ phases was not observed during ageing treatment, and the nucleation of equilibrium β phase was initiated without other metastable precursors phases. The change in precipitation sequences may be attributed to solute segregation, whilst no evidence for segregation at GBs was provided [18]. Whereas there is a report shows that the precipitation sequence is not changed during ageing. For example, 7075 Al alloy was solution treated first, and then subjected to ECAP and followed by natural ageing for two months. With the aid of DSC, X-ray and TEM images, the results indicate that ECAP only changes the precipitation kinetic, but no change in precipitation sequence [134].

2.5 Strengthening modelling in SPD-processed metals

2.5.1 Review of model predictions

The main purpose of SPD processes such as HPT and ECAP is to achieve an UFG or even nano-sized grain structure, thus improving the strength of metallic materials [27–30]. For SPD-processed metals and alloys, ultra-fine grains are mainly achieved when the processes are performed under cold deformation conditions, where dynamic recrystallization is suppressed [159]. With a view to exploiting the benefits of UFG alloys produced by SPD and deformation behaviour in this process, it is crucial to understand the grain refinement mechanisms and possibly able to predict grain size. Accordingly, a number of physical models have been developed to interpret the grain refinement mechanism during SPD. Xu et al. [160] and Langdon [161] derived the models to predict a gradually increasing refinement of the microstructure when continuous dislocations were introduced during SPD process, but the results were inconsistent with some experimental observations. In addition, a grain refinement model was reported by Baik et al. [162]. This dislocation-based model successfully predicted the grain size of Al after different passes of ECAP, but a range of parameters needed to be fitted during the prediction procedure.

Although grain refinement is often thought of as being the main factor in the strengthening of the SPD-processed metals, it was found to be strongly materials dependent and relatively low for Al alloys [163]. As known, plastic deformation mainly takes place by the dislocation movements for metals and metallic alloys. The dislocations are partitioned into dislocations forming a cell structure and those retained within the cell interiors. In principle, the moving dislocations may be stored in grains or impeded by obstacles such as other dislocations or grain boundaries. Also, new dislocations will be generated to continue the deformation process. Conventional dislocation theory indicates [164–166] that a very high dislocation density is generated at the early stage of deformation, which results in the formation of an intragranular structure consisting of a cell with thick cell walls and low misorientation angles. With increasing strain, the thickness of the cell walls reduces and subsequently evolves into grain boundaries, ultimately forming an array of ultra-fine grains with high misorientation angle grain boundaries. Even though some deformation occurs by a mechanism involving twinning or stacking faults (SFs), there is no evidence that these contribute much to the total strengthening effects of SPD-processed materials [167].

Accordingly, dislocation strengthening is considered to be the main factor determining the strengthening of many SPD-processed pure and commercially metals. Several detailed models which incorporate dislocation strengthening contributions were proposed by Ashby [168], Nes [169,170], Huang et al. [171] and Estrin et al. [21]. Ashby described a strengthening model for predicting dislocation formation due to the presence of non-shearable particles in a deforming metallic matrix [168]. Marthinsen and Nes [20] investigated the dislocation behaviours of a conventionally deformed metallic material by applying a model based on grain refinement and dislocation strengthening mechanisms. This model was modified by Nes et al. [170] to analyse the UFG Al alloys processed by SPD.

Furthermore, Hansen et al. [153,171] applied a strengthening model on the deformed metals and found that the grain boundary strengthening follows the H-P relation and dislocations were considered to store within the cell wall only. Estrin et al. [21] constructed a dislocation-based model in which dislocations stored within the grains and subsumed in the cell walls were considered to have the same effect of strengthening. Later, this model was expanded and extensively used to predict the strength of SPD-processed alloys [22].

Starink et al. [172] developed a model based on non-shearable particles and solute-solute interactions to predict the grain refinement through volume averaged number of dislocations formed. Unlike most available models on grain refinement during SPD considering the detail of cell wall and sub-grain boundaries formation, this model does not include any qualitative predictions on cell and sub-grain boundaries formation. The model was applied on several SPD-processed (ECAP or HPT) Al alloys, including Al-7034, Al-1050 (A/B), Al-2024, Al–Zr, Al–Zr–Si–Fe and Al–3Mg–0.2Mn. SEM, TEM, EBSD were performed on these alloys to provide information for the uses of prediction model, such as characterisation of microstructure, grain, sub-grain and grain boundaries misorientation. The predicted grain sizes were compared with the published database on the grain size of SPD Al alloys. Results (see Fig. 2-21) shown that the model predicted grain size with an accuracy of ~22% [172].

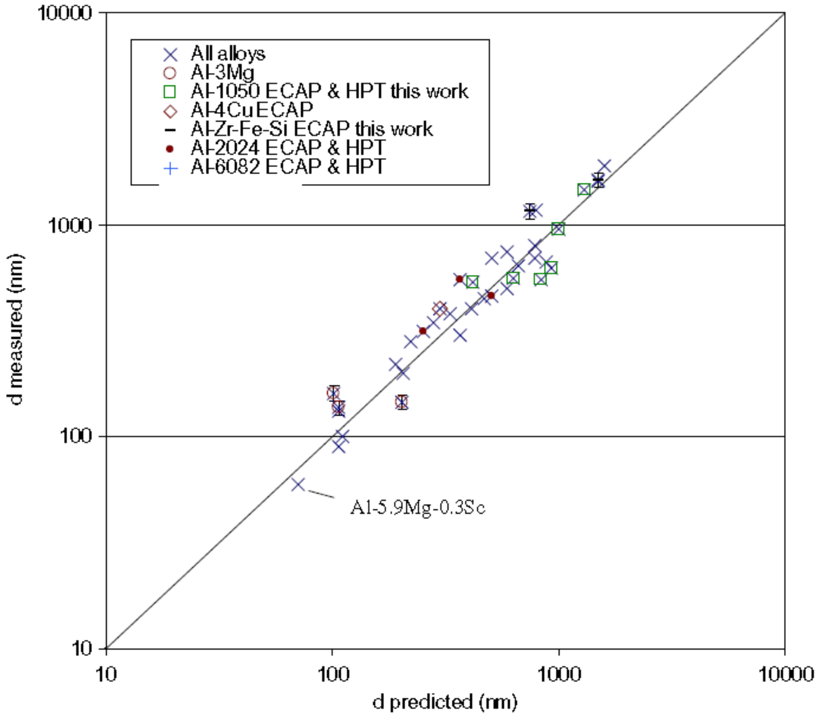

Figure 2- 21. Measured and predicted grain size of a range of Al alloys subjected to ECAP or HPT for total equivalent strains >3. Grain sizes were calculated from EBSD data, TEM or SEM [172].

Moreover, Qiao et al. [163] constructed a computational friendly strengthening model to predict the grain size and yield strength/hardness of the SPD-processed Al alloys with a good prediction accuracy. A range of Al-based alloys, including Al-1050, Al-Zr, Al-Zr-Si-Fe, Al-1200 and AA6061 alloys, were subjected to ECAP, ARB or cold rolling. EBSD, SEM, TEM, and OIM were conducted for microstructural analysis and experimental data use. This model, considering multiple strengthening in terms of grain boundary strengthening, solid solution strengthening, precipitation strengthening, and dislocation hardening, was examined by comparing experimental data and the data obtained from published literature. The measured grain sizes and micro-hardness were compared with the predicted grain sizes and micro-hardness were given in Fig. 2-22 for these ECAP-processed Al-based alloys (Al-1050, Al-Zr, Al-Zr-Si-Fe). The predicted grain size fits the measured grain size to within an average deviation of 24%, and the predicted hardness agrees very well with the experimental data. Besides, the predicted grain size and yield strength of Al-1200 alloy fit the measured values well with root mean square error of 0.33 μm and 2.9 MPa, respectively (Figs. 2-23 (a-b)), which also presents the grain boundary hardening and dislocation strengthening predicted by the model. The predicted results indicate that dislocation strengthening is the main strengthening mechanism [163].

Additionally, this model was applied on the ECAP-processed, ARB-processed and multiple forging-processed AA6061 alloys, and the results are shown in Fig. 2-24 [163]. The predicted micro-hardness fits the measured data excellently for ECAP and multiple forging-processed AA6061 alloys, but the predicted values were lower than the measured data of the ARB-processed sample. The reason for this discrepancy was explained in [173,174], and this is irrelated to the present report here.

Moreover, on this basis, Chen et al. [17] established a physically-based model incorporating cluster strengthening and solute segregation, which successfully predicted the strength of the UFG Al-Cu-Mg alloy. AA2024-T351 alloy was processed by HPT at RT for different number of rotations. Vickers micro-hardness was measured, XRD, TEM and APT were performed on the alloy. The model uses the microstructure data obtained from the above techniques to predict the yield strength of Al alloy. The comparison of the predicted yield strength and measured yield strength is shown in Fig. 2-25. This strengthening model includes short-range order and modulus hardening due to clusters and strengthening due to dissolved atoms, grain boundaries, dislocations, and complex solute-defect clusters provided a excellent fit with the experimental data. In the present research, the model that involves multiple strengthening mechanisms will be used to predict the strength of the HPT-processed and age hardened materials. A detailed description is provided in the following Section 2.5.2.

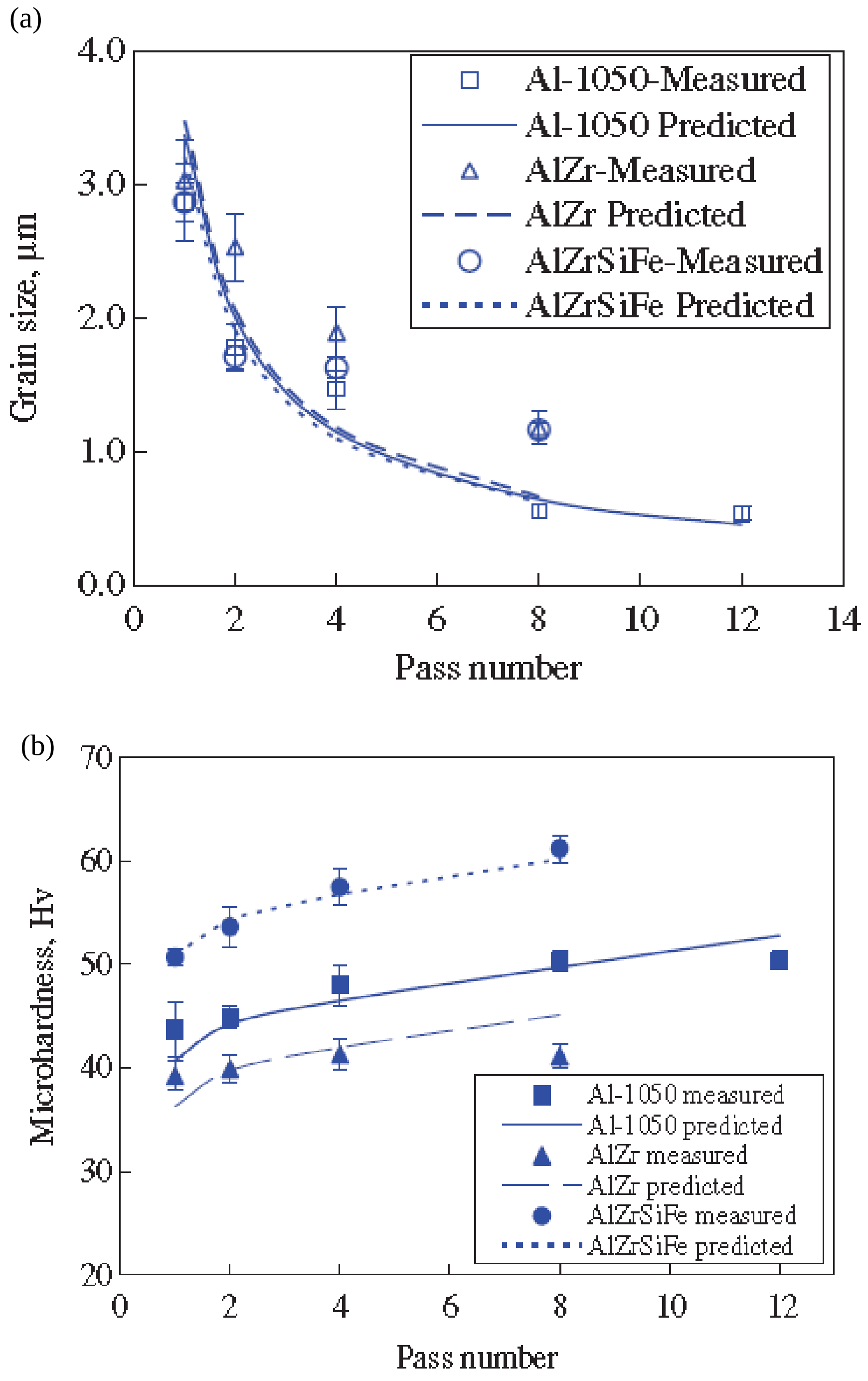

Figure 2- 22. Measured and predicted (a) grain size was calculated from EBSD data and (b) micro-hardness of Al-1050, Al-Zr and Al-Zr-Si-Fe alloys as a function of the pass number [163].

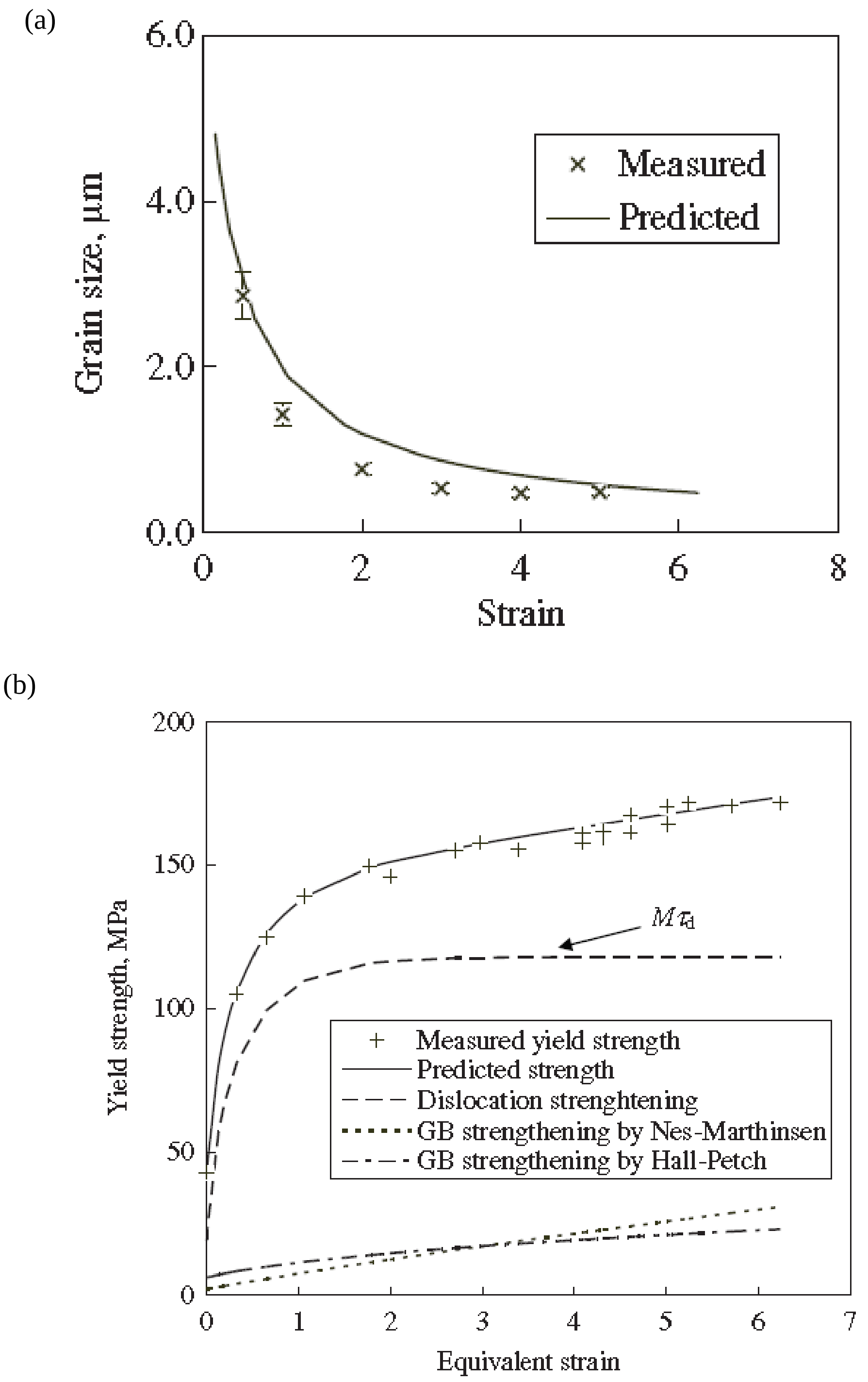

Figure 2- 23. Measured and predicted (a) grain size (calculated from TEM data), and (b) micro-hardness of Al-1200 after the different strain of cold rolling [163].

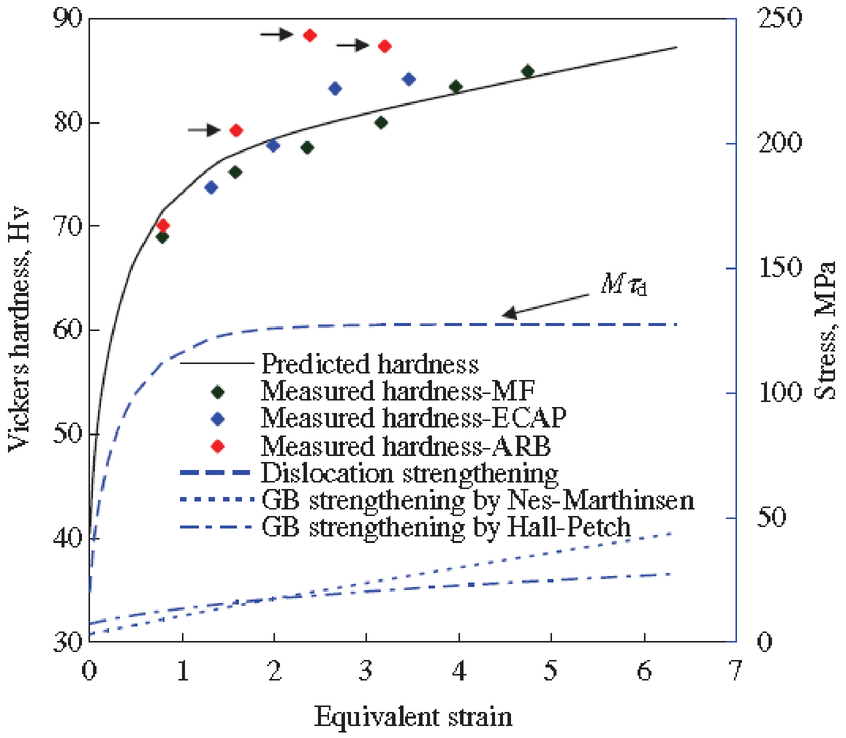

Figure 2- 24. Prediction of micro-hardness of AA6061 processed by ECAP, ARB, multi-axial compression/forgings (MAC/F) and MAC/F + cold rolling [163].

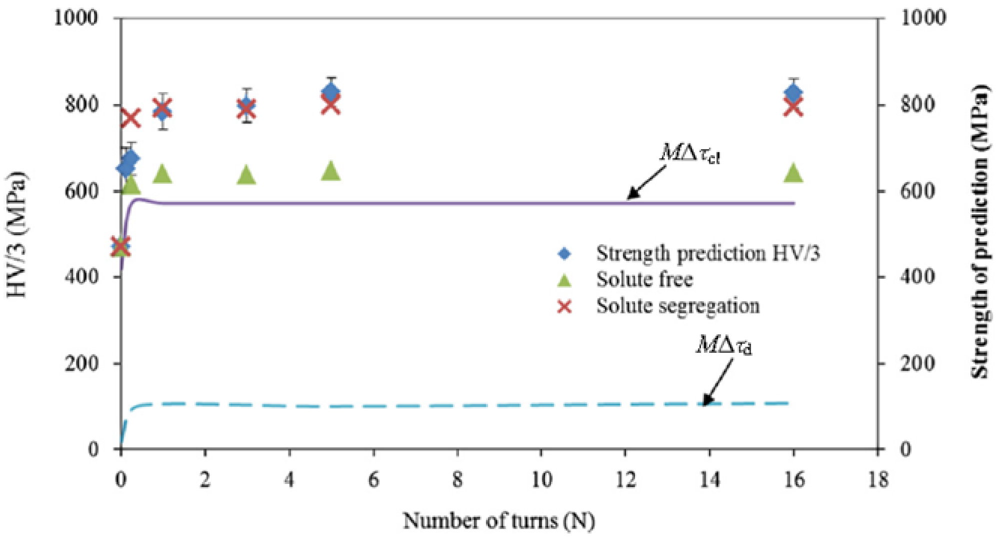

Figure 2- 25. Yield strength measured by Vickers micro-hardness (blue dots) and predicted by strengthening model: green-triangle symbol represents predicted strength without considering co-clusters, and red-cross symbol indicates the predicted strength that is containing co-cluster strengthening [17].

2.5.2 Strengthening models

It has been stated in many publications that the yield strength of polycrystalline material is related to the critically resolved shear stress (CRSS) of the grains and the grain boundary strengthening ($\Delta\sigma_{gb}$). The relationship can be expressed as [107,175–177]:

$$\sigma = \Delta\sigma_{gb} + \Delta M\tau_{tot} \tag{2- 14}$$

Where $\Delta\sigma_{gb}$ is the yield strength increment caused by the grain boundary strengthening; M is a factor often referred to as the 'Taylor factor'; it is an orientation factor related to texture and the orientation of the tensile axis relative to the main axes of the analysed specimen [107,175]; τ_{tot} is the total CRSS of the grains and it is normally influenced by a range of strengthening mechanisms and nanoscale features. A strengthening model that takes overall five contributions into CRSS of grains into account was described by Ying et al. [17]. This model includes the intrinsic CRSS, $\Delta\tau_0$; the contribution due to dislocation, $\Delta\tau_d$; the contribution due to solid solution strengthening $\Delta\tau_{ss}$; and the contribution due to co-clusters $\Delta\tau_{cl}$, which consists of a short range order strengthening component, $\Delta\tau_{SRO}$, and a modulus strengthening component, $\Delta\tau_m$. Consequently, a linear approximation of the superposition of these contributions is given as Eq. 2-15 [107,172,176,178], and the involved strengthening mechanisms are described below.

$$\Delta\tau_{tot} = \Delta\tau_0 + \Delta\tau_d + \Delta\tau_{ss} + (\Delta\tau_{SRO} + \Delta\tau_m) \tag{2- 15}$$

Strengthening due to grain refinement

It has been shown that a power-law dependence of yield stress or flow stress on the grain size can be defined as follows [179,180]:

$$\sigma = \sigma_0 + k_{HP}d^{-x} \tag{2- 16}$$

Where d is the grain size, σ_0 and k_{HP} are constant, the exponents are stated to be in the range from 0 to 1 depending on materials [179,180]. A number of materials have been analysed, and the typical value of x ranges approximately from 0.6 to 1 for FCC structure metals, 0.5 or less for (body-centered cubic) BCC structure metals and 0.2 or even 0 for ceramic materials [181]. So far, there is no theory available that can fully explain these exponents. Taylor forest hardening suggests that $x = 1/2$, which has been widely applied to large number of coarse-grained metals for investigating the strengthening behaviours through the traditional Hall-Petch relation [182]. In addition, a theory based on the fundamental physics of yield and plastic deformation by dislocations implies that $x = 1$ [183], hence:

$$\Delta\sigma = \frac{k}{d} \tag{2- 17}$$

Where k is correlated to the intrinsic materials factors [176] and usually is proportional to the shear modulus and Burgers vector. Therefore:

$$\Delta\sigma_{gb} = \alpha_2 Gb(\frac{1}{b}) \tag{2- 18}$$

Where α_2 is a constant, *d* is the grain size.

Strengthening due to dislocations

The increment of CRSS due to dislocations generally includes contributions from both statistically stored dislocation (SSDs) and geometrically necessary dislocations (GNDs). A classical relation is described by [172]:

$$\Delta\tau_d = \alpha_1 Gb\sqrt{\rho_{tot}} = \alpha_1 Gb\sqrt{\rho_{SSD} + \rho_{GND}} \tag{2- 19}$$

Where α_1 is an empirical constant ranging from 0.2-0.5 [184], *G* is the shear modulus, and *b* is the length of the Burgers vector, ρ_{SSD} is the dislocation density of statistically stored dislocations, ρ_{GND} is the dislocation density of geometrically necessary dislocations.

Strengthening due to solid solution

The increment of CRSS due to solid solution strengthening $\Delta\tau_{ss}$ is given by [175,185]:

$$\Delta\tau_{ss} = \sum k_j c_j^n \tag{2- 20}$$

Where k_j signifies the strengthening factor for individual elements and c_j indicates the concentrations of the alloying elements in solid solution, and *n* is a constant [185].

<u>Strengthening due to co-cluster</u>

The co-cluster strengthening is considered to be due to short-range order strengthening and modulus hardening, where the former is the dominant effect in typical Al alloys [13,14]. The work done by lattice deformation caused by co-clusters impedes the movement of the dislocations is equal to the change in energy-related to short-range order per unit area on slip plans in Al matrix. This gives equation [13]:

$$\Delta\tau_{SRO} = \frac{\gamma_{SRO}}{b} \qquad (2\text{- }21)$$

Where γ_{SRO} is the change in energy per unit area on slip plans on the passing of one dislocation [13]. In addition to this type of strengthening, the clusters possess an elastic modulus that is different from the matrix that will lead to an extra strengthening mechanism. This modulus strengthening mechanism is hard to be explored theoretically, but the simplified treatment has been developed [13,14].

The CRSS due to the difference in shear modulus is approximated as:

$$\Delta\tau_m = \frac{\Delta\mu}{(4\pi\sqrt{2})} f^{\frac{1}{2}} \qquad (2\text{- }22)$$

$$\mu_{cl} = \frac{m\mu_M + \alpha\mu_A + b\mu_B}{m + a + b} \qquad (2\text{- }23)$$

Where f is the volume fraction of the clusters, $\Delta\mu$ is the difference in shear modulus between clusters and their surrounding metallic phase, with the average clusters ($M_mA_aB_b$) modulus, μ_{cl}, indicating a weighted average of the pure substance in Eq. 2-20 [13].

2.6 Characterisation techniques for SPD-processed materials

To investigate the effects of deformations on the microstructure of metallic materials, transmission electron microscopy (TEM) and X-ray diffraction (XRD) are often employed, particularly for evaluating grain size. TEM observations provide direct micrographs of the sample regions with the possibility of identifying, such lattice defects as dislocations, grain boundaries, vacancies, stacking faults, etc. relying on suitable imaging conditions [186]. Whereas the attainment of reliable results is closely dependent on the conditions of the thin specimen, and the thin area may no longer represent the original microstructure due to the defects introduced or removed during the thinning procedure. Besides, the grain overlapping might causes uncertainty of measurements[186,187]. In contrast, sample preparation for XRD is relatively straightforward (unless mistakes are made) [187]. However, a significant computational effort is required to obtain all possible detailed information regarding the microstructure of analysed samples from the raw diffraction patterns. In the present report, both TEM and XRD techniques will be conducted for examining the microstructural characteristics of the Al-Cu-Li alloy. For this reason, a number of methods for the analysis of XRD data are described in the following sections.

2.6.1 X-ray diffraction (XRD)

The diffraction pattern consists of an extremely sharp, narrow and symmetrical peak at the exact Bragg positions for a defect-free material. In practice, the imperfection of crystal lattice leads to deviations from the ideal peak profile, and these deviations are mainly considered to be peak shifts and peak broadening [188]. There are two types of lattice strains associated with nanocrystalline materials. One extends over the entire lattice and results in a shifting of diffraction peak in XRD pattern, and it is often termed as macrostrain. The other extends over a few lattice spacings and originates due to the presence of lattice defects such as dislocations, grain boundaries, stacking faults, vacancies, microstress etc., and leads to peak broadening this is referred to as microstrain [189,190]. In addition, the peak broadening also arises from small crystallite size, which is sometimes referred to as coherently scattering domains size [188,191].

In addition, the shapes of line profiles are also influenced by the instrument, which is termed as instrumental broadening. This arises from the imperfection of the diffractometer, factors such as any misalignment of diffractometer, the axial divergence of the incident or diffracted beam, non-monochromatic radiation, etc. This instrumental broadening needs to be eliminated in order to acquire the broadening exclusively caused by metallurgical effects [187,192].

The main issue with the line broadening analysis is the separation of two effects that contribute to the line broadening, including sample contributions (the small crystallite size and the lattice strain related to the lattice defects) and instrumental contributions [193]. In principle, the experimental profile is the convolution of the instrumental profile and the intrinsic profile (profile provided by sample contribution) [187]. The intrinsic profile can be obtained via unfolding the experimental profile. The simplified method to separate the intrinsic and instrumental profiles is based on assumptions that the shape of two broadening profiles can be approximated by some bell-shaped function in mathematics, such as Gaussian, Cauchy (Lorentz) or the convolution of these peak shape function [187]. A number of quantitative analysis methods have been developed to separate or estimate the crystallite size and lattice strain of the materials, viz., Scherrer’s equation [194], Warren-Averbach method [195], Williamson-Hall [196], Rietveld method [197]. In this work, only Rietveld method (conducted by MAUD) is used for line broadening analysis. Therefore, the details of peak shape functions are described in the next section.

Rietveld refinement method is a full-pattern fit method. It resolves closely separated peaks in an XRD pattern and thereby maximises the available structural information to refine the crystalline structure [197]. In this method, the whole diffraction profile is fitted by the combined function Voigt approximation, the FWHM of the Gaussian and Cauchy profile of the Voigt function is calculated from the Pseudo-Voigt (PV) approximation parameters [198]. The calculation is based on the crystallographic structure models and also take into account the sample and instrumental broadening effects. The model will be refined when the experimental pattern closely matches the calculated pattern, and the model can be simplified from Eq. 2-24 [199].
The residual function χ^2 to be minimized is defined as:

$$\chi^2 = \sum_i w_i \left(I_i^{exp} - I_i^{calc}\right)^2, w_i = \frac{1}{I_i^{exp}} \tag{2- 24}$$

Where I_i^{calc} is defined by the structure factor of the cells, i.e. atoms in the asymmetric unit, symmetry equivalent positions, and temperature factor [199,200].

$$I_i^{calc} = S_F \sum_k L_k \, |F_k|^2 S\,(2\theta_i - 2\theta_k) P_k A + bg_i \tag{2- 25}$$

$$P_k = (r^2 cos^2\, a + \frac{sin^2 a}{r})^{-\frac{3}{2}} \tag{2- 26}$$

Where P_k is denoted as the preferred orientation function, L_k is Lorentz-Polarization factor depending on the instrument such as geometry, monochromator, detector, beam size and sample positioning, etc. Profile shape function S ($2\theta_i$ -$2\theta_k$) obeys Pseudo-Voigt function. This profile shape function is applicable over the whole range of diffraction angles 2θ [200].

Cagliotti formula gives a function that shows the relationship between the FWHM and the diffraction angle 'θ' in terms of Gaussian, pseudo-Voigt and Pearson-VII functions.

$$FWHM^2 = U\,tan^2\,\theta + V\,tan\,\theta + W$$

Where U, V, W are free variables, and U is a factor that strongly associated with strain broadening. The size of the crystallite can be estimated from V and W.

In the present report, Rietveld method is used to refine the XRD pattern and calculate crystallite size and microstrain values, and it is programmed directly by using 'MAUD'. Among the other line profile methods such as Williamson-Hall, Warren-Averbach, Rietveld method has three advantages [201]. Firstly, the crystal structure and microstructural properties of the materials can be refined simultaneously; secondly, both completely and partially overlapping reflections can be analysed with sufficient accuracy; finally, this method takes the correction for preferred orientation into consideration if there is any.

2.6.2 Differential scanning calorimetry (DSC)

DSC is a thermal analytical technique in which the heat absorbed or released by a sample is measured as a function of temperature or time, and it is a method for direct determination of the enthalpy changes associated with the process of interest [202]. It has been extensively used to evaluate material properties for a wide range of materials such as metal, metallic alloys, polymers, composites, etc. [202]. It has become increasingly popular with ultrafine grained materials processed by severe plastic deformation in recent years. The most significant advantage of using DSC is the speed and ease with which it can be used to track the thermal behaviours of materials. The technique substantially measures the heat flow by establishing a nearly zero temperature difference between a substance and a reference material [203]. Based on the operation mechanism, two types of DSC instruments are common today: heat-flux DSC and power-compensation DSC [204].

In the heat-flux DSC, the DSC assembly consists of two crucibles or pans to heat the sample and the reference material in a single furnace. The sample and reference are connected by a low-resistance thermoelectric metal disk, resulting in a rapid compensation of the temperature difference. Any changes of enthalpy or heat capacity in a sample lead to a difference in its temperature with respect to the reference, and thus the difference in the heat flow between sample and reference is the measuring signal [204]. In power compensation DSC, the sample and reference are heated using separate, individual furnaces. The sample and the reference are kept at the same temperature by varying the power input to the two furnaces. Accordingly, the power input that maintains equal temperatures is the measuring signal of the enthalpy or heat capacity changes in the sample with respect to the reference [202].

To provide accurate thermal measurements for the sample investigated, the system is often calibrated in many ways. Baseline calibration is generally performed without placing pans in the furnace so that the baseline slope and offset over the temperature range of interest can be measured. These values are then stored in the DSC system, and the system subtracts the baseline slope and offset from subsequent sample runs to reduce their effects. Besides, the calibration of heat flow can be accomplished by melting a known quantity of a material with a well-known heat of fusion. For example, indium is positioned in the sample pan and scanned against an empty reference pan. The area under the melting peak of DSC curve is related to the known enthalpy of fusion. Moreover, calibration of temperature can be done by evaluating a reference material with a known melting temperature [205]. The reference materials need to be pure, stable to decomposition and oxidation, and preferably have reproducible transitions that have been measured accurately. Consequently, pure In and Zn are now in common use [206].

As mentioned above, DSC technique finds applications in characterizing various materials, and applications comprise the determination of melting point, glass transition temperatures, heat of fusion, and as well as the extent of crystalization. DSC can also be used to study oxidation and other chemical reactions. The kinetic events involved and the temperatures of step transitions are usually indicated by onset temperature, which is the intersection point of the extrapolated baseline and the line tangent of the beginning of the melting. Using DSC to measure melting point, not only the onset of melting, i.e. the melting point (T_m) can be obtained, the peak temperature, which corresponds to the energy that the melting transition needs can also be determined.

Determination of glass transition temperature (T_g) using DSC is one of the most popular applications as polymer undergoes a transition from a glassy to a rubber state at Tg. The step in the glass transition is associated with the change in heat capacity (C_p) due to the changing state of the material. The difference between the heat capacity at the onset and that at the end of the transition represents the change in heat capacity [207,208]. Furthermore, DSC can be used to determine the extent of crystallinity in the crystalline materials by comparing the enthalpy of fusion for the sample of interest (ΔH_t) with the enthalpy of fusion for the pure material crystal (ΔH_f). The Fractional of crystallinity is given by [209]:

$$\text{Fractional of crystallinity} = \frac{\Delta H_t}{\Delta H_f} \qquad (2\text{- }27)$$

In Section 2.4.1, SPD techniques were introduced to generate UFG microstructures by imposing large amounts of plastic strains. The processes including ECAP, HPT and ARB are served to improve dislocation density, refine the grain size, and in many cases strengthen the materials. Besides, the materials may experience a high vacancy concentration and high internal stress when they are subjected to specific processing conditions, this gives UFG materials a thermally unstable behaviour [210]. Given this, investigating the thermal stability of SPD-processed UFG materials by DSC has attracted extensive research over the past several decades. Many research publications are related to the DSC analysis of metallic alloys (i.e. Mg, Al, Cu alloys, etc.) were processed by ECAP, HPT and ARM [211–213]. In the present research, HPT-processed Al alloy was used as experimental material. For this reason, here attention is paid only to Al alloys processed by the HPT technique. There are relatively few publications focusing on HPT processed Al alloys.

DSC was conducted on the 7150 Al-Zn-Mg-Cu (Al-6.30Zn-2.40Mg-2.30Cu-0.12Zr-0.10Fe–0.05Si) wt. % alloy in as-quenched and HPT-processed conditions from ambient temperature to 540 ˚C at a heating rate of 20 ˚C/min. The region I observed for as-quenced sample in Fig. 2-26 is attributed to the formation of GP zones, and the small endothermic effect in region II is due to the dissolution of GP zones. In contrast, no peak due to the formation of GP zones is revealed for the HPT-processed samples. This is thought to reduce vacancy concentration due to high dislocation density induced by HPT, which causes large shearing of grains by dislocation. Hence, the thermograms show that GP zone formation is suppressed due to HPT. The exothermic effect (region III) for as-quenched sample in the range of 150-225˚C is ascribed to the precipitation of η′ ($MgZn_2$). Also, the formation of η phase may occur in the later stages. However, the main precipitation peak of heat effect III in HPT-processed samples shifted to lower temperature as compared to the as-quenched sample, and this is because of the generation of line defects, high and low angle grain boundaries via HPT process have accelerated the precipitation process of equilibrium η (MgZn2) phase. In addition, it is energetically favourable that the equilibrium η phase is likely to be precipitated directly from supersaturated solid solution, as less activation energy barrier needs to be overcome for direct precipitation, this may contribute to a more pronounced heat effect (region III) for HPT- processed samples. An endothermic reaction in region V is attributed to the dissolution of η or η′ phase [214].

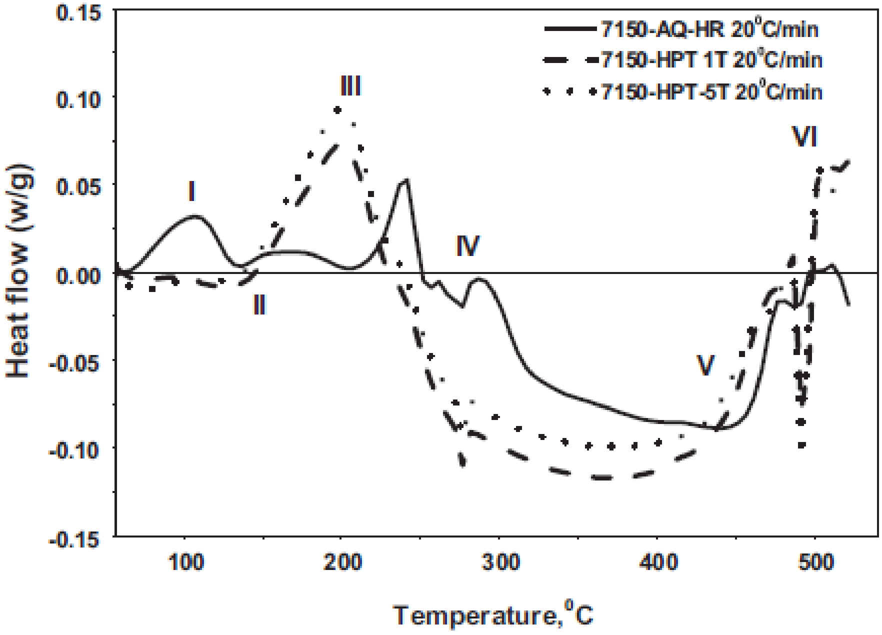

Figure 2- 26. DSC thermograms of as-quenched and HPT-processed 7150 alloys at a heating rate of 20 ˚C/min [214].

The thermal analysis of the Al-4.63Cu-1.51Mg (wt. %) (AA2024) samples processed by HPT for five revolutions was examined by DSC from ambient temperature to 540 ˚C at a heating rate of 10˚C/min. An endothermic effect at 100 - 240˚C for the T351 sample was observed in Fig. 2-27. Whilst the HPT-processed sample gives an exothermic effect with a peak temperature of 170 ˚C mainly due to the formation of Cu-Mg co-cluster. Subsequently, the T351 sample has an exothermic reaction peak at ~260 ˚C, which is interpreted as the formation of S phase (Al_2MgCu). However, there is a shift in the precipitation peaks towards lower temperatures when the material was processed by HPT, which combines two exothermic reactions overlapped at intermediate temperatures, peaking at 210 ˚C and 240 ˚C, respectively [26]. This can be explained as a large number of dislocations were induced by HPT process that hastens the precipitation process of S phase. The following high temperature endothermic reactions for both samples are identified as S phase dissolution (270 ˚C - 490 ˚C).

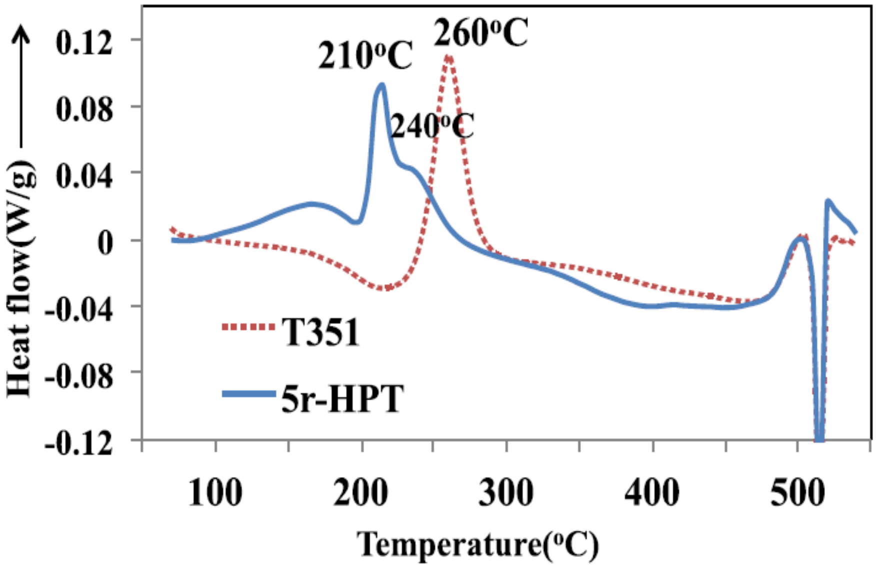

Figure 2- 27. DSC thermograms of Al-4.63Cu-1.51Mg T351 and 5r-HPT samples [26].

2.6.3 Atom probe tomography (APT)

Over the past decade, APT has been fast rising in prominence as a nanoscale analytical technique for a range of materials, despite the fact that metals and alloys are its core applications. In particular, quantitatively characterise the solute distributions has recently gained lots of attention as solutes are commonly used to explain the changes in the mechanical behaviours of materials. For instance, segregation at GBs enhanced fracture toughness, increased crystallization temperature or resulted in a detrimental premature brittle fracture. Solutes segregation at dislocations increases yield strength or strengthened intragranular precipitation [215]. In addition, APT offers direct evidence to map and locate individual atoms in three dimensions, it also reveals the structural arrangement and composition of the atoms inside a material.

The APT setup incorporates laser pulsing capabilities combined with the specimen preparation progress, which includes an intense electric field, a counter electrode and a position-sensitive detector, as depicted in Fig. 2-28 [216]. A needle-shaped specimen with a radius of curvature 50-100 nm is subjected to an electric field generated by a high-voltage direct current (DC), which is below the ionization threshold of the specimen. To achieve time-control of the field evaporation process, laser pulse or high-voltage pulse is superimposed to the high DC field, triggering the field evaporation of ions so that the specimen is evaporated atom by atom. As the specimen is progressively destroyed, the ions fly through a counter-electrode. The ions are then collected by the position-sensitive detector, giving information on each ion's timing and position of impact. This process allows the elemental identification of each evaporated ion by time-of-flight mass spectrometry [216]. The accuracy of the compositional analysis depends on the mass resolving power of APT and noise floor. Thus the background subtraction and peak deconvolution are generally required to improve accuracy.

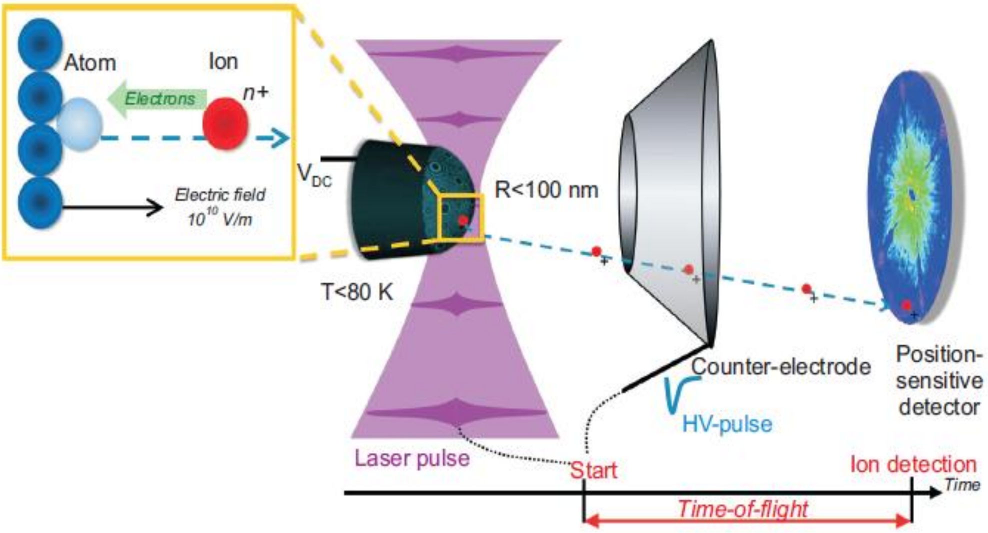

Figure 2- 28. Schematic diagram of the principle of the atom probe microscope [216].

The raw data in APT can be directly drawn from the microscope, and an atomic map is created, where every atomic ion is identified and allocated at a position in the three dimensions reconstruction. A general approach for data reconstruction is that the impact position on the detector is associated with the initial position of the atom on the needle tip, assuming a simple projection law. Accordingly, a sequence of evaporation gives depth information, an atomic map of the analysed volume of material can therefore be built in three dimensions using methods outlined in Ref [217,218]. Once the atomic map has been generated, many approaches can be used to extract and visualise material features. For example, by setting a threshold separation distance between atoms of one or more specific elements and their nearest neighbours, it is possible to isolate individual clusters from the bulk material, and further generate a quantitative analysis of clusters. Comprehensive cluster finding methods were reviewed in [215]. Aside from analysing cluster behaviours, the local concentration within a specific region of interest can be derived from APT data in the form of concentration profile to investigate grain boundaries, second phases, and the ratio of solute atoms, etc.

2.7 Summary

Overall, this chapter presents a comprehensive review on the Al-Cu-Li and Al-Zn-Mg-Cu (Al-7449) alloys, the emphasis is placed on their applications, strengthening mechanisms and precipitation sequences. In addition, the introduction of HPT technique is given. Microstructural evolution, variation of inhomogeneity and strengthening effects caused by HPT processing, and some recent studies on the HPT-processed Al-Cu-Li and Al-Zn-Mg-Cu materials are studied. Moreover, a number of strengthening models and a recently established physically-based model incorporating cluster strengthening and solute segregation are described. Finally, the principle and applications of three characterisation techniques, XRD, DSC and APT are provided.

However, only a few HPT processing has been carried out on Al-Cu-Li materials before. And no study has been conducted on the combined effects of HPT and age hardening on the strength of the Al-Zn-Mg-Cu alloy. Therefore, these motivate the investigation on the yield strength and microstructures of Al-Cu-Li and Al- Zn-Mg-Cu alloys by using the combined HPT method and age hardening in the present study. Besides, the existed strengthening models cannot provide detailed explanations for the strengthening mechanisms that contribute to the high strength of Al-Cu-Li alloy. Therefore, this also motivates the establishment of a new strengthening model to account for the contribution of clustering strengthening to the total strength of the material.

Chapter 3 Materials and experimental procedures

3.1 Material selection

Two age hardenable aluminium alloys were chosen for this work. One alloy is an experimental Al-Cu-Li alloy (Al-2.88Cu-1.34Li-1.03Mg-0.09Zr) originally intended for use in age forming [6]. The abbreviated reference to this alloy throughout this work is as the Al-2.88Cu-1.34Li-1.03Mg alloy, with all compositions provided in wt. % unless otherwise stated. This alloy is not commercially available, although its composition is close to several 3rd generation Al-Li based alloys. The composition of this aluminium Al-Cu-Li alloy is shown in Table 3-1. The second alloy is a commercially available 7xxx series Al-Zn-Mg-Cu alloy with the composition of Al-8.1Zn-2.25Mg-1.75Cu. The composition of this AA-7449 aluminium alloy is shown in Table 3-2.

Table 3- 1 Composition of Al-Cu-Li alloy.

Elements	**Cu**	**Li**	**Mg**	**Zr**
Composition (wt. %)	2.88	1.34	1.03	0.09
Composition (at. %)	1.20	5.09	1.11	0.03

Table 3- 2 Composition of AA-7449 alloy.

Elements	**Zn**	**Mg**	**Cu**	**Fe**	**Si**	**Other**
Composition (wt. %)	8.1	2.25	1.75	0.15	0.12	0.15

3.2 HPT and Ageing treatment

Both Al-Cu-Li and Al-Zn-Mg-Cu 7449 alloys materials were obtained as rolled plates. All the raw materials were initially machined into rods and cut into disks of 0.92 mm in thickness and 9.8 mm in diameter. And then ground on SiC papers to the final thickness of 0.80 mm ± 0.03 mm.

Both alloys were processed by two process conditions:

Process 1: T4 treatment (solution treatment, quench and natural ageing) followed by HPT at RT and an artificial ageing treatment (T4-HPT-AA treatment).

Process 2: T6 treatment (solution treatment, quench and artificial ageing) followed by HPT at RT and artificial ageing treatment (T6-HPT-AA treatment).

Al-Cu-Li

Five Al-Cu-Li disks (samples 1-5) were first solution treated at 515 ^{o}C for 30 min, followed by immediately quenching and then naturally aged for a fixed time period (i.e. T4 treatment). The samples then were processed by quasi-constrained HPT at room temperature for 5 turns under the pressure of 6 GPa. The rotation speed was 1 rotation per minute (rpm). The HPT machine used in this research is shown in Fig. 3-1. It has been demonstrated that rotation speed only has a minor influence on the strengthening of metal alloys as long as it is in the range of ½ to 2 rpm [219]. After HPT, these disk samples were aged at aged at 100 ^{o}C, 110 ^{o}C, 120 ^{o}C, 150 ^{o}C and 170 ^{o}C, respectively (i.e. a T4-HPT-AA treatment).

After ageing treatments, the optimum condition (e.g. ageing temperature and peak ageing time) for Al-Cu-Li alloy to obtain the highest hardness was investigated in Chapter 4 and further examined for microstructural analysis in Chapters 5 and 6. Also, the optimum ageing temperature obtained from T4-HPT-AA condition was used as pre-ageing temperature in the T6-HPT-AA treatment (See Table 3-3).

For T6-HPT-AA treatment, a quenched sample (sample 6) was pre-aged prior to HPT followed by a second artificial ageing treatment after HPT. The same conditions and parameters of HPT were used. This Al-Cu-Li alloy was pre-aged at 110°C for 24h. After 5 turns of HPT process, it was heat treated at 110 °C for a time up to 400h. The process details for each sample have been shown in Table 3-3.

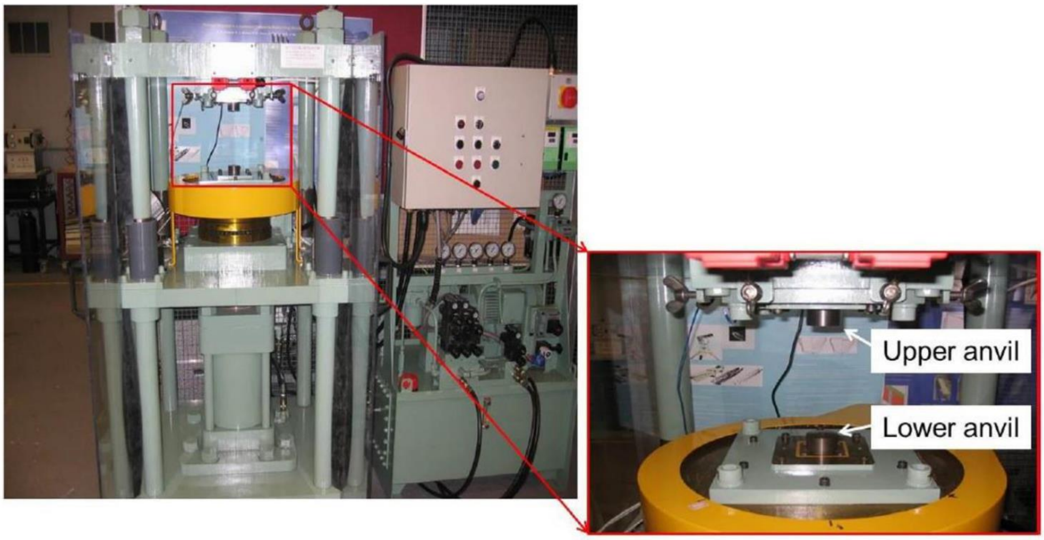

Figure 3- 1. The image of HPT machine used in this research [220].

Table 3- 3. Processing procedures of Al-Cu-Li samples.

Specimens		Processes details
Process 1 T4-HPT-AA	Sample 1	SSS at 515 °C/0.5h + quench + NA + HPT + ageing (100 °C)
	Sample 2	SSS at 515 °C/0.5h + quench + NA + HPT + ageing (110 °C)
	Sample 3	SSS at 515 °C/0.5h + quench + NA + HPT + ageing (120 °C)
	Sample 4	SSS at 515 °C/0.5h + quench + NA + HPT + ageing (150 °C)
	Sample 5	SSS at 515 °C/0.5h + quench + NA + HPT + ageing (170 °C)
Process 2 T6-HPT-AA	Sample 6	SSS at 515 °C (0.5h) + quench + pre-aged at 110°C/24h + HPT +110 °C/400h

SSS: supersaturated solid solution; NA: natural ageing

Table 3-4 provides detailed procedures of optimum conditions for examining the microstructural evolution of Al-Cu-Li alloy described in Chapters 5 and 6.

Table 3- 4. Processing details of Al-Cu-Li samples for microstructural evolution analysis.

Processes	**Processing procedures**
T4-HPT-AA	SSS at 515 °C/0.5h + quench + natural ageing + HPT + aged at 110°C/60hs
T6-HPT-AA	SSS at 515 °C/0.5h + quench+ aged at 110°C/24hs + HPT + aged at 110°C/180hs

Al-Zn-Mg-Cu 7449 alloy

Six Al-Zn-Mg-Cu disks were first solution treated at 475 °C for 30 min, followed by immediately quenching and natural ageing. Thereafter, the samples (samples 1- 6) were processed by HPT using the same conditions and parameters as Al-Cu-Li alloy. After HPT, 6 disks were aged at 80 °C, 90 °C, 100 °C, 110 °C, 130 °C and 150 °C for different periods up to a maximum of 130h, i.e. a T4−HPT−AA treatment.

Another batch of quenched Al-Zn-Mg-Cu samples (samples 7 and 8) was pre-aged at 130 °C and 150 °C for 24h prior to HPT followed by a second ageing treatment after HPT (i.e. a T6-HPT-AA treatment). After the HPT process, they were heat-treated at the same temperature for up to 170h. The full details of procedures, including ageing temperature and time, are given in Table 3-5.

Table 3- 5. Details of procedures including ageing temperature and time for Al-Zn-Mg-Cu alloys.

Specimens		**Processes details**
Process 1 T4-HPT-AA	Sample 1	SSS at 475 °C/0.5h + quench + NA + HPT + ageing (80 °C)
	Sample 2	SSS at 475 °C/0.5h + quench + NA + HPT + ageing (90 °C)
	Sample 3	SSS at 475 °C/0.5h + quench + NA + HPT + ageing (100 °C)
	Sample 4	SSS at 475 °C/0.5h + quench + NA + HPT + ageing (110 °C)
	Sample 5	SSS at 475 °C/0.5h + quench + NA + HPT + ageing (130 °C)
	Sample 6	SSS at 475 °C/0.5h + quench + NA + HPT + ageing (150 °C)
Process 2 T6-HPT-AA	Sample 7	SSS at 475 °C (0.5h) + quench+ ageing at 130°C (24hs) + HPT + 130°C
	Sample 8	SSS at 475 °C (0.5h) + quench+ ageing at 150°C (24hs) + HPT + 150°

3.3 Micro-hardness tests

An empirical equation $\sigma_y \approx 3HV$ with units Hv and MPa has been used to explain the relationship between strength and hardness. Hence, micro-hardness measurements can provide a good indication of the strength of materials. After the processing described above, micro-hardness tests were carried out on mirror-like polished surfaces by micro-hardness tester with a Vickers diamond pyramid indenter. The hardness tests were conducted at room temperature, with dwell time 15s and a load of 300 gf. For each processed sample, five measurements were taken at points halfway between centre and edge of disks to provide a realistic average hardness, marked by red crosses in Fig. 3-2. Five measured positions were separated by around 3 mm to avoid mutual interference between the different selected points. The average micro-hardness and error bar are reported. The error bar obtained by the standard deviation (STD) of 5 indents performed on a single HPT sample, and the STD is taken for a set of indents as:

$$STD = \sqrt{\frac{1}{N_{HV}-1}\sum_{i=1}^{N_{HV}}(x_i^{HV}-\bar{x})^2} \qquad (3\text{- }1)$$

where N_{HV} is the number of indentations, and x_i^{HV} is the value of individual indentation, and $\bar{x}$ is the average value of indentations.

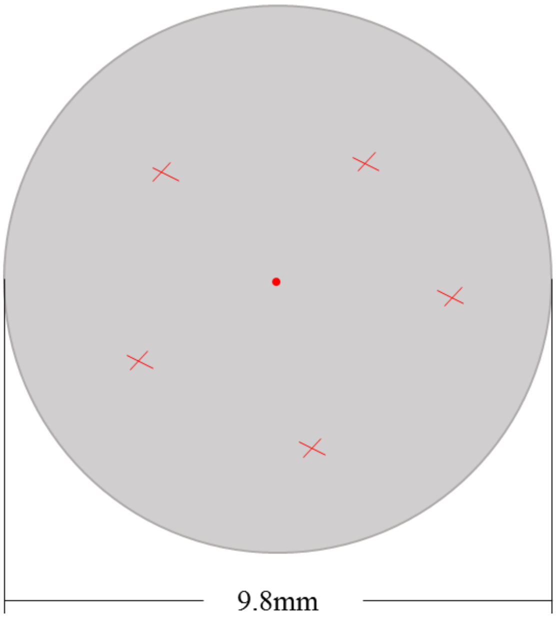

Figure 3- 2. Micro-hardness measurement was taken at the red crosses on the disk sample.

3.4 X-ray diffraction

The XRD experiment was performed on the Al-Cu-Li alloys in all stages of two processing procedures (T4-HPT-AA and T6-HPT-AA) from solution treatment to final ageing hardening aimed at revealing their evolution of microstructure and precipitates. The samples used for investigation need to be processed by the optimum processing condition for obtaining the highest strength. Accordingly, for T4-HPT-AA process, samples processed through post-ageing at 110 ^{o}C for 60h after HPT were chosen for XRD analysis. Furthermore, for T6-HPT-AA, analysed samples were pre-aged at 110 ^{o}C for 24h, followed by HPT and post-ageing at 110 ^{o}C for 180h. Overall, six samples (three for each processing condition) were analysed by XRD. All the samples were processed by quasi-constrained HPT at room temperature for 5 turns under the pressure of 6 GPa. The rotation speed was 1 rotation per minute (rpm).

The XRD samples with a diameter of 4 mm were punched from HPT-processed discs at the peripheral region (0.5 mm from the centre) as shown (dark blue region) in Fig. 3-3 X-ray diffraction (XRD) was carried out using a Rigaku SmartLab X-ray diffractometer equipped with a graphite monochromator Cu Kα radiation at 50 steps per degree and a count time of 1.2s per step. The slit length was chosen as 5 mm. In order to improve the accuracy and reduce errors, the data for each sample were collected by repeating runs, which were collected and saved as a format of raw or text, analysed by DIFFRAC EVA software to identify the precipitates and peak shifts.

Furthermore, to determine crystallite size and microstrains, XRD line broadening analysis was performed using the Materials Analysis using Diffraction (MAUD) software that is based on the full peak X-ray profile refinement using the Rietveld method [186,221]. The principle of this method was presented in Section 2.6.1. In MAUD, calculating models are adjusted step by step until the calculated curve is well matched with the experimental diffraction data. This procedure produces calculations of the microstrain and crystallite size, all as part of the MAUD software.

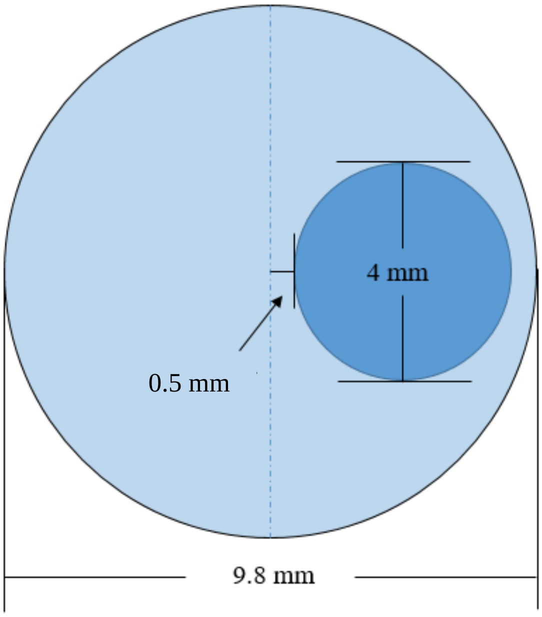

Figure 3- 3. XRD sample punched from HPT-deformed disks.

3.5 Transmission electron microscopy

TEM has been performed on Al-Cu-Li alloy using a FEI Talos 200 TEM/STEM operated at 200kV. The equipment is at Xiamen University of Technology, and TEM was operated by local staff. The disk-samples were mechanically ground down to ~150 μm in thickness first, and smaller disk-shaped samples (blue shaded) with 3 mm in diameter were punched at a position 1 mm from the centre of the disk, shown in Fig. 3-4. After this, the samples were ion polished using Gatan PIPS II polishing system through Ar ion beam milling process to obtain a thin TEM sample. For each condition of sample, bright field and dark field images were captured by both TEM and STEM modes from different locations. Selected area electron diffraction patterns (SAED) were also taken with an aperture of ~1 μm^2. The ring diffraction pattern consisting of many dispersed spots represented the nanocrystalline materials. Additionally, Energy Dispersive Spectroscopy (EDS) detector attached to the TEM was used to determine the chemical composition of any phases or precipitates.

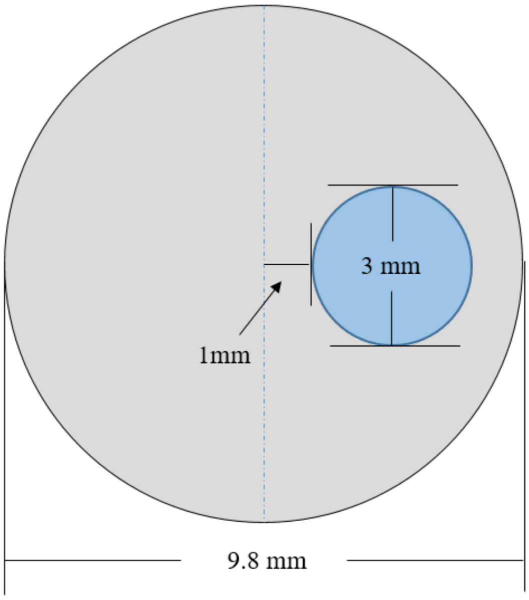

Figure 3- 4. TEM sample (blue shaded) punched from a disk sample.

The following Al-Cu-Li samples will be studied:

For T4-HPT-AA processing condition:

1). After solution treatment (T4)

2). After T4-HPT without subsequent ageing (T4-HPT)

3). After T4-HPT with subsequent ageing (T4-HPT-AA)

For T6-HPT-AA processing condition:

4). After 24h pre-HPT ageing (T6)

5). After T6-HPT without subsequent ageing (T6-HPT)

6). After T6-HPT with subsequent artificial ageing (T6-HPT-AA)

Throughout this report, the average grain size ($\bar{L}$) of each sample was measured using the modified line intercept method described as [172]:

$$\text{mean intercept length } (\bar{L}) = \frac{L_{total}(\text{total length of lines})}{P(\text{total number of intersections})}$$

In the measurement, only the grains with clear boundaries were taken into account. 4-6 straight line segments were randomly drawn on the micrograph, adding up the total grains intersected. In Fig. 3-5, a T6-HPT-AA-processed sample is taken as an example to show the average grain measurement.

The accuracy of the determination of the average grain size for the sample in each processing condition will be calculated by the standard statistical equation:

$$\text{accuracy of the mean} \approx \frac{SD}{\sqrt{N}}$$

Where *SD* is standard deviation, *N* represents the number of measurements, i.e. the number of intercept lengths determined.

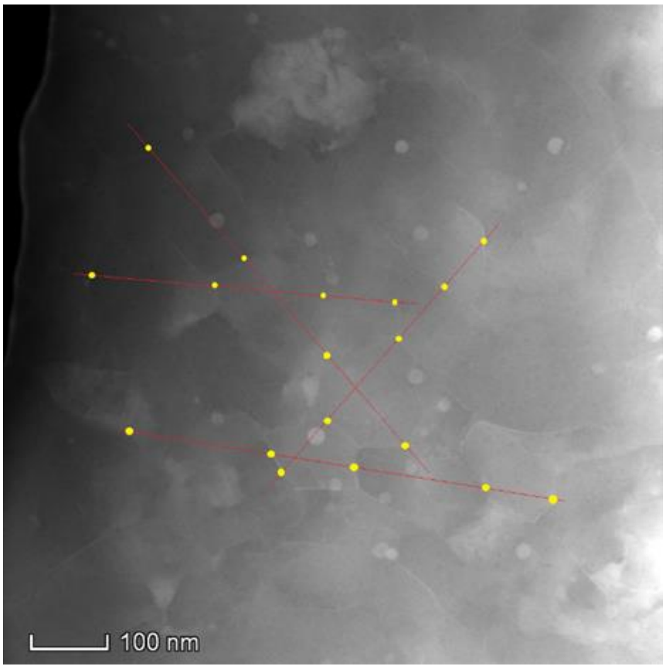

Figure 3- 5. Line intercept method is applied on the TEM micrograph of the T6-HPT-AA-processed Al-Cu-Li alloy.

3.6 Atom probe tomography

Atom probe tomography was carried out on samples processed by T4-HPT-AA and T6-HPT-AA conditions. Needle-shaped specimens for APT analysis were prepared from a thin metal bar with dimensions of 0.5 mm × 0.5 mm × 10 mm cut from HPT disk samples using a standard two-step electro-polishing procedure. A 33% nitric acid and 67% methanol solution were used in stage one (i.e. standard electropolishing), and a

2% perchloric acid and 98% butoxyethanol solution in stage two (i.e. micro-electropolishing), a standard two-step electro-polishing procedure is shown in Fig. 3-6.

APT analysis was conducted using a LEAP 4000 HR at a specimen temperature of 50 K, a pulse repetition rate of 200 kHz, a pulse voltage fraction of 15% and a target evaporation rate of 0.5%. The background vacuum level of the analysis chamber was less than 10^{-8} Pa, and the detection efficiency of the instrument was 36%. The reconstruction and visualization of the APT data were performed using Imago's Integrated Visualization and Analysis Software (IVAS) 3.6.12 software [35]. The IVAS integrated cluster finding and analysis tool was used to investigate cluster features.

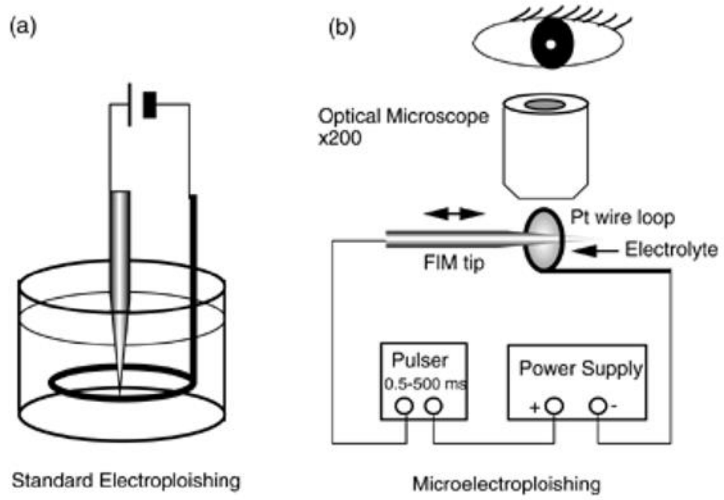

Figure 3- 6. APT sample preparation (a) standard electro-polishing; (b) micro-electropolishing.

Solute-rich features were identified using the maximum separation method, with Cu and Mg as targeting clustering solutes. The maximum separation method relies on the fact that atoms of one or more elements (the 'clustered species') are spaced more closely in the clusters than those within the matrix. This algorithm classifies atoms as belonging to a cluster if solute atoms are separated by a distance that is smaller than a certain threshold distance value, d_{max}, which is referred to as the characteristic distance, and as belonging to the matrix if the distance is larger than d_{max} [15]. In our Al-Cu-Li alloy, Mg, Cu atoms were identified as clustered/segregated if they had a separation distance of < 0.7 nm, that is d_{max} = 0.7 for a meaningful detection of the nearest neighbour.

To detect small solute clusters, the smallest solute clusters taken into account were nominated to contain at least 10 solute atoms. Solute clusters with fewer than 10 solute atoms were neglected in the analysis because such small clusters are ubiquitous in the alloy with solute atoms in a random distribution. These small solute clusters were treated as solute atoms belonging to the Al matrix.

3.7 Differential scanning calorimetry

In order to analyse the stability of phases and solute clusters formed during ageing, DSC was performed on Al-Cu-Li alloy samples. Clusters have the same crystal structure as the host Al matrix, thus showing no sharp interface and only a nuance of composition. Therefore, DSC has been extensively used to evaluate them indirectly. Accordingly, flat cylinders with 6.1 mm in diameter and 0.6 mm in thickness were punched from the periphery of the processed disk samples (see Fig. 3-7) and further prepared by grinding for DSC measurement. Mechanical preparation was done carefully to avoid any further heat input. DSC measurements were performed on disk-shaped samples using a Perkin-Elmer Pyris Diamond calorimeter. Pure Al samples of similar mass and dimension were used as reference samples. Heating was conducted from -50 ^{o}C to 520 ^{o}C at a constant rate of 30K/min. The temperature of 520 ^{o}C was set because the solution treatment temperature used for Al-Cu-Li alloy was 515 ^{o}C, which would be about 10 ^{o}C below the solidus, i.e. the max temperature at which the material is fully in solid-state. Therefore, it is reasonable to heat to the highest possible temperature while staying in the solid state. A Huber TC 100 cooler was used, and the nitrogen gas was purged to provide a protective gas atmosphere. To prevent the measuring device from icing and to keep a constant ambient condition, the device was located under an acrylic glass box, which was flushed with dry air.

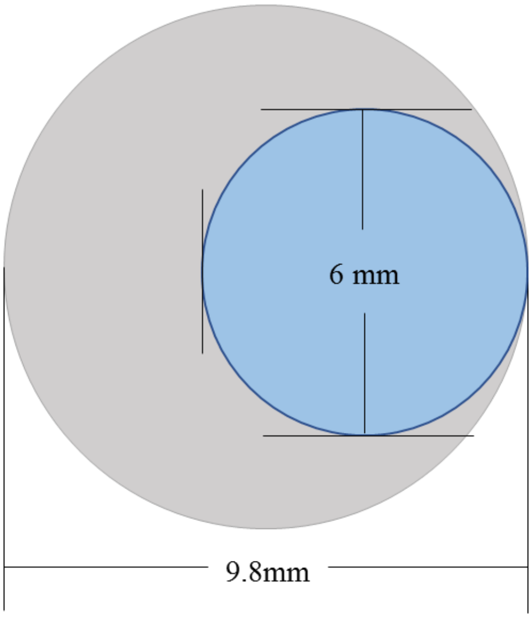

Figure 3- 7. DSC sample (blue shaded) punched from disk-sample.

Chapter 4 Investigating the highest hardness of materials

4.1 Results

4.1.1 Micro-hardness test of Al-Cu-Li alloy

The Al-Cu-Li (Al-2.88Cu-1.34Li-1.03Mg) disks that were HPT processed for 5 turns were aged at 100 °C, 110 °C, 120 °C, 150 °C and 170 °C. Fig. 4-1 shows the variation of micro-hardness when ageing at different temperature for ageing times up to 500h. Fig. 4-1 exhibits that the hardness of HPT-processed Al-Cu-Li depends strongly on both the ageing time and temperature. On ageing at 110 °C, 120 °C and 150 °C the hardness initially increases to the peak age condition and subsequently declines with increasing ageing time, with the peak at 64h, 8h and 4h, respectively. It can be concluded that the higher the ageing temperature, the shorter the time it takes to reach the peak hardness, and this is ubiquitously seen in nearly all age hardening alloys (see also Discussion section). For ageing at 170 °C, a pronounced reduction in hardness from 222 Hv to 154 Hv occurs. Furthermore, a tendency of continuous increment in hardness can be seen in Fig. 4-1 even after ageing for 500h at 100 °C up to~240 Hv, and it seems that there is a potential for a further increase with longer ageing time.

It is noticed that immediately after HPT gives a range of variability in the initial hardness of these disks following the same sample preparation process. Although the highest hardness level of Al-Cu-Li is 244 Hv for 8h ageing at 120 °C (Fig. 4-1), the percentage increase from the as-HPT condition is only ~5.6%. While the maximum percentage increase of~11.3% was achieved for ageing at 100 °C for over 500 hours, and a further increase may be expected. Moreover, a micro-hardness up to ~240 Hv for ageing 110 °C/64h with a percentage increase of 8.5% after as-HPT condition was achieved. In the present research, we mainly focus on the percentage increase of hardness after the complete T4-HPT-AA process. So the impacts of the slight difference in initial hardness of those disks on the subsequent heat treatment are negligible.

Fig. 4-2 illustrates the comparison of the hardness of T4-HPT processed Al-Cu-Li alloy aged at 100 °C and T6 (110 °C/24h) -HPT processed alloy aged at 110 °C for up to 400h. Both process methods depicted an increasing tendency in hardness. A significant increase in hardness was achieved through the T6-HPT-AA (i.e. pre-ageing followed by HPT and post-ageing) process, compared with the samples that have undergone a T4-HPT-AA treatment. It is worth noting that both T4 and T6 processed samples have similar hardness values right after the HPT process (~215 Hv), which means the large hardness increase mainly occurred within the first 24h artificial ageing treatment after HPT. Further long time ageing up to 400h causes the hardness of T6-HPT-AA-processed sample to continue rising to a plateau of ~260 Hv. While the T4-HPT-AA treated sample only increases up to ~240 Hv.

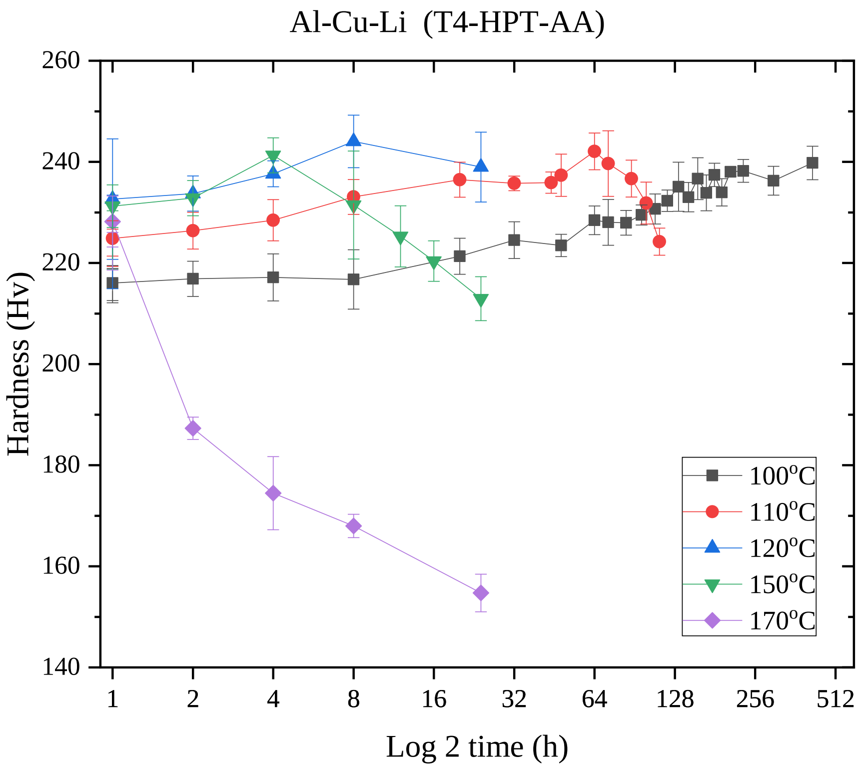

Figure 4- 1. Micro-hardness of the Al-Cu-Li alloy processed by T4-HPT-AA process as a function of ageing time at different temperatures.

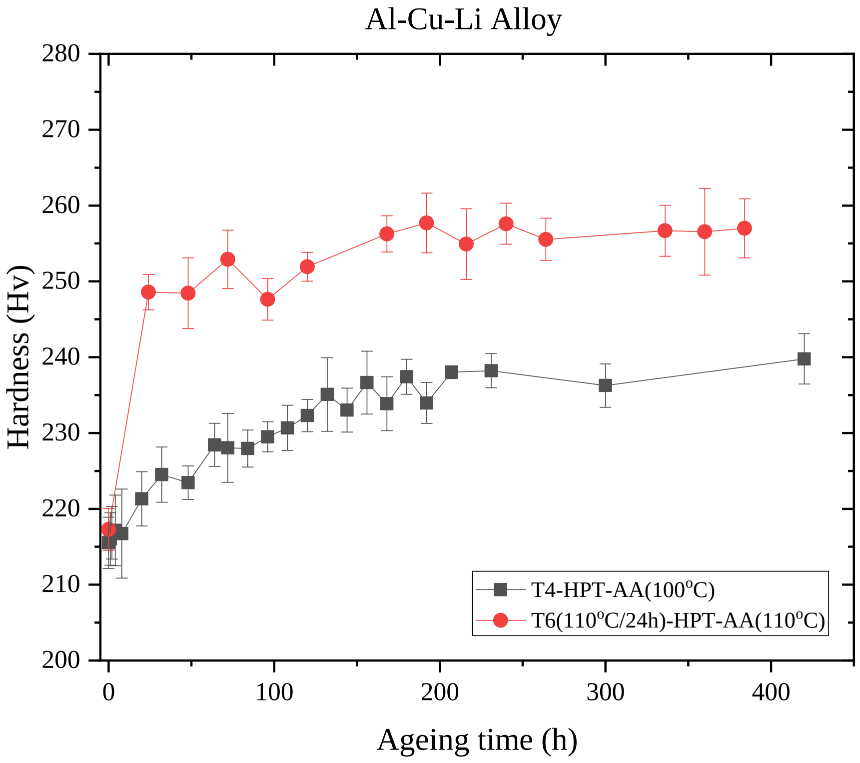

Figure 4- 2. Micro-hardness of the Al-Cu-Li alloy processed by T4-HPT-AA and T6-HPT-AA process as a function of ageing time at different temperatures.

4.1.2 Micro hardness test of Al-Zn-Mg-Cu alloy

As illustrated by Fig. 4-3, the Al-Zn-Mg-Cu alloy does not show an increase in hardness with increasing ageing time at any selected ageing temperature. Thus this alloy appears to have a post-HPT ageing behaviour that is very different from that of the Al-Cu-Li alloy. Ageing at the lower temperatures of 80 ^{o}C and 90 ^{o}C after HPT does not affect the micro-hardness of Al-Zn-Mg-Cu alloy, with hardness values remaining fairly flat. In addition, ageing at a higher temperature of 130 ^{o}C results in a continuous decrease from the beginning of ageing treatment. The hardness was reduced from 240 Hv to 215 Hv within 2 hours and further down to nearly 200 Hv in the next two hours. Further increasing the temperature to 150 ^{o}C results in a sharper reduction in hardness, from 250 Hv to 165 Hv after 4 hours of ageing.

For this Al-Zn-Mg-Cu alloy, the T6-HPT-AA process does not improve the hardness of materials at the ageing temperature of 130 °C and 150 °C. The data in Fig. 4-4 depicts that post-HPT ageing at temperature 130 °C for both T4-HPT-AA and T6-HPT-AA conditions results in softening. However, the softening rate is slightly reduced when samples were processed by T6-HPT-T6 condition, i.e. the T6-HPT-AA condition is more stable than the T4-HPT-AA condition.

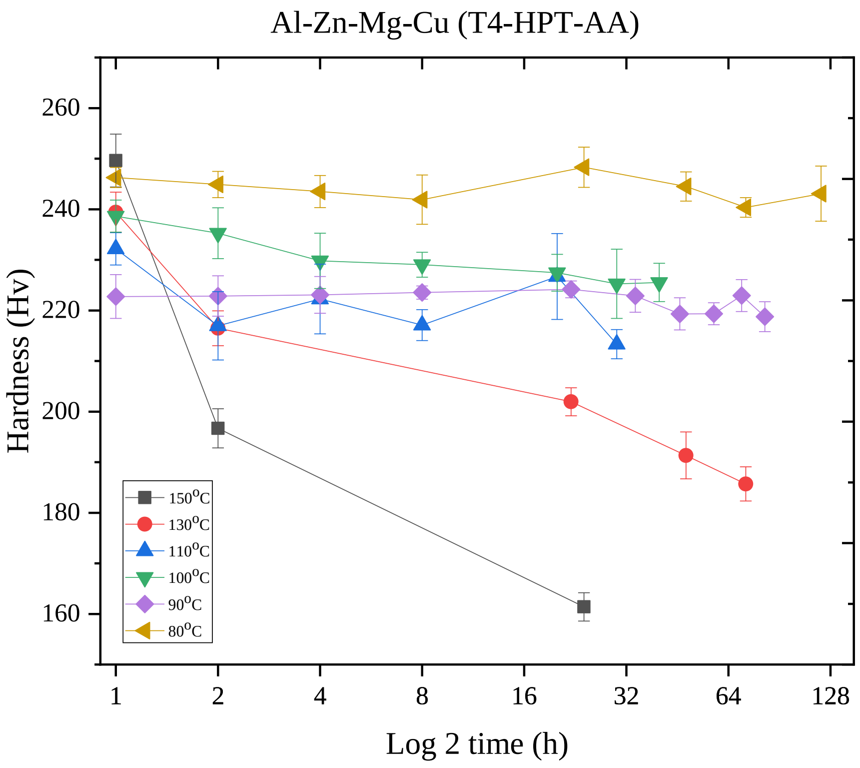

Figure 4- 3. Micro-hardness of the Al-Zn-Mg-Cu alloy processed by T4-HPT-ageing as a function of the ageing time at different temperature.

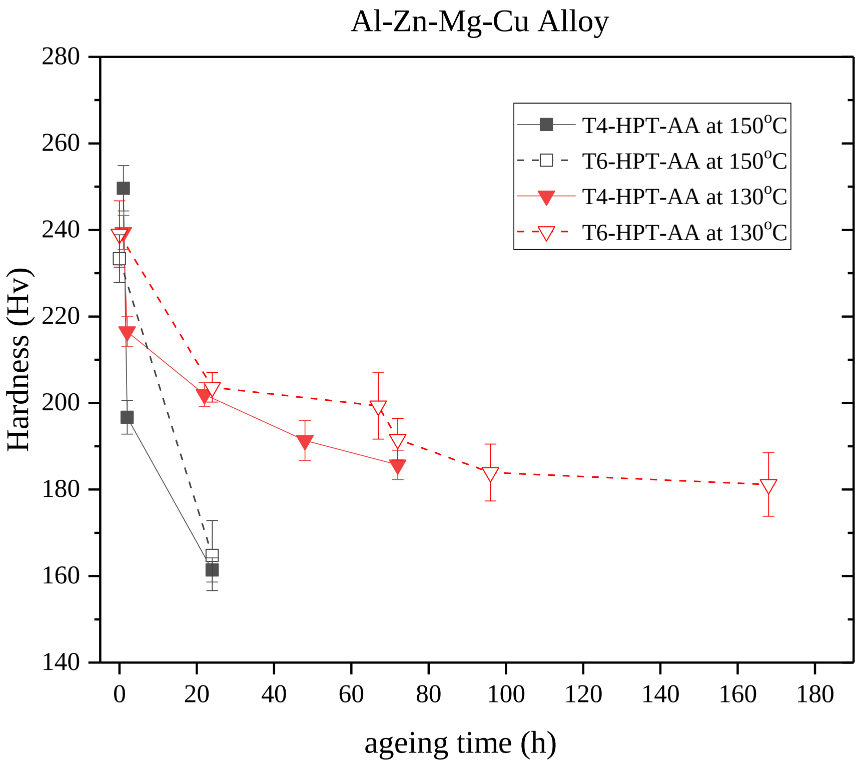

Figure 4- 4. The hardness of T4-HPT-AA and T6-HPT-AA-processed Al-Zn-Mg-Cu at 130 °C and 150 °C.

4.2 Discussion

4.2.1 Al-Cu-Li alloy in T4-HPT-AA and T6-HPT-AA conditions

On post-HPT ageing of the Al-Cu-Li alloy at temperatures of 110 °C, 120 °C and 150 °C, the hardness of the samples first increases with ageing time and reaches a peak value. After peak ageing time, the hardness decreases gradually with ageing time. The shape of the curves is typical of an age hardening curve of heat treatable Al-based alloys processed by conventional age hardening treatment [9,34,135,222–225]. Nevertheless, the hardness is much higher than conventionally age hardening processed Al-Li based alloys. For instance, the micro-hardness of 160±7 Hv was obtained from AA2195 (Al-4Cu-1Li-0.36Mg) alloy processed through 1h solution treatment at 510 °C, followed by stretched to 3% and ageing at 150 °C for 30h [225]. Here in this report, the highest hardness of 244 Hv is achieved by combining HPT and age hardening process.

Kim et al. [226], compared the hardness of a conventionally aged 2024 alloy with that of a severe plastically deformed 2024 alloy. It showed that the deformed (through cryo-rolling) 2024 alloy takes a shorter time to reach its peak hardness as plastic deformation prior to artificial ageing had been shown to strongly influence the Al-Cu-Li alloy precipitation kinetics and T_1 precipitates size. This results in a uniform distribution of T_1 precipitates formed heterogeneously because the plastic deformation increases the number of heterogeneous nucleation sites. T_1 precipitates are thought to be the dominant hardening precipitates. Hence, it is reasonable to speculate that the HPT-processed Al-Cu-Li alloys may also take a shorter time to reach the peak hardness than conventional age hardened Al-Cu-Li alloys.

For a conventional ageing process (i.e. solid solution treatment followed by artificial ageing), the increase of hardness is due to the cease of dislocation movement by the precipitates formed during ageing. When ageing beyond the peak hardness, the reduction in hardness is associated with the increase in inter-particle separation among precipitates, which reduces the degree of complication for the dislocations to bow the precipitates [227]. Besides, the coalescence of the precipitate into larger particles leads to fewer obstacles to dislocation motions, thereby reducing the hardness. Additionally, when the ageing process was performed at a higher temperature (150 ^{o}C), the hardness reaches its highest values in a very short period due to the increase of driving force. This may be explained by the faster precipitation rate of alloying atoms, which results in a faster formation of precipitates. Whereas, at the lower ageing temperature, the formation of precipitates is prolonged because slower diffusion process, the precipitates only appear in the Al matrix after an extended period of ageing time. These processes, known from the conventional ageing treatments, might thus explain the observations on post-HPT ageing of the Al-Cu-Li alloy. It has been reported by Y.H. Zhao et al. [134] that ECAP can increase the precipitation kinetics without changing precipitation sequences and provide a significant strengthening effect on age hardening in 7075 Al alloy. Therefore, it may be reasonable that the obtained hardness curve of solution treatment + HPT + ageing-processed samples in Fig. 4-1 has a similar tendency with that of conventional ageing processed samples.

A similar hardness curve was observed for AA2091 (Al-2.09Li-1.99Cu-1.55Mg-0.12Zr in wt. %) treated by solution treatment at 505°C for 30 mins and subjected to HPT for 5 revolutions at RT followed by ageing at 100°C, 150°C and 190°C [31]. The results indicated that the hardness of AA2091 increased to the peak values when aged at 100°C/223h and 150°C/56h, while a decrease in hardness occurred from the starting of the ageing process at 190°C. The formation of UFG structures with high angle grain boundaries was observed after HPT by TEM dark-field images and SAED [31]. Additionally, TEM micrographs also showed that these UFG structures with high angle grain boundaries were still retained after ageing treatment, even at a high temperature of 190 °C. Besides, at peak age condition of AA2091, fine dispersion δ' (Al_3Li) precipitates were found to exist within the UFGs after ageing, and these fine δ' (Al_3Li) precipitates were thought to be responsible for the age hardening.

Moreover, on ageing beyond the peak age condition, the material becomes over-aged, and the reduction of hardness is most likely due to the coarsening of δ' particles. Therefore, it is reasonable to anticipate that in the HPT-processed Al-2.88Cu-1.34Li-1.04Mg alloy studied in this work, a fine dispersion of precipitate particles is formed in the UFGs, which is responsible for the high hardness. However, the lower content of Li compared with AA2091 (2.09 wt. % Li) makes it unlikely to form δ' phase, and other precipitates such as T phase or co-clusters (Cu-Mg) may exist within the UFGs after ageing, thus confirming the strengthening effect of the combination of grain refinement and precipitation hardening.

It is also relevant to consider work reported on Al-10.8 wt. % Ag alloy processed by solution treatment and ECAP, followed by ageing at 373K (100 °C) and 473K (200 °C) [34]. This work also shows that the rate of increase in hardness, $\partial Hv/\partial t$, is faster at ageing temperature of 473K (200 °C) and the highest Hv values occur after a very short ageing time: after 10h at 473K and 100h at 373K. An AA2024 (Al-Cu-Mg) alloy was also processed by the combination of pre-ECAP solution treatment combined with post-ECAP ageing with a temperature of 373K (100 °C) and 448K (175 °C) [226]. On ageing at 448K, the peak hardness was reached only after 2h ageing, which is similar to the Al-Cu-Li alloy studied in this work aged at 150 °C with a rapid peak ageing time of only 4h. A similar observation has been reported in many Al-based composite materials such as B_4C-6061 and SiC-2124 [228]. Hong and Gray [229] suggested that this accelerated ageing phenomenon was promoted in Al-based composites with high densities of dislocation via the preferential solute-atom segregation at dislocations or preferential nucleation site of solute precipitation on dislocation. This mechanism may also be a factor for the solution treatment + HPT+ ageing processed Al-Cu-Li alloy because of high dislocation density caused by severe plastic deformation. Many works have also reported that the SPD process may induce strong solute atom segregation, as described in Section 2.4.4.

When ageing the Al-Cu-Li alloy at a lower temperature (120 ^oC and 110 ^oC shown in Fig. 4-1), peak ageing is delayed, and slightly higher peak hardness is reached at 8h and 64h, respectively. In addition, Fig. 4-1 shows a pronounced reduction in hardness of Al-Cu-Li from the onset of ageing time on ageing at 170 ^oC. This is similar to observation for AA6061 aged at 175 ^oC and 100 ^oC after processing by solid solution treatment at 530 ^oC/4h followed by ECAP [35]. This hardness drop was ascribed to the recovery effect and grain coarsening of the severely deformed substructure through annealing, which would mask the effect of precipitation hardening during ageing treatment. Furthermore, it has been shown that this softening effect is reduced when ageing Al-6061 alloy at a lower temperature of 100^oC [35]. Hence, the increased hardness of Al-Cu-Li alloy at 100 ^oC, 110 ^oC, and 120 ^oC (Fig. 4-1) implies that the effect of age hardening is more dominant than the softening effect.

According to recently published work on achieving high strength in Al-alloys, the maximum hardness attained was 275 Hv by ageing Al-Li-Cu-Mg (2091) at 150 ^oC for 56h or 100 ^oC for 223h [31]. In this work, the highest hardness level of Al-Cu-Li alloy was found to be 244 Hv at 120 ^oC for 8h ageing, which is lower than AA2091, but the percentage of increase at 120 ^oC is only ~8.9%. However, a tendency of continuous increment in hardness can be seen in Fig. 4-1, hardness measured up to~240 Hv when ageing at 100 ^oC/500h. This is continuously increasing hardness with an increment of ~11.3%, indicating a potential to surpass the highest hardness of AA2091.

The mechanical properties and precipitation evolution of Al-Li-Cu alloys that undergone solution treatment + HPT + ageing treatment have been studied in a few works [31]. In contrast, no research has been conducted on Al-Li-Cu alloys that are processed by the combination of ageing treatment and HPT processing in the sequence of solution treatment + pre-ageing + HPT + post-ageing (i.e. T6-HPT-AA). Therefore, so far, it is hard to explain the possible reason that causes a significant improvement in the hardness of Al-Li-Cu alloy. The microstructure evolution needs to be analysed for further investigation, e.g. XRD and TEM techniques.

4.2.2 Al-Zn-Mg-Cu alloy in T4-HPT-AA and T6-HPT-AA conditions

Unlike the Al-Cu-Li alloy, post-HPT ageing of the Al-Zn-Mg-Cu alloy at 80 ^{o}C and 90 ^{o}C does not affect the micro-hardness, whilst ageing at higher ageing temperature ranges from 100 ^{o}C to 150 ^{o}C causes a drop in hardness. A report on Al-Cu-Mg-Cu-Zr (Al-1Cu-2.8Mg-6.1Zn-0.37-Zr) alloy processed by SPD followed by various artificial ageing in a range of 50 ^{o}C to 300 ^{o}C. It showed that artificially ageing of the strongly deformed alloy at low temperatures (T=50 ^{o}C and T=100 ^{o}C) does not influence the hardness of the alloy. In addition, increase the ageing temperature to 150 ^{o}C and 200 ^{o}C results in a reduction in hardness value. However, these observations were not explained in that report [230].

Although the T6-HPT-AA process does not enhance the hardness of the Al-Zn-Mg-Cu alloy, the reduction of softening rate implies that the T6-HPT-AA process may have a great potential to improve the stability. In order to investigate more details, further works might required.

4.3 Summary

The present experimental work demonstrates the potential for the combination of grain refinement with appropriate ageing treatments to achieve an ultra-high strength for Al-Li-Cu and Al-Zn-Mg-Cu alloys. Two processing conditions were applied on two types of materials: T4-HPT-AA and T6-HPT-AA. In addition, a series of micro-hardness measurements were performed after various ageing temperatures and ageing times. The conclusions are summarised as follows:

1) A hardness of ~240Hv is achieved during T4-HPT-AA treatment (i.e. Al-Li-Cu alloy is aged at 100^{o}C for 500h) with a percentage increase of 11.3% HV after as-HPT condition.

2) A further increased hardness of Al-Li-Cu alloy was achieved through T6-HPT-AA treatments, achieving an ultra-high hardness of ∼260Hv via pre-HPT ageing at 110^{o}C/24h and post-HPT ageing at 110^{o}C/400h.

3) By contrast, ageing after HPT of Al-Zn-Mg-Cu alloys does not provide the desired age-hardenings. On ageing at 100^{o}C to 150^{o}C, the hardness decrease continuously with increasing ageing time and reducing ageing temperature to below 100^{o}C, resulting in a stationary hardness of the Al-Zn-Mg-Cu alloy.

4) Although processing with T6-HPT-AA treatment does not enhance the hardness of the Al-Zn-Mg-Cu alloy, it can increase the ageing stability of the alloy.

After two age hardenable Al alloys were processed by two different processing conditions, both T4-HPT-AA and T6-HPT-AA processes increased the hardness of the Al-Cu-Li alloys. However, neither of them was effective in improving the strength of 7449 Al alloys. Hence, only Al-Cu-Li alloys processed by the optimum condition will be investigated for further microstructural analysis.

Even if a maximum percentage increase of ~ 11.3% HV was achieved when Al-Cu-Li was aged at 100 ^{o}C for over 500 hours (Fig. 4-1), the ageing process is time-consuming. Eventually, ageing at 110 ^{o}C for 60 hours is chosen as the optimum T4-HPT-AA processing condition to obtain the highest hardness of the Al-Cu-Li alloy. Meanwhile, pre-ageing (110 ^{o}C/24h) before HPT combined with a post-ageing (110 ^{o}C/180h) process is chosen as the optimum T6-HPT-AA processing condition.

Chapter 5 Microstructural evolution and strength of Al-Cu-Li alloy

In Chapter 4, the optimum processing temperature and time for both T4-HPT-AA and T6-HPT-AA treatments to achieve maximum hardness/strength Al-Cu-Li alloy were obtained. The microstructure of the material is one of the most essential features that affect the hardness/strength of the metals or alloys. Therefore, to investigate the strengthening mechanisms behind this ultra-high strength Al-Cu-Li alloy, the microstructure evolution of the alloy will be evaluated by Micro-hardness, TEM and XRD in this chapter.

5.1 Results

5.1.1 Micro-hardness

The micro-hardness of Al-Cu-Li alloys at the optimum processing condition of T4, T4-HPT, T4-HPT-AA, T6, T6-HPT and T6-HPT-AA were measured, and the results are shown in Fig. 5-1 (a) and (b). This Fig. 5-1(a) depicts that the micro-hardness after T4 treatment (i.e. solution treatment for 515 ^{o}C /0.5h followed by quenching and natural ageing) was ∼120 Hv. After 5 turns HPT processing, the hardness has dramatically increased to ∼220 Hv, and a continued low temperature ageing treatment (110 ^{o}C/60h) improved the peak-aged hardness further to ∼235 Hv.

On the other hand, processing by T6 treatment (i.e. solution treatment followed by quenching and artificial ageing 110 ^{o}C/24h) does not show any improvement in hardness, compared with the sample that had processed by T4 treatment (Fig. 5-1 (b)). Also, it is obvious that the hardness increases largely from ∼120 Hv to ∼210 Hv after material being processed by the HPT. As expected, a further improvement in the hardness to ~260 Hv was accomplished by a pre-ageing (110 ^{o}C/24h) before HPT in combination with a post-ageing (110 ^{o}C/180h) process. This gives over two times that of the initial T4-processed sample (~120 Hv).

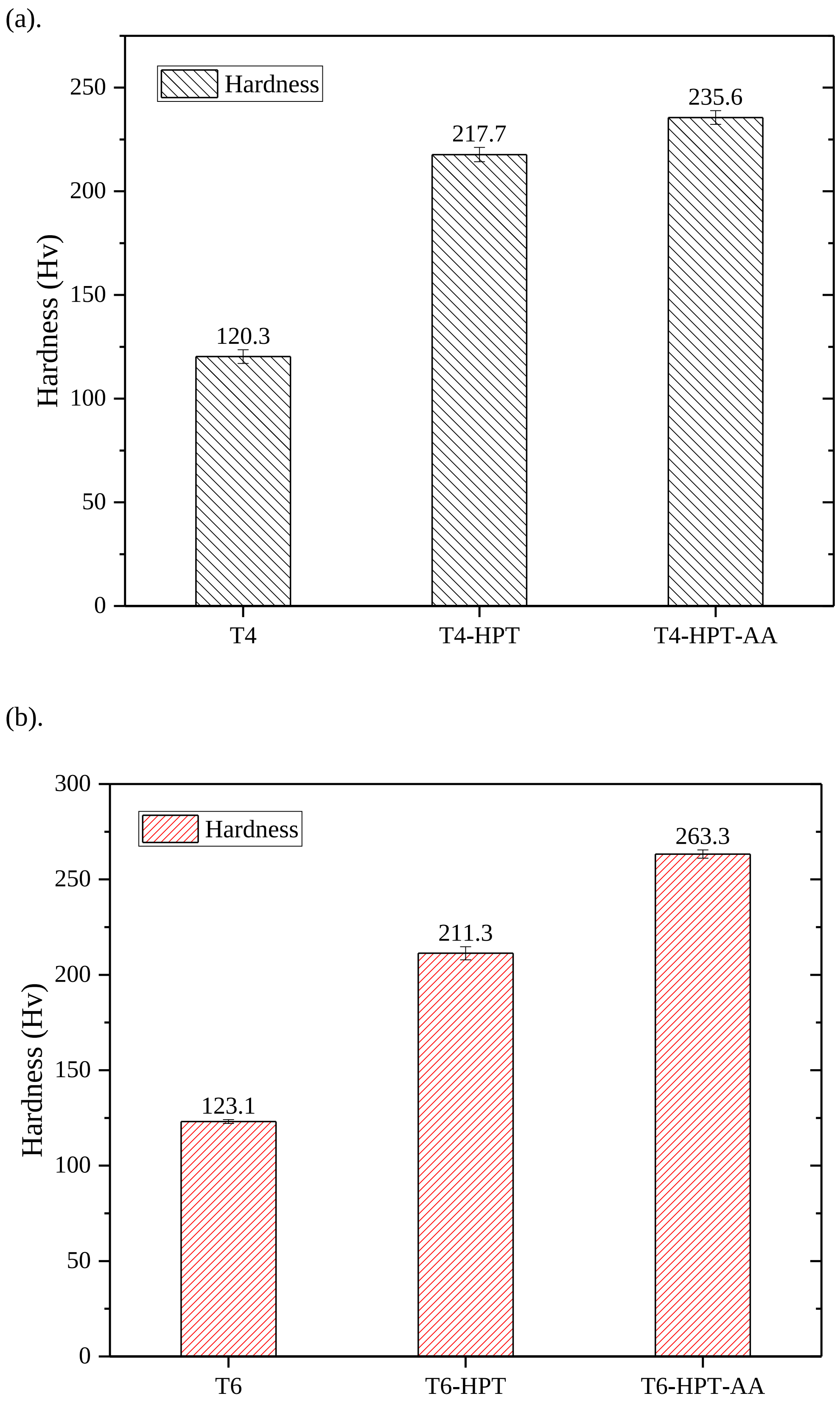

Figure 5- 1. The micro-hardeness of Al-Cu-Li alloy under T4, T4-HPT and T4-HPT-AA (a); T6, T6-HPT and T6-HPT-AA (b) processing conditions.

5.1.2 XRD

XRD diffraction spectra in the 30-90^{o} range were collected for all six samples with a step of 0.02^{o}. Fig. 5-2 (a) depicts the XRD patterns of the T4, T4-HPT, T4-HPT-AA and T6, T6-HPT, T6-HPT-AA-processed Al-Cu-Li-Mg-Zr samples. For all the samples, diffraction peaks due to Al-phase are detected. The observed preferred peaks are due to (1 1 1), (2 0 0), (2 2 0), (3 1 1) and (2 2 2) at 2θ equal to 38^{o}, 45^{o}, 65^{o}, 78^{o} and 82^{o} respectively. However, the spectra of the undeformed samples (i.e. T4 and T6) in addition reveal the presence of additional weak peaks, identified as S (Al_2CuMg) and θ (Al_2Cu) phases. Accordingly, in the absence of S and θ phases in the other four samples suggesting that all these precipitates are dissolved in Al matrix, and a supersaturated solid solution is formed after HPT processing.

Additionally, in the enlarged sections of the spectra between 37^{o} to 46^{o} shown in Fig. 5-2 (b), dash lines are used to compare the position of (1 1 1) and (2 0 0) peaks arising from Al matrix in each stage of two processing procedures (i.e. T4-HPT-AA and T6-HPT-AA). It can be seen that compared with T4 and T6-processed samples, the highest (111) diffraction peaks of T4-HPT and T6-HPT-processed samples slightly shifted towards the lower angles as a result of HPT processing (Fig. 5-2 (b)). It is likely due to a change in the amount of dissolved elements into the Al matrix.

Also, after HPT and post-ageing treatments (i.e. T4-HPT-AA and T6-HPT-AA), these Al-phase diffraction peaks remain present, and no additional peaks arise, which indicates that no new phases are formed due to post-ageing. Besides, the intensity of Al phase peaks reveals that the volume fraction of Al-phase in T6 and T4-processed samples are higher than that of the other HPT-processed samples. Additionally, the peaks intensity of Al phase at (1 1 1), (2 0 0) and (2 2 2) planes varies with different processing conditions, which represents they have the same crystalline structures but with different lattice parameters. This suggests that HPT processing has changed the crystallographic texture of the alloys.

(a)

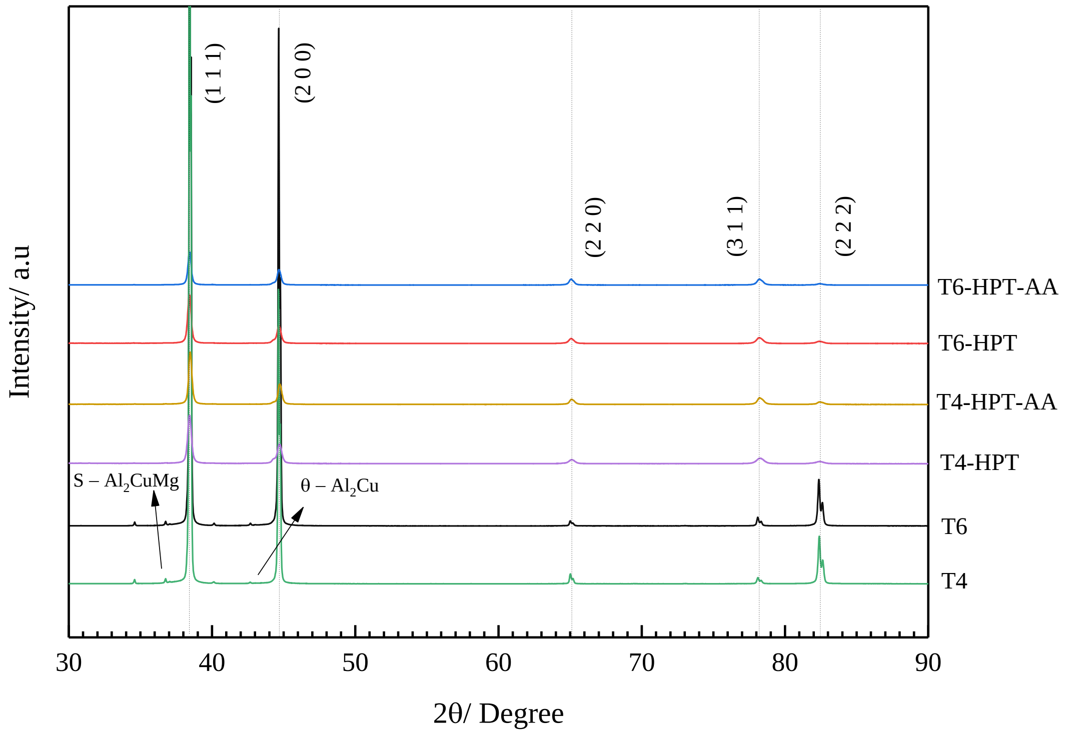
Intensity/ a.u
(1 1 1)
(2 0 0)
(2 2 0)
(3 1 1)
(2 2 2)
T6-HPT-AA
T6-HPT
T4-HPT-AA
T4-HPT
T6
T4
S – Al_2CuMg
θ – Al_2Cu
30
40
50
60
70
80
90
2θ/ Degree

(b)

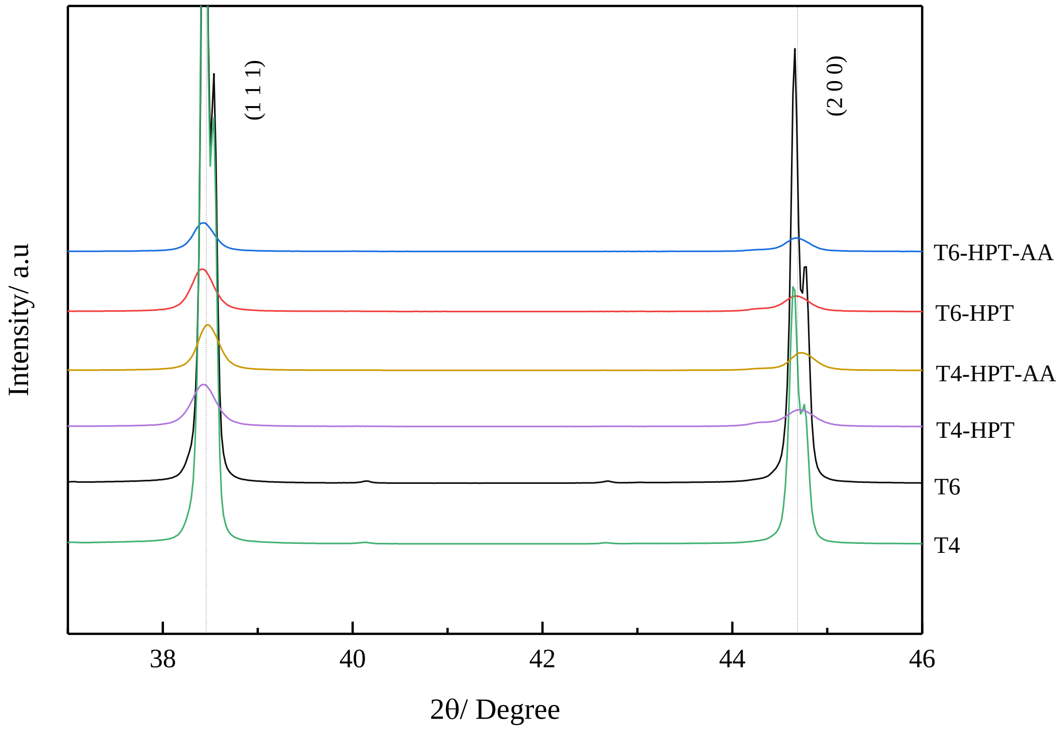
Intensity/ a.u
(1 1 1)
(2 0 0)
T6-HPT-AA
T6-HPT
T4-HPT-AA
T4-HPT
T6
T4
38
40
42
44
46
2θ/ Degree

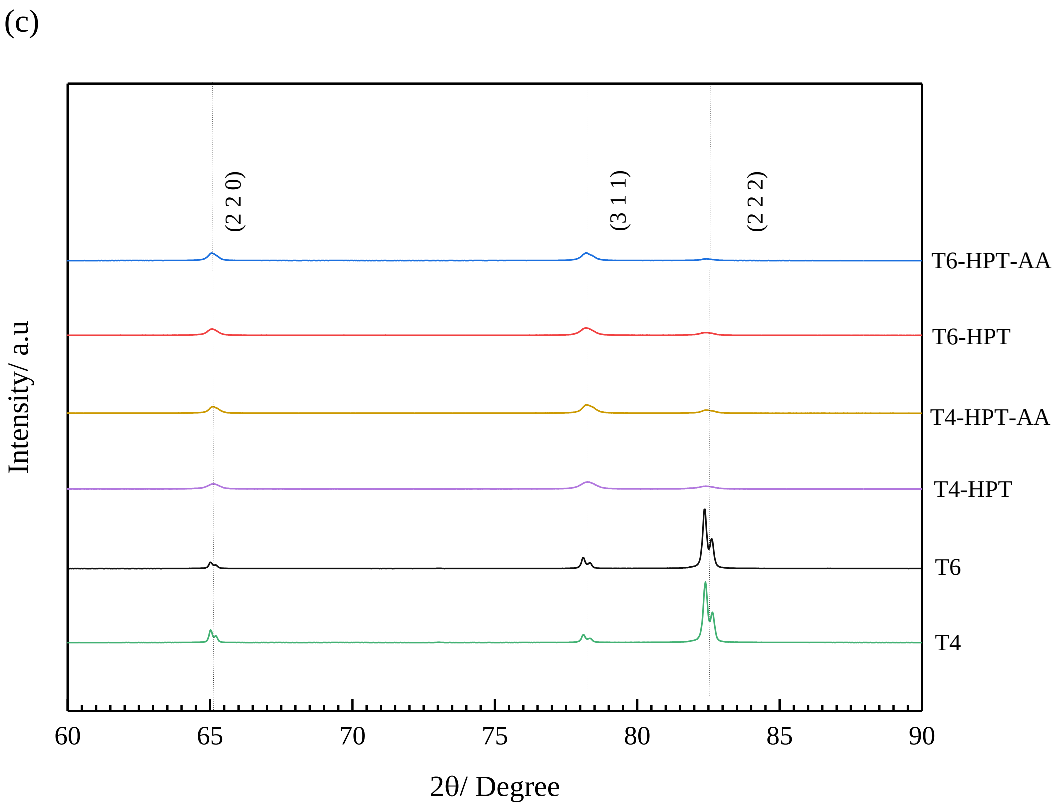

Figure 5- 2. (a) Overview of XRD patterns of the HPT-processed and aged Al-Cu-Li alloys; (b) enlarged section of XRD pattern from 37° to 46°, and (c) enlarged section of XRD patterns from 60° to 90°.

Careful examination of Fig. 5-2 (c) reveals that peak broadening is observed in the profiles of samples processed by HPT, compared with T4 and T6 conditions. In the XRD profile, the peak broadening of HPT-processed samples is caused by a reduction in crystallite size and increased density of lattice defects, mainly dislocations and grain boundaries [188–191]. Besides, the double peaks in T4 and T6-processed samples (shown in Fig. 5-2 (b-c)) are likely due to Kα_1 and Kα_2 doublet. Kα_1 and Kα_2 doublet almost always present, and they overlap heavily at low angles and are more separated at high angles. The peak broadening after HPT and subsequent ageing causes the disappearance of these double peaks.

The microstrain and crystallite size were optimised simultaneously using Rietveld refinement through profile fitting on the XRD data using the ‘MAUD’ software. The values of microstrain and crystallite size determined based on the Rietveld method (see Section 2.6.1) are given in Table 5-1 for six samples processed by different processing conditions. In addition, the dislocation density ρ, defined as the length of dislocation lines per unit volume (m/m^3) can be obtained from the measured microstrains and crystallite size using Eq. 5-1 [134].

$$\rho = \frac{2\sqrt{3} < \varepsilon^2 >^{1/2}}{D_c\ b} \tag{5- 1}$$

Where b is the Burgers vector length and equal to $\sqrt{2}a/2$ for an FCC material (i.e. 0.286 nm for Al), $< \varepsilon^2 >^{1/2}$ is the internal lattice microstrain, D_c is the crystallite size related to coherently scattering domains (i.e. the mean size of dislocation free domains).

Table 5- 1. The microstrain, crystallite size and dislocation densities of Al-Cu-Li alloy processed by different processing conditions, as determined by Rietveld analysis of XRD patterns.

Processing condition	Microstrain/10^{-3}	Crystallite size/nm	Dislocation density/10^{14} m^{-2}
T4	0.48	2047	0.03
T4-HPT	1.63	56	3.50
T4-HPT-AA	0.58	90	0.78
T6	0.34	2212	0.02
T6-HPT	1.06	84	1.50
T6-HPT-AA	0.56	97	0.70

According to the data from Table 5-1, the changes in crystallite size and the dislocation density of the Al-Cu-Li alloy with different processing conditions are plotted in Fig. 5-3. Fig. 5-3 (a) depicts that the crystallite size of T4-processed sample reduces by a factor 30 during 5 turns HPT processing at RT, and then slightly increases during the subsequent ageing for 60h. The dislocation densities have an opposite trend: increasing to the highest level of ~3.5×10^{14} m^{-2} right after HPT, indicating dislocation accumulation during HPT deformation and then dropping to ~0.8×10^{14} m^{-2} after subsequent peak ageing treatment.

The changes in crystallite size and dislocation densities with the consecutive processing conditions T6, T6-HPT and T6-HPT-AA present almost the same trend as with T4, T4-HPT and T4-HPT-AA processing conditions, shown in Fig. 5-3 (b). The crystallite size of T6-processed sample also becomes significantly smaller during HPT deformation from a few micrometres (~2 μm) down to nanoscale level (~80 nm). However, the subsequent artificial peak-ageing treatment almost has no effect on the crystallite size of T6-HPT-processed sample. In addition, the T6-processed sample reveals a large generation of dislocations after being deformed by HPT, with the dislocation density increasing to ~1.5×10^{14} m^{-2}. Subsequently, the dislocation density of the sample gradually drops with increasing ageing time and decreases to ~0.7×10^{14} m^{-2}.

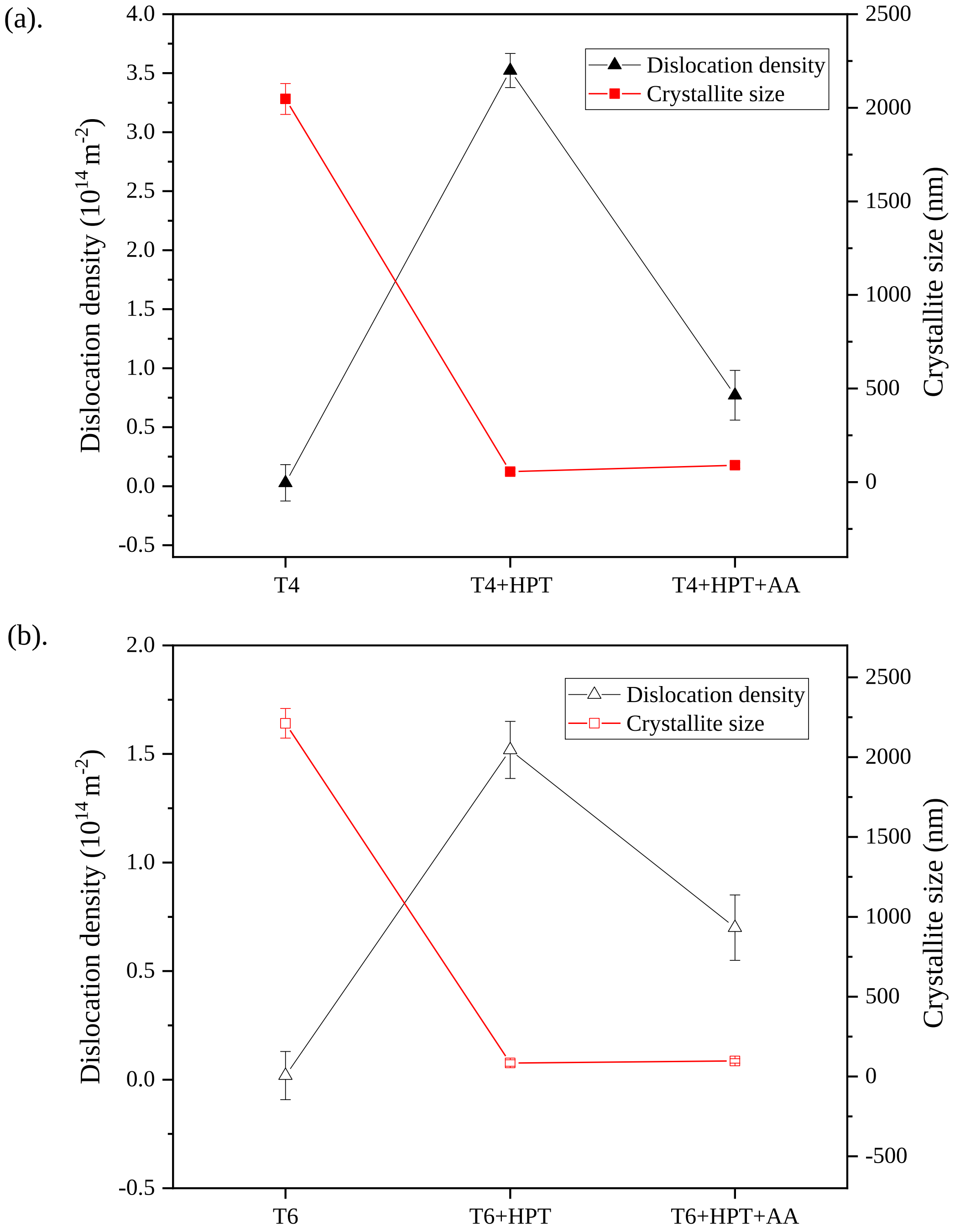

Figure 5- 3. The crystallite size and dislocation density as a function of different processing condition; (a) T4, T4-HPT and T4-HPT-AA, and (b) T6, T6-HPT and T6-HPT-AA processing conditions.

5.1.3 TEM

Al-Li-Cu in T4 condition

Bright-field TEM (BF-TEM) and high angle angular dark field mode of STEM (HAADF-STEM) micrographs of starting material (undeformed Al-Cu-Li alloy) in T4 condition are shown in Fig. 5-4. Large grain size was shown in Fig. 5-4 (a), and the mean grain size calculated by the line intercept method is 3030.3 ± 7.8 nm. Characterization at higher magnification by TEM (Fig. 5-4 (b)) depicts the presence of dislocations in the microstructure of the specimen. The corresponding SAED pattern of the red-circled area was captured (in Fig. 5-4 (b)), which reveals a single Al phase grain. Also, the corresponding elemental mapping was provided by EDS detector equipped with STEM, shown in Fig. 5-4 (c). Careful inspection of the square region microstructure in Fig. 5-4 (a), the spherical-shaped particles with a size of ~50 nm was found within the grain of T4-processed sample (shown in Fig. 5-5 (a)). These particles were detected to be Zr-rich particles by EDS analysis (see Fig. 5-5 (c)). Comparison with literature data on the shape and composition of Zr-rich particles in Al alloys [79–81] indicates that these particles are β' (Al_3Zr) phase.

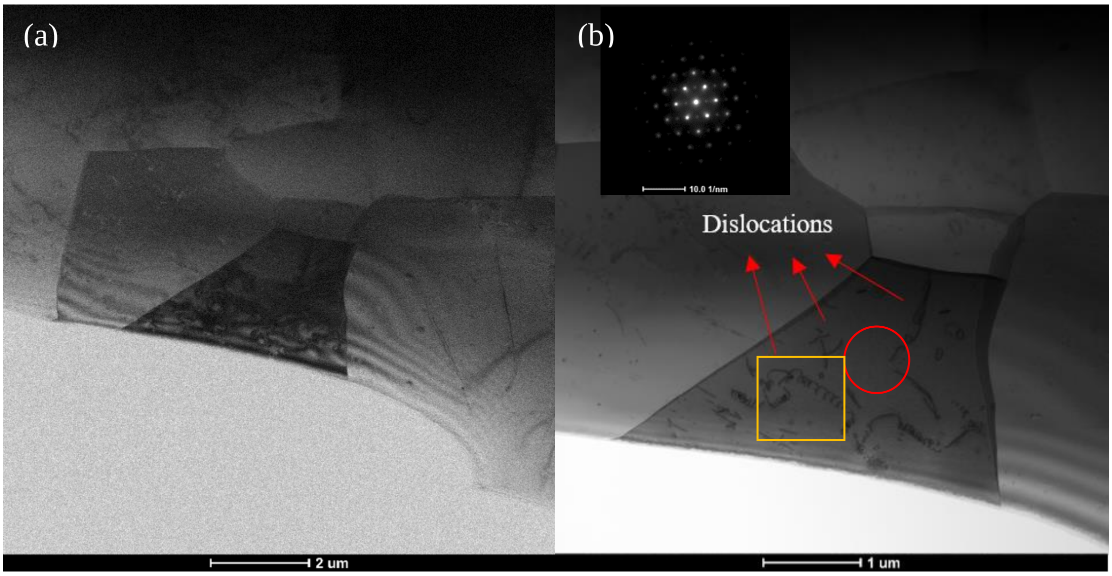

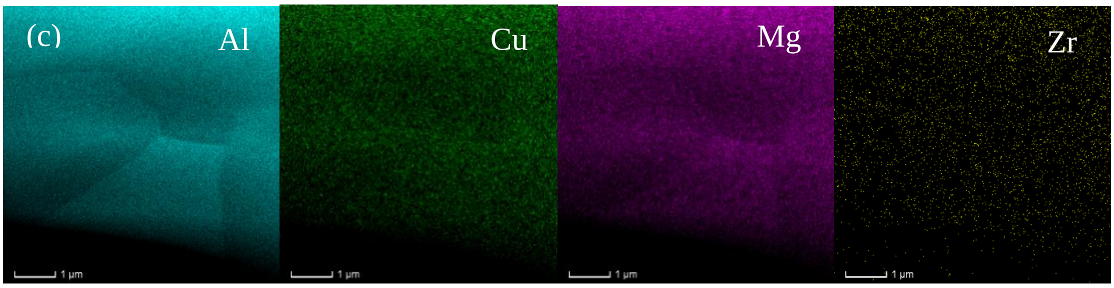

Figure 5- 4. Microstructure of T4-processed Al-Cu-Li alloy: (A) BF-TEM image; (B) HAADF-STEM image; (c) corresponding EDS mapping.

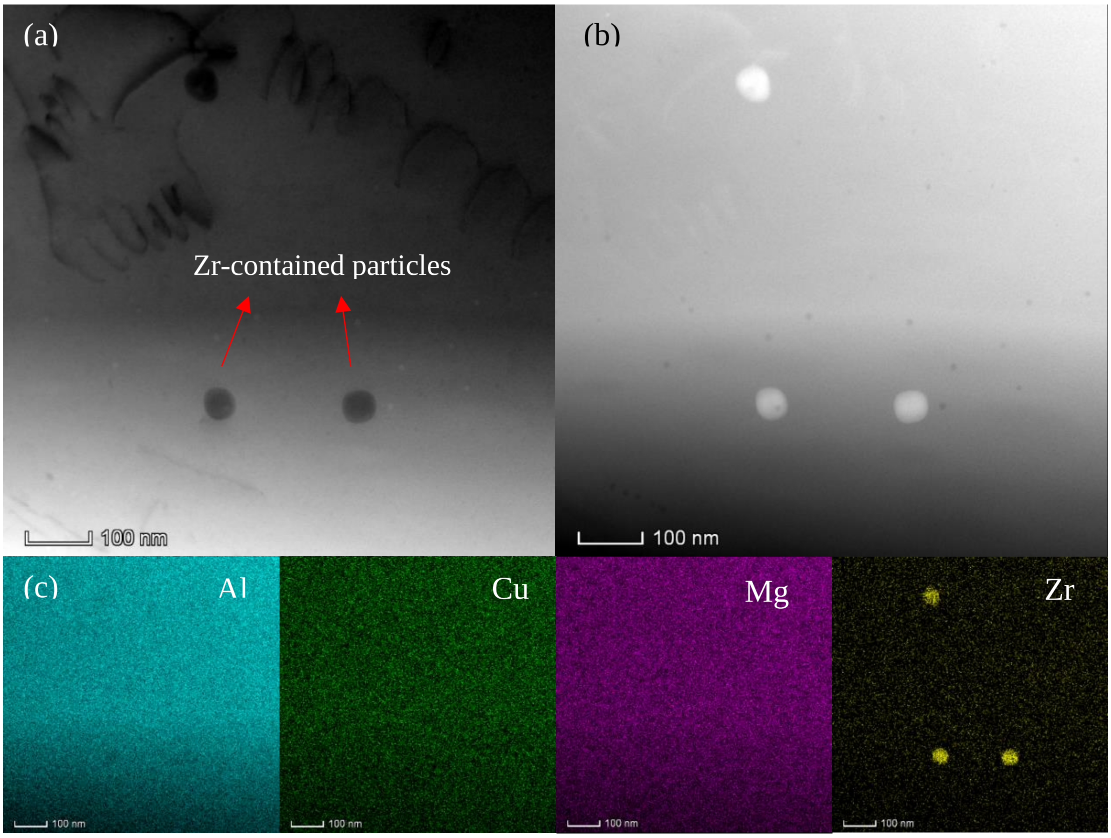

Figure 5- 5. Enlarged TEM image of yellow-square region in Fig. 5-4 (b), (a) BF-STEM image; (b) HAADF-STEM image; (c) corresponding EDS mapping.

<u>*Al-Li-Cu in T4-HPT condition*</u>

Fig. 5-6 contains the results compiled using BF-TEM, DF-TEM, and EDS techniques. Fig. 5-6 (a) and (b) represent bright and dark field images of the specimen processed by 5 turns of HPT deformation at RT. Grains with a size of ~90 nm appear in the microstructure, suggesting that the grain size has been reduced significantly by HPT processing, forming an UFG structure. The mean grain size estimated by the line intercept method is 88.7 ± 5.6 nm. Besides, the elemental distribution within grains was analysed by EDS, see Fig. 5-6 (c). Uniform elemental distribution is seen throughout the grain interior and GBs of the HPT-processed sample, indicating that there is no formation of precipitates during HPT deformation, with the exception of β′ phase (Al_3Zr). Those spherical shaped Zr-containing particles (β′ phase) with an average size of ~50 nm were found mainly at grain boundaries, indicated by arrows in Fig. 5-6 (b). There is no elemental segregation at GBs. (In the type of imaging used here, any dislocations are not visible.) Fig. 5-7 shows the microstructure of the HPT-deformed Al-Cu-Li alloy with a higher magnification compared with Fig 5-6.

Under these higher magnification images Figs. 5-7 (a-b), only a few grains with dark contrast are observed, and grain boundaries are mostly poorly defined, but some of those are identifiable. Additionally, large grains consisting of several sub-grains was observed, but no precipitates are seen in the micrographs.

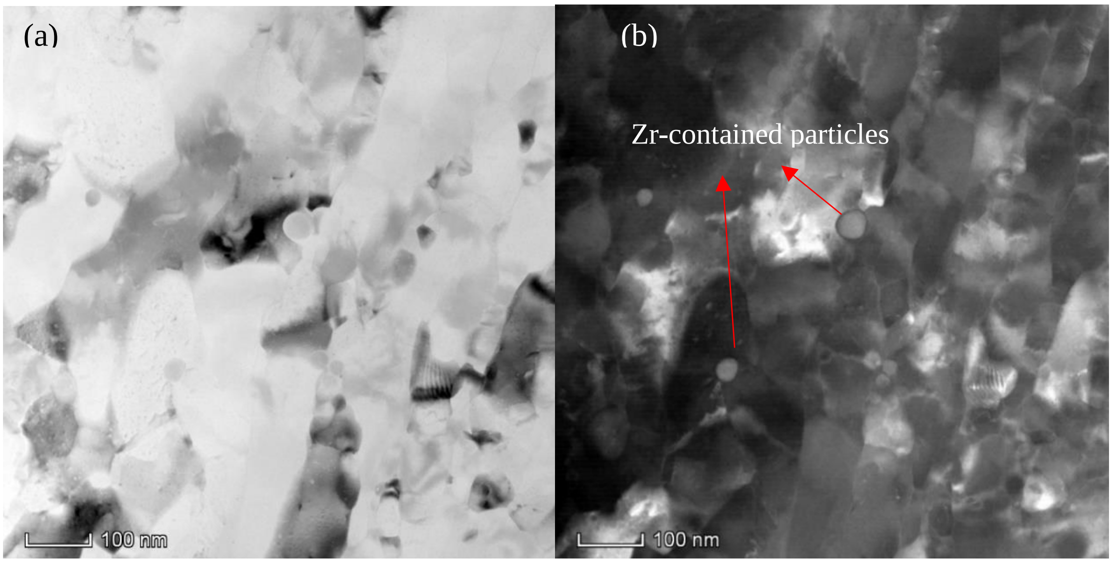

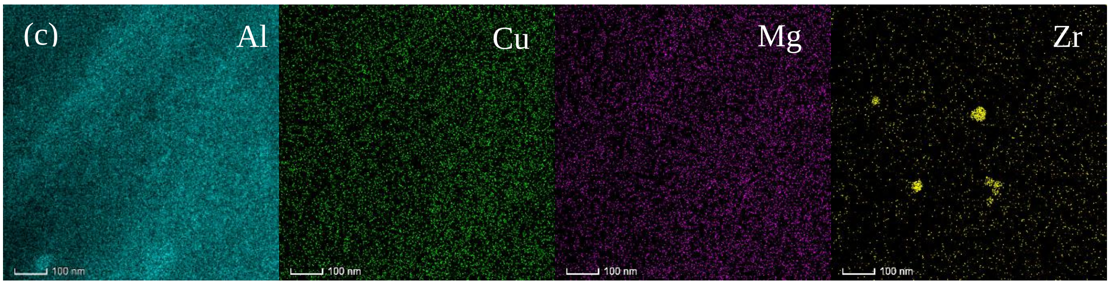

Figure 5- 6. STEM pictures of UFG sample processed by T4-HPT condition: (a) BF-STEM (b) DF-STEM, and (c) elemental composition mapping analysis

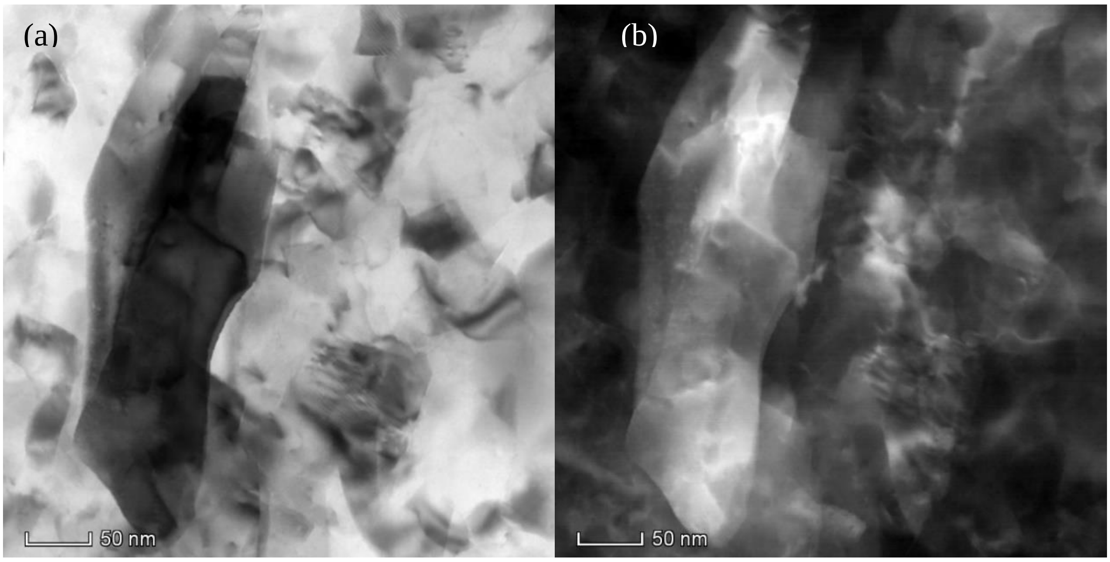

Figure 5- 7. The bright (a) and dark field (b) STEM images taken from T4-HPT-processed sample under high magnification.

<u>Al-Li-Cu in T4-HPT-AA condition</u>

Fig. 5-8 reveals the microstructure of the T4-HPT-AA-processed Al-Cu-Li alloy at peak ageing condition (~60h), which reveals a slight grain growth compared with the T4-HPT condition. As the grain boundaries are clearly defined from Fig. 5-8 (a) and (b), the mean grain size was estimated to be 102.4 ± 9 nm by the line intercept method. Furthermore, the bright, dark field STEM images and the corresponding EDS analysis (see Fig. 5-8 (c)) show a uniform elemental distribution throughout the grains, indicating that no solute segregation and no formation of precipitates occurred during subsequent ageing treatment. The only type of precipitates observed was Zr-containing particles (β′ phase), even it is difficult to identify from STEM images. Besides, no dislocations were observed.

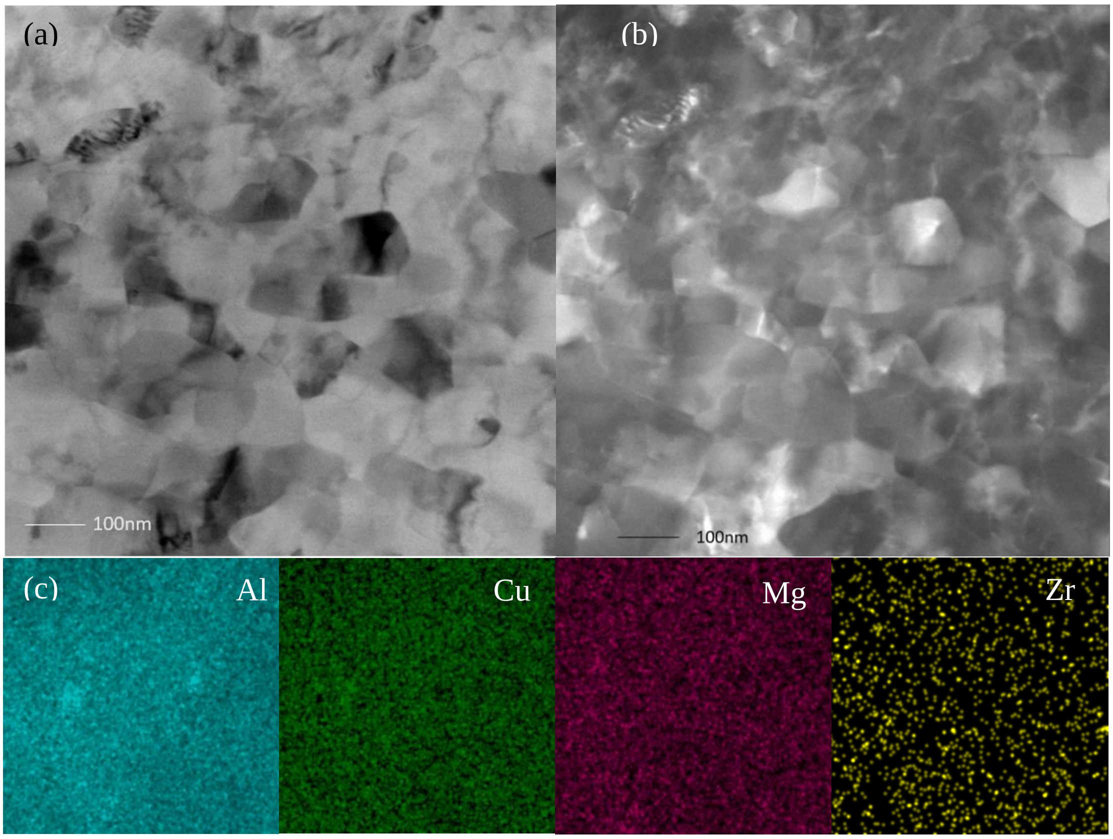

Figure 5- 8. STEM images of Al-Cu-Li alloys processed by T4-HPT-AA processing condition: (a) bright field, and (b) dark field, (c) corresponding elemental distribution mapping of the sample.

Al-Li-Cu in T6 condition

HAADF-STEM micrographs of the undeformed Al-Cu-Li alloy in T6 heat treatment are illustrated in Fig. 5-9. As shown in Fig. 5-9 (a), the grain size in T6 condition is very similar to in T4 condition, which is 3150 ± 11 nm. The same observations were obtained in comparison with the sample processed by T4 condition. In both conditions, well-defined grain boundaries and dislocations were visible in the micrographs, indicated by arrows in Fig. 5-9 (b). Moreover, characterization at higher magnification by STEM (Fig. 5-9 (b)) reveals the presence of particles with a size of about 250 nm, and they are mainly located at grain boundaries. The corresponding elemental mapping was conducted by EDS detector and provided further evidence that these particles contain a high concentration of Cu and Mg atoms, and thus they were identified as S′

phase (Al_2CuMg), the only known precipitate phase that contains Cu and Mg. These particles are indicated by arrows. The SAED pattern corresponding to the TEM image of the square region is given in Fig. 5-9 (d), showing it is an Al phase grain. Furthermore, the spherical-shaped β' phase (Al_3Zr) with a size of ~50 nm was also found everywhere throughout the T6-processed sample, as shown in Fig. 5-9 (e).

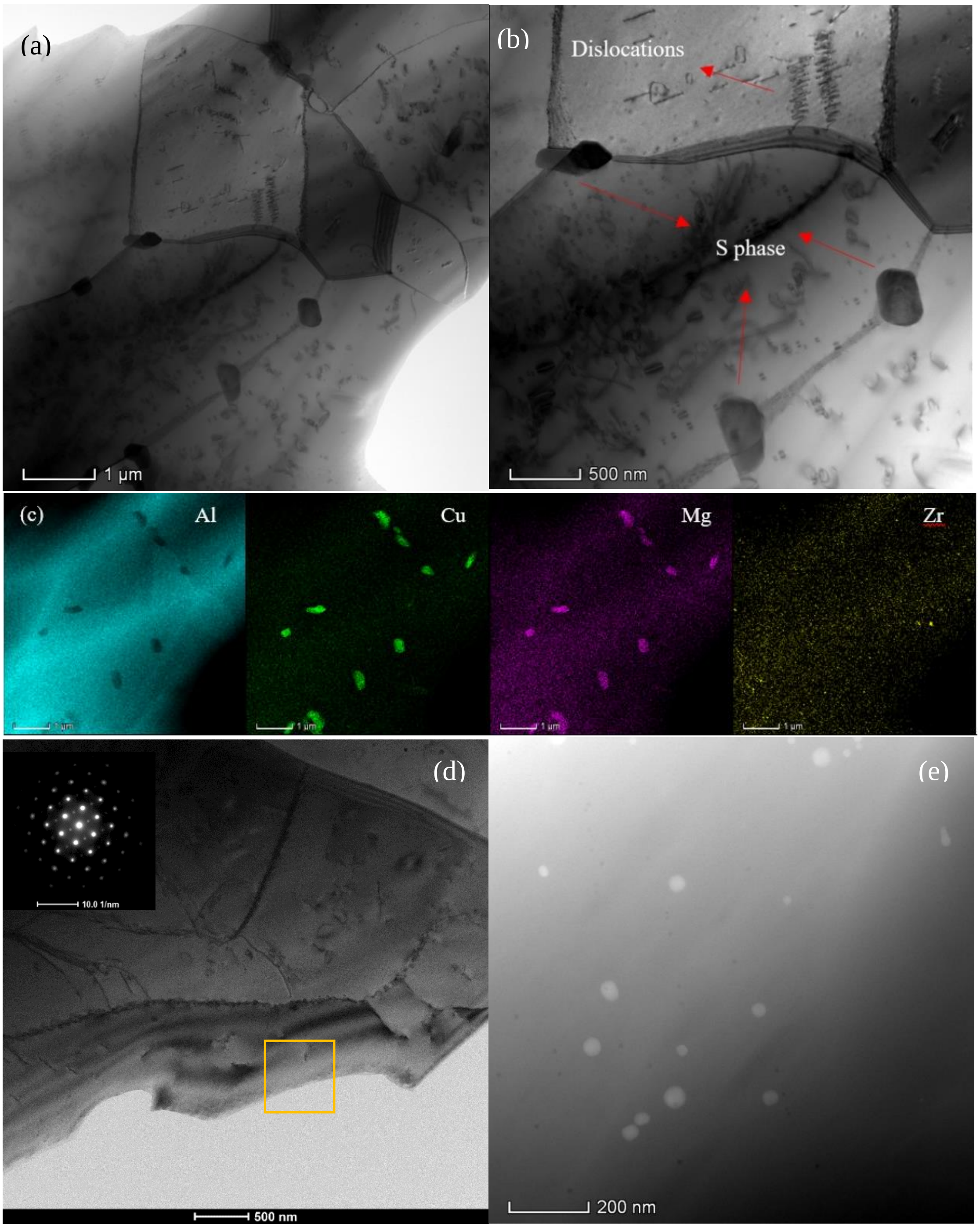

Figure 5- 9. The HAADF-STEM bright-field (BF) micrographs of Al-Cu-Li alloy processed by T6 ageing treatment: (a) lower magnification; (b) higher magnification; (c) EDS mapping; (d) TEM image of microstructure with SAED pattern; (e) Zr- contained particles.

Al-Li-Cu in T6-HPT condition

The BF-TEM, DF-TEM and HAADF-STEM micrographs shown in Fig. 5-10 are representative of the microstructures of the T6 aged materials followed by 5 turns of HPT processing at room temperature. An UFG structure with a mean grain size of 115 ± 13 nm was measured, i.e. it is significantly refined during HPT deformation. In Fig. 5-10 (a), only a few grains with dark contrast can be seen, and most grain boundaries are poorly defined. However, careful inspection of the image (Fig. 5-10 (c)) shows that the grains contained sub-grains. Also, no new precipitates were observed, and no S′ phase particles were found in the micrograph after HPT processing.

Fig. 5-10 (d) illustrates the TEM image captured from the same T6-HPT-processed sample at a different position with higher magnification, and the corresponding SAED pattern is included as an insert. The SAED pattern contains two sets of six spots situated around circles, indicating the presence of two grains and the boundaries having small misorientation angles. Such a pattern further proves that the nanocrystalline structure was achieved through HPT deformation.

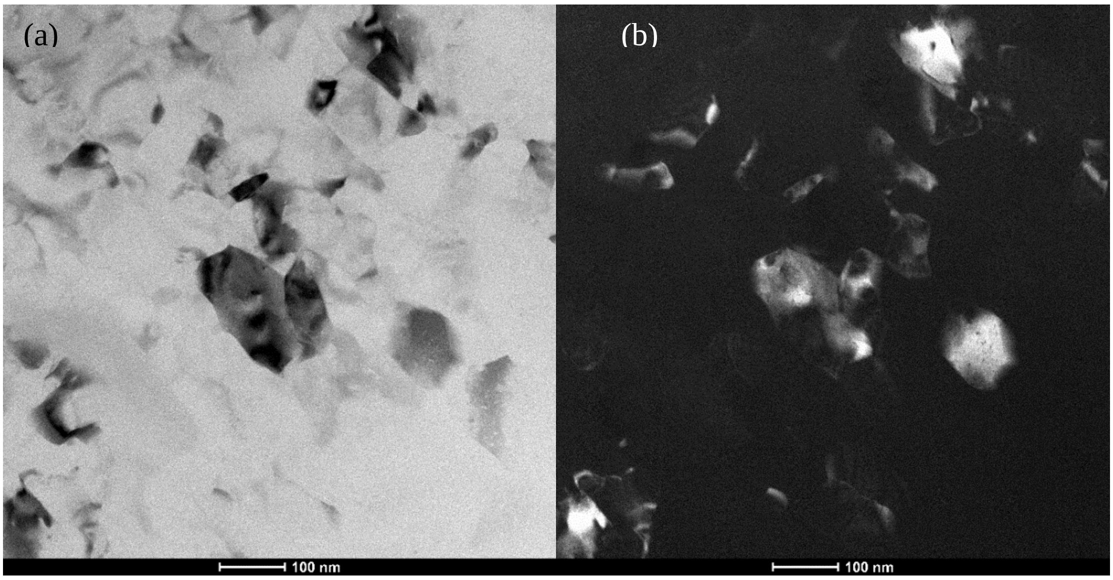

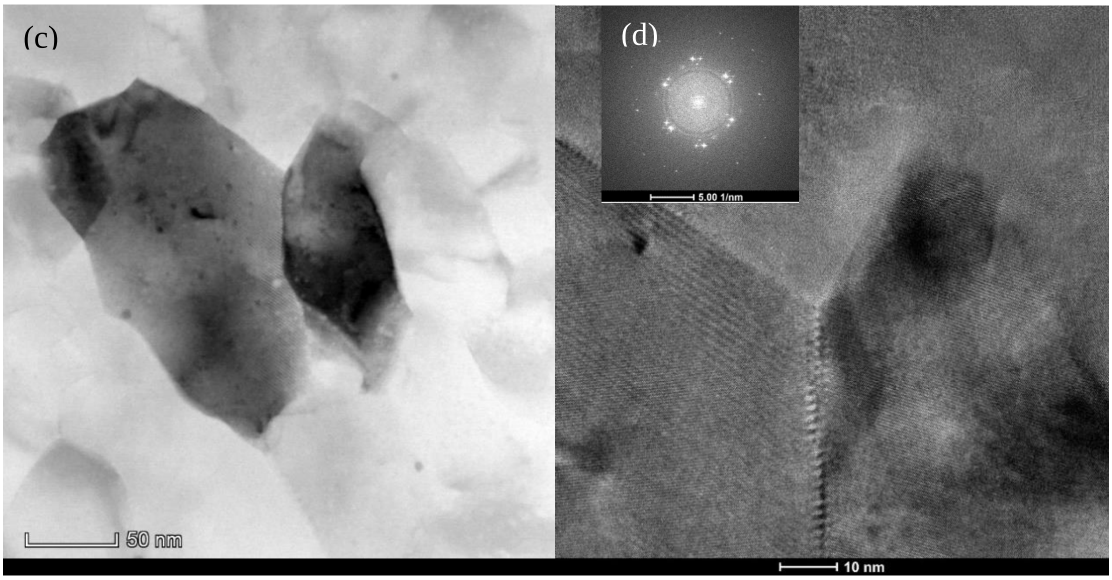

Figure 5- 10. High resolution TEM micrographs: (a) BF-TEM, and (b) DF-TEM. (c) Enlarged image (d) SAED patterns of HPT-processed T6-aged sample.

Al-Li-Cu in T6-HPT-AA condition

Examination of atomic-resolved HAADF-STEM images (Figs. 5-11 (a-b)) revealed that the ultra-fine grain structure with well-defined grain boundaries was obtained after the sample was processed to the T6-HPT-AA condition. The mean grain size was measured as 123.4 ± 10 nm, which has slightly increased compared with as-HPT condition, indicating grain coarsening happened during subsequent ageing treatment. Spherical particles were observed at grain boundaries, but no other precipitates were detected by STEM (dislocations cannot be observed in this imaging mode). The corresponding EDS analysis (see Fig. 5-11 (c)) depicts that the presence of β′ phase (Al_3Zr) and the concentration of Cu is slightly higher in the grain boundaries than the interior of grains.

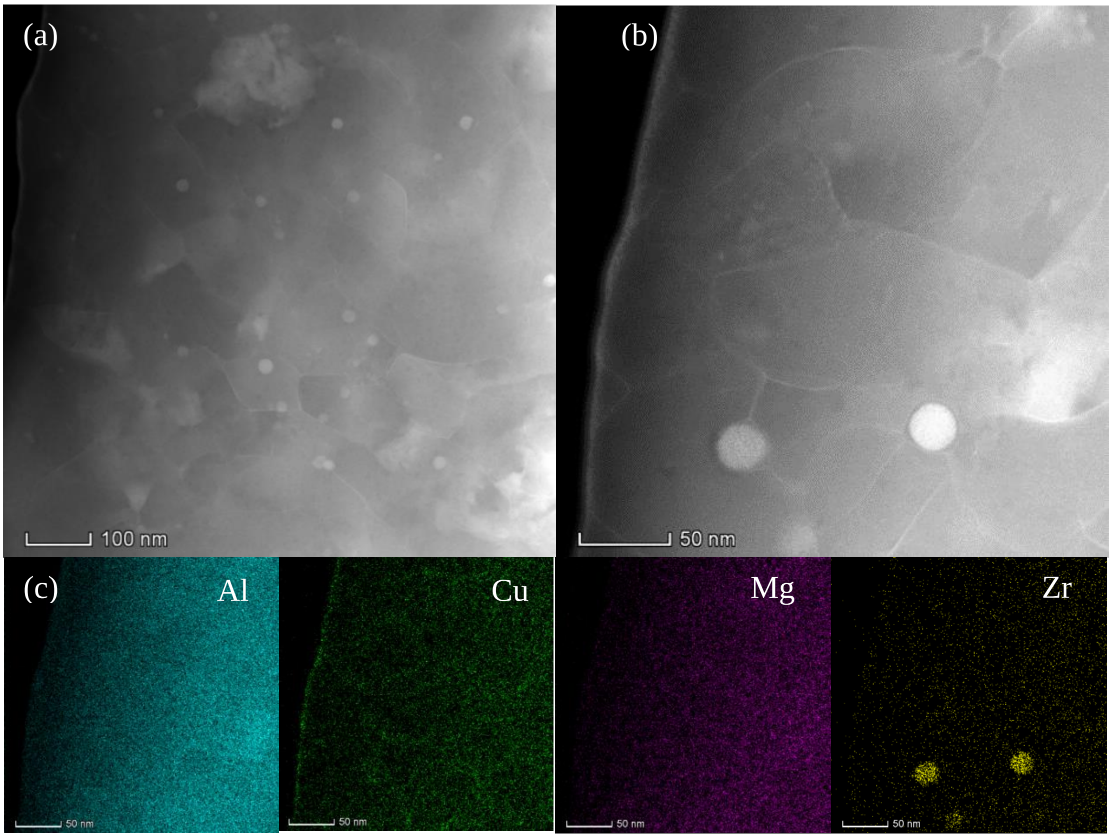

Figure 5- 11. HAADF-STEM images (a) and (b) of Al-Cu-Li alloy processed by T6-HPT-AA condition; (c) the corresponding EDs mapping.

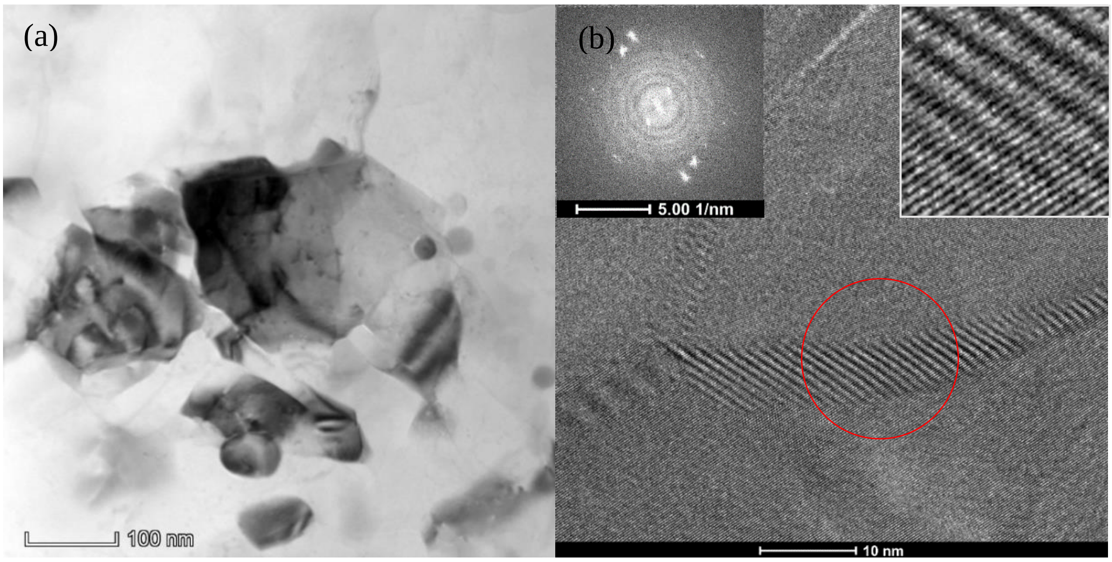

Figure 5- 12. (a) HAADF-STEM bright-field micrograph and (b) TEM image of the T6-HPT-AA condition sample and its corresponding SAED pattern.

Moreover, Fig. 5-12 (a) depicts a bright-field STEM image of the same sample but a different position. Sub-grains were found inside the grains with smaller grain size. In addition, many wavy shaped patterns were observed in the microstructure of the T6-HPT-AA-processed sample, as shown in Fig. 5-12 (b). The corresponding SAED ring pattern confirmed a polycrystalline structure, and it is likely to be the overlap of two grain boundaries with different orientations or one grain boundary under an angle. Sub-grains are also possible but cannot be seen from SAED due to small misorientation.

5.2 Discussion

5.2.1 Microstructural analysis

The present results are significant because they demonstrate the potential for combining HPT and age hardening to achieve an ultra-high strength aluminium alloy. For the Al-Cu-Li alloy studied in this research, an optimum processing procedure of T6-HPT-AA (pre-ageing 110 ^{o}C/24h + 5r-HPT+ post-ageing 110 ^{o}C/180h) improves the hardness by a factor of 2 by comparison with the T4 condition.

For T4 and T6-processed specimens, the TEM micrographs signify very similar observations, including large grains, well-defined grain boundaries, and dislocations retained within the grains. The dislocation densities measured by XRD via the Rietveld method show that only a small number of dislocations existed in the specimens after being processed by T4 and T6 heat treatment. This is an essential factor in explaining the relatively low micro-hardness presented in Section 5.1.1. By examining TEM images of T6-processed sample, S′ phase (Al_2CuMg) was observed mainly at grain boundaries with an average size of ~250 nm, and this S′ phase was also identified in XRD pattern of T6-processed sample. However, no precipitates were found in the TEM images of T4-processed sample even though the XRD pattern shows a weak S′ phase peak. The formation of S′ phase has observed in many research [231–233], the addition of minor Mg (0.5-1.0 wt. %) to higher Cu-containing alloys will suppress the formation of GP zones and θ′ phases, instead of S′ phase will be formed during heat treatment. Due to the large size of S′ precipitates and very limited amounts of them, it is not contributing significantly to the hardening of the Al-Cu-Li alloy.

Microstructural observations of T4-HPT-processed specimens reveals a significant grain size reduction from 3030.3 ± 7.8 nm to 88.7 ± 5.6 nm during HPT processing, the crystallite size measured by XRD line profile gives the same descending trend, compared with T4 condition. Such UFG structure achieved by HPT causes a significant increase in hardness value due to grain boundary hardening. Also, some larger grains were found containing many sub-grains, which can also contribute to the hardness. By contrast, a much higher dislocation density was measured in T4-HPT condition by XRD analysis even though the TEM technique was not able to detect those dislocations due to imaging modes. In fact, it has been shown in several studies that HPT can introduce a large number of dislocations [31,38,119]. Therefore, the high dislocation density also improves the strength of HPT-processed materials. In addition, the peak of S′ phase and θ′ phase in XRD spectra of T4-processed sample disappeared after HPT deformation, suggesting that all the initial precipitates are dissolved into Al matrix and a supersaturated solid solution forms.

Similarity observations have been observed in another study [150]: An artificial peak aged Al-Li 2198-T8 (peak ageing at 175 ^{o}C) alloy processed by HPT under 3 GPa for 2 revolutions with the rotation speed of 0.5 rpm. The HPT processing introduced much finer grains (130 ± 36 nm) with high angles of misorientation and TEM results indicates that the β′ (Al_3Zr), θ′ (Al_2Cu) and T1 (Al_2CuLi) phases existing in the as-received Al-Li 2198-T8 fully dissolved after HPT. Also, numerous dislocations are found within the grains after HPT processing, and no precipitates are visible within the microstructure. The dislocation density of 2198-T8 estimated by Williamson-Hall method has increased from 11.2×10^{14} m^{-2} to 27.8×10^{14} m^{-2} after HPT processing, which is larger than the dislocation densities of T4 and T4-HPT processed Al-Cu-Li alloy measured by the Rietveld method. For HPT-processed 2198-T8, the dislocations and grain boundaries play the dominant role in the strength. Same as 2198-T8, neither XRD nor TEM signifies the presence of any precipitates after HPT processed Al-Cu-Li alloy, it is reasonable to conclude that there are no real precipitates in the material, but the atoms may be clustering at GBs or dislocations.

According to the micro-hardness results, a further improvement in hardness can be achieved by post-peak ageing after HPT processing. The average grain size of the sample in T4-HPT-AA condition measured from TEM images is larger than in T4-HPT condition, whilst it signifies some grain growth occurs during the artificial ageing for 60h. However, the small change of grain size from ~90 nm to ~102 nm after peak ageing treatment indicates that it is possible to retain a reasonably fine-grained structure in this alloy when ageing at 110 ^{o}C/60h. Similar to the HPT-processed sample, no precipitates formed during subsequent ageing neither in TEM nor XRD analysis. However, HPT-processed AA2091 alloy [31] under a pressure of 6 GPa followed by ageing 150 ^{o}C/56h. HRTEM signifies that the formation of δ' precipitates with a size of ∼20 nm was retained within the small grains produced by HPT processing. Such fine dispersion of particles after ageing was responsible for the increase in strength of AA2091 alloy [31]. Here the studied Al-Cu-Li alloy uses a lower ageing temperature of 110 ^{o}C, which might explain the absence of precipitation during ageing treatment.

Furthermore, the dislocation density after 60h ageing treatment drops dramatically in comparison with the sample after HPT. Hence, all the above results, (i.e. grain coarsening, reduction of dislocation density, and the absence of precipitates) leads to the suggestion that an additional hardening mechanism occurs that is not directly detectable by the present methods. In view of studies reported in the literature showing cluster formation, it is thus likely that the formation of clusters or co-cluster in the grain boundaries or on dislocations occurs during the final ageing stage of the T4-HPT-AA samples.

On the other hand, the processing condition T6-HPT-AA has given the highest hardness ∼265 Hv. As discussed above, according to XRD and TEM results, the T6 ageing before HPT does not make any apparent differences compared with the sample that had pre-aged by T4 treatment. Even after the T6-sample was deformed by HPT (i.e. in the T6-HPT condition), both dislocation density and hardness value of Al-Cu-Li alloy have significantly increased, but the Hv and dislocation density are still lower than that of in the T4-HPT-AA condition. It is clear that the nanosized-grains were achieved by HPT, indicating that the hardening achieved in this stage of Al-Cu-Li alloy after HPT is because of the formation of UFG structure and increase in dislocation density through HPT processing.

However, the subsequent artificial ageing after T6-HPT processing leads to a large hardness, which surpasses the hardness of the T4-HPT-AA condition. Examination of TEM images revealed that the UFG structures with high angle GBs are still retained after ageing treatment for 180h, which indicates a limited grain growth occurred during post-ageing treatment. An Mg-8.2Gd-3.2Y-1Zn alloy processed by a similar processing condition (i.e. T6-HPT-T5 peak-aged) obtained a nano-grained structure with a grain size of 35 ± 2 nm in T6-HPT condition, and such small grain size was retained after subsequent T5 peak ageing 200 ^{o}C /48h [18]. Moreover, HPT-processed AA2091 alloy was aged at 100 ^{o}C for 233h. Examination of TEM images revealed that the UFG structures with high angle grain boundaries were still retained after the age treatments. Grain growth occurred when post-aged at 150 ^{o}C and 190 ^{o}C but only minor amount from ~140 nm (as-HPT condition) to ~160 nm (aged at 150 ^{o}C) and ~180 nm aged at 190 ^{o}C) [31]. In principle, with increasing temperature, ageing treatment initially causes recovery due to dislocations, but this would only happen when ageing temperature is sufficiently high. For conventionally processed materials, this occurs at ~250-300 ^{o}C. The low ageing temperature used in this study (110 ^{o}C) should cause only very limited grain coarsening.

It is also expected to have the formation of precipitates during ageing, but there is no precipitation in any TEM pictures and XRD spectra. This is probably due to the very low ageing temperature of 110 ^{o}C. Accordingly, it seems much more likely that there clustering of atoms on dislocations or GBs is occurring. For the post-HPT aged sample (i.e. T6-HPT-AA), the grain size is not the smallest among all six samples, the dislocation density is not the highest, and there is no evidence of formation of real precipitates, but nevertheless, the hardness is the highest. In addition, even if there are no dislocations observed from TEM images may be owing to image conditions, as the hardness of T6-HPT-AA-processed sample is still very high and it has not decreased during ageing. Therefore, it is expected that a high density of dislocations should exist. Indeed, the analysis of XRD data (using the Rietveld method) has shown that the hardness of T6-HPT-AA-processed sample does contain a dislocation density of 0.70×10^{14} m^{-2}, which is substantial. Hence, it is likely that the high dislocation density introduced by HPT and co-clusters are dominant factors that contribute to the ultra-high hardness. Some grains contain sub-grains, which also contribute to the high hardness.

It is worth mentioning that the crystallite size determined by Rietveld analysis of XRD data is not the same as the grain size (or particle size). Crystallite size is a measure of the size of a coherently diffracting domain due to the presence of polycrystalline aggregates. On the other hand, the grain size shown by TEM images is defined by the grain boundaries. For all six samples, the crystallite sizes estimated from the obtained peak broadening of the XRD patterns are smaller than the grain size measured by TEM observation, but the trend is consistent.

Furthermore, in all six samples, the TEM analysis (from Fig. 5-4 to Fig. 5-12) indicates that Zr-rich β' (Al_3Zr) phase has been exsisted right from the start of the processing and is retained even during solution treatment, ageing treatment, and HPT processing. The β' phase particles are observed in many Zr-containing Al alloys after homogenization or solution treatment [74,76,77]. These metastable β' phase particles can nucleate heterogeneously on dislocations and GBs, stabilising the grain growth, inhibiting recrystallization, and effectively pin the grain and sub-grain boundaries. These stabilisation effects are due to the low solid solubility and sluggish diffusion of Zr in Al, and the small misfit between β' and matrix reduces coarsening. Therefore, β' phase particles help the improvement of hardness through influencing grain size and reducing recrystallization. However, as only a limited amount of β' phase particles form, they will not contribute much to the strengthening of the Al-Cu-Li alloy by themselves. It is also noted that β' phase particles have been widely suggested to serve as a nucleation site for θ′ and T_1 phases [80,81], but no such two phases were found in any of the samples, neither from XRD nor TEM results. Apparently, the temperature is too low to cause nucleation of these phases. Therefore, the presence of Cu and Li-containing clusters possibly suppress the formation of these precipitates.

5.2.2 Precipitates determination

In order to further confirm that there are no real precipitates formed during HPT processing, one of the TEM micrographs (for an area 50 nm × 50 nm) of T6-HPT-processed sample was magnified so that alignment of atoms can be seen. The spacing between lattice planes in a TEM image corresponds to atomic spacing, and the distance between those plane layers was measured by software *Image J* (see Fig. 5-13). The software based on grey value to generate a profile plot, the distance between 10 planes peaks were used to calculate average lattice spacing (d-spacing). By counting the circles and divide the distance by the number of circles (i.e. 2 nm/9 peaks), a value of ~0.22 nm was given.

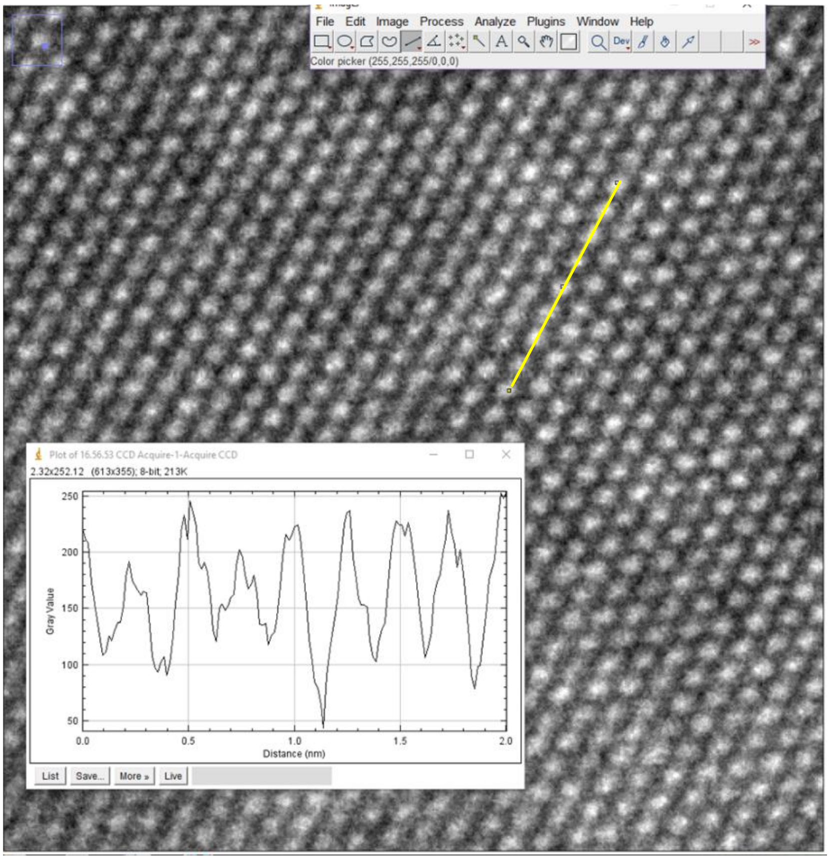

Figure 5- 13. The measurement of lattice spacing in the T6-HPT-processed sample processing by Image J.

This result is consistent with the lattice spacing calculated by the general inter-planar spacing of cubic materials equation:

$$\frac{1}{d^2} = \frac{h^2 + k^2 + l^2}{a^2} \tag{5- 2}$$

Where α is the lattice parameter and h, k and l represent the Miller indices of the adjacent planes being considered. d is lattice spacing, i.e. the distance between two adjacent parallel planes of atoms with the same Miller Indices (d_{hkl}). α is ~0.404 nm for Al, and plane indices are here (1 1 1). The calculation gives a lattice spacing value of 0.23 nm. This is consistent with the lattice spacing value of the Al lattice. This lattice image (Fig. 5-13) does not reveal any precipitates or any kind of ordered structure, further showing no precipitates formed during HPT processing.

EDS scan experiments were conducted to explore the elemental distribution within grains and at grain boundaries of sample processed at different stages. The Cu and Mg elemental mappings were in turn overlapped with the HAADF-STEM image of T6-HPT-AA sample. The overlapped images (see Fig. 5-14) signify that the concentration of Cu and Mg atoms along grain boundaries are higher than those in the Al-matrix in T6-HPT-AA condition. It seems there is a little bit of Cu segregation at the GBs after post-HPT ageing. The solute behaviours in UFG or nanosized-grains Al alloys after SPD processing have been widely studied [23–25,37]. The observations have revealed that the solute atoms can be redistributed and segregated to grain boundaries or dislocations (e.g. AA6060 [37], AA6061 [24] and AA7075 [23]). Such solute segregation will act as obstacles to grain growth and stabilise the nano-sized grains by pinning the GBs, thus contribute to strengthening.

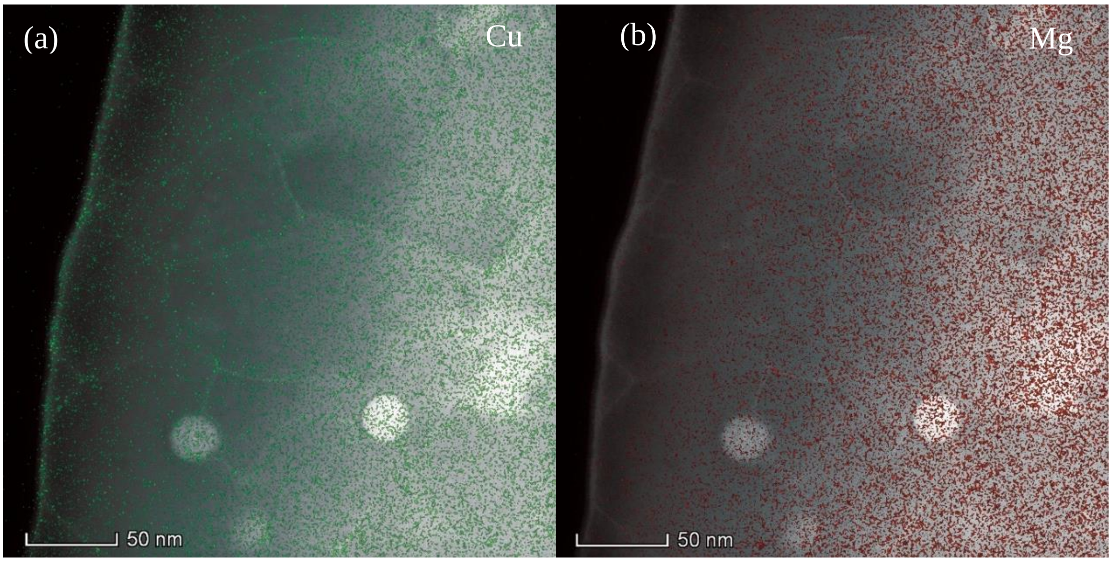

Figure 5- 14. Overlapped pictures of (a) Cu elemental mapping with STEM image and (b) Mg elemental mapping with STEM image of T6-HPT-AA sample.

5.3 Summary

1) The grain size of T4 and T6-processed samples were significantly refined (by a factor of ~30) during HPT deformation, resulting in an UFG structure with grain size of ~88 nm and ~115 nm, respectively.

2) For both T4-HPT and T6-HPT-processed samples, the UFG structure was retained during subsequent artificial ageing at 110 ^{o}C/60h in T4-HPT-AA and 110 ^{o}C/180h in T6-HPT-AA conditions.

3) The dislocation densities of both T4-processed and T6-processed samples reveals a large generation of dislocations after being deformed by HPT. T4-processed sample increases to the highest level of ~3.5×10^{14} m^{-2} right after HPT and then dropping to ~0.8×10^{14} m^{-2} after subsequent peak ageing treatment. The T6-processed sample, with the dislocation density increasing to ~1.5×10^{14} m^{-2}, gradually drops with increasing ageing time and decreases to ~0.7×10^{14} m^{-2}.

4) β′ phase (Al_3Zr) with a size of ∼50 nm were found throughout all stages of processed samples right from the start of the processing and is retained even during solution treatment, ageing treatment, and HPT processing. Nevertheless, it does not contribute to the strengthening of the Al-Cu-Li alloy.

5) Both XRD and TEM do not show any visible precipitates after HPT processing and subsequent ageing treatments, and it likely has the formation of cluster or co-cluster in the grain boundaries or dislocations during HPT processing and post-ageing treatment.

Chapter 6 Segregation of solute elements and clustering at GBs and dislocations

In the previous Chapter 5, the microstructure characteristics of Al-Cu-Li alloys were analysed by XRD and TEM techniques from aspects of grain size, dislocation density, microstrain. Both T4-HPT-AA and T6-HPT-AA processed samples show grain coarsening, reduction of dislocation density and the absence of precipitates, compared with the samples that had processed by HPT, but the hardness is still very high and has not decreased during ageing. As a consequence, all the above results suggest that clustering at GBs or dislocations is an additional hardening mechanism that contributes to the ultra-high hardness of Al-Cu-Li alloy. In this chapter, the distribution of solute atoms and the formation of clusters or co-cluster in the ultrafine-grained Al-Cu-Li alloy will be assessed by APT in all stages of two processing conditions (i.e.T4-HPT-AA and T6-HPT-AA).

6.1 APT results

Al-Li-Cu in T4 and T6 conditions

Fig. 6-1 and Fig. 6-2 show 3D reconstructions of atom position for Cu, Mg, Li and Si elements in the Al-Cu-Li sample processed by T4 and T6 treatment, respectively. All the elements are homogenous uniformly distributed in T4-processed and T6-processed samples. Grain boundaries or larger precipitates are not contained in the volumes. From Fig. 6-1 (e) and Fig. 6-2 (e), a homogenous distribution of fine-scale Cu-Mg clusters can be observed throughout the whole T4 and T6 samples after removing the solute atoms in the matrix. These fine solute clusters were distributed in T4 sample with a number density of 3.01×10^{23} m^{-3} (which was estimated according to the total number of solute clusters identified in the analysed volume) and an average Mg/Cu ratio of 1.12. The solute clusters with a slightly lower number density of 1.33×10^{23} m^{-3} were distributed in T6-processed sample, with a Mg/Cu ratio of 1.04.

It is worth noting that the T6-processed sample shows a denser distribution of clusters in Fig. 6-2(e) but a lower number density compared with T4 condition. This is because the analysed volume of the T6-processed sample (132×132×374nm) is much larger than the T4-processed sample (68×68×190nm), which means it contains overall more solute atoms, thus resulting in a lower number density value in T6 condition.

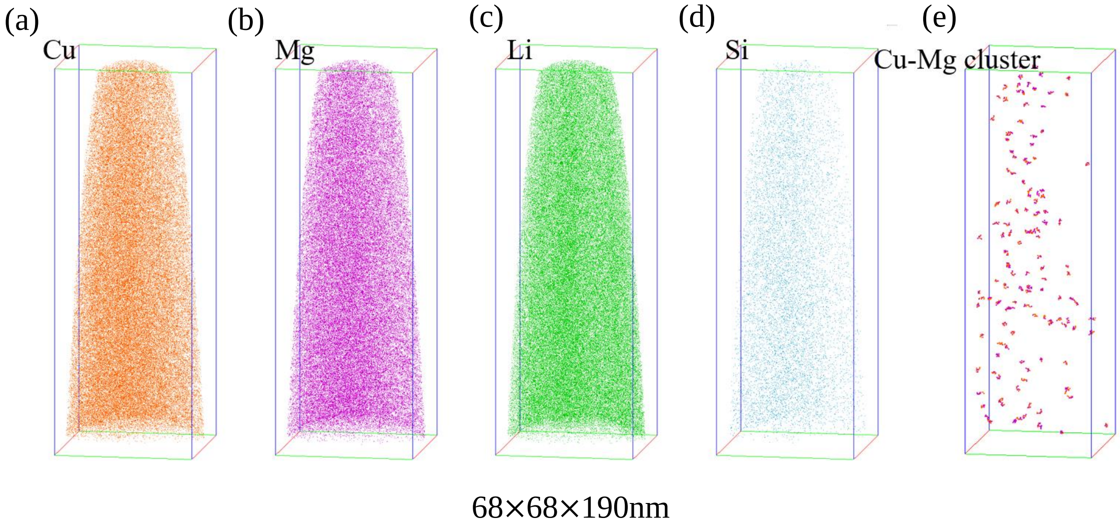

Figure 6- 1. Single-element atom maps of T4-processed Al-Cu-Mg sample (a) Cu map, (b) Mg map, (c) Li map, (d) Si map and (e) Cu-Mg cluster map after removing the matrix solute atoms.

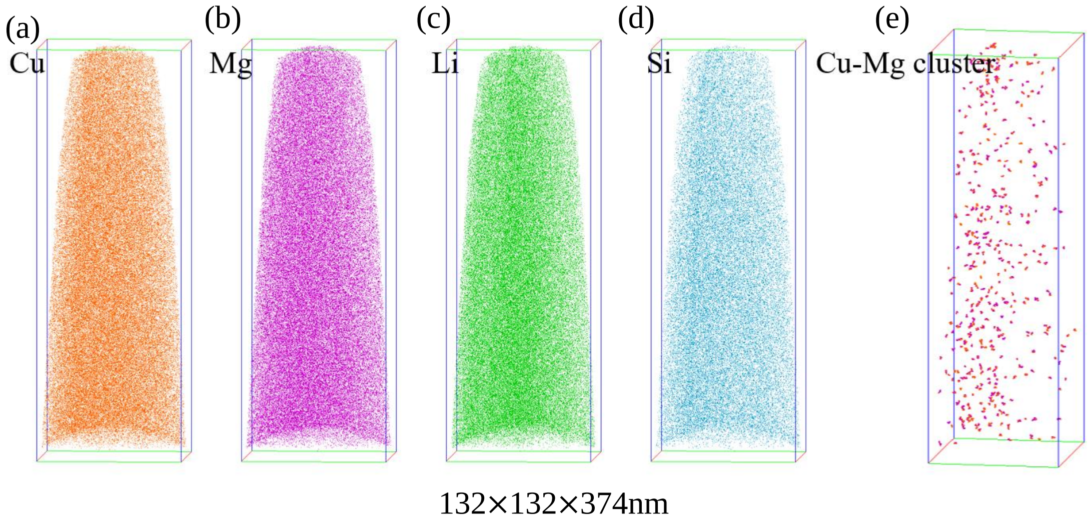

Figure 6- 2. Single-element atom maps of T6-processed Al-Cu-Mg sample (a) Cu map, (b) Mg map, (c) Li map, (d) Si map and (e) Cu-Mg cluster map after removing the matrix solute atoms.

Al-Li-Cu in T4-HPT condition

Fig. 6-3 shows atom maps of a T4-processed sample after 5 turns HPT processing. The analyzed volume contains 7 GBs (s1-s7) segments, and the segregation of elements Cu and Mg are evident at the GBs (Figs. 6-3 (a-b)). As well as the composition profile across each GB shown in Figs. 6-4 (b-h) indicates that all the GBs are enriched with Cu and Mg. The solute composition profiles across the GBs were measured using an elongated analysis box with its long axis normal to the GB plane, as shown in Fig. 6-4 (a). The average peak concentrations of Cu and Mg at the GBs were measured to be 4.2 % and 3.5 at%, respectively. Accordingly, the segregation of Cu at the GBs is relatively stronger than that of Mg. And a Mg: Cu atom ratio of 0.83 at GBs was estimated based on the corresponding peak solute concentrations. Besides, a minor concentration of Si segregated to GBs is also evident in the atom map (Fig. 6-3(d)). These figures show that the concentration of Li at the GBs and within the grains are similar, which implies there is no segregation of Li after HPT. Moreover, there are no clear precipitates and segregation of dislocation were found in the T4-HPT condition. The Cu-Mg clusters in Fig. 6-3 (e) are readily visible in the atom maps after removing the solute atoms in the matrix. The detected Cu-Mg clusters are mainly distributed at the GBs, having a number density of 1.17 ×10^{24} m^{-3} in the analyzed volume and an average Mg/Cu ratio of 0.66.

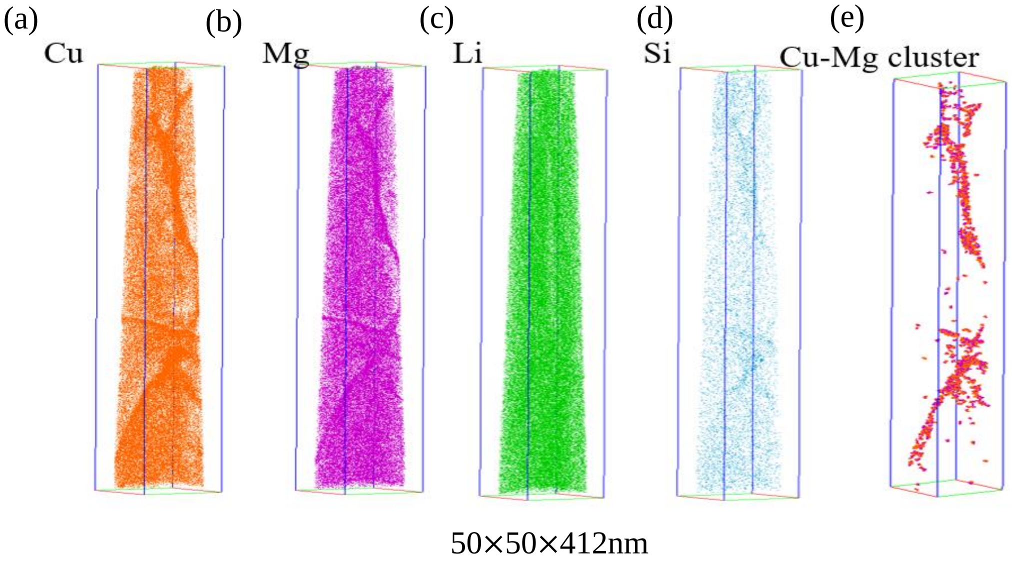

Figure 6- 3. Atom maps of T4-HPT-processed Al-Cu-Mg sample (a) Cu map, (b) Mg map, (c) Li map, (d) Si map and (e) Cu-Mg cluster map after removing the matrix solute atoms.

(a)

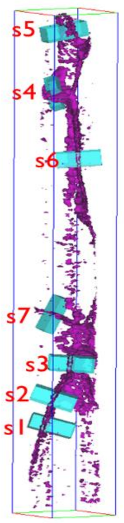
s5
s4
s6
s7
s3
s2
s1

(b)

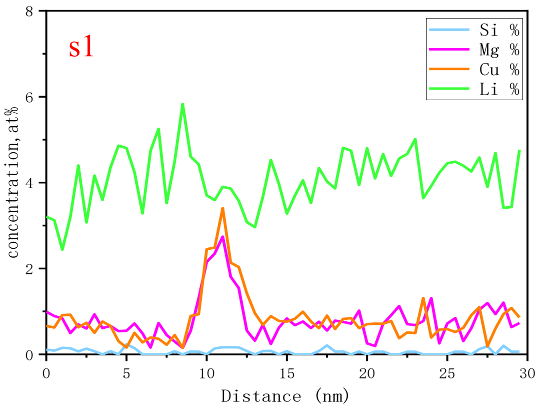
s1
Si %
Mg %
Cu %
Li %
concentration, at%
0
2
4
6
8
0
5
10
15
20
25
30
Distance (nm)

(c)

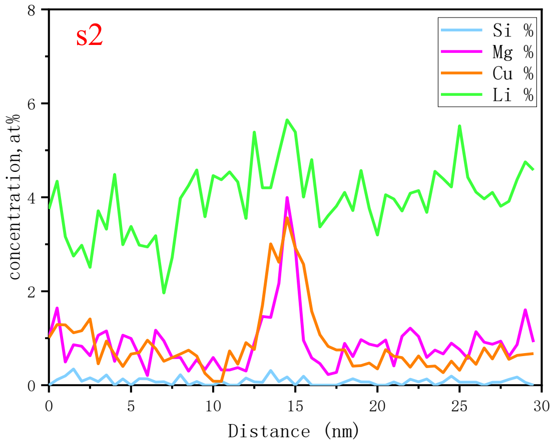
s2
Si %
Mg %
Cu %
Li %
concentration, at%
0
2
4
6
8
0
5
10
15
20
25
30
Distance (nm)

(d)

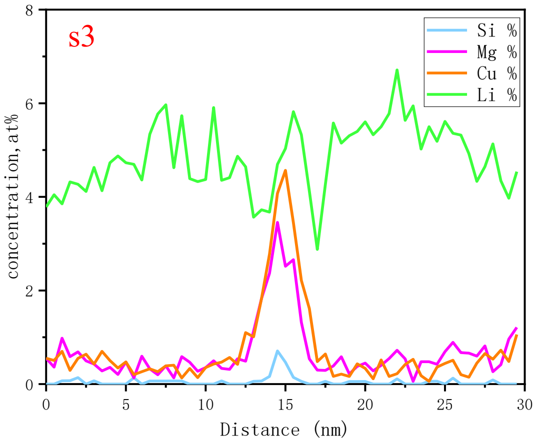
s3
Si %
Mg %
Cu %
Li %
concentration, at%
0
2
4
6
8
0
5
10
15
20
25
30
Distance (nm)

(e)

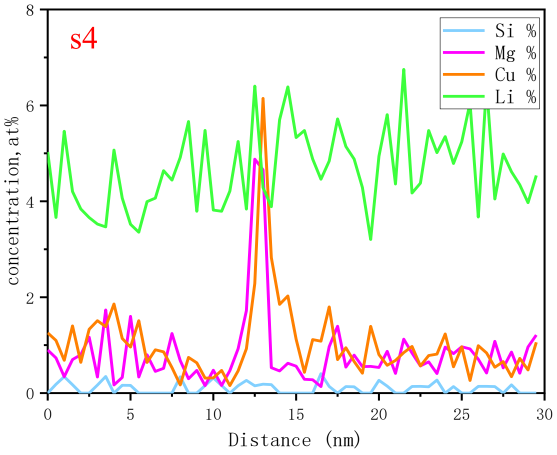
s4
Si %
Mg %
Cu %
Li %
concentration, at%
0
2
4
6
8
0
5
10
15
20
25
30
Distance (nm)

(f)

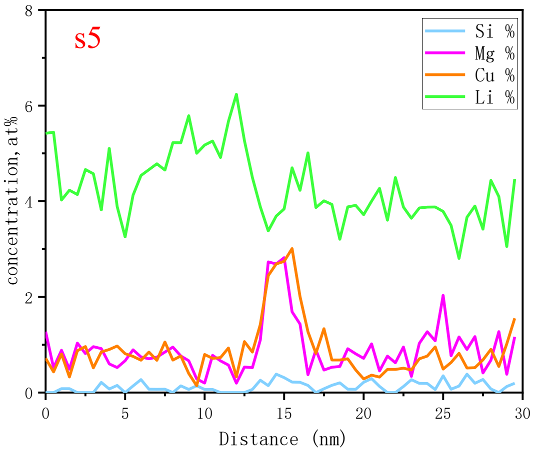
s5
Si %
Mg %
Cu %
Li %
concentration, at%
0
2
4
6
8
0
5
10
15
20
25
30
Distance (nm)

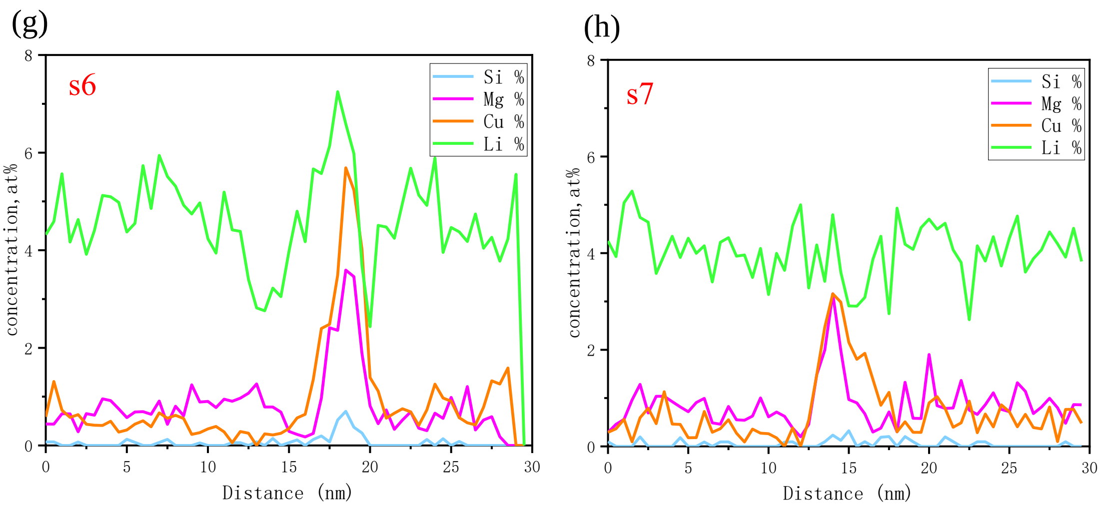

Figure 6- 4. Concentration profiles (b-h) of solutes across seven GBs in the analysed volume of T4-HPT-processed Al-Cu-Li alloy sample.

<u>Al-Li-Cu in T6-HPT condition</u>

Fig. 6-5 shows atom maps for the Cu, Mg, Li and Si distributions from a selected analysed volume of a T6-processed Al-Cu-Li alloy sample after 5 turns HPT processing. These volume atom maps contain only one grain boundary segment that is enriched with Cu and Mg, as seen in Figs. 6-5 (a-b). Fig. 6-6 (b) shows the composition profile across GB, and it is further confirmed that the Cu and Mg solute atoms segregated to GB after T6-processed Al-Cu-Li sample was processed by HPT. The peak concentration of Cu at the GB was measured to have the same value as that of Mg (3.1 at%), which indicates a Cu: Mg atom ratio of 1:1 at GB. Same as T4-HPT condition, a small amount of segregation of Si at GB was also detected in the atom map (Fig. 6-5(d)). Besides, no segregation of Li at the GB, and no clear precipitates and segregation of dislocation were identified after T6-HPT processing.

Cu-Mg clusters were identified mainly at the GBs (see Fig. 6-5(e)), with some of them within the matrix. Quantitative cluster analysis confirmed that a number density of 7.33 $\times 10^{23}$ m^{-3} in the analyzed volume. A mean Mg/Cu solute clusters ratio of 0.47 was also measured, which indicates that more Cu solute atoms formed into clusters than Mg solute atoms.

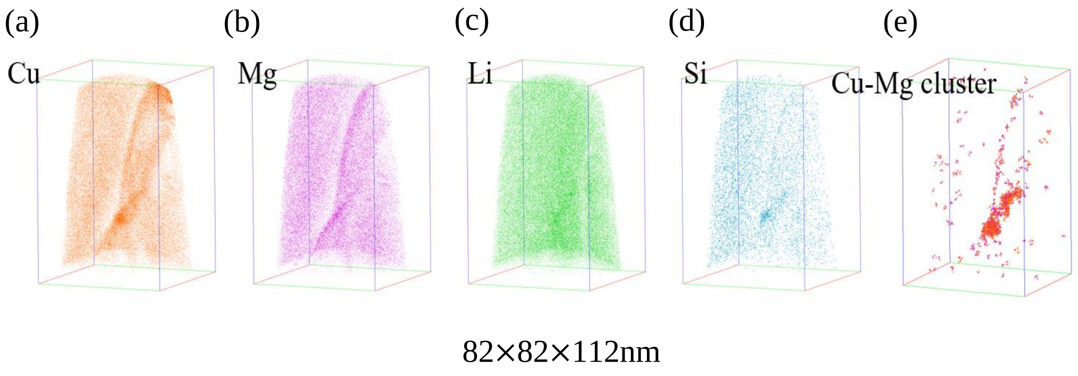

Figure 6- 5. Atom maps of T6-HPT-processed Al-Cu-Mg sample (a) Cu map, (b) Mg map, (c) Li map, (d) Si map and (e) Cu-Mg cluster map after removing the matrix solute atoms.

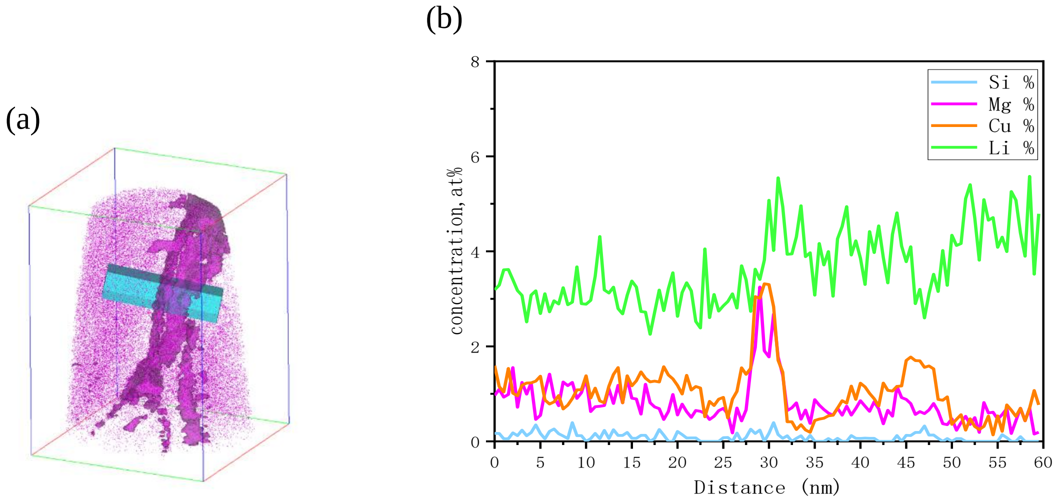

Figure 6- 6. Concentration profiles of solutes across GB in the analysed volume of T6-HPT-processed Al-Cu-Li alloy sample.

<u>Al-Li-Cu in T4-HPT-AA condition</u>

Fig. 6-7 shows alloying elements Cu, Mg, Li and Si atom maps of the Al-Cu-Li sample aged at 110^{o} C for 60h after HPT processing. An analysed volume of sample comprises three forms of solute enriched feature, i.e. at segments of the grain boundaries, at a dislocation line, and in the grain away from these defects. A total of 6 GBs have been analysed in T4-HPT-AA condition, as marked by black arrows in Figs. 6-7 (a-b). The typical concentration profiles of solutes across six GBs (s1-s6) in T4-HPT-AA condition are shown in Fig. 6-8 (b-g), revealing the segregation of Cu and Mg solutes at the GBs. The average peak concentrations of Cu and Mg were measured to be 3.4 at% and 2.9 at%, respectively. Hence a mean atomic concentration ratio of segregation of Cu: Mg at the grain boundaries is given as 1.16. Additionally, a dislocation (marked with yellow boxes) was detected within the analysed volume, which is also enriched with Cu and Mg solute atoms. Segregation of Cu and Mg solutes at a dislocation is evident in Fig. 6-9. The concentration profiles of solutes along and across the dislocation (s7 and s8) are shown in Fig. 6-9 (b-c), with a Mg: Cu atomic ratio of 1.43 at the dislocation. This implies that Mg segregates more than Cu at the dislocation. A limited amount of Si was also observed with localised enrichment at grain boundaries (Fig. 6-7(d)). Besides, no precipitates and segregation of Li were viewed in the observed volume after HPT and subsequent ageing.

During the final artificial ageing treatment, strong Cu-Mg cluster segregation occurs at both GBs and dislocations. Solute clusters at GBs are evident in Fig. 6-7 (e), which reduces the overall Gibbs free energy and enhances the thermal stability of grain boundaries. Quantitative cluster analysis confirms that the detected clusters are distributed mainly at the GBs rather than in the matrix, having a number density of 2.49 $\times 10^{24}$ m^{-3} in the analyzed volume. An average Mg/Cu ratio of solute clusters approximately equal to 1 was measured based on the APT data.

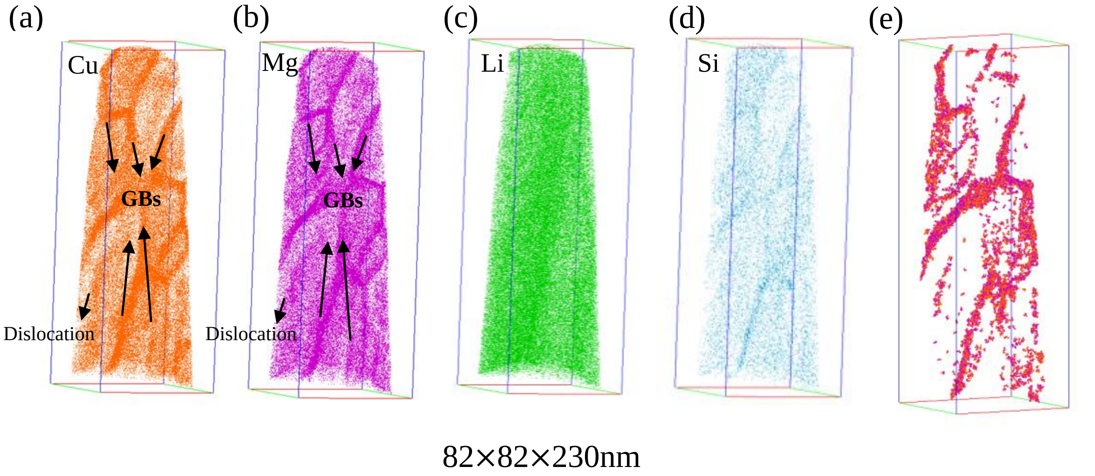

Figure 6- 7. Atom maps of T4-HPT-AA-processed Al-Cu-Mg sample (a) Cu map, (b) Mg map, (c) Li map, (d) Si map and (e) Cu-Mg cluster map after removing the matrix solute atoms.

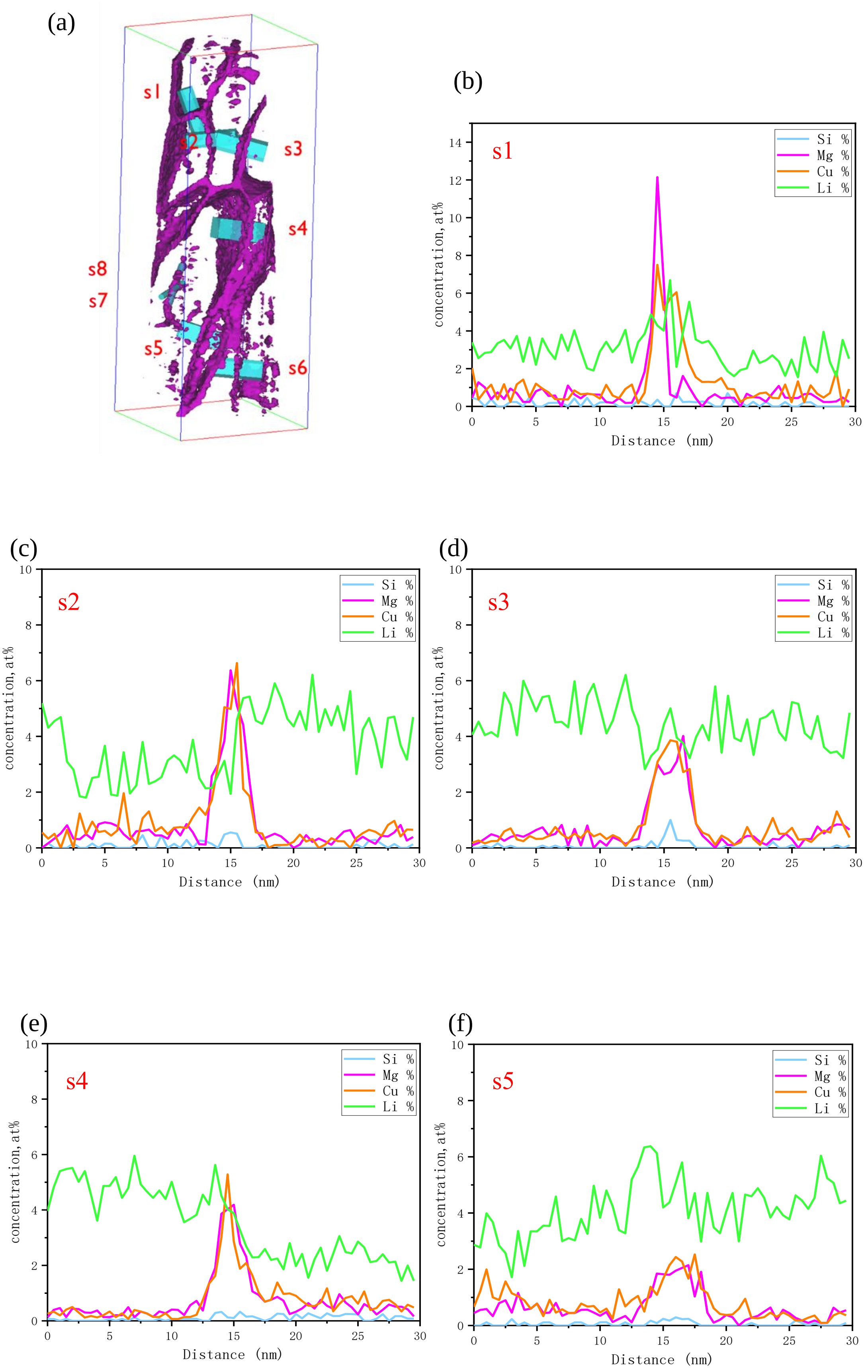
(a)
s1
s2
s3
s4
s5
s6
s7
s8
(b)
s1
(c)
s2
(d)
s3
(e)
s4
(f)
s5
Si %
Mg %
Cu %
Li %
concentration, at%
Distance (nm)
0
5
10
15
20
25
30
2
4
6
8
10
12
14

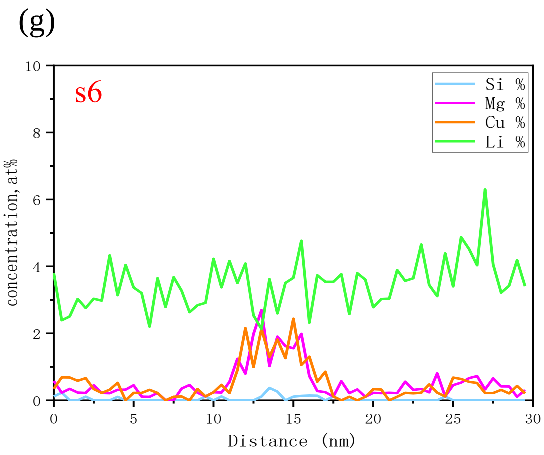

Figure 6- 8. Concentration profiles of solutes across GBs in the analysed volume of T4-HPT-AA-processed Al-Cu-Li alloy sample.

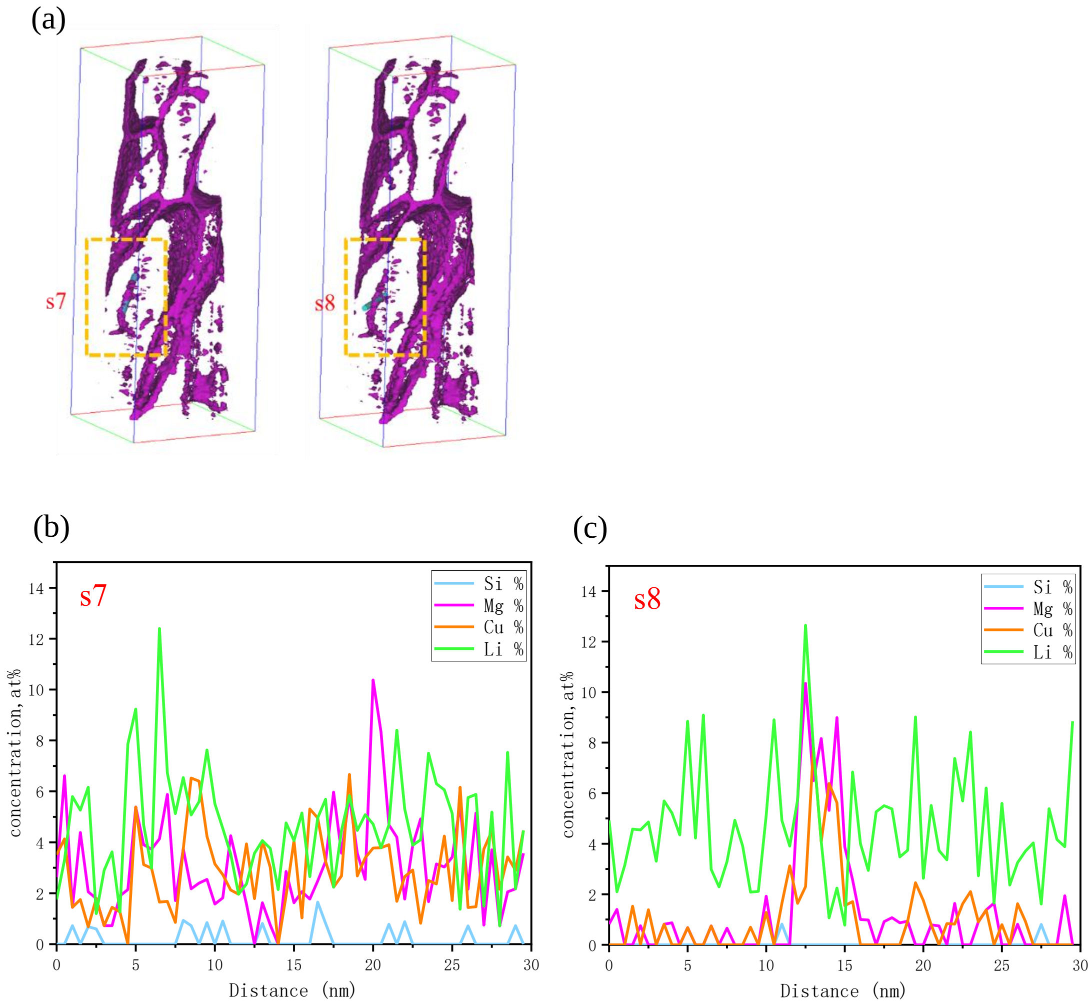

Figure 6- 9. A reconstructed 3-dimension atom map viewed in three directions with dislocation (a) and concentration profiles of solutes (b) along and (c) across the dislocation in the analysed volume of T4-HPT-AA-processed sample.

Al-Li-Cu in T6-HPT-AA condition

Fig. 6-10 shows the APT atom maps of alloying elements Cu, Mg, Li and impurity element Si for the Al-Cu-Li sample pre-aged at 110 °C/24h before HPT and post-HPT aged at 110 °C for approximately 180h. Five GBs (s1-s5) were observed in the T6-HPT-AA-processed sample, marked with black arrows in Figs. 6-10 (a-b). In addition to GBs, one dislocation was also identified in the analysed volume of the sample. Quantitative measurements of the composition profiles of the five pieces of grain boundaries are shown in Fig. 6-11 (b-f), revealing strong segregation of Cu and Mg solutes at GBs. The mean peak concentrations of Cu and Mg were measured to be 3.6 at% and 2.9 at% at GBs, respectively, giving a mean Cu: Mg solute atoms ratio of 1.25 at GBs. Furthermore, the solute peak concentrations with an average of 2.2 at% Cu and 2.5 at% Mg at dislocation were estimated from Fig. 6-12 (b), implying that Mg solute atoms are segregated stronger than Cu solute atoms at dislocation with a Mg/Cu ratio of 1.14. Like T4-HPT-AA-processed sample, no evidence of precipitates and no segregation of Li were detected in the microstructure in this T6-HPT-AA condition.

Strong segregation of Cu-Mg clusters at both GBs and dislocation was observed after the material was processed by T6-HPT-AA condition (see Fig. 6-10(e)). These solute clusters are densely distributed with a number density of 1.33 ×10^{24} m^{-3}. On average, solute clusters had a slightly fewer concentration of Mg than Cu with a ratio of 0.88 (based on the APT data).

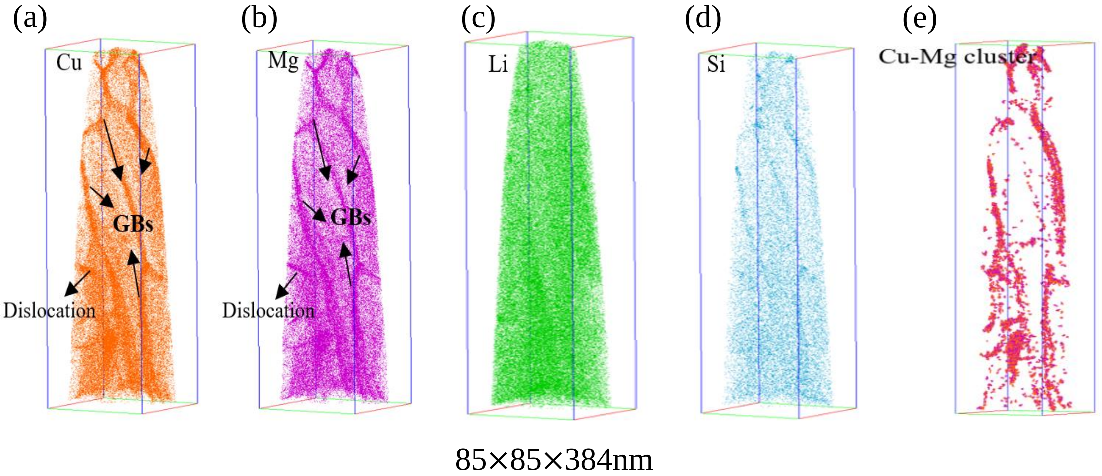

Figure 6- 10. Atom maps of T6-HPT-AA-processed Al-Cu-Mg sample (a) Cu map, (b) Mg map, (c) Li map, (d) Si map and (e) Cu-Mg cluster map after removing the matrix solute atoms.

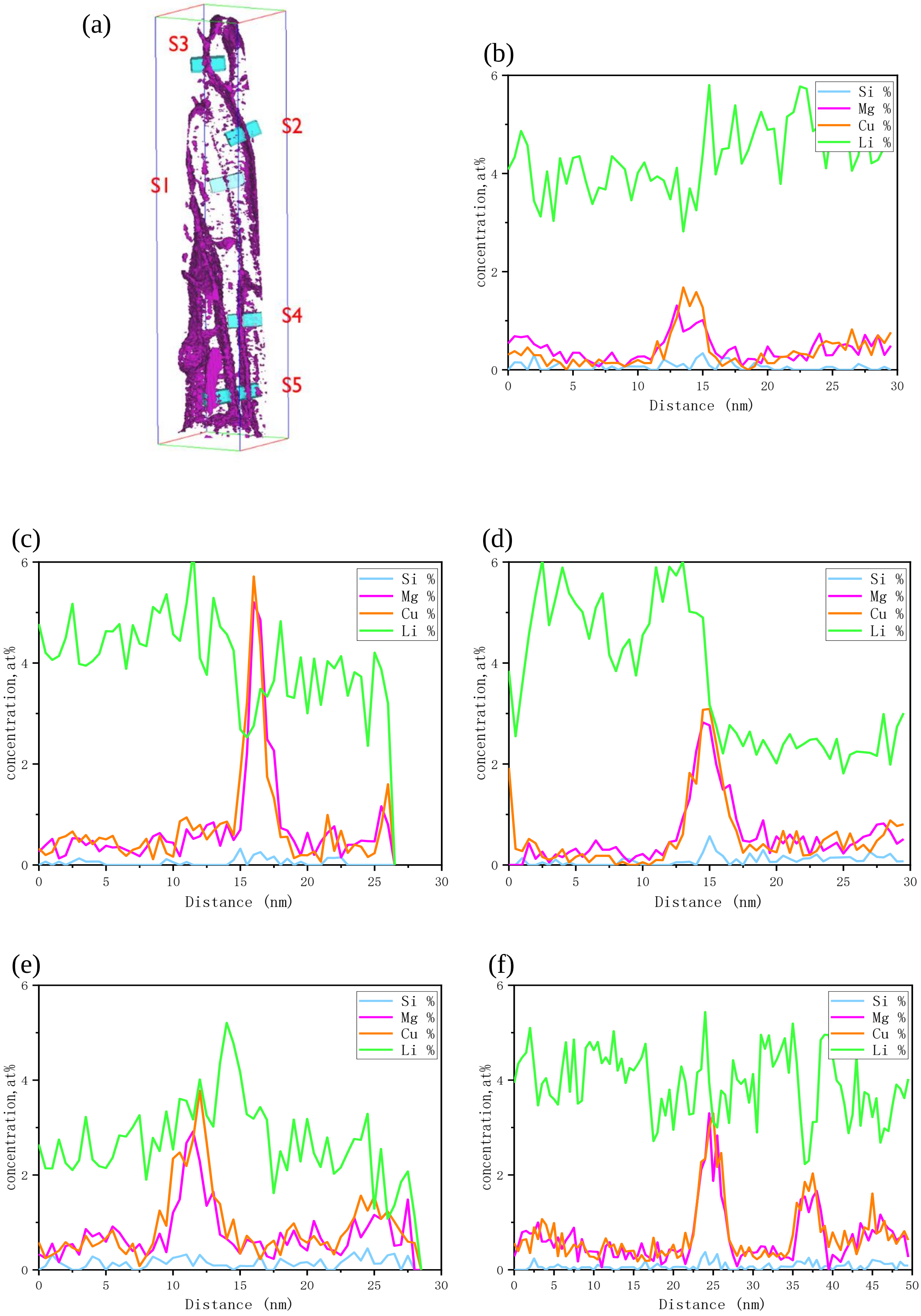

Figure 6- 11. Concentration profiles of solutes across GBs in the analysed volume of T6-HPT-AA-processed Al-Cu-Li alloy sample.

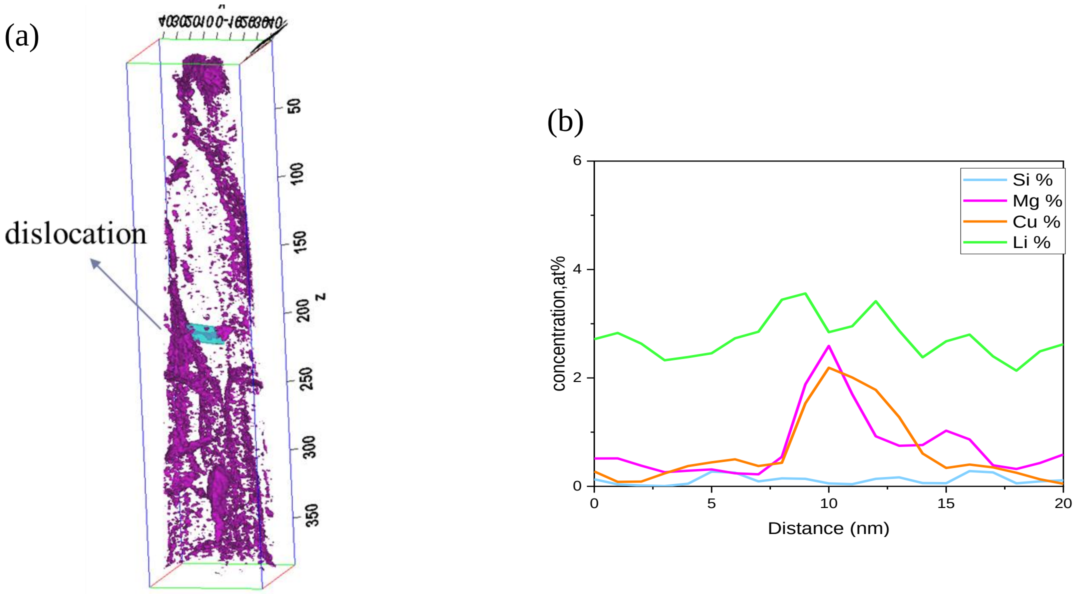

Figure 6- 12. A reconstructed 3-dimension atom map viewed in three directions with dislocation (a) and concentration profiles of solutes (b) across the dislocation in the analysed volume of T6-HPT-AA-processed Al-Cu-Li alloy sample.

6.2 DSC results

DSC curves presented in Fig. 6-13 (a) reveal that several thermal reactions occur during heating up to 330 °C. APT maps in Section 6.1 show that the formation of Cu-Mg cluster after natural ageing and artificial ageing occurred, and no other phase was observed. The low temperature sections up to 100 °C in both T4 and T6 samples were found to have no exothermic reactions, which indicates these clusters do not form to 100 °C. On further heating, multiple endothermic effects occur in the T4 material from 100 °C to 270 °C. This implies that the natural ageing more likely has caused clusters to form, and clusters are dissolved during DSC heating. The occurrence of 2 endothermic peaks indicates that some of the clusters transform into a more thermodynamically stable metastable phase or cluster during DSC above 190 °C before finally dissolving. The T6 sample in the thermogram exhibits thermal effects that are broadly similar (Fig. 6-13(b)), but the first endothermic reaction shifts to a higher temperature compared to T4 sample. Hence, the artificial ageing treatment has increased the thermal stability of clusters or transformed clusters into more stable structures.

The T4-HPT and T4-HPT-AA samples show no distinct endothermic effect up to 230 ^{o}C, indicating that HPT has caused the clusters to transform into a more stable structure. The APT data indicates that these structures are clusters at grain boundaries and dislocations. The exothermic effect occurring in these HPT processed samples starting at 210 ^{o}C, which reaches its peak at about 240 ^{o}C, is likely attributable to recovery (i.e. the rearrangement of the dislocations induced by HPT) and the formation of precipitates [26,234]. T6-HPT and T6-HPT-AA samples have similar thermal effects in the thermogram, but T6-HPT-AA sample shows two exothermic reactions, with peaks respectively at 230 ^{o}C and 255 ^{o}C (Fig. 6-13(b)). At that stage, the hardness of the material will drastically decrease [26] and is hence of no direct interest in this study.

(a)

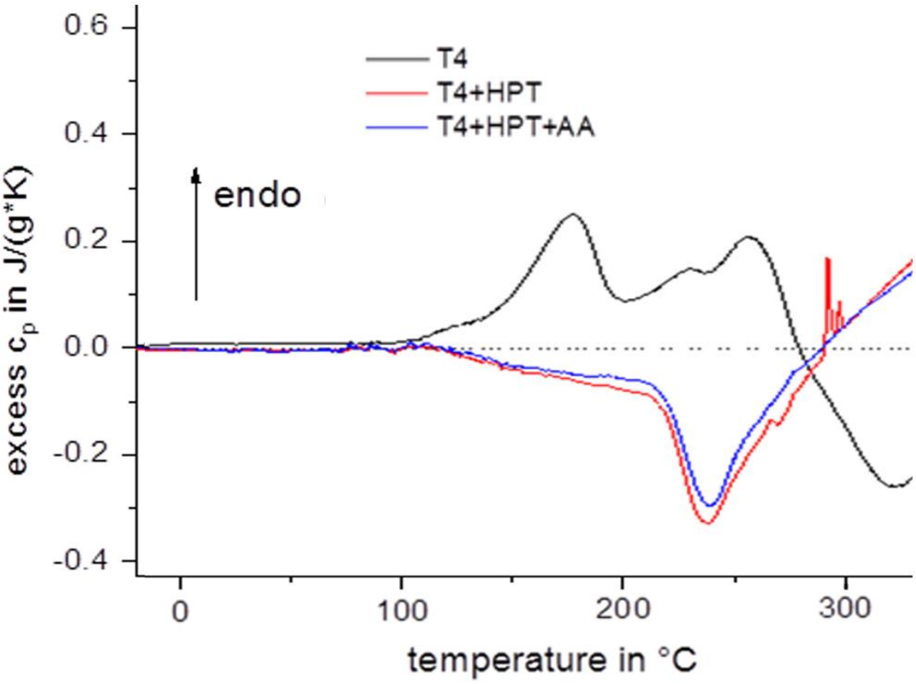

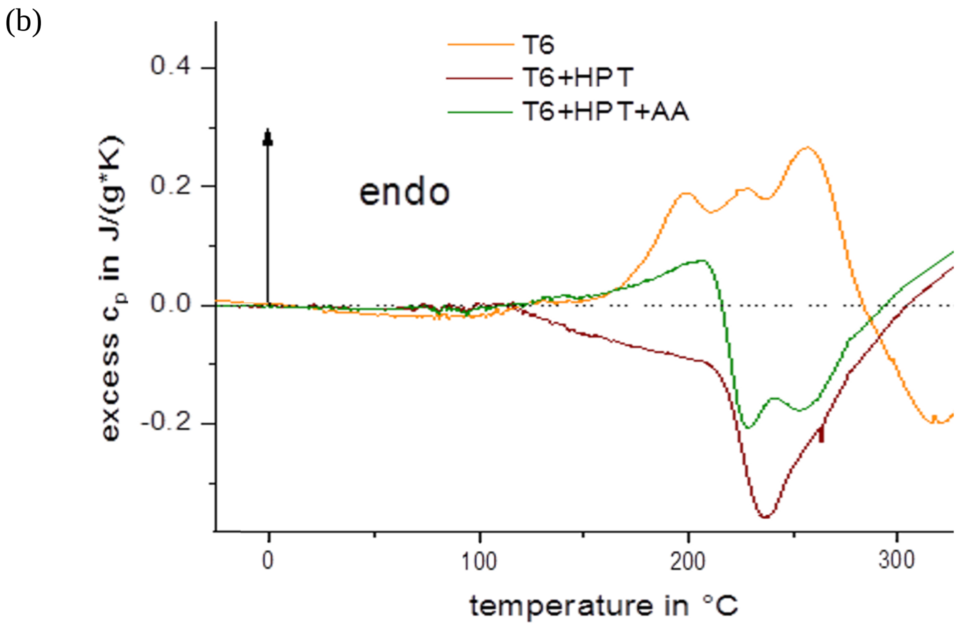

Figure 6- 13. DSC thermogram of Al-Cu-Li alloy in (a) T4, T4-HPT, T4-HPT-AA and (b) T6, T6-HPT, T6-HPT-AA treatments.

6.3 Discussion

6.3.1 Solute segregation in Al-Cu-Li alloy

The precipitation sequence in the 3rd generation Al-Li alloys during conventional ageing treatment is described as: supersaturated solid solution — δ′ (Al_3Li) — δ (AlLi) [235], which is very different with the dynamic precipitation for the Al-Li alloys subjected to HPT processing. Dynamic precipitation of the HPT-processed alloys is believed to be highly reliant on HPT processing temperature, pressure and processing duration [37]. In addition, it is reported that the distribution of solute atoms and solute nanostructures in age hardening alloys could be influenced by SPD in two ways: precipitation (i.e. decomposition of supersaturated solid solution) and segregation of solutes at GBs and dislocations [37]. In this Al-Cu-Li alloy studied here, no δ or δ′ precipitates were identified by TEM, XRD, and APT in all processing conditions as temperature (110 ^{o}C) is too low to cause nucleation of precipitates, leaving sufficient solutes in the matrix available for segregation to GBs or dislocations. In fact, the redistribution of solute atoms [23–25] or the fragment of pre-existing precipitates [138,236] has been demonstrated in many heat-treatable Al alloys processed by SPD technique due to the formation of a large number of lattice defects.

Inspection of those APT data presented in Section 6.1, HPT-processed samples (i.e. T4-HPT and T6-HPT) provide clear details of discrete GB solute enrichment, and this is consistent with similar Cu and Mg solute segregation observed by EDS analysis in Fig. 5-14. These are expected to cause stabilization of segregation-based nanocrystal growth, resisting embrittlement and defect generation [23,237]. Strong segregation of solutes at GBs in an HPT-processed Al-Mg-Si alloy was investigated by EDS, demonstrating that these solutes at GBs can pin GBs from significant grain growth and thereby improved grain refinement as strain increases [145]. Besides, it is proved that the existence of grain boundary segregation during HPT can lead to additional hardening in UFG alloys by retarding lattice dislocations nucleated at GBs [238]. For any GB sliding and rotation, breaking or plastic deformation of the intergranular nanostructures is always needed. Solute segregation at GBs makes these energetically unfavourable and also hinders the process [23].

Quantitative analysis of the solute concentration at GBs illustrates that the relative intensities of Cu and Mg segregation level vary from boundaries to boundaries. This has been found in some research works and ascribes to the fact that GBs may have different segregation characteristics determined by the nature of each GB, such as the disorientation angle of GBs, tilt and rotation components of GBs [25,37]. Furthermore, some of these solute atoms further aggregate to dislocations during the subsequent long time artificial ageing treatments (i.e. T4-HPT-AA and T6-HPT-AA conditions), which reduces the pinning effects of grain growth. Consequently, the grain size slightly grew after T4-HPT-AA and T6-HPT-AA treatments compared with HPT processed samples, which are consistent with the results of TEM observations.

6.3.2 Solute clustering in Al-Cu-Li alloy

A more detailed examination of the APT atom maps reveals information on solute clustering. Solute clustering has long been established in traditional Al alloys and linked to strengthening [23,239,240]. In general, these clusters are deemed ultra-fine dispersion of shearable vacancy-containing clusters, strengthening materials by effectively hindering dislocations under applied shear stress. Interestingly, only Cu-Mg clusters were detected in all processing conditions of an Al-Cu-Li alloy. The formation of such type of cluster often occurs in the precipitation-hardened 2xxx Al-Cu-Mg alloys. Ringer et al. [241] first proposed that the formation of Cu-Mg clusters is responsible for the early stages of precipitation and the initial rapid hardening of an Al-1.1Cu-1.7Mg (at.%) alloy was heat-treated at 150 ^{o}C. These clusters were found to precede the formation of ultra-fine rod-like GPB zones and continuously transform to S (Al_2CuMg) phase. However, in the Al-2.88Cu-1.34Li-1.03Mg alloy, extensive Cu-Mg clusters were observed during natural ageing, segregated to GBs after HPT, and segregated to dislocations after the secondary ageing process. Therefore, a more significant cluster strengthening can be expected.

To date, there are only a few studies working on the 3rd generation of Al-Li alloys processed by HPT, combined with age hardening and none of them has found such co-clusters. This is probably because those ageing temperatures are higher than we used in the present study so that precipitates are preferentially formed instead. Such clustering of various atoms is believed to form through rapid solute diffusion mediated by vacancies inherited from quenching through solution heat treatment. Besides, many studies have stated that not only a large number of dislocations but also a high concentration of vacancies can be introduced by HPT process at RT. The HPT-induced vacancies play an essential role in generating short circuit diffusive pathways, resulting in the formation of co-clusters [242]. Given this, the interactions between different solutes and between the solutes and excess vacancies should be crucial for a particular cluster to form preferably in each alloy [243]. Therefore, it is hard to explain whether Cu-Mg clusters are the only cluster type in the studied Al-Cu-Li alloy by the existing APT technology. Positron annihilation spectroscopy (PAS) might be needed for further investigation of vacancies in solids.

On the other hand, combined with the dislocation densities measured by XRD, a significant reduction in the dislocation density was found after HPT-processed materials were further artificially aged. The observed results are similar to an Al-4.5Cu-1.5Mg alloy aged at 100 ^{o}C /12h after 10% asymmetric rolling (ASR) deformation [242]. A significant decrease in dislocation density was observed after ASR-deformed material was aged at 100 ^{o}C /12h [242]. It was also found that the artificial ageing after 10% ASR generated fewer solute clusters, which is ascribed to the decrease in defects (i.e. dislocations and vacancies) caused by recovery. Thus, it is reasonable to speculate that a recovery is likely to happen during the 100 ^{o}C or 110 ^{o}C subsequent ageing treatment (AA) in our studied Al-Cu-Li alloys, which reduces the number of density of defects, thereby curtailing the short circuit diffusion rate. Therefore, we might expect that the HPT-processed samples (i.e. T4-HPT and T6-HPT) would give rise to a higher diffusion rate and more extensive clustering than those processed by post-ageing (AA). However, we obtained that the T4-HPT-AA and T6-HPT-AA processed materials generated more solute clusters, suggesting that solute mobility is a complex balance of vacancy availability and the availability of fast diffusion pathways such as dislocations and vacancies [244].

APT results reveal that the solute-enrichment at dislocations has a relatively high Mg/Cu ratio of 1.43 (T4-HPT-AA) and 1.14 (T6-HPT-AA), compared with the GBs segregation that has a low Mg: Cu ratio of 0.66 (T4-HPT) and 0.47 (T6-HPT) based on total solute segregation. The observations are consistent with earlier research that

Mg/Cu solute clusters ratio is higher at dislocations than GBs in the 2024 Al-Cu-Mg alloy [240]. The prominent local composition differences at GBs and dislocations suggest that the interactions between solute atoms and GBs differ strongly from those between solute atoms and dislocations. Moreover, solute clustering at GBs and dislocations provides extra strengthening as these solute-defects interactions reduce the Gibbs free energy of the defects via reducing the enthalpy associated with it, resulting in a more stable state [245]. This is consistent with the observation of DSC in Section 6.2, showing that HPT and artificial ageing treatment have increased the thermal stability of clusters by transforming clusters into more stable structures.

6.4 Summary

1) APT maps show that the formation of Cu-Mg cluster after natural ageing, HPT and artificial ageing, and no other phase was observed. Homogeneously distributed Cu-Mg clusters were observed throughout the T4 and T6 samples. During HPT process, the Cu-Mg clusters segregate strongly at the UFG grain boundaries of T4 and T6 materials, and segregation of solute co-cluster at dislocations was revealed during final artificial ageing at 110 ^{o}C.

2) An average Mg/Cu ratio of solute clusters approximately equal to 1 was observed in the T4-HPT-AA condition, but a less Mg/Cu ratio of 0.88 was measured in the T6-HPT-AA condition.

3) T4-HPT and T6-HPT samples signify less distinct solute segregation of grain boundary, and there are no solute enriched features related to dislocations, compared to the post-ageing HPT conditions.

4) Undeformed materials (i.e. T4 and T6) have Mg/Cu solute ratio of approximately 1. Moreover, there is strong preferential segregation of Cu at grain boundaries during HPT process and subsequent ageing. In contrast, the segregation of Mg at the dislocations is comparatively stronger than that of Cu in T4-HPT-AA and T6-HPT-AA conditions.

5) DSC results indicating that HPT and post-ageing have caused the clusters to transform into a more stable structure. The APT data indicates that these structures are clusters at grain boundaries and dislocations.

Chapter 7 Modelling of strength prediction

7.1 Introduction of strengthening models

For the purpose of investigating the mechanisms responsible for the increase in micro-hardness, the prediction of strength by a strengthening model is crucial. In this section, the model described in Section 2.5.2 is applied to Al-Cu-Li alloys processed by T4-HPT-AA and T6-HPT-AA conditions, combined with the microstructure data obtained in Section 5.1 and the model parameters provided in the literature. The grain size used in the model were measured from TEM. Dislocation densities were calculated from the XRD line broadening analysis in Section 5.1.2. The parameters used in the present report are shown in Table 7-1. Moreover, it has been mentioned earlier in this report that the relation between Vickers hardness and yield strength is given approximately as $HV = \frac{\sigma_y}{C}$, where C is a constant that is often taken as ~3, see Refs. [26,176,246]. In our strengthening model, the equation of $\sigma_y \approx 3HV$ is taken for assessment, where the unit of HV has converted into MPa for easy comparison.

As mentioned earlier in Section 2.5.2, the yield strength of polycrystalline material is related to the critically resolved shear stress (CRSS) of the grains and the grain boundary strengthening ($\Delta\sigma_{\mathrm{gb}}$). In the present model, we will consider five strengthening mechanisms that affect the CRSS of grains using a linear superposition (see, e.g. [163,177]), which provides:

$$\sigma_{\mathrm{y}} = \Delta \mathrm{M}\tau_{\mathrm{tot}} + \Delta\sigma_{\mathrm{gb}} \tag{7- 1}$$

$$\Delta\tau_{tot} = \Delta\tau_0 + \Delta\tau_d + \Delta\tau_{ss} + (\Delta\tau_{SRO} + \Delta\tau_m) \tag{7- 2}$$

Hence:

$$\sigma_{\mathrm{y}} = \Delta\sigma_{\mathrm{gb}} + M(\Delta\tau_0 + \Delta\tau_{\mathrm{d}} + \Delta\tau_{\mathrm{ss}} + (\Delta\tau_{\mathrm{SRO}} + \Delta\tau_{\mathrm{m}})) \tag{7- 3}$$

Where σ_{y} is the yield strength; $\Delta\sigma_{\mathrm{gb}}$ is strength increase due to grain boundary strengthening; $\Delta\tau_{tot}$ is total shear stress, and *M* is the crystallographic orientation factor related to texture and the orientation of the tensile axis relative to the main axes of the analysed specimen (often referred to as the Taylor factor). In the present study, 2.6 is used throughout the strength prediction calculations) [107,175]; the contribution due to dislocation strengthening, $\Delta\tau_{\mathrm{d}}$; the contribution due to solid solution strengthening, $\Delta\tau_{\mathrm{ss}}$; and cluster strengthening consists of short-range order strengthening, $\Delta\tau_{\mathrm{SRO}}$ [13,14]; and modulus hardening, $\Delta\tau_{\mathrm{m}}$ [247,248]; the intrinsic strength of annealed Al involving small contribution of Mn, Fe, and Si impurities, $\Delta\tau_0$. The intrinsic strength of pure Al is very low, and 10 MPa is taken for $\Delta\tau_0$ (see for instance [107,175]). As XRD, TEM, and APT all reveal no precipitates were formed during HPT and post-ageing, the strengthening due to long-range ordered precipitation will be negligible. The detailed descriptions of each strengthening mechanism are given below.

Strengthening due to grain refinement

The strengthening due to grain boundaries can be defined as follows :

$$\sigma_{\mathrm{gb}} = k_{\mathrm{HP}} d^{-\mathrm{x}} \tag{7- 4}$$

Where k_{HP} is a material-dependent parameter (often termed the Hall-Petch constant [249]; d is the grain size. $x = \frac{1}{2}$ has been widely applied in large number of coarse-grained metals for investigating the purpose of strengthening behaviours in the traditional Hall-Petch relation [182]; k_{HP} = 0.062 MPa/m^{-2} was taken here, see Ref [26]. Grain size d was measured from TEM images.

Strengthening due to dislocation strengthening

The strengthening contribution of dislocation is considered to follow the below relation:

$$\sigma_{\mathrm{dis}} = M\alpha_1 G b\sqrt{\rho_{\mathrm{dis}}} \tag{7- 5}$$

Where α_1 is a constant equalling 0.3 [17,26], G is shear modulus (26 Gpa for Al), *b* is burgers vector (0.286 nm for Al) [17,250], and ρ_{dis} is the dislocation density calculated by microstrain and crystallite size obtained from MAUD software line broadening analysis, see Eq. 5-1 in Section 5.1.2.

Strengthening due to solid solution

The increment of strength due to solid solution strengthening $\Delta\tau_{ss}$ is given by:

$$\sigma_{\mathrm{ss}} = M\sum k_j c_j^n \tag{7- 6}$$

Where k_j signifies the strengthening caused by individual elements and c_j indicates the concentrations of the alloying elements in solid solution [185,251], and *n* is a constant *n* = 1 [175,185].

It has been reported in many works of literature that the dissolved (non-clustered) solutes contribute very limited conventional solid solution strengthening as only a small amount of solutes will remain dissolved in the sample after natural aged or SPD processed condition [13,14,23,252].

Strengthening due to co-cluster

The co-cluster strengthening is considered to be due to short-range order strengthening, $\Delta\tau_{SRO}$; and modulus hardening, $\Delta\tau_m$. The former has been widely studied and proved to be the dominant cluster strengthening effect in typical Al alloys [8,9,26]. The work done by lattice deformation that is caused by co-clusters impedes the movement of dislocations, and it is equal to the change in energy-related to short-range order per unit area on slip plans in Al matrix. This gives equation [8]:

$$\Delta\tau_{\mathrm{SRO}} = \frac{\gamma_{\mathrm{SRO}}}{b} \tag{7- 7}$$

Where γ_{SRO} is the energy change per unit area on slip plans on the passing of one dislocation, and *b* is the Burgers vector [13]. A detailed calculation regarding the change in area density of A-B nearest neighbour bonds crossing the slip plane on the passing of one dislocation is simplified as the Eq.7-8 below [13]:

$$\Delta\tau_{\mathrm{SRO}} = \frac{\gamma_{SRO}}{b} = \frac{\Delta H_{A-B}}{b}[\rho_{A-B}(n_d = 0) - \rho_{A-B}(n_d = 1)] = C\frac{\Delta H_{A-B}}{b^3}(y_A + y_B) \quad (7\text{-}\ 8)$$

where $\rho_{A-B}(n_d = 0)$ and $\rho_{A-B}(n_d = 1)$ are the area density of A–B nearest neighbour bonds crossing the slip plane {111} before and after the passage of one dislocation; $\Delta H_{\mathrm{A-B}}$ stands for the enthalpy of the nearest neighbour bond (i.e. A-B clusters in the matrix); y_A and y_B are the amount of A and B atoms in the co-clusters, respectively. More derivation of the above equation can be found in [13].

The formation of the clusters is accompanied by an elastic modulus that is different from the matrix, leading to an extra strengthening for materials, $\Delta\tau_m$. This strengthening mechanism has been adopted in many works [13]. The strengthening produced by the difference in shear modulus is given as:

$$\Delta\tau_m = \frac{\Delta\mu}{4\pi\sqrt{2}}\sqrt{f^{cl}} \quad (7\text{-}\ 9)$$

Where f^{cl} is the volume fraction of the clusters, $\Delta\mu$ is the difference in shear modulus between clusters (μ_{cl}) and their surrounding metallic phase. For a $M_mA_aB_b$ cluster can be measured by approximating a weighted average of the pure substances as:

$$\mu_{cl} = \frac{m\mu_M + \alpha\mu_A + b\mu_B}{m + a + b} \quad (7\text{-}\ 10)$$

The above equation gives an approximate 30 Gpa for μ_{cl} , using μ_{Al}= 26.2 GPa, μ_{Cu}= 48.3 GPa and μ_{Mg}= 17.3 GPa, see Ref [253] thus providing $\Delta\mu$ = 3.4 GPa [17], which will be used in this study. The detailed estimation of modulus strengthening can be found in [13].

Table 7- 1. Parameters used in the strengthening prediction model.

Parameters	Value	Refs
$\boldsymbol{M}$	2.6	[107,175]
$\boldsymbol{k}_{\mathbf{HP}}$	0.062 MPa/m^{-2}	[254]
$\Delta\boldsymbol{\tau}_{\mathbf{0}}$	10 MPa	[107,175]
$\boldsymbol{\alpha}_{\mathbf{1}}$	0.3	[176]
$\boldsymbol{G}$	26 Gpa	[176]
$\boldsymbol{K}_{\boldsymbol{Cu}}$	10 Mpa/at% Cu	[175,185,255]
$\boldsymbol{K}_{\boldsymbol{Mg}}$	6 Mpa/at% Mg	[185,255]
$\boldsymbol{K}_{\boldsymbol{Li}}$	6 Mpa/at% Li	[256]
$\boldsymbol{n}$	1	[185,255]
$\boldsymbol{\alpha}_{\mathbf{2}}$	2	[172]
$\boldsymbol{c}_{\boldsymbol{Cu}}$	1.20 at%	See Section 7.2
$\boldsymbol{c}_{\boldsymbol{Mg}}$	1.11 at%	See Section 7.2
$\boldsymbol{c}_{\boldsymbol{Li}}$	5.09 at%	See Section 7.2
$\boldsymbol{b}$	0.286	[107,175]
$\Delta\boldsymbol{H}_{\mathbf{A-B}}$	34.5 ± 0.5 kJ/mol	[13]
$\boldsymbol{C}$	1.54	[176,177]
$\Delta\boldsymbol{\mu}$	3.4 GPa	[26]

7.2 Strength prediction by models

In the present alloys, no experimental results provide the concentration of solute elements dissolved in solid solution. However, the publication [13] contains thermodynamic information on the solvus of Cu-Mg clusters and presents the amount of energy that is released in DSC due to the cluster formation, which is proportional to the amount of cluster formed. After a quantitative evaluation of APT data, the amounts of Cu and Mg in the co-clusters in the model can be estimated using the analysis of thermodynamic data on Al-Cu-Mg alloys [13], i.e. the stoichiometry of the clusters is considered to be y_{Cu}: y_{Mg} =1. We adopt the assumption that 80% of Cu and Mg atoms are clustering in samples and only 20% of them stay in the solid solution for all the samples, signifying only Li entirely contributes to solid solution strengthening. The contribution of Mn, Fe and Si to solution strengthening are much smaller than those of Cu, Li and Mg, and their small contribution will be treated as part of intrinsic strength $\Delta\tau_0$ [175]. For the present Al-2.88Cu-1.34Li-1.03Mg-0.09Zr (wt. %) alloy, which is equivalent to Al-1.20Cu-5.09Li-1.11Mg-0.03Zr (at. %). If we assume all the solute have dissolved, the values of c_{Cu}, c_{Mg} and c_{Li} can be considered the same as the atomic percentage of those in Al matrix, which are 1.20 at%, 1.11 at% and 5.09 at%.

The results of the model predictions are illustrated in Fig. 7-1 and the corresponding values of each strengthening mechanism are listed in Table 7-2. The yield strength of six processing condition groups was given, and each group represents the comparison of the yield strength predicted by the strengthening model and the strength measured from hardness results. It seems that the grain boundary hardening and cluster strengthening are very substantial and can be thought of as the main strengthening mechanisms in this work. Whilst the dislocation hardening is small for HPT-processed samples, and it is possible because the dislocation density of this studied Al-Cu-Li alloy measured by XRD line profile is small than other Al alloys that have measured in the literature [134,150,257–259]. The contribution of solute solution strengthening is also minimal in both HPT-processed and post-ageing-treated samples, and many research publications have stated that the solid solution strengthening has a relatively small contribution to the overall strength, typically 0.5-1% [13,14].

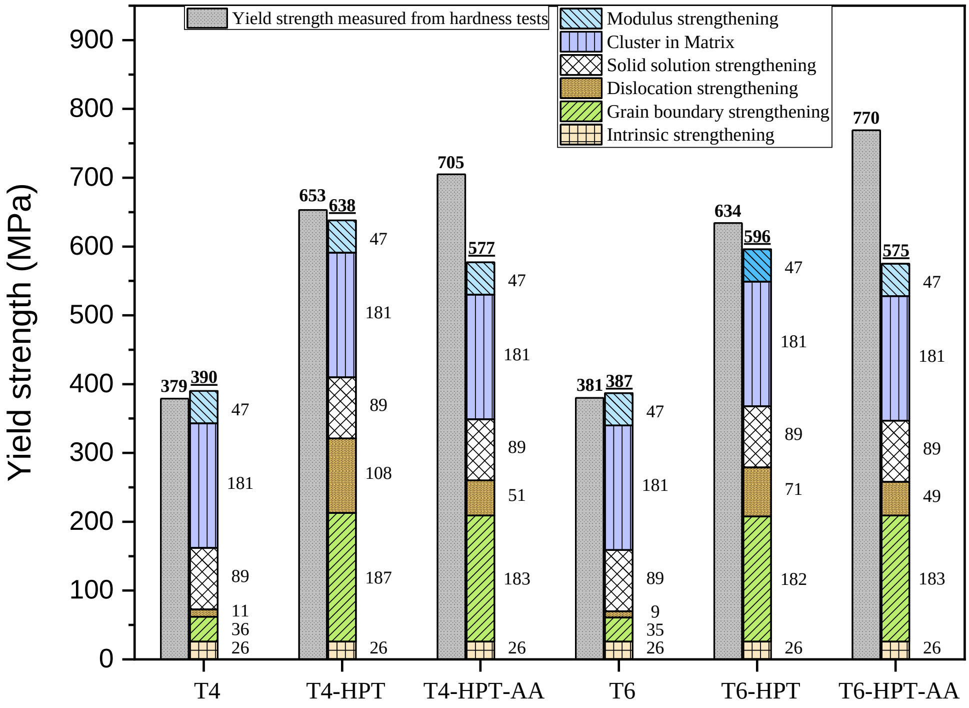

Figure 7- 1. Comparison between yield strength measured from strengthening model and micro-hardness tests.

Table 7- 2. Strength contributed by different strengthening mechanisms.

	σ_0	σ_{gb}	σ_{dis}	σ_{ss}	σ_{sro}	$\sigma_{modulus}$
T4	26.0 MPa	35.6	10.0	88.8	181.2	46.9
T4-HPT	26.0 MPa	197	108.5	88.8	181.2	46.9
T4-HPT-	26.0 MPa	193.8	51.2	88.8	181.2	46.9
T6	26.0 MPa	34.9	8.2	88.8	181.2	46.9
T6- HPT	26.0 MPa	182.8	71.0	88.8	181.2	46.9
T6-HPT-	26.0 MPa	181.7	48.5	88.8	181.2	46.9

Overall, the predicted yield strengths of HPT-processed samples are lower than the strengths measured from Vickers hardness, and the post-ageing-treated samples show a relatively large part of strength is missing (see Fig. 7-1). Such differences are likely due to the lack of consideration of the interaction between HPT-induced defects and clusters by referring to the strength prediction model established by Ying et al. [17]. Above results were calculated based on the model that considers solute atoms and dislocations as two utterly different strengthening effects. Nevertheless, the segregation of solute clusters at GBs and dislocations was clearly revealed by APT analysis (See Section 6.1), contributing extra strengthening [245]. These defects-solute interactions reduce Gibbs free energy of the defects, producing a more stable state. A stronger strengthening effect provided by the dislocation-solute complexes has been discussed, and a model regarding to short-range order cluster strengthening in terms of solute-dislocation is proposed by Ying et al [17], given as:

$$\Delta\tau_{SRO} = C\frac{\Delta H_{A-B-dis}}{b^3}(y_A + y_B) \tag{7- 11}$$

Where $\Delta H_{A-B-dis}$ is the average enthalpy of the various types of A-B dislocation clusters and can be estimated by [17]:

$$\Delta H_{A-B-dis} = f_1\,\Delta H_{A-B} + f_2\,\Delta H_{A-dis} + f_3\,\Delta H_{B-dis} + f_4\,\Delta H_{(A-B)n-dis} \tag{7- 12}$$

where f_1 to f_4 are the fraction of A-B cluster, the fraction of A segregated to dislocations, the fraction of B segregated to dislocations, and the fraction of A-B co-clusters segregated to dislocations, respectively; ΔH_{A-B} is the enthalpy of A-B co-clusters in a matrix, ΔH_{A-dis} and ΔH_{B-dis} are the enthalpy of single atom A or B at dislocations; $\Delta H_{(A-B)n-dis}$ is the enthalpy of co-clusters at dislocations.

The present model has taken various types of A-B dislocation clusters into account but not consider the strengthening effect caused by the segregation of clusters at GBs. Also, the model lacks detailed explanations for each type of cluster strengthening mechanism, i.e. clusters in the matrix, clustering at GBs and dislocations. Therefore, a new concept of cluster strengthening will be introduced and explained in the next section.

7.3 A modified cluster strengthening model

The APT atom maps in Section 6.1 show that three types of short-range order clusters are present: (i) intragranular solute clusters, i.e. clusters in matrix, (ii) clustering at GBs, (iii) clustering at dislocations. In the present model, we will consider that all three types have a distinct enthalpy of formation associated with them, and hence they will each have a distinct strengthening effect. Our new short-range order clusters strengthening model is then represented as:

$$\Delta\tau_{SRO-Matrix} \cong \frac{\Delta H_{A-B}}{b}\frac{4}{\sqrt{3}b^2}\frac{2}{3}(y_{A,1}+y_{B,1}) \tag{7- 13}$$

$$\Delta\tau_{SRO-gb} \cong \frac{\Delta H_{A-B-gb}}{b}\frac{4}{\sqrt{3}b^2}\frac{2}{3}(y_{A,2}+y_{B,2}) \tag{7- 14}$$

$$\Delta\tau_{SRO-dis} \cong \frac{\Delta H_{A-B-dis}}{b}\frac{4}{\sqrt{3}b^2}\frac{2}{3}(y_{A,3}+y_{B,3}) \tag{7- 15}$$

Where $\Delta H_{\mathrm{A-B}}$ here stands for the enthalpy of Cu-Mg clusters in matrix, $\Delta H_{\mathrm{A-B-gb}}$ is the enthalpy of Cu-Mg clusters at the GBs and $\Delta H_{\mathrm{A-B-dis}}$ signifies the enthalpy of Cu-Mg clusters at dislocations. $y_{\mathrm{A},1}$ and $y_{\mathrm{B},1}$ defined as the number of Cu atoms and Mg atoms per volume in the clusters of matrix, respectively; $y_{\mathrm{A},2}$ and $y_{\mathrm{B},2}$ are the number of Cu atoms and Mg atoms per volume in the clusters-GBs complexes, respectively; $y_{\mathrm{A},3}$ and $y_{\mathrm{B},3}$ are the number of Cu atoms and Mg atoms per volume in the clusters-dislocations complexes, respectively.

As the ratio of Cu and Mg atoms composition in the cluster (y_{A}: y_{B}) is considered to be 1. We assume that all the clusters have an equal amount of Cu and Mg. Hence $y_A = y_B$, then:

$$y_{A,1} + y_{A,2} + y_{A,3} = y_{B,1} + y_{B,2} + y_{B,3}$$

$$y_{A,1} = y_{B,1}$$

$$y_{A,2} = y_{B,1}$$

$$y_{A,3} = y_{B,3}$$

In Section 7.2, We estimated that 80% of Cu and Mg atoms formed as clusters in samples, and 20% of them in the solid solution for all the samples. Thus, the overall amount of Cu and Mg atoms (y_A and y_B) in the clusters of material must less than the atomic percentages of the Cu and Mg atoms in Al-Cu-Li alloy, which gives:

$$y_{A,1} + y_{A,2} + y_{A,3} < x_{Cu}$$

$$y_{B,1} + y_{B,2} + y_{B,3} < x_{Mg}$$

For instance, $x_{Cu} = x_{Mg} = 1.11\% = 0.0111$ if all the Cu atoms go into clusters.

7.4 Estimate the amount of Cu and Mg atoms clustered on the GBs and dislocations

In Section 6.1, the APT atom maps show Cu-Mg clusters strongly segregate to GBs during HPT. Further artificial ageing after HPT gives rise to the segregation of them at dislocations. To investigate the amount of A and B atoms (in our alloys Cu and Mg) clustered on the GBs ($y_{\mathrm{A},2}$ and $y_{\mathrm{B},2}$), we consider A and B located around the grain boundary as a plane. Grain boundary density can then be calculated and with the aid of concentration profiles of APT, so that $y_{\mathrm{A},2}$ and $y_{\mathrm{B},2}$ can be obtained.

On the other hand, in order to work out the amount of A and B atoms clustered at dislocations ($y_{\mathrm{A},3}$ and $y_{\mathrm{B},3}$), we consider A and B located around dislocation as a cylinder. $y_{\mathrm{A},3}$ and $y_{\mathrm{B},3}$ can be calculated utilising dislocation density measured from

XRD and solute concentration profiles of APT. The detailed calculations will be discussed below.

As mentioned above $y_{A,1} + y_{A,2} + y_{A,3} < x_{Cu}$, once $y_{A,2}$, $y_{A,3}$ obtained, we assumed 80% of Cu and Mg atoms formed as clusters, the amount of A and B atoms clustered at matrix $y_{A,1} = y_{B,1}$ can be calculated by $80\% \times x_{Cu} - (y_{A,2} + y_{A,3})$.
$x_{Cu} = x_{Mg} = 1.11\% = 0.0111$ as mentioned above if all the Cu atoms go into clusters.

7.4.1 The amount of A and B atoms clustered at the GBs

Considering cluster around GBs as a plane, the total volume of grain boundaries per volume is given as:

$$\text{Total volume of grain boundaries per volume} = \rho_{\text{gb}} \times \text{thickness} \tag{7- 16}$$

Where ρ_{gb} is the grain boundary density; thickness is the average thickness of the layer (plane) measured from the APT solutes concentration profiles of materials.

To calculate grain boundary density (ρ_{gb}), T4-HPT-AA processed sample is taken as an example. If a grain is assumed as a cube, 6 grains are shown in the T4-HPT-AA sample from APT atom map. The total volume of the sample is divided by 6, giving each cube a volume of 2.6×10^{-22} m^3; a side length of a cube is then equal to 63 nm. Now the surface area of one grain boundary (a plane) can be calculated and multiplied by 6 to give the total surface area of all the GBs inside the sample.

The grain boundary density is given by:

$$\rho_{gb} = \frac{\text{Total GBs surface area within the sample}}{\text{The volume of sample}} \tag{7- 17}$$

Then the ρ_{gb} according to Eq. 7-17 can be measured as 1.6×10^7 m^{-1}. An average thickness of 5.6 nm is measured from the full width of the peak value of the solutes concentration profile across the GBs. Therefore, the total volume of grain boundaries per volume can be calculated by Eq. 7-16, giving a value of 9.0%. Hence, there is 9.0 at% cluster zone around grain boundary, and they contain an average of 4% Cu and 4% Mg (estimated from solutes concentration profile in Figs. 6-8(b-g)). Finally, the amount of Cu and Mg atoms at the GBs is $y_{\mathrm{A},2} = y_{\mathrm{B},2}$ = 9.0% × 0.04 = 0.0036.

Follow the same steps, $y_{\mathrm{A},2}$ and $y_{\mathrm{B},2}$ for the samples processed by T4-HPT, T6-HPT and T6-HPT-AA can be obtained. The corresponding parameters used in each process condition are listed in Table 7-3.

Table 7- 3. The parameters used for obtaining $y_{\mathrm{A},2}$ and $y_{\mathrm{B},2}$ in different process conditions.

Conditions	V_{Sample} (m^3)	V_{grain} (m^3)	$\mathrm{Area}_{\mathrm{gb}}$ (m^2)	Total $\mathrm{Area}_{\mathrm{gb}}$ (m^2)	ρ_{gb} (m^{-1})	Thickness (m)
T4-HPT	$1.03\mathrm{x}10^{-21}$	$2.1\mathrm{x}10^{-22}$	$3.5\mathrm{x}10^{-15}$	$2.4\mathrm{x}10^{-14}$	$2.3\ \mathrm{x}10^{7}$	$5.2\ \mathrm{x}10^{-9}$
T4-HPT-AA	$1.55\mathrm{x}10^{-21}$	$2.6\mathrm{x}10^{-22}$	$4.1\mathrm{x}10^{-15}$	$2.4\mathrm{x}10^{-14}$	$1.6\ \mathrm{x}10^{7}$	$5.6\ \mathrm{x}10^{-9}$
T6-HPT	$7.53\ \mathrm{x}10^{-22}$	$3.8\mathrm{x}10^{-22}$	$5.2\mathrm{x}10^{-15}$	$1.0\mathrm{x}10^{-14}$	$1.3\mathrm{x}10^{7}$	$7.5\ \mathrm{x}10^{-9}$
T6-HPT-AA	$2.77\mathrm{x}10^{-21}$	$5.5\mathrm{x}10^{-22}$	$6.7\mathrm{x}10^{-15}$	$4.0\mathrm{x}10^{-14}$	$1.45\ \mathrm{x}10^{7}$	$7.0\ \mathrm{x}10^{-9}$

T4-HPT

ρ_{gb} × thickness = 0.121 = 12.1%

This means 12.1 at% cluster zone around GB, containing 3.1% Cu and 3.1% Mg. So $y_{\mathrm{A},2} = y_{\mathrm{B},2}$ for cluster at GBs = 12.3% × 0.031 = 0.0038.

T6-HPT

ρ_{gb} × thickness = 0.099 = 10.0 %

This means 10.0 at% cluster zone around GB, and they contain 3.6% Cu and 3.6% Mg So $y_{\mathrm{A},2} = y_{\mathrm{B},2}$ for cluster at GBs = 10.0% × 0.036 = 0.0036.

T6-HPT-AA

ρ_{gb} × thickness = 0.102 = 10.2%

This means10.2 at% cluster zone around GB, and they contain 3.2% Cu and 3.2% Mg So y_{A} for cluster on dislocation 10.2% × 0.032 = 0.0033.

7.4.2 The amount of A and B atoms clustered on the dislocations

Considering cluster around dislocation as a cylinder, the total volume of dislocations per volume is given as:

$$\text{Total volume of dislocations per volume} = \rho_d \, \pi r^2 \tag{7- 18}$$

Where ρ_d is dislocation density, which is defined as the total length of dislocations per volume; r is the radius of the cylinder, obtained from the full width of the peak value of the solutes concentration profile across the dislocation. The parameters used to calculate $y_{A,3}$ and $y_{B,3}$ for T4-HPT-AA and T6-HPT-AA process condtions are given in Table 7-4.

Table 7- 4. Parameters used to calculate $y_{A,3}$ and $y_{B,3}$.

Conditions	ρ_d (10^{14}m/m^{-3})	Radius (nm)	Total Vol of dislocations per volume (m^3)	Average concentration of Cu and Mg (at%)
T4-HPT-AA	0.78	2	9.8×10^{-4} (≈0.1%)	7
T6-HPT-AA	0.70	5	5.5×10^{-5} (0.55%)	2.3

T4-HPT-AA

There are 0.1 at% cluster zone around dislocations, and they contain 7% Cu and 7% Mg (obtained from concentration profile in Fig. 6-9 (c)); then $y_{A,3}$ for clusters at the dislocation is equal to 0.1% × 0.07 = 0.00007 = $y_{A,3} = y_{B,3}$.

T6-HPT-AA

There are 0.35 at% cluster zone around dislocations, and they contain 2.3% Cu and 2.3% Mg (obtained from concentration profile in Fig. 6-12 (b)), then $y_{A,3}$ for cluster on dislocation is equal to 0.55% × 0.023 = 0.00013 = $y_{A,3} = y_{B,3}$.

For T4 and T6 samples, APT results have shown that the Cu and Mg atoms are homogeneously distributed throughout the matrix, and no segregation of clusters was identified. Hence, no $y_{A,2}$ and $y_{A,3}$ values are given. For T4-HPT and T6-HPT samples, clusters were found in the matrix and segregated to GBs; thus, no value for $y_{A,3}$. For

T4-HPT-AA and T6-HPT-AA samples, clusters were found dispersed at matrix, GBs and dislocations, thus $y_{\mathrm{A},1}$, $y_{\mathrm{A},2}$ and $y_{\mathrm{A},3}$ values are given in Table 7-5. This table summarises the $y_{\mathrm{A},1}$, $y_{\mathrm{A},2}$ and $y_{\mathrm{A},3}$ in different processing conditions. As $y_{A,1} = y_{B,1}$, $y_{A,2} = y_{B,2}$, $y_{A,3} = y_{B,3}$. Therefore, $y_{\mathrm{B},1}$, $y_{\mathrm{B},2}$ and $y_{\mathrm{B},3}$ will not be shown in the table.

Table 7- 5. A summary of the $y_{\mathrm{A},1}$, $y_{\mathrm{A},2}$ and $y_{\mathrm{A},3}$ in different processing conditions.

Conditions	$y_{\mathrm{A},1}$ **(matrix)**	$y_{\mathrm{A},2}$ **(GBs)**	$y_{\mathrm{A},3}$ **(dislocations)**
T4	0.0088	No clusters at GBs	No clusters at dislocations
T6	0.0088	No clusters at GBs	No clusters at dislocations
T4-HPT	0.0053	0.0036	No clusters at dislocations
T6-HPT	0.0053	0.0036	No clusters at dislocations
T4-HPT-AA	0.0051	0.0038	0.00007
T6-HPT-AA	0.0056	0.0033	0.00013

7.5 The limitations of the Rietveld method/ misfit of solute atoms

The Rietveld method uses line broadening to determine crystallite size and dislocation density. For analysis, the method assumes that polycrystals contain crystals (grains) separated by grain boundaries with dislocations in the grains. It does not consider solute clustering at dislocations or grain boundaries.

Mg dissolved in a binary Al-Mg alloy increases the lattice parameter, and Cu dissolved in a binary Al-Cu alloy decreases the lattice parameter. In other words, the atomic radius of Mg is larger than an Al atom, and Cu is smaller than an Al atom. Therefore, Cu and Mg atoms dissolved in the Al-rich FCC phase cause local strains on the nanoscale. A schematic diagram in Figs. 7-2 (b-c) is used to illustrate that adding a larger or smaller atom into a lattice will cause misfit stresses and strain in the lattice. In addition to this, dislocations also generate nanostrains. As shown in Fig. 7-2 (a), the compressive and tensile lattice strains are introduced by dislocation. The changes in atom positions near the dislocation cause slight variations in the local lattice parameter, which cause line broadening in an XRD diffraction analysis.

If Mg and Cu atoms cluster near a dislocation, there will be interactions that cause small changes in the local positions of the atoms due to these size effects. Cu and Mg atoms segregate around dislocation will find atomic sites more suited to their radii. Therefore, smaller Cu atom can be located close to the dislocation in the compressive field of the dislocation, and larger Mg can be located in the tension field of the dislocation. The Cu and Mg atoms will preferentially move to these positions because it reduces the free energy of the sample (e.g. this positioning reduces local strain fields). This positioning of Cu and Mg atoms near the dislocation effectively reduces nanostrains around the dislocation because the net effect of this positioning is that the total energy-related to the nanostrains is reduced. Smaller and larger substitutional atoms located into strained regions around dislocations will partially cancel solute-dislocation lattice strains. Therefore, the Rietveld analysis of such a sample will then detect that as a narrowing of the diffraction peak, the Rietveld analysis (conducted with MAUD) finds a lower microstrain, and ascribes that to a lower density of defects.

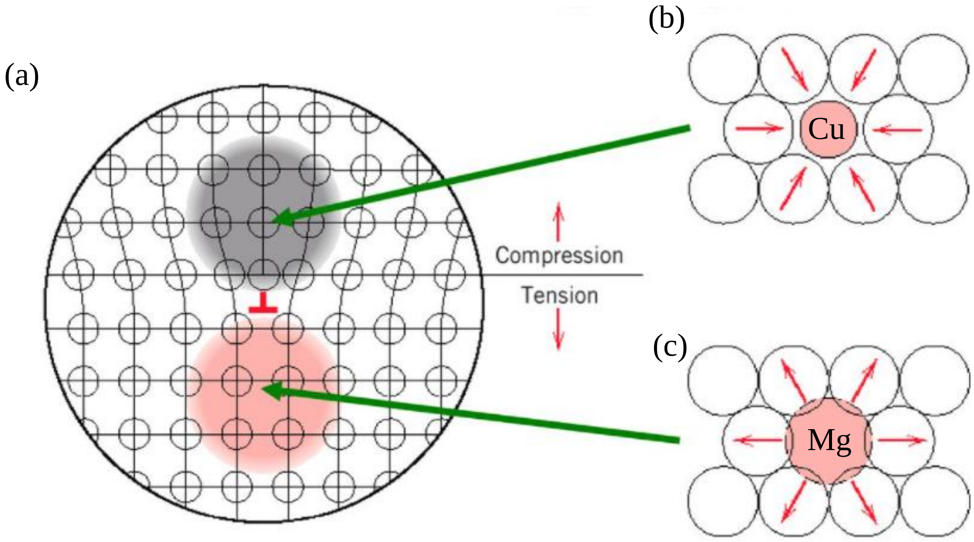

Figure 7- 2. Illustration of (a) compressed and tensioned fields in the edge dislocated crystal lattice, and adding a larger or smaller atom into a lattice will cause misfit stresses and strain the lattice: (b) Cu atom in Al-rich phase, (c) Mg atom in Al-rich phase [260].

Rietveld analysis of dislocation density/strength model

The data on the Al-Cu-Mg-Li shows changes in dislocation density. The Rietveld method analysis of XRD data indicates that artificial ageing (AA) treatment after the T4-HPT and the T6-HPT materials decreases the dislocation density in the materials (see Table 5-1). However, this result is most likely inaccurate because i) APT data shows that the further artificial ageing treatment causes Cu and Mg atoms to cluster at dislocations, which is not considered in the Rietveld analysis method; ii) the hardness of the materials increases after AA treatment whilst APT shows no indication of a known hardening reaction that could compensate for the reduction in dislocation hardening.

It is thought that rather than a reduction in dislocation density, in fact, Cu and Mg clustering at dislocations reduces the local nanostrains (small deviations of atomic positions) during the final ageing stage. Such a reduction in nanostrains is possible because in the Al-rich phase the effective atomic radius of Mg is larger than Al whilst Cu is smaller than Al. Hence, they can effectively reduce nanostrains, causing a narrowing of the diffraction peaks. The Rietveld analyses such a narrowing diffraction peak, finds a lower microstrain, and ascribes it to a lower density of defects (e.g. dislocations). Hence, the dislocation density then should be unaltered. We can now assume that the dislocation density after HPT remains unaltered during subsequent low temperature ageing in the strength model.

In support of the above interpretation, it is noted that in published works on post SPD ageing of Al and its alloys, generally no reduction in dislocation density was reported for the low artificial ageing temperature applied in this work [17,37]. Instead, a reduction in dislocation density was reported in AA6069 during ECAP processing at 170 ^{0}C [142] and in AA7036 during ECAP processing at 200 ^{0}C due to annihilation of dislocations [141].

7.6 Enthalpy estimation

In Section 7.3, three short-range order cluster effects are separated out in the modified model on the basis of clusters in the matrix, GBs and dislocations. ΔH_{A-B} is the enthalpy of Cu-Mg clusters in the matrix, which has been determined as 34.5 ± 0.5 kJ/mol [13]. ΔH_{A-B-gb} is the enthalpy of Cu-Mg clusters at the GBs, which has been determined as 50 ± 5 kJ/mol using data on UFG Al-Cu-Mg alloys [17]. $\Delta H_{\mathrm{A-B-dis}}$ signifies the enthalpy of Cu-Mg clusters at dislocations. To date, very little is known about the enthalpy change of clustering at GBs and dislocations. Hence, in this section, ΔH_{A-B-gb} and $\Delta H_{A-B-dis}$ will be discussed and estimated to achieve the best possible fit between the measured and model predicted strength.

In the T4 treated alloy Cu-Mg clusters readily form, whilst HPT at RT causes the formation of Cu-Mg clusters at GBs. This indicates that the formation of clusters at the GB has a stronger effect in reducing the free energy of the sample as compared to the formation of clusters in the grain away from defects. As the enthalpy of formation is the primary influence, this suggests $\Delta H_{A-B-gb} > \Delta H_{A-B}$. Ageing of the HPT processed materials does not alter the clustering at the GBs to any detectable extend, and instead, the formation of clusters at dislocations is the main change that is observed. This indicates that the formation of dislocation-cluster complexes causes the largest decrease in free energy, which is energetically favourable. It suggests that $\Delta H_{A-B-dis} > \Delta H_{A-B-gb} > \Delta H_{A-B}$.

Estimating $\Delta H_{A-B-dis}$

The DSC curves show that whilst the T4-treated Al-Li-Cu-Mg alloy heating in the range 100-200 °C causes a strong endothermic effect due to the dissolution of clusters, heating of the T4-HPT sample causes an exothermic effect. The APT data indicates that this exothermic effect must be primarily due to the formation of cluster-dislocation complexes. Whilst no change in cluster-GB complexes are observed, which indicates the Cu-Mg cluster-dislocation complexes are significantly more stable than the Cu-Mg clusters in the grain, i.e. $\Delta H_{A-B-dis}$ must be substantially larger than ΔH_{A-B-gb}.

The DSC data shows that for the T4 treated material, the rate of dissolution of Cu-Mg clusters peaks at about 175 °C, i.e. this temperature is approximately the solvus for these Cu-Mg clusters. For the T4-HPT and T4-HPT-AA material, no dissolution effect is observed at least up to 220 °C. At that stage, exothermic formation effect of a further precipitation reaction starts to dominate the DSC curve. We may thus conclude: $\Delta H_{A-B-dis}/\Delta H_{A-B}$ > (220+273)/(175+273) = 1.1.

The above analysis provides some limited insight, but it can not provide an accurate determination of the ratio $\Delta H_{A-B-dis}/\Delta H_{A-B}$. Hence, another way of estimating $\Delta H_{A-B-dis}/\Delta H_{A-B}$ will be considered. In the analysis of $\Delta H_{A-B-dis}$, we could attempt to consider from dislocation elastic energy aspect.

As mentioned in the previous section, dislocations in a crystal increase the free energy of the material. Away from the very centre of the dislocation the energy is predominantly due to elastic lattice distortion. When atoms cluster at and around a dislocation, the free energy of the material decrease due to the clustering process reducing the elastic energy. Clustering of Cu and Mg atoms around a dislocation can be very effective in reducing the elastic energy because the atomic radius of Mg (160 pm) is larger than an Al atom (143 pm), and Cu (128 pm) is smaller than an Al atom with difference typically in the order of 10%.

Dislocations in a crystal increase the elastic energy of the material predominantly due to elastic lattice distortion. The expression for elastic energy caused by lattice distortion is [261].

$$U_{\mathrm{el}} = \frac{Gb^2}{4\pi(1-\nu)}\, ln\frac{R}{r_o}(1-\nu\, cos^2\alpha) \tag{7- 19}$$

Where U_{el} is the elastic energy associated with a dislocation, G is shear modulus, taken as 26 GPa here, b is burgers vector, ν is Poisson's ratio, 0.3 was used for Al alloy, r_o is the core radius of the dislocation (r_o= 2b), α is a geometrical factor that represents the angle between the burgers vector and the dislocation line. For screw dislocation, α = 0;

for edge dislocation, α = π/2, R is the outer radius of dislocation or dislocation spacing can be determined by:

$$R = {\rho_{dis}}^{-\frac{1}{2}} \tag{7- 20}$$

Where ρ_{dis} is dislocation density, R = 100 nm (valid for a dislocation density 1×10^{14} m^{-2}, which is typical for HPT processed Al-Cu-Mg type alloys).

If we assume these are all edge dislocations within the sample, and then Eq. 7-19 can be simplified as :

$$U_{\mathrm{el}} = \frac{Gb^2}{4\pi(1-\nu)}\, ln\frac{R}{r_o} \tag{7- 21}$$

Therefore, we may calculate the free energy change of the dislocations-containing lattice due to clustering of Cu and Mg atoms around dislocations, under the assumption that the change in elastic energy is the dominant factor, and the clustering can effectively dissipate all of the elastic energy due to the dislocation. To do this, we first calculate the elastic energy per dislocation line length for R = 100 nm by using Eq. 7-21, $\frac{U_{\mathrm{el}}}{l_{dis}} = 3.4\ nJ/m$ is obtained, where l_{dis} is the dislocation length.

Next, we estimate the amount of Cu and Mg that are clustered at and around the dislocation from APT data shown in Fig. 6-9. This figure shows that the zone of clustered Cu and Mg atoms around the dislocation has a radius of about 2 nm and a Mg and Cu composition of about 0.07. From that we can determine the cluster density to be 21 Cu atoms per nm of dislocation length. (And 21 Mg atoms per nm of dislocation length.)

Combining the above data, and assuming that effectively all elastic energy is eliminated by the clustering at and around the dislocation, we obtain the change in elastic energy for $r > r_o$ due to clustering as: 1.6×10^{-19} J per Cu-Mg pair at the dislocation = 95 kJ per mol Cu-Mg pairs at the dislocation ($1.6 \times 10^{-19} \times 6.02 \times 10^{23}$ = 95kJ). We will term this $\Delta U_{el(A-B-dis)}$.

The total enthalpy changes due to clustering near the dislocation will be the sum of the change due to the elastic strain field plus the change due to near neighbour Cu-Mg interactions. From the above, we may thus conclude that a good approximation for $\Delta H_{A-B-dis} \approx \Delta U_{el(A-B-dis)} + \Delta H_{A-B} = 95 + 34.5 = 130$ kJ/mol. This is, however, an approximation. A factor that makes this a possible underestimate is that very close to the core of the dislocation, and the stress will substantially increase. Clustering may also reduce this energy and hence $\Delta U_{el(A-B-dis)}$ maybe larger than the above estimated 95 kJ/mol. We might consider estimating this extra contribution by taking r_o as the near neighbour distance, i.e. $r_o = b$. That produces $\Delta U_{el(A-B-dis)} \approx 108$ kJ/mol. It is important to note that the calculations are based on the assumption that only 20% of Cu/Mg are in solid solution, and 80% are formed as clusters, so Mg and Cu composition that contributes to clusters is 1.25 lower. Therefore, a better estimation may be $\Delta U_{el(A-B-dis)} \times 1.25 \approx 135$ kJ/mol. In conclusion of this assessment and discussion, we take $\Delta H_{A-B-dis} \approx \Delta U_{el(A-B-dis)} + \Delta H_{A-B} = 135 + 34.5 \approx 170$ kJ/mol.

There may also be a source of overestimation, and particularly it may be considered that clustering will not be able to completely eliminate the strain energy of the dislocation in the region that is considered ($r > r_o$). However, this is thought to be a very small possible deviation. In conclusion of this assessment and discussion, we take $\Delta H_{A-B-dis} \approx 165$ kJ/mol. The accuracy of this determination is difficult to assess, so we will not discuss it in the present work.

In summary, the enthalpy values of three types of short-range order cluster effects (clusters in the matrix, GBs and dislocations) in the modified cluster strengthening model are now estimated as below:

$\Delta H_{A-B} = 34.5$ kJ/mol
$\Delta H_{A-B-gb} = 50$ kJ/mol
$\Delta H_{A-B-dis} = 165$ kJ/mol

7.7 Strength prediction based on the modified model

After adjusting dislocation density and substituting enthalpy values into the modified short-range order cluster strengthening model, the amended strength prediction results are illustrated in Fig. 7-3. The corresponding values of each strengthening mechanism are listed in Table 7-6. The Fig. 7-3 shows a good correspondence between the strength predicted by the model and the measured strength from Vickers hardness for T4, T4-HPT, T4-HPT-AA, T6, T6-HPT processed samples. Among the model predictions for total strength, only the prediction of the strength of T6-HPT-AA sample is substantially outside the typical accuracy (percentage error) of 4%, and it is most likely due to the estimation of $\Delta H_{A-B-dis}$ value or some other strengthening mechanisms have not yet been quantified. This analysis shows that grain boundary strengthening is still the crucial mechanism for HPT-processed materials, but it accounts for only ¼ of the total strength. The Cu-Mg clusters contribute substantially to the strength in all conditions. The combined effect of all three types of clusters due to short-range order mechanism is dominant for all conditions studied, with a small modulus strengthening effect. Therefore, the whole clusters in total have the strengthening larger than grain boundaries.

For these types of alloys, co-cluster strengthening has been found to be the largest in all contributions and examined as the main strengthening mechanism. Furthermore, it has been shown that in several heat-treatable ternary Al alloys such as Al-Cu-Mg [17] and Al-Mg-Si alloys [14], the presence of co-clusters is a dominant strengthening mechanism.

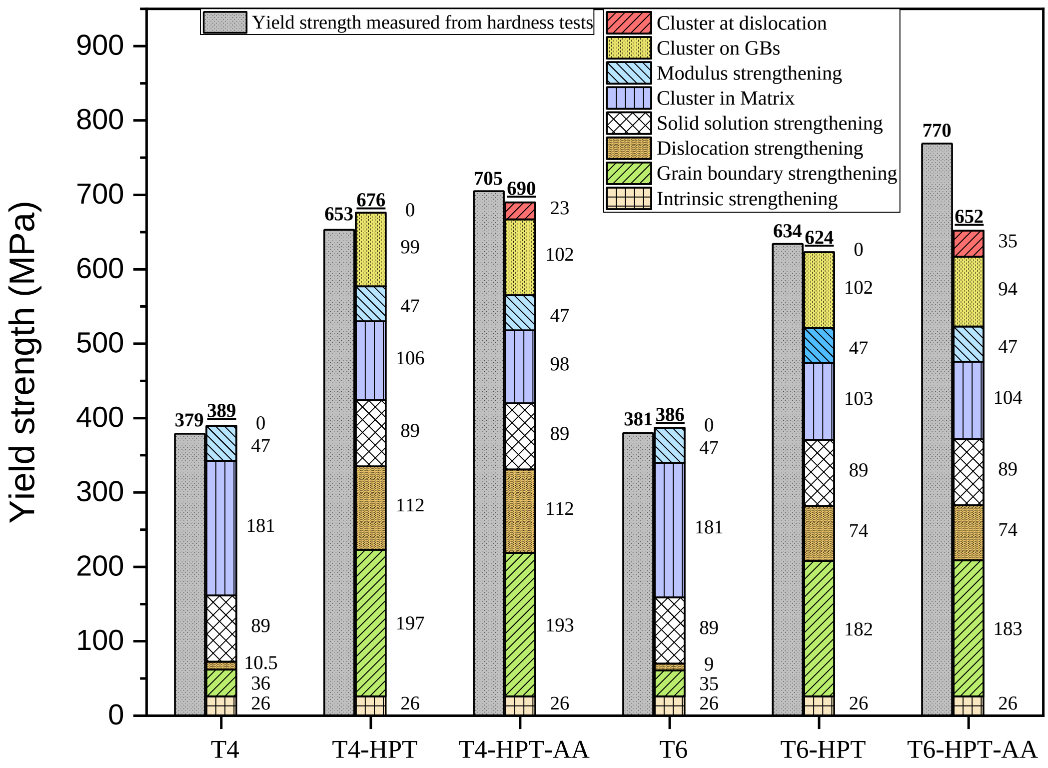

Figure 7- 3. An updated yield strength comparison between the measured values from micro-hardness tests and the predicted values from strengthening model based on a new cluster strengthening model.

Table 7- 6. Measured strength (MPa) by Vickers hardness and strength (MPa) caused by different strengthening mechanisms in six processing conditions.

Conditions	Hv	σ_0	σ_{gb}	σ_{d}	σ_{ss}	$\sigma_{sro-matrix}$	$\sigma_{modulus}$	$\sigma_{sro-Gbs}$	$\sigma_{sro-dis}$
T4	379	26	36	10.5	89	181	47	0	0
T4-HPT	653	26	197	112	89	106	47	99	0
T4-HPT-	705	26	193	112	89	98	47	102	23
T6	381	26	35	9	89	181	47	0	0
T6- HPT	634	26	182	74	89	103	47	102	0
T6-HPT-	770	26	183	74	89	104	47	94	35

7.8 Summary

1. A new cluster strengthening model has been established, which separates out three types of short-range order clusters: (i) intragranular solute clusters, i.e. clusters in matrix, (ii) clustering at GBs, (iii) clustering at dislocations.

2. The amount of Cu and Mg atoms clustered on the GBs ($y_{\mathrm{A},2}, y_{\mathrm{B},2}$) and dislocations ($y_{\mathrm{A},3}$, $y_{\mathrm{B},3}$) were estimated by grain boundary density and dislocation density, respectively.

3. The Rietveld method analysis does not consider solute clustering at dislocations or grain boundaries. The method detects the narrow diffraction peak and ascribes that to a reduction dislocation density. The fact is that narrowing peak is caused by reduction of nanostrains by positioning of Cu and Mg atoms near the dislocation, so the dislocation density should remain unchanged after HPT process.

4. The enthalpy value of ΔH_{A-B} , ΔH_{A-B-gb} are discussed, and the value of $\Delta H_{A-B-dis}$ in the new cluster strengthening model is determined as $\Delta H_{A-B-dis} = 165\ \mathrm{kJ/mol}$ by dislocation elastic energy.

5. The assessment of strengthening mechanisms has shown that all three types of short-range order strengthening due to clustering contribute to the high strength of HPT-processed Al-Cu-Li alloy.

6. Five out of six predictions show a good correspondence between measured and predicted values. Only T6-HPT-AA sample shows an underpredicted strength, and it is most likely due to the estimation of $\Delta H_{A-B-dis}$ value.

7. The combined effect of all three types of short-range order clusters is the dominant mechanism for all conditions studied.

Chapter 8 Conclusions and Future works

8.1 General conclusion

In summary, this present work has reported novel multi-stage processes through the combination of age hardening and HPT to obtain superior strength of Al-Li-Cu alloy. After performing a series of micro-hardness measurements at various ageing temperatures and ageing times on the material, a hardness of ~240Hv was achieved in the T4-HPT-AA treatment aged at 110 ^oC/60h. Besides, an ultra-high hardness of ~260Hv was achieved through pre-HPT ageing at 110^oC/24h followed by post-HPT ageing at 110^oC/180h (T6-HPT-AA). By contrast, neither of them (i.e. T4-HPT-AA and T6-HPT-AA) was effective in improving the strength of 7449 Al alloys, but it increases the ageing stability of the alloy. Therefore, Al-Cu-Li alloys processed by two processing conditions were investigated for microstructural analysis.

TEM observations show that an UFG structure is formed when T4 and T6-treated samples deformed by HPT, the grain size was significantly refined (by a factor of ~30), resulting in grain size of ~90 nm and ~115 nm, respectively. The UFG structure was still retained during subsequent artificial ageing at 110 ^oC/60h in T4-HPT-AA and 110 ^oC/180h in T6-HPT-AA conditions. β′ phase (Al_3Zr) with a size of ∼50 nm were found everywhere in all stages of processed samples and is retained even during solution treatment, ageing treatment, and HPT processing. However, it does not contribute much to the strengthening of the Al-Cu-Li alloy. Besides, HPT process induces a large number of dislocations, which were measured by MAUD based on the full peak X-ray profile refinement. Results show that T4-processed sample has the highest dislocation density level of $\sim3.5\times10^{14}$ m^{-2}, and the dislocation density of T6-processed sample increases to $\sim1.5\times10^{14}$ m^{-2} right after HPT. XRD also reveals that both processes cause the dislocation density of the materials to drop gradually with increasing ageing time.

Neither XRD nor TEM shows any visible precipitates after HPT process and subsequent ageing treatments. Instead, APT maps show the formation of Cu-Mg cluster after natural ageing, HPT and artificial ageing. Cu-Mg clusters were found homogeneously distributed throughout the T4 and T6 samples, strongly segregated to

GBs during HPT and further segregated to dislocations during post-ageing treatment at 110 ^{o}C. An average Mg/Cu ratio of solute clusters approximately equal to 1 was observed in the T4-HPT-AA condition, but a less Mg/Cu ratio of 0.88 was measured in the T6-HPT-AA condition. Mg/Cu solute ratio of approximately 1 was measured in T4 and T6 processed materials. Strong segregation of Cu at GBs was noticed during HPT process and subsequent ageing. However, the segregation of Mg at the dislocations is comparatively stronger than that of Cu in T4-HPT-AA and T6-HPT-AA conditions. In addition, DSC results show that HPT and post-ageing have caused the clusters to transform into a more stable structure. The APT data indicates that these structures are clusters at grain boundaries and dislocations.

Finally, a new cluster strengthening model was developed in this work, which incorporates three different types of short-range order clusters: clusters in matrix, clustering at GBs, and clustering at dislocations. The amount of Cu and Mg atoms clustered at the GBs, dislocations were estimated. The enthalpy value of $\Delta H_{A-B-dis}$ was discussed, and an appropriate value of 165kJ/mol was proposed by dislocation elastic energy. A model consists of grain boundary hardening, dislocation strengthening, solid solution strengthening and the new short-range order cluster strengthening mechanisms was applied to evaluate the contributions of each strengthening mechanism and to predict the yield strength of Al-Cu-Li alloy. The results show the combined effect of all three types of clusters due to short-range order mechanism is dominant for all conditions studied. Additionally, the predicted strengths from the model are compared with the strength measured from Hv hardness, which demonstrated that 5 out of 6 predictions show good correspondence. Only T6-HPT-AA sample shows an underpredicted strength, it is most likely due to the estimation of $\Delta H_{A-B-dis}$ value.

8.2 Future works

Work on this research has identified some experiments and analyses arising from current findings that should be pursued and addressed in the future on the following research areas:

1. The estimation of $\Delta H_{A-B-dis}$

The predicted strength and measured strength of T6-HPT-AA sample are not corresponding well using our modified strengthening model. One of the possible reasons is that the estimation of $\Delta H_{A-B-dis}$ value (165 kJ/mol) obtained by the aid of dislocation elastic energy in the present study may still underestimate. The accuracy of this determination is difficult to assess, future works or more favourable evidence thereby should be pursued in the future. In addition, despite the value of $\Delta H_{A-B-dis}$ was estimated by dislocation elastic energy, other possible approaches, such as through heat content of DSC effects and stability limit, can be contemplated further.

2. The effects of Li on the strength of Al-Cu-Li alloy

It may seem strange that the strength of an Al-Cu-Li alloy mainly results from Cu-Mg clusters. However, no Al_3Li particles (δ' phase), Al_2CuLi (T_1 phase) or any other Li-related clusters were identified in all stages of two processing procedures (T4-HPT-AA and T6-HPT-AA) via TEM, XRD and APT techniques. Except for the minor solid solution strengthening effect due to Li atoms, no more evidence shows that Li contributes much to the superior strength of Al-Cu-Li alloy by means of HPT and age hardening. Therefore, further works are needed to investigate the effects of Li on the strength of Al-Cu-Li alloy.

3. More characterisation analysis

More TEM experiments need to be carried out to analyse more TEM images, particularly SEAD patterns for phase determination. Furthermore, Electron backscatter diffraction (EBSD) will be needed for obtaining statistical information of the UFG microstructure, including distribution of grain size and grain boundary misorientation angles, grain orientation map. In addition, vacancies play a crucial role in forming clusters, and the interactions between the solutes and excess vacancies are vital for a particular cluster to form preferably in each alloy. Hence, Positron annihilation spectroscopy (PAS) will be needed to investigate vacancies in solids, and it might explain why the Cu-Mg clusters as the only cluster type occurred in the Al-Cu-Li alloy.

4. Measurement of dislocation density

Study more about the dislocation density, using a higher resolution XRD to explore the dislocation density within small area of HPT-processed samples. Also, learning XRD line broadening analysis in more detail, using different methods such as Williamson-Hall and Warren-Averbach methods to measure dislocation densities of different samples, so that the comparisons of the results can be made. Additionally, the accuracy of the dislocation density measurements needs to be improved. Besides, improve the accuracy of all the measurements, e.g. grain size, crystallite size, microstrain, hardness, dislocation density, etc.

References

[1] R.J. Rioja, J. Liu, The Evolution of Al-Li Base Products for Aerospace and Space Applications, Metall. Mater. Trans. A. 43 (2012) 3325–3337.

[2] N. Prasad, A. Gokhale, R. Wanhill, Aluminum-lithium alloys: processing, properties, and applications, 2013.

[3] T. Warner, Recently-developed aluminium solutions for aerospace applications, in: Mater. Sci. Forum, Trans Tech Publ, 2006: pp. 1271–1278.

[4] N. Nayan, N.P. Gurao, S.N. Murty, A.K. Jha, B. Pant, S.C. Sharma, K.M. George., Microstructure and micro-texture evolution during large strain deformation of an aluminium–copper–lithium alloy AA 2195, Mater. Des. 65 (2015) 862–868.

[5] T. Dursun, C. Soutis, Recent developments in advanced aircraft aluminium alloys, Mater. Des. 56 (2014) 862–871.

[6] N. Kamp, M.J. Starink, I. Sinclair, N. Gao, P.J. Gregson, P.D. Pitcher, S. Gardiner, Development of Al-Cu-Mg-Li (Mn,Zr,Sc) alloys for age-forming, Mater. Forum. 28 (2004) 369–375.

[7] N. Kamp, I. Sinclair, M.J. Starink, Toughness-Strength Relations in the Overaged 7449 Al-Based Alloy, Metall. Mater. Trans. A. 33 (2002) 1125–1136.

[8] J. Davis, Corrosion of aluminum and aluminum alloys: Classifications and Designations, ASM international, 1999.

[9] C. Fai Tan, M. Said, M.R. Said, Effect of Hardness Test on Precipitation Hardening Aluminium Alloy 6061-T6, 36 (2009) 276–286.

[10] M. Jr, J. Morris, The Influence of Grain Size on the Mechanical Properties of Steel, In: International Symposium on Ultrafine Grained Steels. (2001) 34.

[11] J.R. Bowen, P.B. Prangnell, F.J. Humphreys, Microstructural evolution during formation of ultrafine grain structures by severe deformation, Mater. Sci. Technol. 16 (2000) 1246–1250.

[12] A.P. Zhilyaev, T.G. Langdon, Using high-pressure torsion for metal processing: Fundamentals and applications, Prog. Mater. Sci. 53 (2008) 893–979.

[13] M. Starink, S. Wang, The thermodynamics of and strengthening due to co-clusters: general theory and application to the case of Al–Cu–Mg alloys, Acta Mater. 57 (2009) 2376–2389.

[14] M. Starink, L. Cao, P. A. Rometsch, A model for the thermodynamics of and strengthening due to co-clusters in Al–Mg–Si-based alloys, Acta Mater. 60 (2012) 4194–4207.

[15] L.T. Stephenson, M.P. Moody, P. V. Liddicoat, S.P. Ringer, New Techniques for the Analysis of Fine-Scaled Clustering Phenomena within Atom Probe Tomography (APT) Data, Researchgate.Net. 13 (2007) 448–463.

[16] M.J. Starink, N. Gao, J.L. Yan, The origins of room temperature hardening of Al–Cu–Mg alloys, Mater. Sci. Eng. 387–389 (2004) 222–226.

[17] Y. Chen, N. Gao, G. Sha, S. Ringer, M. Starink, Strengthening of an Al–Cu–Mg alloy processed by high-pressure torsion due to clusters, defects and defect–cluster complexes, Mater. Sci. Eng. 627 (2015) 10–20.

[18] W. Sun, X. Qiao, M. Zheng, X. Zhao, H. Chen, Achieving ultra-high hardness of nanostructured Mg-8.2 Gd-3.2 Y-1.0 Zn-0.4 Zr alloy produced by a combination of high pressure torsion and ageing treatment, Scr. Mater. 155 (2018) 21–25.

[19] M.F. Ashby, The deformation of plastically non-homogeneous materials, Philos. Mag. 21 (1970) 399–424.

[20] K. Marthinsen, E. Nes, A general model for metal plasticity, Mater. Sci. Eng. 234–236 (1997) 1095–1098.

[21] Y. Estrin, L. Toth, A. Molinari, Y. Bréchet, A dislocation-based model for all hardening stages in large strain deformation, Acta Mater. 46 (1998) 5509–5522.

[22] O. Rezvanian, M. Zikry, Inelastic contact behavior of crystalline asperities in rf MEMS devices, Eng. Mater. Technol. 131 (2009) 011002-1–011002-10.

[23] P. Liddicoat, X. Liao, Y. Zhao, Y. Zhu, Nanostructural hierarchy increases the strength of aluminium alloys, Nature. 1 (2010) 1–7.

[24] G. Nurislamova, X. Sauvage, M. Murashkin, R. Islamgaliev, R. Valiev, Nanostructure and related mechanical properties of an Al–Mg–Si alloy processed by severe plastic deformation, Philos. Mag. Lett. 88 (2008) 459–466.

[25] G. Sha, L. Yao, X. Liao, S. Ringer, Z. Duan, Segregation of solute elements at grain boundaries in an ultrafine grained Al–Zn–Mg–Cu alloy, Ultramicroscopy. 111 (2011) 500–505.

[26] Y. Chen, N. Gao, G. Sha, S. Ringer, MJ Starink, Microstructural evolution, strengthening and thermal stability of an ultrafine-grained Al–Cu–Mg alloy, Acta Mater. 109 (2016) 202–212.

[27] A.P. Zhilyaev, T.R. McNelley, T.G. Langdon, Evolution of microstructure and microtexture in fcc metals during high-pressure torsion, J. Mater. Sci. 42 (2007) 1517–1528.

[28] Z. Yang, U. Welzel, Microstructure–microhardness relation of nanostructured Ni produced by high-pressure torsion, Mater. Lett. 59 (2005) 3406–3409.

[29] A. Vorhauer, R. Pippan, On the homogeneity of deformation by high pressure torsion, Scr. Mater. 51 (2004) 921–925.

[30] C. Xu, Z. Horita, T.G. Langdon, The evolution of homogeneity in an aluminum alloy processed using high-pressure torsion, Acta Mater. 56 (2008) 5168–5176.

[31] S. Lee, Z. Horita, S. Hirosawa, K. Matsuda, Age-hardening of an Al–Li–Cu–Mg alloy (2091) processed by high-pressure torsion, Mater. Sci. Eng. A. 546 (2012)

82–89.

[32] M.H. Shaeri, M.T. Salehi, S.H. Seyyedein, M.R. Abutalebi, J.K. Park, Microstructure and mechanical properties of Al-7075 alloy processed by equal channel angular pressing combined with aging treatment, Mater. Des. 57 (2014) 250–257.

[33] M. Vaseghi, A.K. Taheri, S.I. Hong, H.S. Kim, Dynamic ageing and the mechanical response of Al–Mg–Si alloy through equal channel angular pressing, Mater. Des. 31 (2010) 4076–4082.

[34] K. Ohashi, T. Fujita, K. Kaneko, Z. Horita, T.G. Langdon, The aging characteristics of an Al–Ag alloy processed by equal-channel angular pressing, Mater. Sci. Eng. A. 437 (2006) 240–247.

[35] J.K. Kim, H.G. Jeong, S.I. Hong, Y.S. Kim, W.J. Kim, Effect of aging treatment on heavily deformed microstructure of a 6061 aluminum alloy after equal channel angular pressing, Scr. Mater. 45 (2001) 901–907.

[36] Z. Horita, K. Ohashi, T. Fujita, K. Kaneko, T.G. Langdon, Achieving high strength and high ductility in precipitation-hardened alloys, Adv. Mater. 17 (2005) 1599–1602.

[37] G. Sha, K. Tugcu, X.Z. Liao, P.W. Trimby, My. Murashkin, R.Z. Valiev, S.P. Ringer, Strength, grain refinement and solute nanostructures of an Al–Mg–Si alloy (AA6060) processed by high-pressure torsion, Acta Mater. 63 (2014) 169–179.

[38] A. Loucif, R.B. Figueiredo, M. Kawasaki, T. Baudin, F. Brisset, R. Chemam, T.G. Langdon, Effect of aging on microstructural development in an Al–Mg–Si alloy processed by high-pressure torsion, J. Mater. Sci. 47 (2012) 7815–7820.

[39] S. Wernick, R. Pinner, P.G. Sheasby, The surface treatment and finishing of aluminum and its alloys, 5th ed., ASM international Materials Park, 1992.

[40] J.R. Davis, Aluminum and aluminum alloys, ASM international, 1993.

[41] I. Polmear, 3 - Wrought aluminium alloys in Light Alloys, 4th ed., Butterworth-Heinemann, 2005.

[42] I. Polmear, 4 - Cast aluminium alloys in Light Alloys, 4th ed., Butterworth-Heinemann, 2005.

[43] J. Hirsch, B. Skrotzki, G. Gottstein, Aluminium alloys: the physical and mechanical properties, John Wiley & Sons, 2008.

[44] I. Polmear, Light alloys: from traditional alloys to nanocrystals, Elsevier, 2005.

[45] J. Hirsch, Aluminium sheet fabrication and processing, in: Fundam. Alum. Metall., Elsevier, 2011: pp. 719–746.

[46] E.J. Lavernia, T.S. Srivatsan, F.A. Mohamed, Strength, deformation, fracture behaviour and ductility of aluminium-lithium alloys, J. Mater. Sci. 25 (1990) 1137–1158.

[47] K. K, H. T, S. T, Effect of lithium and copper contents on the mechanical properties of Al–Cu–Li alloys Proceedings of the 4th International Conference on Aluminum Alloys: Their Physical and Mechanical Properties., in: 1994: pp. 297–304.

[48] K.S. Kumar, F.H. Heubaum, The effect of Li content on the natural aging response of Al-Cu-Li-Mg-Ag-Zr alloys, Acta Mater. 45 (1997) 2317–2327.

[49] R.K. Gupta, N. Nayan, G. Nagasireesha, S.C. Sharma, Development and characterization of Al–Li alloys, Mater. Sci. Eng. A. 420 (2006) 228–234.

[50] T.S. Srivatsan, E.J. Lavernia, N.E. Prasad, V. V Kutumbarao, Aluminum-Lithium Alloys: Chapter 10. Quasi-Static Strength, Deformation, and Fracture Behavior of Aluminum–Lithium Alloys, Elsevier Inc. Chapters, 2013.

[51] N. Jiang, G. Xiang, Z.-Q. Zheng, Microstructure evolution of aluminum-lithium alloy 2195 undergoing commercial production, Trans. Nonferrous Met. Soc. China. 20 (2010) 740–745.

[52] N.E. Prasad, T.R. Ramachandran, Aluminum-Lithium Alloys: Chapter 3. Phase Diagrams and Phase Reactions in Al–Li Alloys, Butterworth-Heinemann, 2013.

[53] Z. Chen, S. Li, Reinterpretation of precipitation behavior in an aged AlMgCu alloy, J. Mater. Sci. 49 (2014) 7659–7668.

[54] B. Gault, F. De Geuser, L. Bourgeois, B.M. Gabble, S.P. Ringer, B.C. Muddle, Atom probe tomography and transmission electron microscopy characterisation of precipitation in an Al–Cu–Li–Mg–Ag alloy, Ultramicroscopy. 111 (2011) 683–689.

[55] M. Song, D. Xiao, F. Zhang, Effect of Ce on the thermal stability of the Ω phase in an Al-Cu-Mg-Ag alloy, Rare Met. 28 (2009) 156–159.

[56] R. Yoshimura, T.J. Konno, E. Abe, K. Hiraga, Transmission electron microscopy study of the evolution of precipitates in aged Al–Li–Cu alloys: the θ′ and T1 phases, Acta Mater. 51 (2003) 4251–4266.

[57] X. Xiong, M. Weyland, Microstructural characterization of an Al-Li-Mg-Cu alloy by correlative electron tomography and atom probe tomography, Microsc. Microanal. 20 (2014) 1022–1028.

[58] B.M. Gable, A.A. Csontos, E.A. Starke Jr, A quench sensitivity study on the novel Al–Li–Cu–X alloy AF/C 458, J. Light Met. 2 (2002) 65–75.

[59] J.M. Silcock, The structural ageing characteristics of aluminium-copper-lithium alloys, J. Inst. Met. 88 (1960).

[60] C.-S. Tsao, C.-Y. Chen, T.-Y. Kuo, T.-L. Lin, M.-S. Yu, Size distribution and coarsening kinetics of δ′ precipitates in Al–Li alloys considering temperature and concentration dependence, Mater. Sci. Eng. A. 363 (2003) 228–233.

[61] B. Noble, S.J. Harris, K. Dinsdale, The elastic modulus of aluminium-lithium alloys, J. Mater. Sci. 17 (1982) 461–468.

[62] M.J. Starink, P. Wang, I. Sinclair, P.J. Gregson, Microstrucure and strengthening of Al–Li–Cu–Mg alloys and MMCs: II. Modelling of yield strength, Acta Mater. 47 (1999) 3855–3868.

[63] Y. Lin, Z. Zheng, S. Li, X. Kong, Y. Han, Microstructures and properties of 2099 Al-Li alloy, Mater. Charact. 84 (2013) 88–99. https://doi.org/https://doi.org/10.1016/j.matchar.2013.07.015.

[64] N. Gao, M.J. Starink, L. Davin, A. Cerezo, S.C. Wang, P.J. Gregson, Microstructure and precipitation in Al–Li–Cu–Mg–(Mn, Zr) alloys, Mater. Sci. Technol. 21 (2005) 1010–1018.

[65] Z. Chen, K. Zhao, L. Fan, Combinative hardening effects of precipitation in a commercial aged Al–Cu–Li–X alloy, Mater. Sci. Eng. A. 588 (2013) 59–64.

[66] A.K. Vasudevan, R.D. Doherty, Aluminum Alloys--Contemporary Research and Applications: Contemporary Research and Applications, Elsevier, 2012.

[67] B. Decreus, A. Deschamps, F. De Geuser, P. Donnadieu, C. Sigli, M. Weyland, The influence of Cu/Li ratio on precipitation in Al–Cu–Li–x alloys, Acta Mater. 61 (2013) 2207–2218.

[68] A. Abd El-Aty, Y. Xu, X. Guo, S.-H. Zhang, Y. Ma, D. Chen, Strengthening mechanisms, deformation behavior, and anisotropic mechanical properties of Al-Li alloys: A review, J. Adv. Res. 10 (2018) 49–67.

[69] X. Chen, X. Ma, H. Xi, G. Zhao, Y. Wang, X. Xu, Effects of heat treatment on the microstructure and mechanical properties of extruded 2196 Al-Cu-Li alloy, Mater. Des. 192 (2020) 108746. https://doi.org/https://doi.org/10.1016/j.matdes.2020.108746.

[70] P. Donnadieu, Y. Shao, F. De Geuser, G.A. Botton, S. Lazar, M. Cheynet, M. De Boissieu, A. Deschamps, Atomic structure of T1 precipitates in Al–Li–Cu alloys revisited with HAADF-STEM imaging and small-angle X-ray scattering, Acta Mater. 59 (2011) 462–472.

[71] H. Li, Y. Tang, Z. Zeng, Z. Zheng, F. Zheng, Effect of ageing time on strength and microstructures of an Al–Cu–Li–Zn–Mg–Mn–Zr alloy, Mater. Sci. Eng. A. 498 (2008) 314–320.

[72] Z.M. Wang, R.N. Shenoy, Microstructural characterization of aluminum-lithium alloys 1460 and 2195, National Aeronautics and Space Administration, Langley Research Center, 1998.

[73] B.M. Gable, A.W. Zhu, A.A. Csontos, E.A. Starke Jr, The role of plastic deformation on the competitive microstructural evolution and mechanical properties of a novel Al–Li–Cu–X alloy, J. Light Met. 1 (2001) 1–14.

[74] A.K. Khan, J.S. Robinson, Effect of cold compression on precipitation and conductivityof an Al–Li–Cu alloy, J. Microsc. 232 (2008) 534–538.

[75] G. Itoh, Q. Cui, M. Kanno, Effects of a small addition of magnesium and silver on the precipitation of T1 phase in an Al-4% Cu-1.1%Li-0.2%Zr alloy, Mater. Sci. Eng. A. 211 (1996) 128–137.

[76] S.C. Wang, M.J. Starink, Precipitates and intermetallic phases in precipitation hardening Al–Cu–Mg–(Li) based alloys, Int. Mater. Rev. 50 (2005) 193–215. https://doi.org/10.1179/174328005X14357.

[77] M.J. Styles, C.R. Hutchinson, Y. Chen, A. Deschamps, T.J. Bastow, The coexistence of two S (Al2CuMg) phases in Al–Cu–Mg alloys, Acta Mater. 60 (2012) 6940–6951. https://doi.org/https://doi.org/10.1016/j.actamat.2012.08.044.

[78] K. Lv, C. Zhu, J. Zheng, X. Wang, B. Chen, Precipitation of T1 phase in 2198 Al–Li alloy studied by atomic-resolution HAADF-STEM, J. Mater. Res. 34 (2019) 3535–3544. https://doi.org/10.1557/jmr.2019.136.

[79] N. Ryum, Precipitation and recrystallization in an A1-0.5 WT.% Zr-alloy, Acta Metall. 17 (1969) 269–278.

[80] F.W. Gayle, J.B. Vander Sande, "Composite" precipitates in an Al-Li-Zr alloy, Scr. Metall. 18 (1984) 473–478.

[81] P.J. Gregson, H.M. Flower, δ′ precipitation in Al-Li-Mg-Cu-Zr alloys, J. Mater. Sci. Lett. 3 (1984) 829–834.

[82] J.M. Galbraith, M.H. Tosten, P.R. Howell, On the nucleation of θ′ and T 1 on Al 3 Zr precipitates in Al-Li-Cu-Zr alloys, J. Mater. Sci. 22 (1987) 27–36.

[83] K.M. Knowles, W.M. Stobbs, The structure of {111} age-hardening precipitates in Al–Cu–Mg–Ag alloys, Acta Crystallogr. Sect. B Struct. Sci. 44 (1988) 207–227.

[84] S.C. Wang, M.J. Starink, N. Gao, Precipitation hardening in Al–Cu–Mg alloys revisited, Scr. Mater. 54 (2006) 287–291.

[85] A. Garg, J.M. Howe, Nucleation and growth of Ω phase in Al-4.0 Cu-0.5 Mg-0.5 Ag alloy—An in situ hot-stage TEM study, Acta Metall. Mater. 39 (1991) 1925–1937.

[86] A. Garg, Y.C. Chang, J.M. Howe, Precipitation of the Ω phase in an Al-4.0 Cu-0.5 Mg alloy, Scr. Metall. Mater. 24 (1990) 677–680.

[87] M.P. Moody, L.T. Stephenson, P. V Liddicoat, S.P. Ringer, Contingency table techniques for three dimensional atom probe tomography, Microsc. Res. Tech. 70 (2007) 258–268.

[88] T. Honma, S. Yanagita, K. Hono, Y. Nagai, M. Hasegawa, Coincidence Doppler broadening and 3DAP study of the pre-precipitation stage of an Al–Li–Cu–Mg–Ag alloy, Acta Mater. 52 (2004) 1997–2003.

[89] R.K.W. Marceau, G. Sha, R. Ferragut, A. Dupasquier, S.P. Ringer, Solute clustering in Al–Cu–Mg alloys during the early stages of elevated temperature ageing, Acta Mater. 58 (2010) 4923–4939.

[90] M. Murayama, K. Hono, Pre-precipitate clusters and precipitation processes in Al–Mg–Si alloys, Acta Mater. 47 (1999) 1537–1548.

[91] G. Sha, A. Cerezo, Characterization of precipitates in an aged 7xxx series Al alloy, Surf. Interface Anal. An Int. J. Devoted to Dev. Appl. Tech. Anal. Surfaces, Interfaces Thin Film. 36 (2004) 564–568.

[92] J. Lamb, J. Sanders, The Effect of Cu on the Decomposition of Al-Zn-Mg-(Cu) Alloys, J Mater. Sci Eng. 6 (2017) 404. https://doi.org/10.4172/2169-0022.1000404.

[93] G. Sha, A. Cerezo, Early-stage precipitation in Al–Zn–Mg–Cu alloy (7050), Acta Mater. 52 (2004) 4503–4516.

[94] L.K. Berg, J. Gjønnes, V. x Hansen, X.Z. Li, M. Knutson-Wedel, D. Schryvers, L.R. Wallenberg, GP-zones in Al–Zn–Mg alloys and their role in artificial aging, Acta Mater. 49 (2001) 3443–3451.

[95] A.K. Mukhopadhyay, Guinier-Preston zones in a high-purity Al-Zn-Mg alloy, Philos. Mag. Lett. 70 (1994) 135–140.

[96] H. Löffler, I. Kovács, J. Lendvai, Decomposition processes in Al-Zn-Mg alloys, J. Mater. Sci. 18 (1983) 2215–2240.

[97] V. Hansen, O.B. Karlsen, Y. Langsrud, J. Gjønnes, Precipitates, zones and transitions during aging of Al-Zn-Mg-Zr 7000 series alloy, Mater. Sci. Technol. 20 (2004) 185–193.

[98] P.N.T. Unwin, R.B. Nicholson, The nucleation and initial stages of growth of grain boundary precipitates in Al-Zn-Mg and Al-Mg alloys, Acta Metall. 17 (1969) 1379–1393.

[99] J.D. Embury, R.B. Nicholson, The nucleation of precipitates: the system Al-Zn-Mg, Acta Metall. 13 (1965) 403–417.

[100] J. Chen, L. Zhen, S. Yang, W. Shao, S. Dai, Investigation of precipitation behavior and related hardening in AA 7055 aluminum alloy, Mater. Sci. Eng. A. 500 (2009) 34–42.

[101] X. Fan, D. Jiang, Q. Meng, Z. Lai, X. Zhang, Characterization of precipitation microstructure and properties of 7150 aluminium alloy, Mater. Sci. Eng. A. 427 (2006) 130–135.

[102] L.F. Mondolfo, Aluminum alloys: structure and properties, Elsevier, 2013.

[103] J.T. Staley, Aging kinetics of aluminum alloy 7050, Metall. Trans. 5 (1974) 929–932.

[104] N.Q. Chinh, J. Lendvai, D.H. Ping, K. Hono, The effect of Cu on mechanical and precipitation properties of Al–Zn–Mg alloys, J. Alloys Compd. 378 (2004) 52–60.

[105] A. Association, Aluminum: properties and physical metallurgy, ASM international, 1984.

[106] K.-I. Hirano, R.P. Agarwala, M. Cohen, Diffusion of iron, nickel and cobalt in aluminum, Acta Metall. 10 (1962) 857–863.

[107] M.J. Starink, S.C. Wang, A model for the yield strength of overaged Al–Zn–Mg–Cu alloys, Acta Mater. 51 (2003) 5131–5150.

[108] A. Dupasquier, R. Ferragut, M.M. Iglesias, M. Massazza, G. Riontino, P. Mengucci, G. Barucca, C.E. Macchi, A. Somoza, Hardening nanostructures in an AlZnMg alloy, Philos. Mag. 87 (2007) 3297–3323.

[109] W.J. Poole, J.A. Sæter, S. Skjervold, A model for predicting the effect of deformation after solution treatment on the subsequent artificial aging behavior of AA7030 and AA7108 alloys, Metall. Mater. Trans. A. 31 (2000) 2327–2338.

[110] A. Deschamps, F. Livet, Y. Brechet, Influence of predeformation on ageing in an Al–Zn–Mg alloy—I. Microstructure evolution and mechanical properties, Acta Mater. 47 (1998) 281–292.

[111] A.J. Ardell, On the coarsening of grain boundary precipitates, Acta Metall. 20 (1972) 601–609.

[112] J.J. Hoyt, On the coarsening of precipitates located on grain boundaries and dislocations, Acta Metall. Mater. 39 (1991) 2091–2098.

[113] A. Azushima, R. Kopp, A. Korhonen, D.-Y. Yang, F. Micari, G.D. Lahoti, P. Groche, J. Yanagimoto, N. Tsuji, A. Rosochowski, Severe plastic deformation (SPD) processes for metals, CIRP Ann. 57 (2008) 716–735.

[114] N. Tsuji, Y. Saito, S. Lee, Y. Minamino, ARB (Accumulative Roll-Bonding) and other new techniques to produce bulk ultrafine grained materials, Adv. Eng. Mater. 5 (2003) 338–344.

[115] R.Z. Valiev, T.G. Langdon, Principles of equal-channel angular pressing as a processing tool for grain refinement, Prog. Mater. Sci. 51 (2006) 881–981.

[116] N. Tsuji, Research Trend on Ultrafine Grained Light Metals (From a Viewpoint of Physical Metallurgy), Mater. Japan. 43 (2004) 405–410.

[117] M. Richert, Q. Liu, N. Hansen, Microstructural evolution over a large strain range in aluminium deformed by cyclic-extrusion–compression, Mater. Sci. Eng. A. 260 (1999) 275–283.

[118] J.Y. Huang, Y.T. Zhu, H. Jiang, T.C. Lowe, Microstructures and dislocation configurations in nanostructured Cu processed by repetitive corrugation and straightening, Acta Mater. 49 (2001) 1497–1505.

[119] A.P. Zhilyaev, G. V Nurislamova, B.-K. Kim, M.D. Baró, J.A. Szpunar, T.G. Langdon, Experimental parameters influencing grain refinement and microstructural evolution during high-pressure torsion, Acta Mater. 51 (2003) 753–765.

[120] T.G. Langdon, Twenty-five years of ultrafine-grained materials: Achieving exceptional properties through grain refinement, Acta Mater. 61 (2013) 7035–7059.

[121] G. Sakai, K. Nakamura, Z. Horita, T.G. Langdon, Developing high-pressure torsion for use with bulk samples, Mater. Sci. Eng. A. 406 (2005) 268–273.

[122] H. Jiang, Y.T. Zhu, D.P. Butt, I. V Alexandrov, T.C. Lowe, Microstructural evolution, microhardness and thermal stability of HPT-processed Cu, Mater. Sci. Eng. A. 290 (2000) 128–138.

[123] C. Xu, Z. Horita, T.G. Langdon, The evolution of homogeneity in processing by high-pressure torsion, Acta Mater. 55 (2007) 203–212.

[124] A.P. Zhilyaev, S. Lee, G. V Nurislamova, R.Z. Valiev, T.G. Langdon, Microhardness and microstructural evolution in pure nickel during high-pressure torsion, Scr. Mater. 44 (2001) 2753–2758.

[125] Z. Horita, Y. Tang, T. Masuda, Y. Takizawa, Severe Plastic Deformation under High Pressure: Upsizing Sample Dimensions, Mater. Trans. 61 (2020). https://doi.org/10.2320/matertrans.mt-m2020074.

[126] K. Edalati, Z. Horita, Scaling-Up of High Pressure Torsion Using Ring Shape, Mater. Trans. 50 (2009) 92–95. https://doi.org/10.2320/matertrans.MD200822.

[127] Y. Harai, Y. Ito, Z. Horita, High-pressure torsion using ring specimens, Scr. Mater. 58 (2008) 469–472. https://doi.org/https://doi.org/10.1016/j.scriptamat.2007.10.037.

[128] Y. Ito, Y. Harai, T. Fujioka, K. Edalati, Z. Horita, Use of ring sample for high-pressure torsion and microstructural evolution with equivalent strain, Mater. Sci. Forum. 584-586 PART 1 (2008) 191–196. https://doi.org/10.4028/www.scientific.net/msf.584-586.191.

[129] K. Edalati, T. Fujioka, Z. Horita, Microstructure and mechanical properties of pure Cu processed by high-pressure torsion, Mater. Sci. Eng. A. 497 (2008) 168–173. https://doi.org/https://doi.org/10.1016/j.msea.2008.06.039.

[130] Y. Harai, K. Edalati, Z. Horita, T.G. Langdon, Using ring samples to evaluate the processing characteristics in high-pressure torsion, Acta Mater. 57 (2009) 1147–1153. https://doi.org/https://doi.org/10.1016/j.actamat.2008.10.046.

[131] P. Zhang, S.X. Li, Z.F. Zhang, General relationship between strength and hardness, Mater. Sci. Eng. A. 529 (2011) 62–73.

[132] C.A. Schuh, T.G. Nieh, T. Yamasaki, Hall–Petch breakdown manifested in abrasive wear resistance of nanocrystalline nickel, Scr. Mater. 46 (2002) 735–740.

[133] A. Sato, M. Meshii, Solid solution softening and solid solution hardening, Acta Metall. 21 (1973) 753–768. https://doi.org/https://doi.org/10.1016/0001-6160(73)90040-0.

[134] Y.H. Zhao, X.Z. Liao, Z. Jin, R.Z. Valiev, Y.T. Zhu, Microstructures and mechanical properties of ultrafine grained 7075 Al alloy processed by ECAP and their evolutions during annealing, Acta Mater. 52 (2004) 4589–4599.

[135] S. Lee, Z. Horita, Enhancement of strength and ductility of Al-Ag alloys processed by high-pressure torsion and aging, Metall. Mater. Trans. A. 44 (2013) 3221–3231.

[136] K. Edalati, D. Akama, A. Nishio, S. Lee, Y. Yonenaga, J.M. Cubero-Sesin, Z. Horita, Influence of dislocation–solute atom interactions and stacking fault energy on grain size of single-phase alloys after severe plastic deformation using high-pressure torsion, Acta Mater. 69 (2014) 68–77.

[137] R. Pippan, S. Scheriau, A. Taylor, M. Hafok, A. Hohenwarter, A. Bachmaier, Saturation of fragmentation during severe plastic deformation, Annu. Rev. Mater. Res. 40 (2010) 319–343.

[138] M. Murayama, Z. Horita, K. Hono, Microstructure of two-phase Al–1.7 at% Cu alloy deformed by equal-channel angular pressing, Acta Mater. 49 (2001) 21–29.

[139] C. Xu, M. Furukawa, Z. Horita, T.G. Langdon, Influence of ECAP on precipitate distributions in a spray-cast aluminum alloy, Acta Mater. 53 (2005) 749–758.

[140] I. Gutierrez-Urrutia, M.A. Munoz-Morris, D.G. Morris, The effect of coarse second-phase particles and fine precipitates on microstructure refinement and mechanical properties of severely deformed Al alloy, Mater. Sci. Eng. A. 394 (2005) 399–410.

[141] G. Sha, Y.B. Wang, X.Z. Liao, Z.C. Duan, S.P. Ringer, T.G. Langdon, Influence of equal-channel angular pressing on precipitation in an Al–Zn–Mg–Cu alloy, Acta Mater. 57 (2009) 3123–3132.

[142] M. Cai, D.P. Field, G.W. Lorimer, A systematic comparison of static and dynamic ageing of two Al–Mg–Si alloys, Mater. Sci. Eng. A. 373 (2004) 65–71.

[143] H.J. Roven, M. Liu, J.C. Werenskiold, Dynamic precipitation during severe plastic deformation of an Al–Mg–Si aluminium alloy, Mater. Sci. Eng. A. 483 (2008) 54–58.

[144] G. Sha, J.H. Li, W. Xu, K. Xia, W.Q. Jie, S.P. Ringer, Hardening and microstructural reactions in high-temperature equal-channel angular pressed Mg–Nd–Gd–Zn–Zr alloy, Mater. Sci. Eng. A. 527 (2010) 5092–5099.

[145] K. Tugcu, G. Sha, X.Z. Liao, P. Trimby, J.H. Xia, M.Y. Murashkin, Y. Xie, R.Z. Valiev, S.P. Ringer, Enhanced grain refinement of an Al–Mg–Si alloy by high-pressure torsion processing at 100 C, Mater. Sci. Eng. A. 552 (2012) 415–418.

[146] J. Weissmüller, Alloy effects in nanostructures, Nanostructured Mater. 3 (1993) 261–272.

[147] R. Kirchheim, Grain coarsening inhibited by solute segregation, Acta Mater. 50 (2002) 413–419.

[148] Z.C. Duan, X.Z. Liao, M. Kawasaki, R.B. Figueiredo, T.G. Langdon, Influence of high-pressure torsion on microstructural evolution in an Al–Zn–Mg–Cu alloy, J. Mater. Sci. 45 (2010) 4621–4630.

[149] S. Sabbaghianrad, M. Kawasaki, T.G. Langdon, Microstructural evolution and the mechanical properties of an aluminum alloy processed by high-pressure torsion, J. Mater. Sci. 47 (2012) 7789–7795.

[150] Z. Zhu, J. Han, C. Gao, M. Liu, J. Song, Z. Wang, H. Li, Microstructures and mechanical properties of Al-Li 2198-T8 alloys processed by two different severe plastic deformation methods: A comparative study, Mater. Sci. Eng. A. 681 (2017) 65–73.

[151] N. Hansen, R.F. Mehl, New discoveries in deformed metals, Metall. Mater. Trans. A. 32 (2001) 2917–2935.

[152] Y. Miyajima, S. Okubo, H. Abe, H. Okumura, T. Fujii, S. Onaka, M. Kato, Dislocation density of pure copper processed by accumulative roll bonding and equal-channel angular pressing, Mater. Charact. 104 (2015) 101–106.

[153] N. Hansen, Hall–Petch relation and boundary strengthening, Scr. Mater. 51 (2004) 801–806.

[154] M.A. Munoz-Morris, D.G. Morris, Severe plastic deformation processing of Al–Cu–Li alloy for enhancing strength while maintaining ductility, Scr. Mater. 63 (2010) 304–307.

[155] X. Sauvage, N. Enikeev, R. Valiev, Y. Nasedkina, M. Murashkin, Atomic-scale analysis of the segregation and precipitation mechanisms in a severely deformed Al–Mg alloy, Acta Mater. 72 (2014) 125–136.

[156] W.T. Sun, X.G. Qiao, M.Y. Zheng, C. Xu, S. Kamado, X.J. Zhao, H.W. Chen, N. Gao, M.J. Starink, Altered ageing behaviour of a nanostructured Mg-8.2 Gd-3.8 Y-1.0 Zn-0.4 Zr alloy processed by high pressure torsion, Acta Mater. 151 (2018) 260–270.

[157] J. Zhang, N. Gao, M.J. Starink, Al–Mg–Cu based alloys and pure Al processed by high pressure torsion: The influence of alloying additions on strengthening, Mater. Sci. Eng. A. 527 (2010) 3472–3479.

[158] J. Čížek, M. Janeček, T. Vlasák, B. Smola, O. Melikhova, D. SV, The development of vacancies during severe plastic deformation, Mater. Trans. 60 (2019) 1533–1542.

[159] A.A. Zisman, V. V Rybin, S. Van Boxel, M. Seefeldt, B. Verlinden, Equal channel angular drawing of aluminium sheet, Mater. Sci. Eng. A. 427 (2006) 123–129.

[160] C. Xu, M. Furukawa, Z. Horita, T.G. Langdon, The evolution of homogeneity and grain refinement during equal-channel angular pressing: A model for grain refinement in ECAP, Mater. Sci. Eng. A. 398 (2005) 66–76.

[161] T.G. Langdon, The principles of grain refinement in equal-channel angular pressing, Mater. Sci. Eng. A. 462 (2007) 3–11.

[162] S.C. Baik, Y. Estrin, H.S. Kim, R.J. Hellmig, Dislocation density-based modeling of deformation behavior of aluminium under equal channel angular pressing, Mater. Sci. Eng. A. 351 (2003) 86–97.

[163] X.G. Qiao, N. Gao, M.J. Starink, A model of grain refinement and strengthening of Al alloys due to cold severe plastic deformation, Philos. Mag. 92 (2012) 446–470.

[164] R.Z. Valiev, Y. V Ivanisenko, E.F. Rauch, B. Baudelet, Structure and deformaton behaviour of Armco iron subjected to severe plastic deformation, Acta Mater. 44 (1996) 4705–4712.

[165] J.G. Sevillano, E. Aernoudt, Low energy dislocation structures in highly deformed materials, Mater. Sci. Eng. 86 (1987) 35–51.

[166] A.D. Rollett, U.F. Kocks, A review of the stages of work hardening, in: Solid State Phenom., Trans Tech Publ, 1993: pp. 1–18.

[167] J.W. Christian, S. Mahajan, Deformation twinning, Prog. Mater. Sci. 39 (1995) 1–157.

[168] A. Kelly, R. Nicholson, Strengthening methods in crystals, Elsevier publishing company, 1971.

[169] E. Nes, Recovery revisited, Acta Metall. Mater. 43 (1995) 2189–2207.

[170] E. Nes, B. Holmedal, E. Evangelista, K. Marthinsen, Modelling grain boundary strengthening in ultra-fine grained aluminum alloys, Mater. Sci. Eng. A. 410 (2005) 178–182.

[171] X. Huang, N. Kamikawa, N. Hansen, Strengthening mechanisms in nanostructured aluminum, Mater. Sci. Eng. A. 483 (2008) 102–104.

[172] M.J. Starink, X.G. Qiao, J. Zhang, N. Gao, Predicting grain refinement by cold severe plastic deformation in alloys using volume averaged dislocation generation, Acta Mater. 57 (2009) 5796–5811.

[173] S.H. Lee, Y. Saito, T. Sakai, H. Utsunomiya, Microstructures and mechanical properties of 6061 aluminum alloy processed by accumulative roll-bonding, Mater. Sci. Eng. A. 325 (2002) 228–235.

[174] B. Cherukuri, T.S. Nedkova, R. Srinivasan, A comparison of the properties of SPD-processed AA-6061 by equal-channel angular pressing, multi-axial compressions/forgings and accumulative roll bonding, Mater. Sci. Eng. A. 410 (2005) 394–397.

[175] S.C. Wang, Z. Zhu, M.J. Starink, Estimation of dislocation densities in cold rolled Al-Mg-Cu-Mn alloys by combination of yield strength data, EBSD and strength models, J. Microsc. 217 (2005) 174–178.

[176] C. Qiao, Z. Chen, Y. Zeng, L. Xu, Optimal Strategy-Proof Wireless Resources Auction, in: 2011 Int. Conf. Netw. Comput. Inf. Secur., IEEE, 2011: pp. 446–450.

[177] J. Zhang, N. Gao, M.J. Starink, Microstructure development and hardening during high pressure torsion of commercially pure aluminium: Strain reversal experiments and a dislocation based model, Mater. Sci. Eng. A. 528 (2011) 2581–2591.

[178] M.J. Starink, A. Deschamps, S.C. Wang, The strength of friction stir welded and friction stir processed aluminium alloys, Scr. Mater. 58 (2008) 377–382.

[179] D.J. Dunstan, A.J. Bushby, The scaling exponent in the size effect of small scale plastic deformation, Int. J. Plast. 40 (2013) 152–162.

[180] D.J. Dunstan, A.J. Bushby, Grain size dependence of the strength of metals: The Hall–Petch effect does not scale as the inverse square root of grain size, Int. J. Plast. 53 (2014) 56–65.

[181] S. Korte, W.J. Clegg, Discussion of the dependence of the effect of size on the yield stress in hard materials studied by microcompression of MgO, Philos. Mag. 91 (2011) 1150–1162.

[182] E.O. Hall, The deformation and ageing of mild steel: III discussion of results, Proc. Phys. Soc. Sect. B. 64 (1951) 747.

[183] Brooks H, Theory of internal boundaries, in: Metalinterfaces, AMS, 1952: pp. 20–64.

[184] H. Gao, Y. Huang, W.D. Nix, J.W. Hutchinson, Mechanism-based strain gradient plasticity—I. Theory, J. Mech. Phys. Solids. 47 (1999) 1239–1263.

[185] M.J. Starink, N. Gao, L. Davin, J. Yan, A. Cerezo, Room temperature precipitation in quenched Al–Cu–Mg alloys: a model for the reaction kinetics and yield strength development, Philos. Mag. 85 (2005) 1395–1417.

[186] L. Lutterotti, S. Gialanella, X-ray diffraction characterization of heavily deformed metallic specimens, Acta Mater. 46 (1998) 101–110.

[187] Z. Zhang, F. Zhou, E.J. Lavernia, On the analysis of grain size in bulk nanocrystalline materials via X-ray diffraction, Metall. Mater. Trans. A. 34 (2003) 1349–1355.

[188] P. Scardi, M. Leoni, R. Delhez, Line broadening analysis using integral breadth methods: a critical review, J. Appl. Crystallogr. 37 (2004) 381–390.

[189] G. Madhu, V.C. Bose, K. Maniammal, A.S.A. Raj, V. Biju, Microstrain in nanostructured nickel oxide studied using isotropic and anisotropic models, Phys. B Condens. Matter. 421 (2013) 87–91.

[190] K. Maniammal, G. Madhu, V. Biju, X-ray diffraction line profile analysis of nanostructured nickel oxide: shape factor and convolution of crystallite size and microstrain contributions, Phys. E Low-Dimensional Syst. Nanostructures. 85 (2017) 214–222.

[191] T. Ungár, L. Balogh, G. Ribárik, Defect-related physical-profile-based X-ray and neutron line profile analysis, Metall. Mater. Trans. A. 41 (2010) 1202–1209.

[192] K. Kapoor, D. Lahiri, I.S. Batra, S.V.R. Rao, T. Sanyal, X-ray diffraction line profile analysis for defect study in Cu-1 wt.% Cr-0.1 wt.% Zr alloy, Mater. Charact. 54 (2005) 131–140.

[193] D. Rafaja, V. Klemm, G. Schreiber, M. Knapp, R. Kužel, Interference phenomena observed by X-ray diffraction in nanocrystalline thin films, J. Appl. Crystallogr. 37 (2004) 613–620.

[194] S. Sivasankaran, K. Sivaprasad, R. Narayanasamy, P. V Satyanarayana, X-ray peak broadening analysis of AA 6061100− x− x wt.% Al2O3 nanocomposite prepared by mechanical alloying, Mater. Charact. 62 (2011) 661–672.

[195] B.E. Warren, X-ray studies of deformed metals, Progr. Met. Phys. 8 (1959) 147.

[196] G.K. Williamson, W.H. Hall, X-ray line broadening from filed aluminium and wolfram, Acta Metall. 1 (1953) 22–31.

[197] H.M. Rietveld, A profile refinement method for nuclear and magnetic structures, J. Appl. Crystallogr. 2 (1969) 65–71.

[198] P. Thompson, D.E. Cox, J.B. Hastings, Rietveld refinement of Debye–Scherrer synchrotron X-ray data from Al2O3, J. Appl. Crystallogr. 20 (1987) 79–83.

[199] R.A. Young, D.B. Wiles, Profile shape functions in Rietveld refinements, J. Appl. Crystallogr. 15 (1982) 430–438.

[200] O. Novelo-Peralta, G. González, G.A. Lara-Rodríguez, Characterization of precipitation in Al–Mg–Cu alloys by X-ray diffraction peak broadening analysis, Mater. Charact. 59 (2008) 773–780.

[201] J. Ghosh, S.K. Chattopadhayay, A.K. Meikap, S.K. Chatterjee, Microstructure characterization of titanium-base aluminium alloys by X-ray diffraction using Warren–Averbach and Rietveld method, J. Alloys Compd. 453 (2008) 131–137.

[202] G. Höhne, W.F. Hemminger, H.-J. Flammersheim, Differential scanning calorimetry, Springer Science & Business Media, 2013.

[203] M.J. Starink, Analysis of aluminium based alloys by calorimetry: quantitative analysis of reactions and reaction kinetics, Int. Mater. Rev. 49 (2004) 191–226.

[204] C. Michaelsen, K. Barmak, T.P. Weihs, Investigating the thermodynamics and kinetics of thin film reactions by differential scanning calorimetry, J. PHYSICS-LONDON-D Appl. Phys. 30 (1997) 3167–3186.

[205] O. Koshy, L. Subramanian, S. Thomas, Differential Scanning Calorimetry in Nanoscience and Nanotechnology, in: Therm. Rheol. Meas. Tech. Nanomater. Charact., Elsevier, 2017: pp. 109–122.

[206] M.E. Brown, P.K. Gallagher, Handbook of Thermal Analysis and Calorimetry: Applications to inorganic and miscellaneous materials, Elsevier, 2003.

[207] C. Schick, D. Lexa, L. Leibowitz, Differential scanning calorimetry and differential thermal analysis, Charact. Mater. (2002) 1–13.

[208] T. Hatakeyama, F.X. Quinn, Thermal analysis: fundamentals and applications to polymer science, 2nd ed., John Wiley & Sons Ltd, 1999.

[209] D.A. Skoog, D.M. West, F.J. Holler, S.R. Crouch, Fundamentals of analytical chemistry, Cengage learning, 2013.

[210] N. Gao, M.J. Starink, T.G. Langdon, Using differential scanning calorimetry as an analytical tool for ultrafine grained metals processed by severe plastic

deformation, Mater. Sci. Technol. 25 (2009) 687–698.

[211] G. Angella, P. Bassani, A. Tuissi, D. Ripamonti, M. Vedani, Microstructure evolution and aging kinetics of Al-Mg-Si and Al-Mg-Si-Sc alloys processed by ECAP, in: Mater. Sci. Forum, Trans Tech Publ, 2006: pp. 493–498.

[212] B. Mingler, O.B. Kulyasova, R.K. Islamgaliev, G. Korb, H.P. Karnthaler, M.J. Zehetbauer, DSC and TEM analysis of lattice defects governing the mechanical properties of an ECAP-processed magnesium alloy, J. Mater. Sci. 42 (2007) 1477–1482.

[213] Y. Zhao, J. Liu, T.D. Topping, E.J. Lavernia, Precipitation and aging phenomena in an ultrafine grained Al-Zn alloy by severe plastic deformation, J. Alloys Compd. 851 (2021) 156931.

[214] K.S. Ghosh, N. Gao, M.J. Starink, Characterisation of high pressure torsion processed 7150 Al–Zn–Mg–Cu alloy, Mater. Sci. Eng. A. 552 (2012) 164–171.

[215] E.A. Marquis, J.M. Hyde, Applications of atom-probe tomography to the characterisation of solute behaviours, Mater. Sci. Eng. R Reports. 69 (2010) 37–62.

[216] B. Gault, A brief overview of atom probe tomography research, Appl. Microsc. 46 (2016) 117–126.

[217] P. Bas, A. Bostel, B. Deconihout, D. Blavette, A general protocol for the reconstruction of 3D atom probe data, Appl. Surf. Sci. 87 (1995) 298–304.

[218] J.M. Hyde, A. Cerezo, R.P. Setna, P.J. Warren, G.D.W. Smith, Lateral and depth scale calibration of the position sensitive atom probe, Appl. Surf. Sci. 76 (1994) 382–391.

[219] P. Serre, R.B. Figueiredo, N. Gao, T.G. Langdon, Influence of strain rate on the characteristics of a magnesium alloy processed by high-pressure torsion, Mater. Sci. Eng. A. 528 (2011) 3601–3608.

[220] C.T. Wang, Tribological Behaviour of Ultrafine-Grained Alloys Formed by Severe Plastic Deformation, University of Southampton, 2013.

[221] L.B. McCusker, R.B. Von Dreele, D.E. Cox, D. Louër, P. Scardi, Rietveld refinement guidelines, J. Appl. Crystallogr. 32 (1999) 36–50.

[222] A. Akter, S. M., H. Rashed, Effect of ageing on the mechanical and electrical properties of Al-Zn-Mg-Cu alloy, in: 2016.

[223] B. Geetha, K. Ganesan, The effects of ageing temperature and time on mechanical properties of A356 aluminium cast alloy with red mud addition and treated by T6 heat treatment, Mater. Today Proc. 2 (2015) 1200–1209.

[224] B. AN, S. Ranganathan, Aging behaviour in copper bearing high strength low alloy steels, ISIJ Int. 44 (2004) 115–122.

[225] M. Khushaim, T. Boll, J. Seibert, F. Haider, T. Al-Kassab, Characterization of precipitation in Al-Li alloy AA2195 by means of atom probe tomography and

transmission electron microscopy, Adv. Condens. Matter Phys. (2015) 1–11.

[226] W.J. Kim, C.S. Chung, D.S. Ma, S.I. Hong, H.K. Kim, Optimization of strength and ductility of 2024 Al by equal channel angular pressing (ECAP) and post-ECAP aging, Scr. Mater. 49 (2003) 333–338.

[227] A.S.A.U.S. NA, Effects of the artificial-aging temperature and time on the mechanical properties and springback behavior of AA6061, Mater. Tehnol. 49 (2015) 487–493.

[228] Y. Li, T.G. Langdon, Creep behavior of an Al-6061 metal matrix composite reinforced with alumina particulates, Acta Mater. 45 (1997) 4797–4806.

[229] S.I. Hong, G.T. Gray III, Microstructure and microchemistry of an Al-Zn-Mg-Cu alloy matrix-20 vol.% SiC composite, Acta Metall. Mater. 40 (1992) 3299–3315.

[230] V. V Stolyarov, V. V Latysh, V.A. Shundalov, D.A. Salimonenko, R.K. Islamgaliev, R.Z. Valiev, Influence of severe plastic deformation on aging effect of Al-Zn-Mg-Cu-Zr alloy, Mater. Sci. Eng. A. 234 (1997) 339–342.

[231] A. Chen, Y. Peng, L. Zhang, G. Wu, Y. Li, Microstructural evolution and mechanical properties of cast Al-3Li-1.5 Cu-0.2 Zr alloy during heat treatment, Mater. Charact. 114 (2016) 234–242.

[232] R.E. Crooks, E.A. Starke, The Microstructure and tensile properties of a splat-quenched Al-Cu-Li-Mg-Zr alloy, Metall. Trans. A. 15 (1984) 1367–1377.

[233] X. Zhang, L. Zhang, G. Wu, W. Liu, C. Shi, J. Tao, J. Sun, Microstructural evolution and mechanical properties of cast Al-2Li-2Cu-0.5 Mg-0.2 Zr alloy during heat treatment, Mater. Charact. 132 (2017) 312–319.

[234] S.K. Moghanaki, M. Kazeminezhad, Effects of non-isothermal annealing on microstructure and mechanical properties of severely deformed 2024 aluminum alloy, Trans. Nonferrous Met. Soc. China. 27 (2017) 1–9.

[235] B. Noble, G.E. Thompson, Precipitation characteristics of aluminium-lithium alloys, Met. Sci. J. 5 (1971) 114–120.

[236] W. Huang, Z. Liu, M. Lin, X. Zhou, L. Zhao, A. Ning, S. Zeng, Reprecipitation behavior in Al–Cu binary alloy after severe plastic deformation-induced dissolution of θ′ particles, Mater. Sci. Eng. A. 546 (2012) 26–33.

[237] T.D. Shen, R.B. Schwarz, S. Feng, J.G. Swadener, J.Y. Huang, M. Tang, J. Zhang, S.C. Vogel, Y. Zhao, Effect of solute segregation on the strength of nanocrystalline alloys: Inverse Hall–Petch relation, Acta Mater. 55 (2007) 5007–5013.

[238] M.M. Abramova, N.A. Enikeev, R.Z. Valiev, A. Etienne, B. Radiguet, Y. Ivanisenko, X. Sauvage, Grain boundary segregation induced strengthening of an ultrafine-grained austenitic stainless steel, Mater. Lett. 136 (2014) 349–352. https://doi.org/https://doi.org/10.1016/j.matlet.2014.07.188.

[239] S.P. Ringer, K. Hono, Microstructural evolution and age hardening in aluminium

alloys: atom probe field-ion microscopy and transmission electron microscopy studies, Mater. Charact. 44 (2000) 101–131.

[240] G. Sha, R.K.W. Marceau, X. Gao, B.C. Muddle, S.P. Ringer, Nanostructure of aluminium alloy 2024: Segregation, clustering and precipitation processes, Acta Mater. 59 (2011) 1659–1670.

[241] S.P. Ringer, T. Sakurai, I.J. Polmear, Origins of hardening in aged Al-Gu-Mg-(Ag) alloys, Acta Mater. 45 (1997) 3731–3744.

[242] Z. Chen, J. Ren, Z. Yuan, S.P. Ringer, Enhanced strength-plasticity combination in an Al–Cu–Mg alloy–atomic scale microstructure regulation and strengthening mechanisms, Mater. Sci. Eng. A. 787 (2020) 139447.

[243] S. Bai, Z. Liu, X. Zhou, P. Xia, S. Zeng, Mg-controlled formation of Mg–Ag co-clusters in initial aged Al–Cu–Mg–Ag alloys, J. Alloys Compd. 602 (2014) 193–198.

[244] R.C. Picu, D. Zhang, Atomistic study of pipe diffusion in Al–Mg alloys, Acta Mater. 52 (2004) 161–171. https://doi.org/https://doi.org/10.1016/j.actamat.2003.09.002.

[245] R. Kirchheim, Reducing grain boundary, dislocation line and vacancy formation energies by solute segregation. I. Theoretical background, Acta Mater. 55 (2007) 5129–5138.

[246] J.W. Zhang, M.J. Starink, N. Gao, W.L. Zhou, Influence of Strain Reversals during High Pressure Torsion Process on Strengthening in Al-Cu-Mg (-Li) Alloy, in: Mater. Sci. Forum, Trans Tech Publ, 2011: pp. 809–814.

[247] E. Nembach, Precipitation hardening caused by a difference in shear modulus between particle and matrix, Phys. Status Solidi. 78 (1983) 571–581.

[248] P. Gomiero, Y. Brechet, F. Louchet, A. Tourabi, B. Wack, Microstructure and mechanical properties of a 2091 AlLi alloy—II. Mechanical properties: Yield stress and work hardening, Acta Metall. Mater. 40 (1992) 857–861.

[249] S.N. Naik, S.M. Walley, The Hall–Petch and inverse Hall–Petch relations and the hardness of nanocrystalline metals, J. Mater. Sci. 55 (2020) 2661–2681.

[250] I.F. Mohamed, Y. Yonenaga, S. Lee, K. Edalati, Z. Horita, Age hardening and thermal stability of Al–Cu alloy processed by high-pressure torsion, Mater. Sci. Eng. A. 627 (2015) 111–118.

[251] H.R. Shercliff, M.F. Ashby, A process model for age hardening of aluminium alloys—I. The model, Acta Metall. Mater. 38 (1990) 1789–1802.

[252] Y.-H. Zhao, X.-Z. Liao, S. Cheng, E. Ma, Y.T. Zhu, Simultaneously increasing the ductility and strength of nanostructured alloys, Adv. Mater. 18 (2006) 2280–2283.

[253] C.J. Smithells, Metals reference book, Elsevier, 2013.

[254] M.J. Starink, X. Cheng, S. Yang, Hardening of pure metals by high-pressure

torsion: a physically based model employing volume-averaged defect evolutions, Acta Mater. 61 (2013) 183–192.

[255] Ø. Ryen, B. Holmedal, O. Nijs, E. Nes, E. Sjölander, H.-E. Ekström, Strengthening mechanisms in solid solution aluminum alloys, Metall. Mater. Trans. A. 37 (2006) 1999–2006.

[256] M.J. Starink, P.J. Gregson, Hardness profiles of solution treated SiC p-reinforced Al-Li-Cu-Mg-Zr sheet, J. Mater. Sci. Lett. 14 (1995) 1767–1769.

[257] S.G. Chowdhury, A. Mondal, J. Gubicza, G. Krállics, A. Fodor, Evolution of microstructure and texture in an ultrafine-grained Al6082 alloy during severe plastic deformation, Mater. Sci. Eng. A. 490 (2008) 335–342.

[258] N.Q. Chinh, J. Gubicza, T.G. Langdon, Characteristics of face-centered cubic metals processed by equal-channel angular pressing, J. Mater. Sci. 42 (2007) 1594–1605.

[259] M.Y. Murashkin, A.R. Kil'mametov, R.Z. Valiev, Structure and mechanical properties of an aluminum alloy 1570 subjected to severe plastic deformation by high-pressure torsion, Phys. Met. Metallogr. 106 (2008) 90–96.

[260] Dislocations and Strengthening mechanism, Univ. Virginia, Dept. Mater. Sci. Eng. (n.d.). https://slideplayer.com/slide/13819356/ (accessed 4 June 2021).

[261] D. Hull, D.J. Bacon, Chapter 4 - Elastic Properties of Dislocations, in: D. Hull, D.J. Bacon (Eds.), Introd. to Dislocations, 5th ed., Butterworth-Heinemann, Oxford, 2011: pp. 63–83. https://doi.org/https://doi.org/10.1016/B978-0-08-096672-4.00004-9.